

**What is the possible origin of the  $^{195}\text{Pt}$  NMR shielding in the solid state? X-ray diffraction, solid-state NMR studies of deceptively simple  $\text{C}_2[\text{PtX}_6]$  salts (C = various cations, X =  $\text{Cl}^-$  and  $\text{Br}^-$ )**

by

James Arthur Odendal

*Dissertation presented for the degree of Doctor of Science in the  
Faculty of Science at  
Stellenbosch University*



Supervisor: Prof. Klaus R. Koch

Co-supervisor: Prof. Leonard J. Barbour

March 2015

### **Declaration**

By submitting this thesis electronically, I declare that the entirety of the work contained therein is my own, original work, that I am the sole author thereof (save to the extent explicitly otherwise stated), that reproduction and publication thereof by Stellenbosch University will not infringe any third party rights and that I have not previously in its entirety or in part submitted it for obtaining any qualification.

March 2015

# Abstract

The primary objective of the work presented in this thesis is to investigate the sensitivity and nature of the  $^{195}\text{Pt}$  chemical shift in the solid-state, as a function of temperature. We have carried out a series of experimental single crystal X-ray diffraction (SCXRD), solid state nuclear magnetic resonance (SSNMR) and density functional theory (DFT) experiments and calculations on various *dication hexachloridoplatinate(IV)* salts to paint a picture of the nature of the  $^{195}\text{Pt}$  shielding in the solid state.

The results obtained from SCXRD analyses performed as a function of temperature on  $\text{Rb}_2\text{PtCl}_6$ ,  $(\text{NH}_4)_2\text{PtCl}_6$  and  $[(\text{N}(\text{CH}_3)_4)_2\text{PtCl}_6]$  salts give a detailed account on the changing inter- and intramolecular interactions in *dication hexachloridoplatinate(IV)* salts upon lattice expansion, as a function of increasing temperature. The  $^{195}\text{Pt}$  SSNMR measurements of these salts have a peculiar  $^{195}\text{Pt}$  chemical shift sensitivity to changes in temperature. The  $^{195}\text{Pt}$  chemical shift trends performed as a function of temperature of the  $\text{Rb}_2\text{PtCl}_6$  salt resulted in a linear-like trend with the slope of  $\delta^{195}\text{Pt}/T = 0.362 (0.008) \text{ ppm/K}$ . The  $(\text{NH}_4)_2\text{PtCl}_6$  salt trend showed some non-linear characteristics at lower temperatures and tended towards linearity at a higher temperature with the slope  $\delta^{195}\text{Pt}/T = 0.228 (0.0126) \text{ ppm/K}$ . The  $^{195}\text{Pt}$  chemical shift of the  $[(\text{N}(\text{CH}_3)_4)_2\text{PtCl}_6]$  had quite a different trend due to its well-known structural phase transitions as a function of temperature. The expected sensitivity range of the  $^{195}\text{Pt}$  chemical shift, predicted from experimental temperature dependent (100 K and 400 K) SCXRD measurements of  $\text{Rb}_2\text{PtCl}_6$  and  $(\text{NH}_4)_2\text{PtCl}_6$  salts coincide well with that of experimental  $^{195}\text{Pt}$  chemical shift sensitivity.

The atomic coordinates obtained from SCXRD analyses performed as a function of temperature were used to conduct DFT calculations to extract SSNMR parameters together with electrostatic potentials in order to study the local molecular and electronic structures of  $\text{Rb}_2\text{PtCl}_6$  and  $(\text{NH}_4)_2\text{PtCl}_6$  salts. The computed  $^{195}\text{Pt}$  SSNMR parameters gave an account of chemical shift parameters and quadrupolar coupling parameters, which show excellent agreement with experimental  $^{195}\text{Pt}$  chemical shift SSNMR measurements. These calculations shed some light on the  $^{35}\text{Cl}$  SSNMR parameters, which to date are still unobtainable by means of conventional experimental SSNMR measurements. The computed  $^{35}\text{Cl}$  SSNMR shielding parameters showed that the electronic environments of the  $\text{Cl}^-$  ion in *dication hexachloridoplatinate(IV)* salts are central to the understanding and interpretation of experimental  $^{195}\text{Pt}$  chemical shift sensitivity. These

computational analyses gave the means to propose a theory whereby the : “polarization of electronic charge density from the  $\text{Pt}^{\text{IV}}$  ion towards the  $\text{Cl}^-$  ion as the interaction between the anion and cation are being weakened due to lattice expansion as a function of increasing temperature”.

This thesis shows that the combination of these three usually independently used analytical techniques are crucial in understanding the behaviour of experimental  $^{195}\text{Pt}$  chemical shift *dication hexachloridoplatinate(IV)* salts in the solid state.



## Abstract (Afrikaans)

Die primêre doel van die werk wat in hierdie tesis beskryf word was om die sensitiwiteit en die aard van die  $^{195}\text{Pt}$  chemiese afskerming tensor in die vaste toestand as 'n funksie van temperatuur te ondersoek. Ons het 'n reeks enkelkristal X-straal diffraksie (SCXRD) en vastestof kernmagnetiese resonansie (SSNMR) eksperimente asook (kwantum meganiese) DFT (*density functional theory*) berekeninge op verskeie dikatioon heksachloroplatinaat (IV) soute uitgevoer ten einde 'n beeld te vorm van die aard van die  $^{195}\text{Pt}$  kern in die vaste toestand.

Die resultate verkry deur SCXRD ontledings van die soute  $\text{Rb}_2\text{PtCl}_6$ ,  $(\text{NH}_4)_2\text{PtCl}_6$  en  $[(\text{N}(\text{CH}_3)_4)_2\text{PtCl}_6]$ , uitgevoer as 'n funksie van temperatuur, gee gedetailleerde informasie rakende die veranderende inter-en intramolekulêre interaksies in hierdie heksachloroplatinaat (IV) soute tydens uitsetting van die kristalstruktuur as 'n funksie van toenemende temperatuur. Die  $^{195}\text{Pt}$  SSNMR metings van hierdie soute toon 'n eienaardige  $^{195}\text{Pt}$  chemiese afskerming sensitiwiteit tot temperatuurveranderinge. Die  $^{195}\text{Pt}$  chemiese afskerming in die sout  $\text{Rb}_2\text{PtCl}_6$  bepaal as 'n funksie van die temperatuur lei tot 'n effektief lineêre tendens; die tendens vir die  $(\text{NH}_4)_2\text{PtCl}_6$  sout toon 'n aantal nie-lineêre eienskappe by laer temperature en neig tot lineariteit by hoër temperatuur. Die  $^{195}\text{Pt}$  chemiese afskerming van  $[(\text{N}(\text{CH}_3)_4)_2\text{PtCl}_6]$  het 'n merkbaar verskillende tendens as gevolg van sy welbekende strukturele faseveranderinge as 'n funksie van temperatuur. Die verwagte sensitiwiteit van die  $^{195}\text{Pt}$  chemiese afskerming soos voorspel vanaf eksperimentele temperatuur afhanklikheid (100 K en 400 K) SCXRD metings van  $\text{Rb}_2\text{PtCl}_6$  en  $(\text{NH}_4)_2\text{PtCl}_6$  soute stem goed ooreen met die eksperimentele  $^{195}\text{Pt}$  chemiese afskerming sensitiwiteit.

Die atoomkoördinate verkry vanaf SCXRD ontledings uitgevoer as 'n funksie van temperatuur is gebruik om DFT berekeninge van SSNMR parameters en elektrostatiese potensiale uit te voer en sodoende die plaaslike molekulêre en elektroniese struktuur van die  $\text{Rb}_2\text{PtCl}_6$  en  $(\text{NH}_4)_2\text{PtCl}_6$  soute te bestudeer. Die berekende  $^{195}\text{Pt}$  SSNMR parameters verskaf 'n rekening van chemiese afskerming parameters en quadrupoolkoppeling parameters wat oortuigende ooreenkomste toon met eksperimentele  $^{195}\text{Pt}$  SSNMR metings. Hierdie berekeninge werp ook lig op die  $^{35}\text{Cl}$  SSNMR parameters, tot dusver nog onbekombaar deur middel van konvensionele eksperimentele SSNMR metings. Die berekende  $^{35}\text{Cl}$  SSNMR parameters het getoon dat die elektroniese omgewings van die Cl-ioon in dikatioon heksachloroplatinaat (IV) soute sentraal staan in die begrip en interpretasie van  $^{195}\text{Pt}$  chemiese afskerming sensitiwiteit. Hierdie kwantum meganiese berekeninge fasiliteer 'n voorstel van "polarisering van elektroniese ladingsdigtheid van die Pt-ioon na die Cl-ioon as die

interaksie tussen die anioon en kation verswak weens kristalstruktuuruitsetting as 'n funksie van die toenemende temperatuur".

Hierdie tesis toon dat die kombinasie van hierdie drie analitiese tegnieke, wat meestal onafhanklik gebruik word, van kardinale belang is in die begrip van die gedrag van  $^{195}\text{Pt}$  chemiese afskerming in dikation heksachloroplatinaat (IV) soute in die vaste toestand.

# Acknowledgements

Firstly, I would like to thank my supervisor Prof. Klaus Koch who guided me through the first six years of my academic research career. To my co-supervisor Prof. Len Barbour, for allowing me to engage with his research group, whom I bugged tremendously for assistance with the crystallographic part of my PhD studies. I am truly grateful that you gave me the opportunity to work under your supervision for my PhD project. I would also like to thank Prof. Delia Haynes for being so awesome and who introduced me to the world of Supramolecular chemistry.

To all PGM research group members, old and new, thank you for creating such a great environment during the past six years of my post-graduate studies. I would also like to thank the members of the Supramolecular Nanostructured Functional Materials Group.

I would also like to thank my mother and father, Without the two of you, none of this would be possible and so I thank you for bringing me into this world.

Lastly, to my loving fiancée Katharina and our bundle of joy, our little boy Timothy. I have no words to describe the joy both of you have brought into my life.

## Conferences

### 1. 40th South African Chemical Institute convention (2011)

**Poster Presentation** - Investigating intra and intermolecular bond displacement in *dication hexahaloplatinate (IV)* salts as a function of temperature using Single-Crystal X-ray Diffraction,  $^{195}\text{Pt}$  Solid-state NMR and Density functional Theory (DFT)

**Awarded:** The Dalton Transactions prize for Inorganic Chemistry

<http://bit.ly/fDpet>

### 2. Indaba 7 - The South African Crystallographic Society (2012)

**Poster Presentation** - What is the possible origin of the  $^{195}\text{Pt}$  NMR shielding trends in the solid state? X-ray diffraction, solid-state NMR and Density functional Theory (DFT) studies of deceptively simple  $\text{X}_2[\text{PtCl}_6]$  salts (C= various cations)

## International Oral Presentations

### 1. Invited Lecture at Humboldt University, Berlin Germany (2013)

Presentation at Inorganic Chemistry Department in the group of Dr. K. Ray and Prof. Dr. K. Rademann.

**Title:** Probing the sensitivity of the  $^{195}\text{Pt}$  shielding tensor in the solid state, a SSNMR, XRD and DFT study

Contactable References:

<http://www.chemie.hu-berlin.de/forschung-en/ray/ray-en>

### 2. Invited Lecture at Free University, Berlin Germany by Dr. Axel Rodenstein (2012)

Presentation at Inorganic Chemistry Department in Prof. Ulrich Abram research group

**Title:** Probing the sensitivity of the  $^{195}\text{Pt}$  shielding tensor in the solid state, a SSNMR, XRD and DFT study

Contactable References:

[http://www.bcp.fu-berlin.de/chemie/ac/arbeitsgruppen/prof\\_abram.html](http://www.bcp.fu-berlin.de/chemie/ac/arbeitsgruppen/prof_abram.html)

3. **Invited Lecture at Friedrich-Alexander-University, Erlangen-Nuremberg, Erlangen, Germany**

Presented at Department of Inorganic Chemistry in groups of Prof. Dr. Karsten Meyer

**Title:** Probing the sensitivity of the  $^{195}\text{Pt}$  shielding tensor in the solid state, a SSNMR, XRD and DFT study

Contactable References:

<http://www.inorganic-chemistry.net/kmpages/index.html>

4. **Invited Lecture at University of Zurich , Department of Inorganic Chemistry, Zurich, Switzerland**

Presentation at Inorganic Chemistry Department in group of Prof. Dr. R. Alberto

**Title:** Probing the sensitivity of the  $^{195}\text{Pt}$  shielding tensor in the solid state, a SSNMR, XRD and DFT study

Contactable References:

<http://www.chem.uzh.ch/research/alberto.html>

# TABLE OF CONTENTS

Declaration .....	iii
Abstract (English) .....	iv
Abstract (Afrikaans) .....	v
Acknowledgements.....	vi
Conferences and International Oral Presentations .....	vii

## Chapter 1 General Introduction to $^{195}\text{Pt}$ NMR

Introduction .....	1
Aims and Objectives .....	7
References.....	10

## Chapter 2 Solid state hydration of the $[\text{PtCl}_6]^{2-}$ anion

Synopsis .....	11
Introduction .....	12
Experimental .....	15
2.1 Synthesis of dication (dibenzo-24-crown-8)-dication hexachloroplatinate(IV) .....	15
2.1.1 Synthesis of dibenzo-24-crown-8-ether disodium hexachloroplatinate(IV) salts .....	15
2.1.2 Synthesis of dibenzo-24-crown-8-ether dipotassium hexachloroplatinate(IV) salts .....	16
2.2 Cambridge Structural Database search .....	16
2.2.1 Dibenzo-24-crown-8-ether with $\text{Na}^+$ and $\text{K}^+$ search .....	16

2.2.2 CSD analysis of crystal structures containing $[\text{PtCl}_6]^{2-}$ and $\text{H}_2\text{O}$ .....	16
2.3 Single-Crystal X-ray Diffraction Analyses (SCD/XRD) .....	17
Results .....	18
2.4 Crown ether complexes with (dication)-hexachloroplatinate(IV) .....	18
2.4.1 Dibenzo-24-crown-8 disodium hexachloroplatinate(IV) salts .....	18
2.4.2 Dibenzo-24-crown-8 dipotassium hexachloroplatinate(IV) salts.....	19
2.5 Cambridge Structural Database Analyses .....	21
2.5.1 Dibenzo-24-crown-8 with a $\text{Na}^+$ and $\text{K}^+$ Analysis .....	22
2.6 CSD search for $\text{H}_2\text{O}$ associated with $[\text{PtCl}_6]^{2-}$ anions .....	27
Discussion and Concluding Remarks .....	37
References.....	45

## **Chapter 3 Single Crystal X-ray Diffraction Analysis of Dication Hexachloroplatinate(IV) Salts as a Function of Temperature**

Synopsis .....	47
Introduction .....	48
Experimental .....	50
3.1 Synthesis of dication hexachloroplatinate(IV)salts .....	50
3.1.1 Synthesis of dication hexachloroplatinate(IV) salt $[\text{Rb}_2\text{PtCl}_6]$ , $[(\text{NH}_4)_2\text{PtCl}_6]$ and $[(\text{N}(\text{CH}_3)_4)^+]_2\text{PtCl}_6$ .....	50
Results and Discussion .....	52
3.2 Single crystal X-ray diffraction characterization of dirubidium hexachloroplatinate(IV) salt, $[\text{Rb}_2\text{PtCl}_6]$ as a function of temperature .....	52

3.3 Single crystal X-ray diffraction characterization of diammonium hexachloroplatinate(IV) salt, [(NH <sub>4</sub> ) <sub>2</sub> PtCl <sub>6</sub> ] as a function of temperature .....	58
3.4 Single crystal X-ray diffraction characterization bis(tetramethylammonium) hexachloroplatinate(IV) salt [N(CH <sub>3</sub> ) <sub>4</sub> ] <sub>2</sub> PtCl <sub>6</sub> ] as a function of temperature .....	65
References.....	74

## Chapter 4 Solid State Nuclear Magnetic Resonance Spectroscopy of C<sub>2</sub>PtCl<sub>6</sub> Salts to Probe the Temperature Dependence of the <sup>195</sup>Pt NMR Shielding

Introduction.....	75
4.1 Solid-state Nuclear Magnetic Resonance Theory .....	77
4.1.1 Nuclei in a static uniform field .....	77
4.1.2 Nuclear spin interaction .....	79
4.1.3 Interaction tensors in solid-state NMR .....	81
4.1.4 Graphical Summary of Internal spin interactions .....	84
4.1.5 Magic-angle Spinning (MAS).....	87
4.1.6 Cross-polarization (CP) Techniques .....	88
4.1.7 Cross-polarization Magic Angle Spinning (CPMAS) .....	88
Experimental .....	89
4.2 Instrument Details .....	89
4.3 Synthesis of dication hexachloroplatinate(IV) [C <sub>2</sub> PtCl <sub>6</sub> ] salts (C = Various cation) .....	89
4.4 <sup>195</sup> Pt and <sup>87</sup> Rb MAS SSNMR of Rb <sub>2</sub> PtCl <sub>6</sub> , <sup>195</sup> Pt for (NH <sub>4</sub> ) <sub>2</sub> PtCl <sub>6</sub> and,	



<sup>195</sup> Pt for [(CH <sub>3</sub> ) <sub>4</sub> N] <sub>2</sub> PtCl <sub>6</sub> .....	89
Results and Discussion .....	90
4.5.1 <sup>195</sup> Pt CP MAS SSNMR of (NH <sub>4</sub> ) <sub>2</sub> PtCl <sub>6</sub> .....	90
4.5.2 <sup>195</sup> Pt CP MAS SSNMR of Rb <sub>2</sub> PtCl <sub>6</sub> .....	97
4.5.3 <sup>87</sup> Rb MAS SSNMR experimental analysis of Rb <sub>2</sub> PtCl <sub>6</sub> .....	101
4.5.4 <sup>195</sup> Pt CP MAS SSNMR of [(CH <sub>3</sub> ) <sub>4</sub> N] <sub>2</sub> PtCl <sub>6</sub> .....	105
Concluding Remarks .....	108
References.....	110

## **Chapter 5 A DFT computational Assessment of the possible Origin of the Temperature Dependence of the <sup>195</sup>Pt shielding in the solid state in C<sub>2</sub>[PtCl<sub>6</sub>] (C = Rb<sup>+</sup> and NH<sub>4</sub><sup>+</sup>)**

Synopsis .....	112
Introduction .....	113
5.1 Background definitions of the NMR parameters .....	115
5.2 Identification of NMR parameters from SSNMR spectra .....	116
Experimental .....	118
5.3 Convergence of computed NMR parameters .....	119
Results and Discussion .....	121
5.4 NMR-CASTEP Computational results of <sup>195</sup> Pt isotropic chemical shift of (NH <sub>4</sub> ) <sub>2</sub> PtCl <sub>6</sub> and Rb <sub>2</sub> PtCl <sub>6</sub> .....	121
5.5 The Pt <sup>4+</sup> ion electrostatic potential calculations by VAMP of (NH <sub>4</sub> ) <sub>2</sub> PtCl <sub>6</sub> and Rb <sub>2</sub> PtCl <sub>6</sub> .....	127
5.6 NMR-CASTEP Computational results of <sup>35</sup> Cl isotropic, anisotropic chemical shift, and quadrupolar coupling of (NH <sub>4</sub> ) <sub>2</sub> PtCl <sub>6</sub> and Rb <sub>2</sub> PtCl <sub>6</sub> .....	128

5.7 The Cl <sup>-</sup> ion electrostatic potential calculations by VAMP for (NH <sub>4</sub> ) <sub>2</sub> PtCl <sub>6</sub> and Rb <sub>2</sub> PtCl <sub>6</sub> .....	132
5.8 NMR-CASTEP Computational results of <sup>87</sup> Rb isotropic chemical shift of Rb <sub>2</sub> PtCl <sub>6</sub> and <sup>14</sup> N isotropic, <sup>1</sup> H isotropic anisotropic and quadrupolar coupling of (NH <sub>4</sub> ) <sub>2</sub> PtCl <sub>6</sub> .....	133
5.9 The electrostatic potential calculations by VAMP of the cations: Rb <sup>+</sup> ion in Rb <sub>2</sub> PtCl <sub>6</sub> and N <sup>+</sup> and H <sup>+</sup> ion in (NH <sub>4</sub> ) <sub>2</sub> PtCl <sub>6</sub> .....	139
Concluding Remarks .....	142
References.....	143

## Chapter 6 Conclusions and Recommendation for Future work

Conclusions .....	145
Recommendation for future work.....	150
Reference.....	152

## APPENDICES

Appendix A.....	153
Appendix B.....	154
Appendix C.....	157
Appendix D.....	160

## On Additional CD

*"It is the nature of great research that one cannot predict what basic new insights about the workings of nature will emerge, nor can one dream of what practical applications will follow."*

*- John Rigden in "Hydrogen: The Essential Element",  
Harvard University Press, 2002.*

# Chapter 1

## General Introduction to $^{195}\text{Pt}$ NMR and Solvation of the $[\text{PtCl}_6]^{2-}$ Anion

South Africa is the world's primary producer of platinum, contributing more than three quarters of the world supply in 2012 in addition to producing a large proportion of the associated platinum group metals (PGMs, Pt, Pd, Rh, Ru, Ir and Os).<sup>1</sup> This highlights the need for our South African scientific community to push boundaries in understanding the chemistry of precious metals; not only to find means to rapidly extract and deplete this precious metal resource for export but also to elucidate the chemical blueprint of this noble metal. During the precious metal refinery process platinum is usually extracted as the *hexachloridoplatinate(IV)*  $[\text{PtCl}_6]^{2-}$  anionic complex due to its known stability in highly acidic, chloride-rich matrices, which are still the favoured conditions for selective separation and extraction. This thesis studies the Pt atom in its  $[\text{PtCl}_6]^{2-}$  anionic form in a variety of different chemical analogues *dication hexachloridoplatinate(IV)* salts, *crown-ether dication hexachloridoplatinate(IV)* and hydrated *hexachloridoplatinate(IV)*.

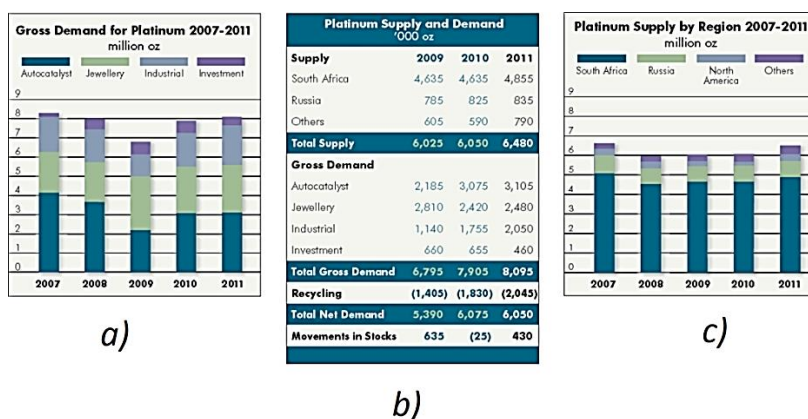


Figure 1.1 Platinum report 2012, published by Johnson Matthey, May 2012 a) World demand of Pt b) World supply of Pt and c) Pt supply by region<sup>2</sup> (all redrawn from the Johnson Matthey 2012 report)

Platinum is one of the noble transition metal elements, with 32 atomic isotopes. Only three of these isotopes have a significant natural abundance, *i.e.*  $^{194}\text{Pt}$  (32.9%),  $^{195}\text{Pt}$  (33.8%) and  $^{196}\text{Pt}$  (25.3%) of which  $^{195}\text{Pt}$  is the only active NMR isotope.<sup>2</sup> The first reports giving some insights into the sensitivity of the  $^{195}\text{Pt}$  NMR nuclear shielding only appeared in the late 1960's, in which Pidock *et al.*<sup>3</sup> and von Zelewsky<sup>4</sup> attributed the sensitivity to the ligand present in the coordination sphere and stereochemistry. The  $^{195}\text{Pt}$  chemical shift has been reported to be particularly sensitive to changes in the atom's metal oxidation states,<sup>5</sup> ligand substitution<sup>6</sup>, molecular composition<sup>7</sup>, conformation<sup>8</sup>, temperature and pressure. In these studies, the  $^{195}\text{Pt}$  NMR chemical shift shows remarkable response to any change which occurs within its chemical environment. Moreover, it was found that the range of the  $^{195}\text{Pt}$  chemical shielding span is an enormous 13 000 ppm.<sup>9</sup>

In heavy atoms the isotropic shielding ( $\sigma$ ) of a nucleus can be approximately formulated as a sum of at least four terms.

$$\sigma_{\text{overall}} = \sigma_d + \sigma_p + \sigma_{SO} + \sigma_{\text{other}}$$

$\sigma_d$  = diamagnetic term

$\sigma_p$  = paramagnetic term

$\sigma_{SO}$  = spin orbit term

$\sigma_{\text{other}}$  = due to factors such as solvation, temperature and pressure

The first reported attempt to understand NMR shielding was made by Ramsey *et al.*<sup>10</sup> in which they highlighted the main physical contributing factors responsible for experimentally observed NMR shielding *i.e.* paramagnetic and diamagnetic terms for light elements. They later showed that for heavier elements, spin-orbit term and solvation effects also contribute to experimentally observed chemical shielding.<sup>11</sup> The work done by Wolff *et al.*<sup>12</sup> and later by Koch *et al.*<sup>13</sup> showed how individual isotropic chemical shielding parameters influence the  $^{195}\text{Pt}$  shielding, which established that paramagnetic and spin-orbit parameters were the main contributors to experimentally observed  $^{195}\text{Pt}$  isotropic chemical shielding. The experimental and theoretical studies carried out by Jameson *et al.*<sup>14</sup> showed how the sensitivity of  $^{195}\text{Pt}$  nuclear shielding is due to changes in the nucleus chemical environment, which is as a result of an atom's spin-orbit splitting in the valence p-shell (d-shell for transition elements) from a free atom in its ground state. These findings of Jameson<sup>15</sup> were later correlated with a range of chemical shifts from NMR active nuclei.

The theoretical and experimental studies carried out on the  $[\text{PtCl}_6]^{2-}$  type complexes showed that the sensitivity of  $^{195}\text{Pt}$  nuclear magnetic shielding can be determined by observed isotope shifts and temperature dependence chemical shielding in the zero pressure limits.<sup>16</sup> Since the  $^{35}/^{37}\text{Cl}$  isotopes have different atomic masses, it would naturally imply a difference for  $\text{Pt}-^{35}\text{Cl}$  and  $\text{Pt}-^{37}\text{Cl}$  bond length. The theoretical and experimental studies carried out by Jameson *et al.*<sup>17</sup> underline the significant dependence of  $^{195}\text{Pt}$  nuclear magnetic shielding on the inter-nuclear distance between the NMR active nuclei and bounding ligands.

The additional experimental and theoretical work carried out by Koch *et al.*<sup>14</sup> confirmed the findings of Jameson *et al.*<sup>17</sup>, showing that the Pt-Cl bond displacement is a key factor contributing to the sensitivity of  $^{195}\text{Pt}$  chemical shift for a series of octahedral  $[\text{PtX}_{6-n}]^{2-}$  complexes for (X = Cl, Br, F, I). These calculations were performed to assess the accuracy of experimental NMR chemical shielding in order to gain additional insight into the dominant  $^{195}\text{Pt}$  isotropic chemical shielding contributing factors *i.e.* diamagnetic, paramagnetic and spin orbital shielding contributions. This work has shown that the  $^{195}\text{Pt}$  chemical shift sensitivity is correlated to the Pt-X bond displacement in  $[\text{PtX}_{6-n}]^{2-}$  complexes (where X = Cl, Br, F, I). These results showed that the  $^{195}\text{Pt}$  chemical shift is largely dependent on the halide ions which show decreasing  $^{195}\text{Pt}$  chemical shift from 248, 183, 157 to 120 ppm/picometer for  $[\text{PtF}_6]^{2-}$ ,  $[\text{PtCl}_6]^{2-}$ ,  $[\text{PtBr}_6]^{2-}$  and  $[\text{PtI}_6]^{2-}$  respectively. The work carried out by Koch *et al.*<sup>14</sup> and Jameson *et al.*<sup>17</sup> in the gaseous and aqueous phase both suggest that changes in Pt-Cl bond displacement will dramatically influence the observed  $^{195}\text{Pt}$  chemical shift (Figure 1.2). The computational results from the Koch *et al.*<sup>14</sup> study showed the  $^{195}\text{Pt}$  chemical shift sensitivity to Pt-Cl bond displacement to be 18 300 ppm/Å.

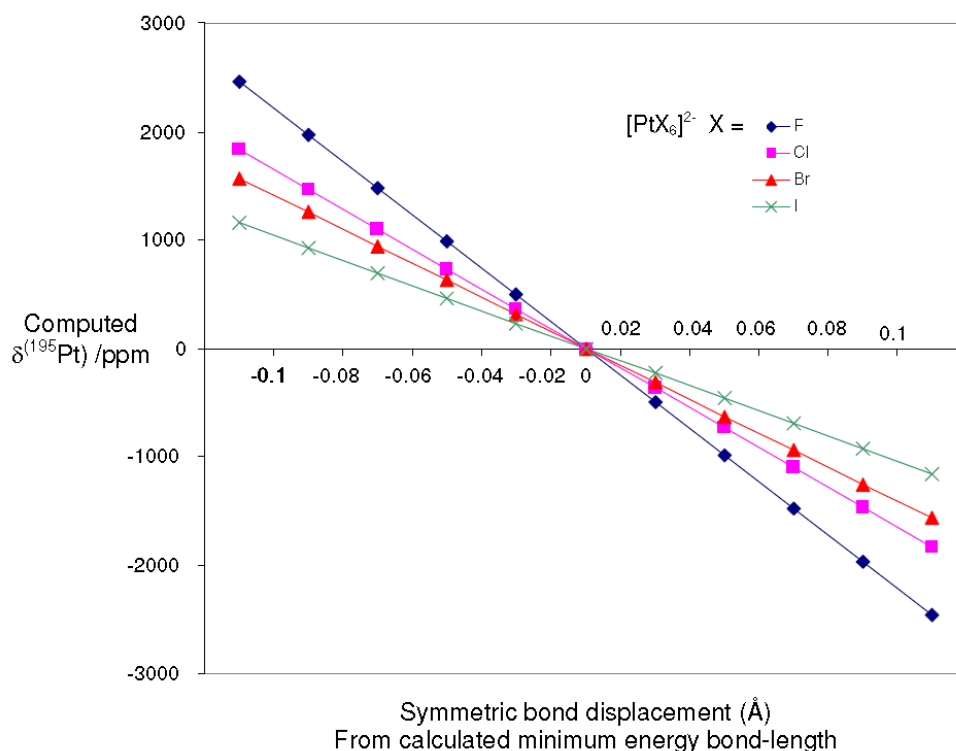


Figure 1. 2 Summary of the sensitivity  $\partial(\delta_{(195\text{Pt})}) / \partial(\text{Pt-X})$  of the total shielding tensor of the platinum nucleus for the  $[\text{PtX}_6]^{2-}$  complexes, where  $\text{X} = \text{F}, \text{Cl}, \text{Br}$  and  $\text{I}$  as a function of symmetrical bond displacements relative to the minimum energy value of the optimized octahedral complex in the gas-phase. (Image from reference 14)

The recent developments in advanced density functional theory (DFT) computational methodology have made it easier to compute reliable NMR shielding parameters.<sup>17</sup> This provided a means to gain a more fundamental insight into the nature of experimentally observed  $^{195}\text{Pt}$  chemical shift, leading to a better interpretation of experimental NMR shielding. The first researchers to investigate the nature of  $^{195}\text{Pt}$  NMR shielding using computational methods were Schreckenbach & Ziegler.<sup>18</sup> They used gauge including atomic orbitals (GIAO) with the DFT approach, which produced close to accurate experimentally observed  $^{195}\text{Pt}$  chemical shift. The theoretical work carried out by Gilbert & Ziegler<sup>19</sup> significantly improved the computational method for predicting NMR chemical shifts by incorporating relativistic corrections for heavy metal nuclei which included spin-orbital effects. The use of zeroth order regular approximation (ZORA) relativistic corrections gave Wolff *et al.*<sup>20</sup> an advantage, which made it possible to accurately predict  $^{195}\text{Pt}$  chemical shielding for a series of simple Pt(II) complexes for the first time.

The new DFT insights highlighted the limitations of the then widely used Dean & Green equations for the semi-quantitative understanding of NMR shielding of heavy metal nuclei.<sup>21</sup> The

review by Autschbach *et al.*<sup>22</sup> entails a comprehensive overview of the latest developments of DFT methodology to predict  $^{195}\text{Pt}$  chemical shift of several inorganic complexes. The theoretical work carried out by Autschbach shed some light on several challenges and limitations which, if perfected, could aid in computing more accurate NMR shielding parameters of heavier metal complexes.

In hindsight, the experimental and theoretical work carried out by Jameson *et al.*<sup>23</sup> in order to understand the factors which affect the NMR shielding of the heavy metal nuclei should be mentioned as relevant to simple metal complexes of type  $(\text{MX}_6)^{n\pm}$  complexes. Autschbach<sup>24</sup> drew attention to several challenges which remain in the computation of more accurate NMR shielding parameters of metal complexes, such as the importance of unspecific solvent-solute effects. The computational and experimental studies done by Koch *et al.*<sup>25</sup> investigated how solvent-solute effects influence  $^{195}\text{Pt}$  chemical shifts. Their findings demonstrate the effect that different solvents have on the  $^{195}\text{Pt}$  chemical shifts of the  $[\text{PtCl}_6]^{2-}$  anion (Figure 1.3). This brings into question what role the  $\text{Cl}^-$  ion plays in the experimentally observed  $^{195}\text{Pt}$  chemical shift. It is however, not possible to investigate the chemical environment of the  $\text{Cl}^-$  ion of  $[\text{PtCl}_6]^{2-}$  anion using solution NMR since it has such fast relaxation times in solution. This makes it quite difficult to assess how these different solvents influence the electronic structure of the  $\text{Cl}^-$  ion of the  $[\text{PtCl}_6]^{2-}$  anion which is then translated to the  $\text{Pt}^{\text{IV}}$  ion.

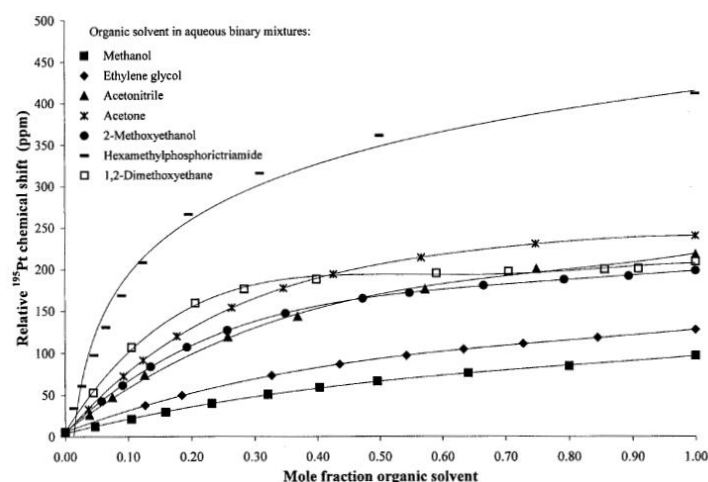


Figure 1. 3 The variation of  $\delta^{195}\text{Pt}$  as a function of bulk solvent composition for various aqueous binary mixtures ( $\text{D}_2\text{O}$  + organic solvents) containing  $\text{PtCl}_6^{2-}$ , best-fit trend lines have been inserted. (Image from reference 26)

The DFT and Molecular Dynamics (MD) study carried out by Naidoo *et al.*<sup>26</sup> on the structure and geometry of the hydration shells surrounding the  $[\text{PtCl}_6]^{2-}$  anion, reveals a well-defined hydration



shell in close proximity to the chlorido-anion (Figure 1.4). These findings led them to speculate that the sensitivity of experimentally observed  $^{195}\text{Pt}$  chemical shifts of  $[\text{PtCl}_6]^{2-}$  complexes to solvent composition may in part be due to the intimate solvent-solute interactions. They further concluded that the solvent-solute interaction could lead to subtle changes within the covalent Pt-Cl bond lengths. This was further investigated by computationally assessing the effect that a water molecule interaction with the  $\text{Cl}^-$  ion of the  $[\text{PtCl}_6]^{2-}$  anion has on the  $^{195}\text{Pt}$  chemical shift. The hydrogen bonding interaction ( $\text{Pt}-\text{Cl}\cdots\text{H}-\text{O}$ ) between the anion and water molecule were investigated within the inner hydration shell of  $[\text{PtCl}_6]^{2-}$  anion.<sup>27</sup> The results from these calculations show how both strength and orientation of the hydrogen bonding interaction ( $\text{Pt}-\text{Cl}\cdots\text{H}-\text{O}$ ) between the anion and water molecule induces a substantial downfield and upfield shift relative to the isolated  $[\text{PtCl}_6]^{2-}$  anion in the gas phase. These calculations show how the solvent interaction associating with the  $[\text{PtCl}_6]^{2-}$  anion is crucial in assessing how the  $\text{Cl}^-$  ion is influenced by the solvent solute interaction which in turn influences the  $^{195}\text{Pt}$  chemical shift.

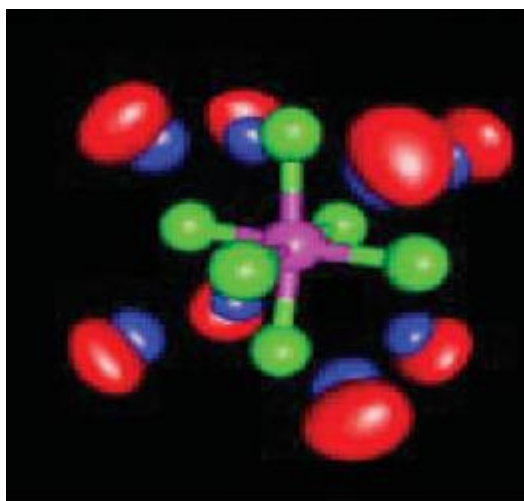


Figure 1. 4 PGM complex chlorido anions with water is probability density surfaces (oxygen in red and hydrogen in blue), at 50% greater than bulk for  $[\text{PtCl}_6]^{2-}$  (image from Ref. 27)

These experimental and theoretical studies that were carried out have paved the way for attempting to understand the sensitivity of  $^{195}\text{Pt}$  chemical shift in solution and gas-phase, respectively. However, little work exists which systematically investigates the sensitivity of this  $^{195}\text{Pt}$  chemical shift in solid-state. The  $^{195}\text{Pt}$  chemical shift measured using SSNMR carried out by Sparks *et al.*<sup>28</sup> explored the effects that static and MAS SSNMR experiments had on  $^{195}\text{Pt}$  chemical shift. They concluded that the strong dipolar coupling of the  $^{35/37}\text{Cl}$  isotopes influences the  $^{195}\text{Pt}$  chemical shift line width. They

performed a series of  $^{195}\text{Pt}$  MAS SSNMR measurements of  $\text{Pt}(\text{en})\text{Cl}_x$  ( $\text{en} = 1,2$  – diaminoethane,  $x = 2, 3, 4$ ) complexes to monitor the changing isotropic and anisotropic parameters.<sup>29</sup> Solid state  $^{195}\text{Pt}$  NMR measurements have been used to study crystal symmetry in numerous solid state systems.<sup>30</sup> The work by Hayashi *et al.*<sup>31</sup> discussed the dipole-dipole and indirect spin coupling between the  $^{35/37}\text{Cl}$  isotopes to the  $^{195}\text{Pt}$  nucleus. They also discuss the influence of strong quadrupolar coupling of  $^{35/37}\text{Cl}$  isotopes and its influence on the  $^{195}\text{Pt}$  line broadening.

## Aims and Objectives

This thesis essentially has two overall aims:

1. To investigate the hypothesis that  $[\text{PtCl}_6]^{2-}$  anions are hydrated and to establish the nature of the interaction of water molecules with the  $[\text{PtCl}_6]^{2-}$  anion in simple salts. This involved the investigation of a hydration shell of the  $[\text{PtCl}_6]^{2-}$  anions in the solid state using single crystal diffraction studies. We attempt to develop cation chelated crown-ether with the  $[\text{PtCl}_6]^{2-}$  anions crystal systems with the aim of crystalizing water in the vicinity of the  $[\text{PtCl}_6]^{2-}$  anion. The variable temperature single crystal x-ray diffraction data obtained from these experiments will be used to investigate the effect that weakening intramolecular interactions between the  $[\text{PtCl}_6]^{2-}$  anion and surrounding water molecules would have on the Pt-Cl bond displacement within the  $[\text{PtCl}_6]^{2-}$  anion. The hydration shell around the  $[\text{PtCl}_6]^{2-}$  anion will be investigated using an additional Cambridge Structural Database (CSD) analysis to search the current literature for crystal structures that may exhibit similar features to the computed hydration shell around the  $[\text{PtCl}_6]^{2-}$  anion. The combination of these two investigations will be used to give some insight into the degree of hydration of the  $[\text{PtCl}_6]^{2-}$  anion in the solid-state.
2. To determine the temperature dependence of the  $^{195}\text{Pt}$  NMR chemical shifts of simple  $\text{X}_2[\text{PtCl}_6]$ , ( $\text{X} =$  various cations) salts, with a view of understanding its origin, and to probe the link of the temperature dependence of the  $\delta(^{195}\text{Pt})$  NMR shielding (measured as the chemical shift) on the anticipated Pt-Cl bond displacement increase as a function of temperature. In Chapter 3 three *dication hexachloridoplatinate(IV)* salts are crystallized *i.e.* *dirubidium hexachloridoplatinate(IV)*  $\text{Rb}_2\text{PtCl}_6$ , *diammonium hexachloridoplatinate(IV)*  $(\text{NH}_4)_2\text{PtCl}_6$  and *bis(tetramethylammonium) hexachloridoplatinate(IV)*  $[\text{N}(\text{CH}_3)_4]_2\text{PtCl}_6$  salts. The *rubidium* salt which has a purely electrostatic interaction ( $\text{Rb}^+ \cdots \text{Cl}-\text{Pt}$ ) to the  $[\text{PtCl}_6]^{2-}$  anion is different to the

*ammonium* salt, that induces a partially electrostatic and strongly directed hydrogen bonding interaction ( $\text{N-H}\cdots\text{Cl-Pt}$ ). The *tetramethylammonium* ion is larger than the *rubidium* and *ammonium* cations which would have multiple hydrogen bonding interactions with the  $[\text{PtCl}_6]^{2-}$  anion, due to its methyl groups. These three crystals although already well-studied in the literature, are used to perform a series of temperature dependent SCXRD measurements. The results from these measurements are then used to give insight into the degree of atomic displacement, which would occur as a result of lattice expansion as a function of increasing temperature. The Pt-Cl bond lengths obtained from the SCXRD measurements performed as a function of temperature of the  $\text{Rb}_2\text{PtCl}_6$  and  $(\text{NH}_4)_2\text{PtCl}_6$  salts are used to calculate the expected  $^{195}\text{Pt}$  chemical shift.

In Chapter 4, the same three crystal structures are to be used to perform temperature dependent  $^{195}\text{Pt}$  MAS SSNMR experiments in order to assess the sensitivity of this nucleus in the solid state. The temperature dependence SCXRD data of all three salts will be inspected to see if any Pt-Cl bond displacement within the  $[\text{PtCl}_6]^{2-}$  anion occurs. The Pt-Cl bond displacement within the  $[\text{PtCl}_6]^{2-}$  anion has been suggested to be one of the central factors which contributes to the sensitivity of the  $^{195}\text{Pt}$  chemical shift in the gas and solution phase, respectively. This investigation would attempt to correlate the proposed hypothesis of Pt-Cl bond displacement in order to see if this is the case in the solid state. The temperature dependence SCXRD data can also be used to interpret the experimental  $^{195}\text{Pt}$  chemical shift trends. These experiments are used to see how the three cations (*rubidium*, *ammonium*, and *tetramethylammonium*) could possibly have an influence on the experimentally observed temperature dependence  $^{195}\text{Pt}$  chemical shift trends. The expected  $^{195}\text{Pt}$  chemical shift calculated from SCXRD analysis will be compared to that of the experimental  $^{195}\text{Pt}$  chemical shift as a function of temperature. Only a limited amount of structural information can be extracted from conventional SSNMR and SCXRD data and therefore cannot account for all possible long or short range changing effects such as atomic electrostatics and quantum mechanics during lattice expansion.

In Chapter 5, the final aim is to compute SSNMR and electrostatic potentials from atomic coordinates obtained from temperature dependent SCXRD measurements. This would

be computed using the solid-state quantum mechanics software interface Material Studio. The computed SSNMR parameters will be compared to that of the experimentally observed parameters. The quantum mechanically derived electrostatic potentials charges would then be used to gain additional insight into the electrostatics of *dication hexachloridoplatinate(IV)* salts in the hope that it would aid in the interpretation of the experimental  $^{195}\text{Pt}$  chemical shift trends.

This thesis contributes to the overall understanding and interpretation of complex temperature dependence SSNMR measurements by the use of three analytical methodologies. A comment on the interpretation of solid-state temperature dependence SCXRD analyses in *dication hexachloridoplatinate(IV)* salts crystal structure is given, which could be applied to other crystallographic systems also undergoing lattice expansion or contraction as a function of temperature.

---

## References

---

1. J. Butler, Platinum 2012 report, Johnson Matthey, May **2012**, T. Kendal, *Platinum 2005: Interim Review*, Johnson Matthey PLC, 2005.
2. J. R. L. Priqueler, I. S. Butler, F. D. Rochon, *Appl. Spec. Rev.*, **2006**, 41, 185.
3. A. Pidcock, R. E. Richards; L. M. Venanzi, *J. Chem. Soc. A*, **1968**, 1970.
4. A. V. Zelewsky, *Helv. Chim. Acta*, **1968**, 51, 803.
5. E. Wagner, M. Haukka, J. J. R. Frausto de Silva, A. J. L. Pambeiro, V. V. Kukushkin, *Inorg. Chem.*, **2001**, 40, 264.
6. I. A Kotze, W. J. Gerber, J.M McKenzie, K. R. Koch, *Eur. J. Inorg. Chem.* **2009**, 17, 2560.
7. P. Murray, K. R. Koch, *J. Coord. Chem.* **2010**, 63, 2561.
8. H. Majid, R. Mehdi, *J. Organom. Chem.*, **2005**, 4, 982.
9. R. K. Harris, B. E. Mann, *NMR and the Periodic Table*, Academic Press Inc., New York, **1978**.
10. N. F. Ramsey, *Phys. Rev.*, **1950**, 78, 699.
11. N. F. Ramsey, *Phys. perspect.*, **1999**, 1, 123.
12. S. K. Wolff, T. Ziegler, E. van Lenthe, E. J. Baerends, *J.Chem. Phys.*, **1999**, 110, 7689.
13. M. R. Burger, J. Kramer, H. Chermette, K. R. Koch, *Magn. Reson. Chem.*, **2010**, 48, S38.
14. C.J. Jameson, H. S. Gutowsky, *J.Chem. Phys.*, **1964**, 40, 1714.
15. C. J. Jameson, J. Mason; *In Multinuclear Nuclear Magnetic Resonance*, **1987**, 51–88. London: Plenum
16. C. J. Jameson, A. K. Jameson, *J. Chem. Phys.*, **1986**, 85, 5448.
17. E. J. Baerends, J. Autschbach, A. Berces, C. Bo, P. M. Boerrigter, L. Cavallo, Chong, D. P., L. Deng, R. M. Dickson, D. E. Ellis, M. v.F, L. Fan, T. H. Fischer, C. Fonseca, S. J. A. Guerra, J. van Gisbergen, A. Groeneveld, O. V. Gritsenko, M. Gruning, F. E. Harris, P. van den Hoek, H. Jacobsen, L. Jensen, G. van Kessel, F. Kootstra, E. van Lenthe, D.A. McCormack, A. Michalak, V. P.Osinga, S. Patchkovskii, P.H.T. Philipsen, D. Post, C. C. Pye, W. Ravenek, P. Ros, P. R. T. Schipper, G. Schreckenbach, J. G. Snijders, M. Sola, M. Swart, D. Swerhone, G. te Velde, P. Vernooijs, L. Versluis, O. Visser, F. Wang, E. van Wezenbeek, G. Wiesenekker, S.K. Wolff, T.K. Woo, A.L. Yakovlev, T. Ziegler, Amsterdam Density Functional, ADF2005.01, SCM, The Netherlands, Amsterdam: Theoretical Chemistry, Vrije Universiteit. <http://www.scm.com>.
18. G. Schreckenbach, T. Ziegler, *J. Phys. Chem.*, **1995**, 99, 606.
19. T.M. Gilbert, T. Ziegler, *J.Phys. Chem. A*, **1999**, 103, 7535.
20. S. K. Wolff, T. Ziegler, E. van Lenthe, E. J. Baerends, *J.Chem. Phys.*, **1999**, 110, 7689.
21. R. R. Dean, J. C. J. Green, *J. Am. Chem. Soc.*, **1968**, 3047.
22. J. Autschbach, *Coord. Chem. Rev.*, **2007**, 251, 1796.
23. C. J. Jameson, D. Rehder, M: Hoch, *J Am. Chem. Soc.*, **1987**, 109, 2589; C. J. Jameson; A. C. de Dios, *J Chem. Phys.*, **1993**, 98, 2208.
24. M. Sterzel & J. Autschbach, *Inorg. Chem.*, **2006**, 45, 3316.
25. A. N. Westra, Thesis : High resolution NMR studies concerning the solvation/hydration and coordination chemistry of Pt(II/IV) compounds, PhD thesis, Stellenbosch University, **2005**.
26. K. J. Naidoo, G. Klatt, K. R. Koch, D. J. Robinson, *Inorg. Chem*, **2002**, 41, 1845.
27. Klaus R. Koch, M. R. Burger, J. Kramer , A. N. Westra, *Dalton Trans.*, **2006**, 3277.
28. S. W. Sparks, P. D. Ellis, *J. Am. Chem. Soc.*, **1986**, 108, 3215.
29. E. J. W. Austin, P. J. Barrie, R. J. H. Clark, *J. Chem. Soc. Chem. Commun.*, **1993**, 403.
30. P. J. Heard, K. Kite, A. E. Aliev, *Polyhedron*, **1998**, 17, 2543.
31. S. Hayashi, K. Hayamizu, *Magn. Reson. Chem.*, **1992**, 30, 658

# Chapter 2

## Solid State Hydration of the $[\text{PtCl}_6]^{2-}$ Anion

### Synopsis

This chapter investigates the extent of hydration of the *hexachloridoplatinate(IV)* anion in the solid-state. The theoretical calculations carried out on the  $[\text{PtCl}_6]^{2-}$  anion in the presence of water suggests that the anion is hydrated by up to eight water molecules. This computational calculation also produced radial distribution functions values of the interatomic distance of  $\text{Cl}^-$  ion to O atom,  $\text{Cl}^-$  ion to H atom,  $\text{Pt}^{\text{IV}}$  ion to O atom and  $\text{Pt}^{\text{IV}}$  ion to H atom which describes the hydration shell of the  $[\text{PtCl}_6]^{2-}$  anion. A crystal engineering approach is taken to design a molecular system, which could allow water molecules to associate with the  $[\text{PtCl}_6]^{2-}$  anion in a similar manner to that of the simulated hydration shell of this anion. A Cambridge Structural Database (CSD) survey, which displays features of the computed hydration shell of the  $[\text{PtCl}_6]^{2-}$  anion in water is discussed. These results show that the  $[\text{PtCl}_6]^{2-}$  anion is hydrated by up to four water molecules in an approximately similar position to that of the hydration shell of the anion. The crystal structures obtained from the CSD survey are used to validate the accuracy of the simulated radial distribution function values of the atomic position for the solution structure of the hydration shell around the  $[\text{PtCl}_6]^{2-}$  anion in water. The hydration shell calculation shows that the H atom of the water molecules point towards the faces of the  $[\text{PtCl}_6]^{2-}$  anion. A comment on the directionality of hydrogen bonding interactions to the anion is given.

---

## Introduction

---

The structure of the primary water hydration shell of the  $[\text{PtCl}_6]^{2-}$  anion has been predicted by “conductor-like screening model” (COSMO) calculations (see Fig. 2.1)<sup>1</sup> and raises the question of the veracity of this model. This calculation was used to determine the electrostatic interactions of the  $[\text{PtCl}_6]^{2-}$  anion with water acting as a solvent. If the simulation is indeed correct, then one might expect crystal structures which show a few water molecules associating with the  $[\text{PtCl}_6]^{2-}$  anion in the solid-state. The simulations carried out by Naidoo *et al.*<sup>1</sup> produces characteristic values for the radial distribution functions for the  $[\text{PtCl}_6]^{2-}$  anion in solution (water). Their work suggests that the atoms of the water molecules solvating the  $[\text{PtCl}_6]^{2-}$  anion have a well defined position in solution. The  $\text{Cl}^-$  ion to O atom,  $\text{Cl}^-$  ion to H atom,  $\text{Pt}^{\text{IV}}$  ion to O atom, and  $\text{Pt}^{\text{IV}}$  ion to H atom inter- atomic distances were found to be 3.22 Å, 2.49 Å, 4.15 Å, and 3.29 Å respectively. The simulation<sup>1</sup> also suggests that the H atom of the water molecules is solvating the  $[\text{PtCl}_6]^{2-}$  anion point to the octahedral face of the  $[\text{PtCl}_6]^{2-}$  anion.

A crystal engineering approach was taken to design a crystal system (Fig. 2.2) in which water molecules could associate with the  $[\text{PtCl}_6]^{2-}$  anion, with the intention of obtaining water molecules in similar positions to that of the computed hydration shell structure around the anion. This would then be used to perform variable temperature single crystal X-ray experiments to probe the effect that weakening interaction between water and the  $[\text{PtCl}_6]^{2-}$  anion would have on the Pt-Cl bond displacement.

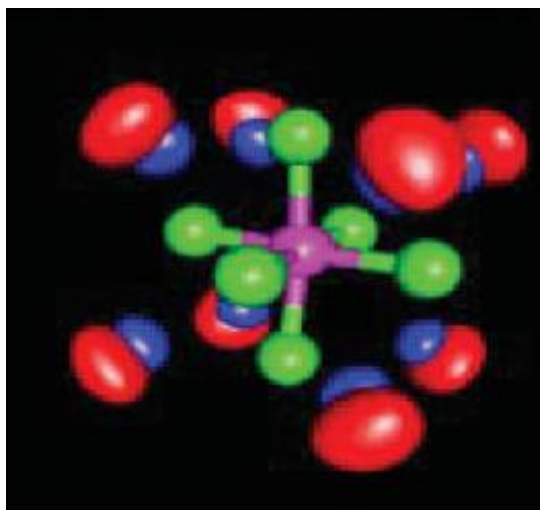


Figure 2.1 The theoretical primary hydration shell calculation carried out on the  $[\text{PtCl}_6]^{2-}$  anion<sup>1</sup> in water solvent shows the H atom of the water molecules are pointing towards the face of the  $[\text{PtCl}_6]^{2-}$  anion

The crystal structure reported by Steinborn *et al.*<sup>2</sup> has a water molecule crystallized within the cavity of the 18-crown-6-ether that surrounds the  $[\text{PtCl}_5(\text{H}_2\text{O})]^{2-}$  anion. The crown ether in Steinborn's paper crystallized above and below the  $[\text{PtCl}_5(\text{H}_2\text{O})]^{2-}$  anion, thus sandwiching the anion. Our intention is to induce a similar sandwich effect on the  $[\text{PtCl}_6]^{2-}$  anion using the cations  $\text{K}^+$  and  $\text{Na}^+$  to interact via a complexation interaction with the cavity of the crown ether, allowing the  $[\text{PtCl}_6]^{2-}$  anion to bind the two cations (see Fig. 2.2). A variety of crown ethers were used (Fig. 2.3) to theoretically increase the molecular steric effects, which could allow additional space to crystallize water molecules around the  $[\text{PtCl}_6]^{2-}$  anion.

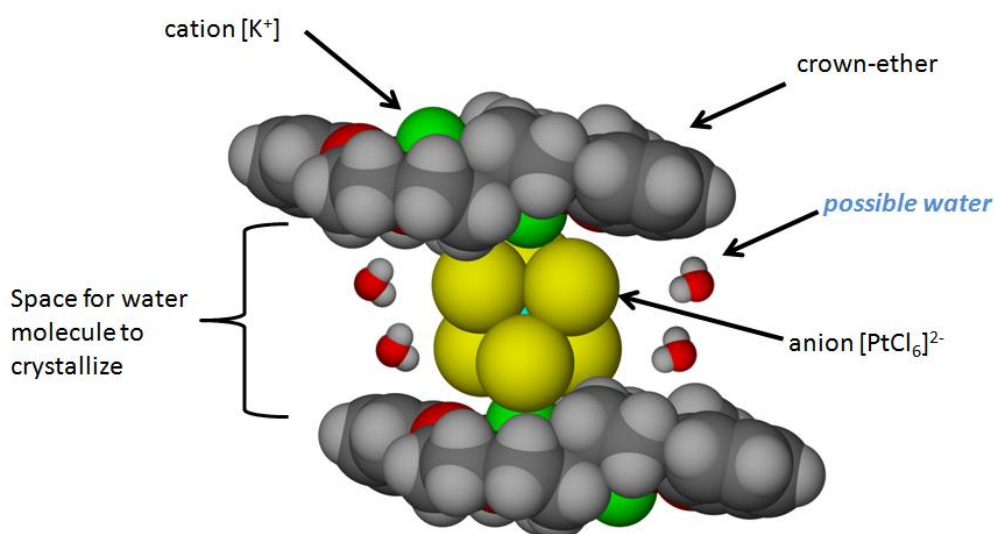


Figure 2.2 Schematic of the sandwich conformations to allow for space for water to crystallize around the  $[\text{PtCl}_6]^{2-}$  anion



In addition to the crown ether experiments, we surveyed the Cambridge Structural Database (CSD) for crystal structures obtained from X-ray diffraction experiments. The CSD database of crystal structures shows that the  $[\text{PtCl}_6]^{2-}$  anion is associated with water molecules within a 5 Å range. A detailed account is given on the structures found in the literature, which have water of crystallization around the  $[\text{PtCl}_6]^{2-}$  anion and which display similar features to that of the hydration shell of the  $[\text{PtCl}_6]^{2-}$  anion. The structural data obtained from these searches are used to authenticate the radial distribution function values obtained from the simulation carried out by Naidoo *et al.*<sup>1</sup>

If the crown ether experiments produce crystal structures which can be reproduced, then they are used to perform variable temperature SCXRD analyses in order to investigate the effect that changing intermolecular interactions between the water and  $[\text{PtCl}_6]^{2-}$  anion would have on the Pt-Cl bond displacement as a function of temperature.

The theoretical and experimental studies carried out by Jameson *et al.*<sup>3</sup> and Koch *et al.*<sup>4</sup> suggests that the degree of Pt-Cl bond displacement within the  $[\text{PtCl}_6]^{2-}$  anion is central to understanding the sensitivity of the  $^{195}\text{Pt}$  NMR shielding. We had hoped to investigate the sensitivity of the  $^{195}\text{Pt}$  nuclear magnetic resonance (NMR) chemical shifts using the above-mentioned crystal structures and using  $^{195}\text{Pt}$  solid state NMR as a function of temperature in order to correlate the Pt-Cl bond displacement with  $^{195}\text{Pt}$  chemical shift.

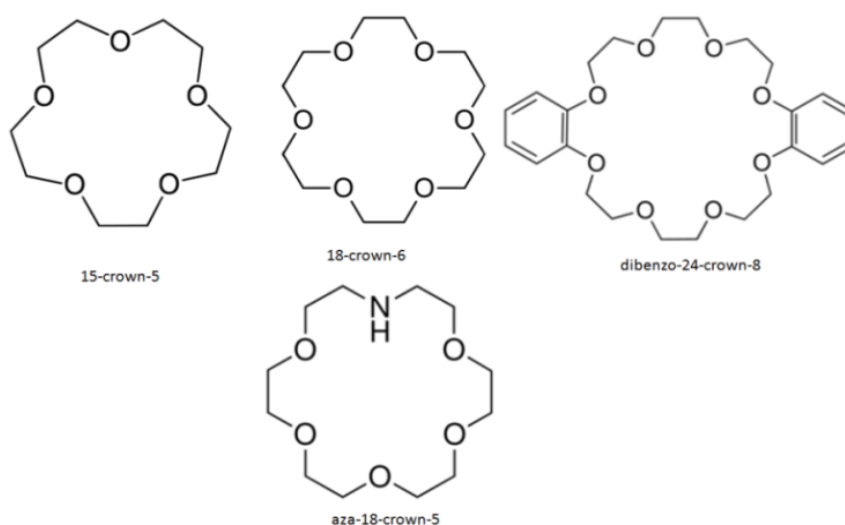


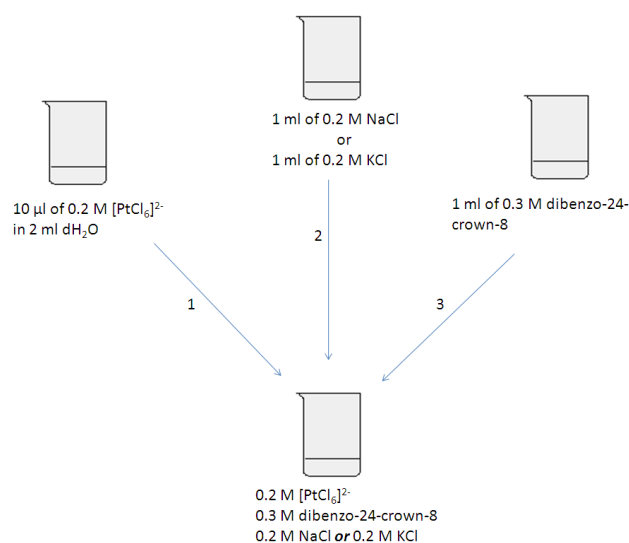
Fig. 2.3 Crown ether used in the his study to perform the experiments

## Experimental

### 2.1 Synthesis of dication (*dibenzo-24-crown-8*)-dication hexachloridoplatinate(IV)

#### 2.1.1 Synthesis of (*dibenzo-24-crown-8*)-disodium hexachloridoplatinate(IV) salts

A 10  $\mu\text{l}$  aliquot of 0.2 M  $[\text{PtCl}_6]^{2-}$  solution was pipetted from a stock solution of 0.2 M  $[\text{PtCl}_6]^{2-}$  in 6 M HCl. To this solution 2 ml of distilled water was added. The  $\text{Cl}^-$  concentration was kept quite high to prevent water ligand exchange with  $\text{Cl}^-$  ion of the  $[\text{PtCl}_6]^{2-}$  anion. In separately prepared flasks, 0.2 M NaCl and 0.3 M *dibenzo-24-crown-8* solutions were made up from a solvent mixture consisting of methanol, water and acetonitrile in a 1:1:1 ratio. After mixing, the solution (see Scheme 2.1) was immediately placed in a preheated oven at 85°C and allowed to completely evaporate all the solvents over 2 days. 0.02 g of a yellow salt precipitate was obtained, which was presumed to be the Pt containing sample product. The yellow precipitate was re-dissolved in 4 ml of the same solvent mixture and allowed to slowly evaporate at room temperature, which resulted in orange plate crystals.



Scheme 2.1 Schematic showing the synthesis of (*dibenzo-24-crown-8*)-dication hexachloridoplatinate(IV) salts

### 2.1.2 Synthesis of (dibenzo-24-crown-8)-dipotassium hexachloridoplatinate(IV) salts

The above procedure was followed but instead of using 0.2 M NaCl a 0.2 M KCl solution was used to form the potassium derivate of the crystal structure.

## 2.2 Cambridge Structural Database search

### 2.2.1 (Dibenzo-24-crown-8) with Na<sup>+</sup> and K<sup>+</sup> CSD analysis

A search of the CSD<sup>5</sup> for *dibenzo-24-crown-8* with Na<sup>+</sup> as the cation resulted in eight hits. After removing all the crystal structures that were structural derivatives of the *dibenzo-24-crown-8* structure a subset of six structures remained. The subset of structures was then investigated to see what effect the Na<sup>+</sup> cation had on the structural conformation of the crowns. Searching for the *dibenzo-24-crown-8* with a K<sup>+</sup> cation resulted in ten hits. After removing all the *dibenzo-24-crown-8* derivatives and some structures which had more than just the K<sup>+</sup> cation competing to interact with the crown ether's cavity, only three structures remained for analysis. A CSD search for the *dibenzo-24-crown-8* and Rb<sup>+</sup> cation structural fragments produced no hits. The search for *dibenzo-24-crown-8-ether* and Cs<sup>+</sup> cation resulted in three hits. However, in these structures the anions were interacting with the Cs<sup>+</sup> cation and the anion in all three crystal structures were competing for interaction with the crown cavity in a similar manner to that of the structures in the *dibenzo-24-crown-8* and K<sup>+</sup> cation analysis. The structural conformations of both the crown searches are displayed and discussed at length in the discussion of this chapter.

### 2.2.2 CSD analysis of crystal structures containing [PtCl<sub>6</sub>]<sup>2-</sup> anion and water

A search for the CSD for [PtCl<sub>6</sub>]<sup>2-</sup> anion and water molecule fragments resulted in 32 hits. The subset of 32 structures was searched with an additional restriction parameter, which only considered structures where the Cl<sup>-</sup> ion was within a 5 Å radius of the O atom in water. Only 17 structures met this additional requirement.

### *2.3 Single-Crystal X-ray Diffraction Analyses (SCXRD)*

The single crystals used during variable temperature XRD analysis were placed on the end of a MiTeGen mount using paratone oil. Intensity data were collected on a Bruker SMART<sup>6</sup> APEX single-crystal X-ray diffraction equipped with a Mo fine-focus sealed tube, Monocap collimator and an APEXII detector or a Bruker APEX DUO single-crystal diffractometer with Incoatec  $\text{I}\mu\text{S}$  molybdenum and copper microfocus X-ray sources and an APEXII detector. The temperatures on both instruments were regulated with an Oxford Cryosystems. Data were reduced using SAINT<sup>7</sup> and empirical corrections were performed where necessary using multi-scan SADABS.<sup>8</sup> The programs are included in the APEX 2 software package. The crystal structures were all solved and refined using the SHELX-97 suite of programs from direct methods. X-Seed<sup>9</sup> software was used as a graphic interface for SHELX. All atoms except for hydrogen atoms were refined anisotropically by means of full-matrix least-squares calculations for  $F^2$  using SHELXL-97, an interfaced with the X-Seed software package. Hydrogen atoms were placed using a riding model and isotropic thermal parameters were assigned values of 1.2 – 1.5 times the  $U_{\text{eq}}$  of their parent atoms.

## Results

### 2.4 Crown ether complexes with (dication)-hexachloridoplatinate(IV)

The outcome of the crown ether salt and  $[\text{PtCl}_6]^{2-}$  anion experiments are tabulated in Table 2.1, which shows that, of the eight experiments, only two yielded crystal structures. The two crystal structures are discussed below. The *aza-18-crown-5* produced a crystal for the  $\text{K}^+$  salt but it was twinned and could not be refined as some of the atoms were disordered over multiple positions making it unsuitable for discussion in this section.

Table 2.1 Crown ether salt of  $[\text{PtCl}_6]^{2-}$  experiments that were successfully crystallized.

Crown-ethers used	$\text{Na}^+ + [\text{PtCl}_6]^{2-}$	$\text{K}^+ + [\text{PtCl}_6]^{2-}$
<b>15-crown-5</b>	No crystal obtained	No crystal obtained
<b>18-crown-6</b>	No crystal obtained	No crystal obtained
<b>Dibenzo-24-crown-8</b>	<b>Crystal obtained</b>	<b>Crystal obtained</b>
<b>Aza-18-crown-5</b>	No crystal obtained	Twinned structure

#### 2.4.1 (dibenzo-24-crown-8)-disodium hexachloridoplatinate(IV) salts

The crown ether complex crystallized in a monoclinic space group  $Cc$ , with one  $[\text{PtCl}_6]^{2-}$  anion and two *dibenzo-24-crown-8* molecules that are folded around the two  $\text{Na}^+$  cations in the unit cell (Fig 2.4). The packing diagram viewed along the  $a$ -axis (Fig. 2.5) shows how the anions are situated between the crown ethers. Interestingly, the *dibenzo-24-crown-8* is folded around the  $\text{Na}^+$  and completely envelopes the cation. The structure, however, did not result in any water molecules crystallizing around the  $[\text{PtCl}_6]^{2-}$  anion as the crown ether completely folds leaving no space around the anion for water to crystallize.

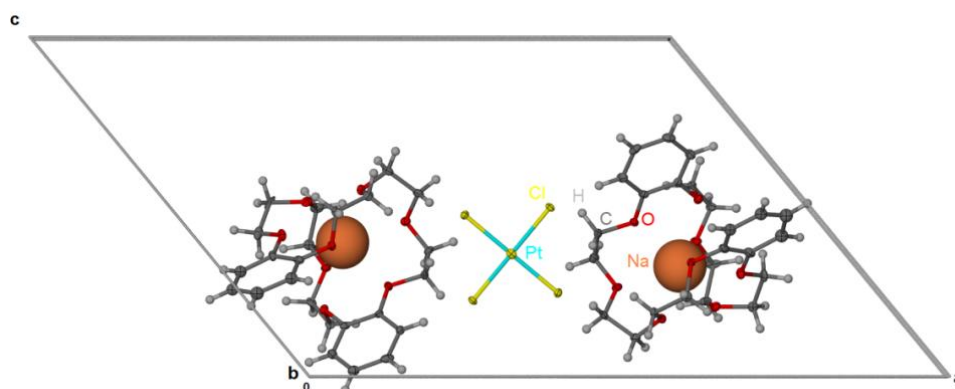


Fig. 2.4 Perspective view of a unit cell containing the *dibenzo-24-crown-8 disodium hexachloridoplatinate(IV)* salts

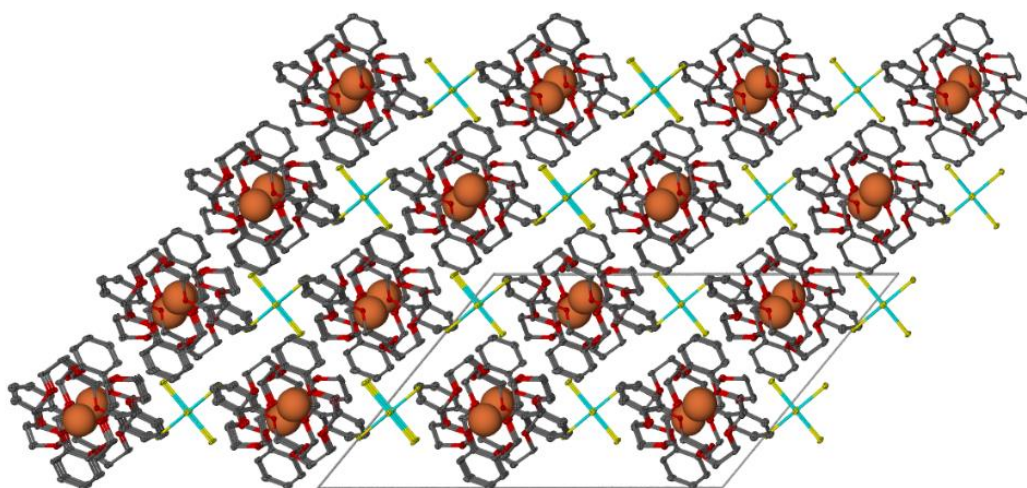


Fig. 2.5 Packing diagram of the *dibenzo-24-crown-8 disodium hexachloridoplatinate(IV)* salts along the *a*-axis, hydrogen atoms removed for clarity

Solution  $^{23}\text{Na}$  NMR carried out by Popov *et al.*<sup>10</sup> and Detellier *et al.*<sup>11</sup> on the *dibenzo-24-crown-8* folding in the presence of  $\text{Na}^+$  cation suggests that this crown ether also has this preferred structural confirmation in solution. A survey of the CSD was performed to investigate whether this conformation is extended to the solid state. The results from this investigation will be discussed in Section 2.7 of this chapter.

#### 2.4.2 (*dibenzo-24-crown-8*)-dipotassium-hexachloridoplatinate(IV) salts

The unit cell (Fig. 2.6) contains a  $[\text{PtCl}_6]^{2-}$  anion and two  $\text{K}^+$  cations, which are situated within the cavity of the *dibenzo-24-crown-8*. The complex crystallized in the triclinic space group *P1*. The crown ether contains two  $\text{K}^+$  cations arranged in columns parallel to the *c*-axis. The  $\text{K}^+$

cations are between two *dibenzo-24-crown-8* molecules. In this crystal structure the  $K^+$  cation does not induce the type of folding observed in the  $Na^+$  cation derivate of the same structure. The effect of the  $K^+$  cation on the *dibenzo-24-crown-8* molecules has, however, not been studied in as much detail as that of the  $Na^+$  cation, probably as this cation does not induce the preferred structural orientation upon complexation with the *dibenzo-24-crown-8*. The structures did not crystallize with water around the anion even though the anion is sandwiched by the crown ether molecules. A CSD analysis was carried out to investigate the influence of  $K^+$  cation on the *dibenzo-24-crown-8* molecules (see Section 2.7).

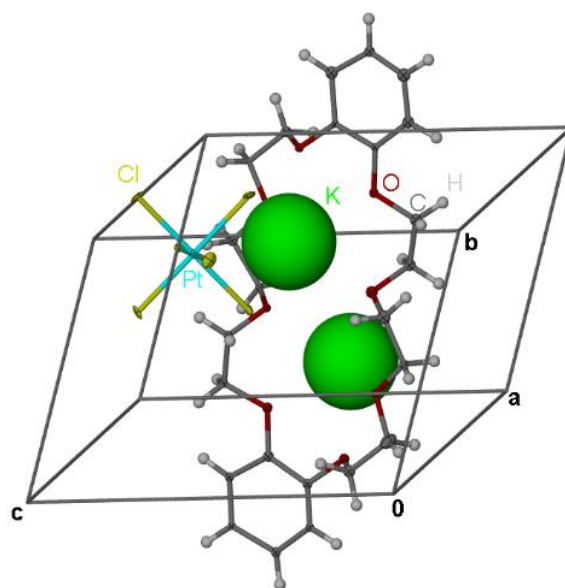


Fig. 2.6 The unit cell containing the *dibenzo-24-crown-8* dipotassium hexachloridoplatinate(IV) salts

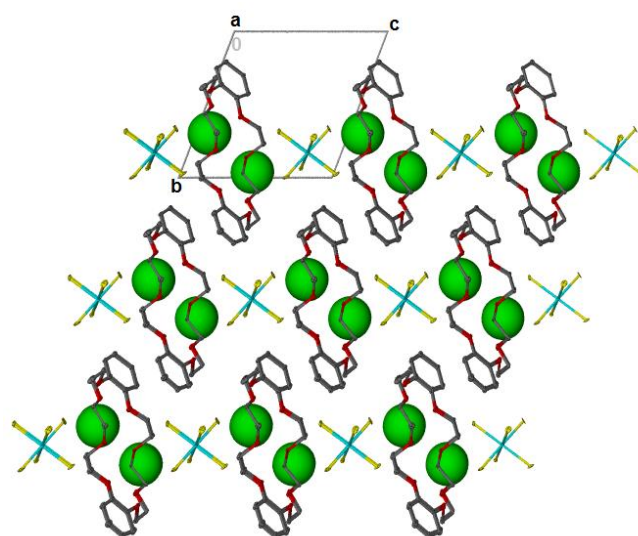


Fig. 2.7 Packing diagram of the *dibenzo-24-crown-8* dipotassium hexachloridoplatinate(IV) salts as viewed along the a-axis



## 2.5 Cambridge Structural Database Analyses Search

A CSD search for the *dibenzo-24-crown-8* with  $\text{Na}^+$  cation structural fragments produced eight hits. After eliminating all the crystal structures that are structural derivatives of the *dibenzo-24-crown-8* molecule a subset of six structures remained. The subset of structures was then investigated to see what affect the  $\text{Na}^+$  cation has on the structural conformation of the crown ether molecules upon complexation. The CSD search for the *dibenzo-24-crown-8* with  $\text{K}^+$  cation structural fragments produced ten hits. After removing all the *dibenzo-24-crown-8* derivatives and some structures which had more than just the  $\text{K}^+$  cation interaction with the cavity of the crown-ether (see Fig. 2.8), only three structures remained for analysis. A CSD search for the *dibenzo-24-crown-8* and  $\text{Rb}^+$  cation structural fragments yielded no hits. The search for the *dibenzo-24-crown-8* and  $\text{Cs}^+$  cation produced three hits; however, the anions in these structures are interacting with the  $\text{Cs}^+$  cation. In addition, the  $\text{Cs}^+$  cation and anion are competing for the crown ether cavity similarly to structures in the *dibenzo-24-crown-8* and  $\text{K}^+$  cation analysis.

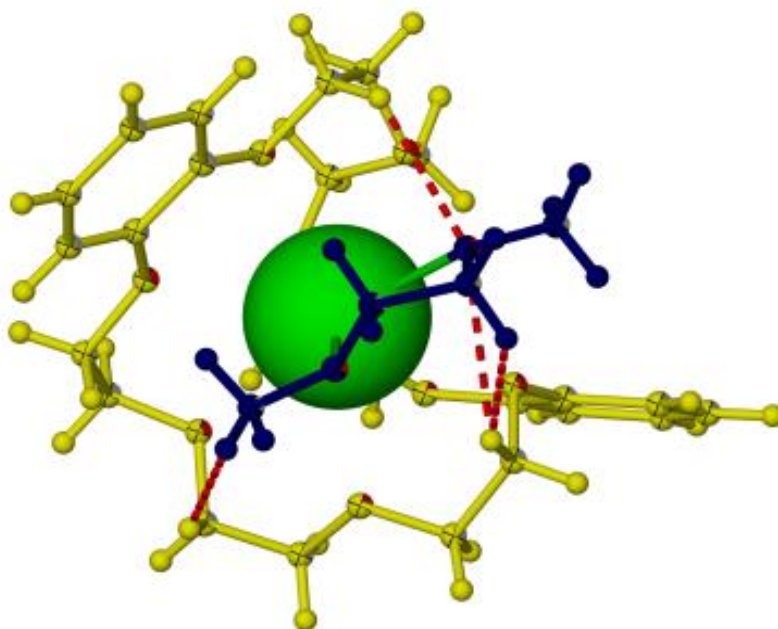


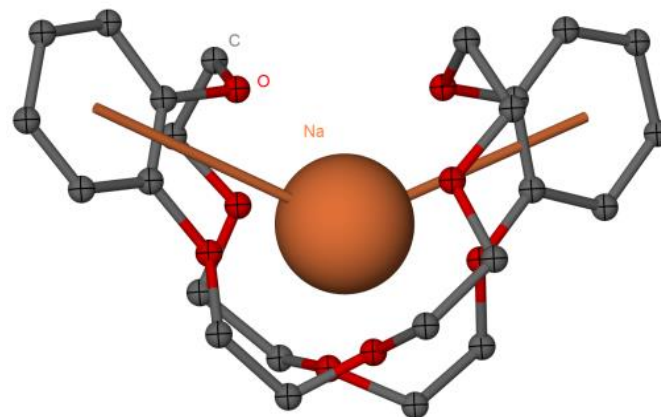
Figure 2.8 The 1,2-dimethoxyethane solvate (blue) covalently interacts (red) with the  $\text{K}^+$  (green) and hydrogen bonds (red) with the crown ether (yellow). CSD refcode: LUDCET



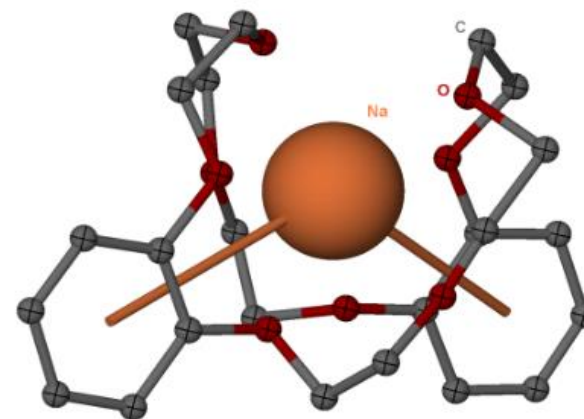
### 2.5.1 Dibenzo-24-crown-8 with a $\text{Na}^+$ and $\text{K}^+$ Analysis

The six crystal structures obtained from the CSD search on the *dibenzo-24-crown-8* with the  $\text{Na}^+$  cation fragments have a preferred structural conformation upon complexation with  $\text{Na}^+$  cation (see Fig. 2.9). The structures are fairly similar to those which we observed experimentally, further confirming and extending the preferred structural conformation to the solid state.

The subset of structures obtained from the CSD search of the *dibenzo-24-crown-8* and of the  $\text{K}^+$  cation structural fragments were investigated to determine if the *dibenzo-24-crown-8* has a preferred conformation upon complexation with  $\text{K}^+$  cation. The three crystal structures have a preferred structural conformation where two cations are situated within the cavity of the crown ether (see Fig. 2.10). The cations in these crystal structures all seem to be situated above on either side of the crown ether cavity.

Fig. 2.9 In all six crystal structures of dibenzo-24-crown-8-ether complexes with the Na<sup>+</sup> cation and adopt a folded conformation around the Na<sup>+</sup> cation**Refcode:** CADCAM<sup>12</sup>**Names:** (dibenzo-24-crown-8)-sodium iodide**Formula:** C<sub>24</sub>H<sub>32</sub>NaO<sub>8</sub><sup>+</sup>, I<sup>-</sup>**Refcode:** EBUQOH<sup>13</sup>

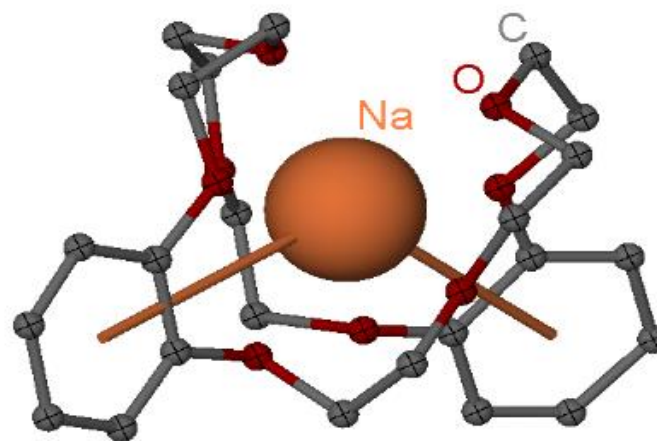
**Names:** catena-((Dibenzo(b,n)-24-crown-8)-sodium (m9-4-(5,10,15-tris(4-carboxyphenyl)-20-porphyrinato)benzoato)-(m9-4,4'-(5,15-bis(4-carboxyphenyl)-10,20-porphyrinato)dibenzoato)-bis(m2-hydroxo)-bis(pyridine-N)-tetra-sodium-di-zinc(ii) methanol solvate)

**Formula:** (C<sub>24</sub>H<sub>32</sub>NaO<sub>8</sub><sup>+</sup>)<sub>n</sub>, n(C<sub>106</sub>H<sub>65</sub>N<sub>10</sub>Na<sub>4</sub>O<sub>18</sub>Zn<sup>2+</sup>), 12n(CH<sub>4</sub>O)

**Refcode:** GICRUG<sup>14</sup>

**Names:** tris((Dibenzo-24-crown-8)-sodium) (m12-arsenato)-  
tetracosakis(m2-oxo)-dodecaoxo-dodeca-molybdenum  
nonahydrate

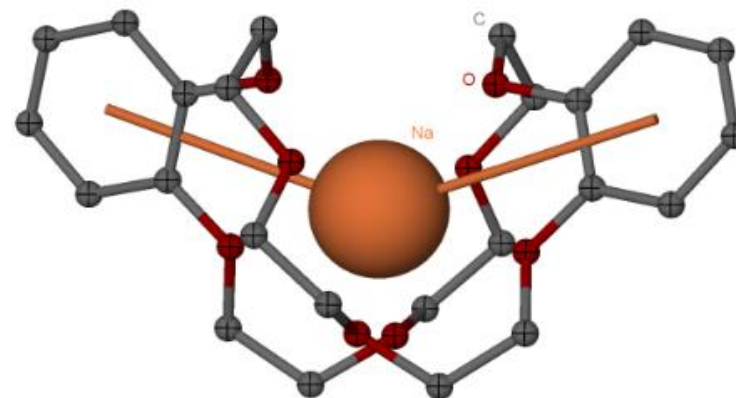
**Formula:**  $3(\text{C}_{24}\text{H}_{32}\text{NaO}_8^+)$ ,  $\text{AsMo}_{12}\text{O}_{40}_3^-$ ,  $9(\text{H}_2\text{O})$



**Refcode:** KAMHIP<sup>15</sup>

**Names:** (dibenzyl-18-crown-6)-sodium hexafluorophosphate

**Formula:**  $\text{C}_{24}\text{H}_{32}\text{NaO}_8^+$ ,  $\text{F}_6\text{P}^-$



## Solid state hydration of hexachloroplatinate anion

## Chapter 2

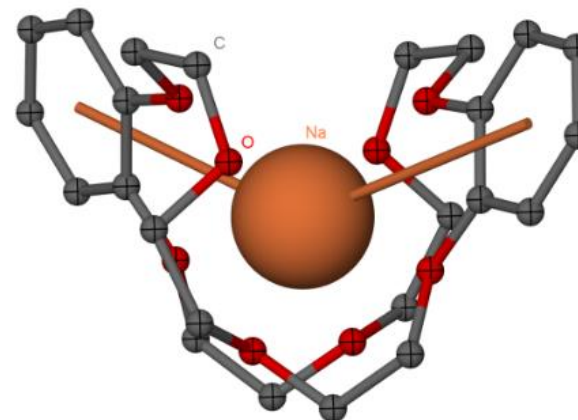
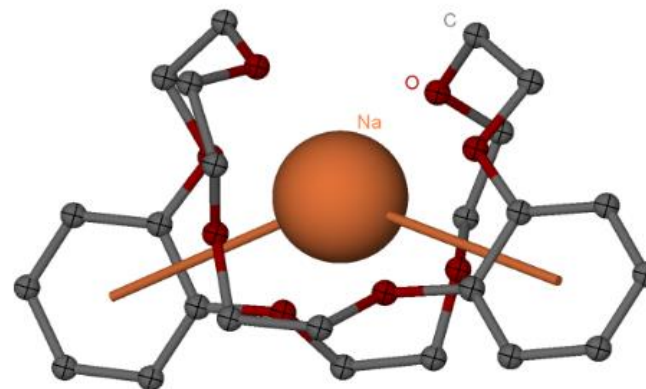
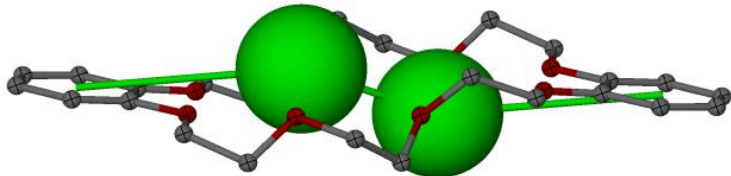
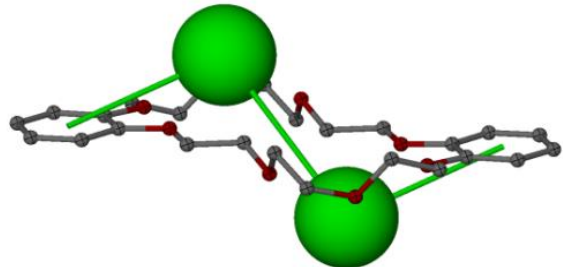
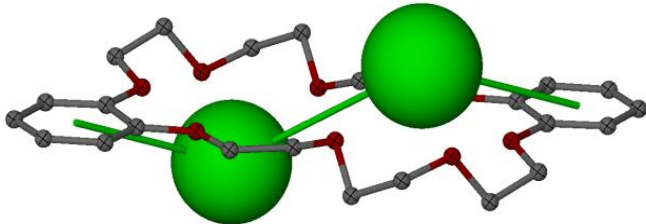
**Refcode:** XEVYOM<sup>16</sup>**Names:** catena-((Dibenzo-24-crown-8)-sodium clathrate mer-tris(m2-thiocyanato)-cadmium(II))**Formula:** (C<sub>24</sub>H<sub>32</sub>NaO<sub>8</sub><sup>+</sup>)<sub>n</sub>, n(C<sub>3</sub>CdN<sub>3</sub>S<sub>3</sub><sup>-</sup>)**Refcode:** YOYSAG<sup>17</sup>**Names:** bis(24-Crown-8-sodium) (μ<sub>6</sub>-oxo)-dodecakis(μ<sub>2</sub>-oxo)-hexa-oxo-penta-molybdenum-tungsten**Formula:** 2(C<sub>24</sub>H<sub>32</sub>NaO<sub>8</sub><sup>+</sup>), Mo<sub>5</sub>O<sub>19</sub>W<sub>2</sub><sup>-</sup>

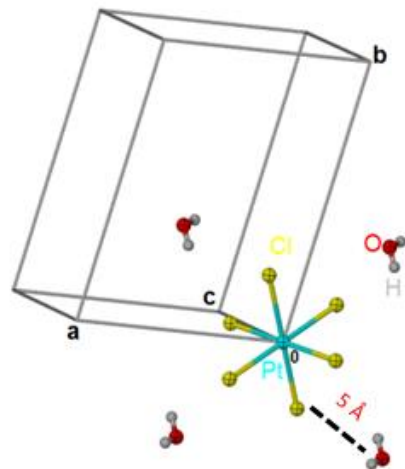
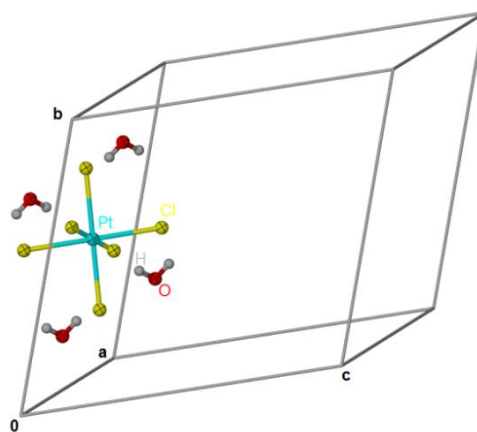
Fig. 2.10 In all three crystal structures the dibenzo-24-crown-8-ether is adopting an open crown conformation with two  $K^+$  in its cavity

<p><b>Refcode:</b> HBXCTK<sup>18</sup></p> <p><b>Names:</b> Dibenzo-24-crown-8 bis(potassium isothiocyanate)</p> <p><b>Formula:</b> C<sub>26</sub>H<sub>32</sub>K<sub>2</sub>N<sub>2</sub>O<sub>8</sub>S<sub>2</sub></p>	
<p><b>Refcode:</b> SOFKAZ<sup>19</sup></p> <p><b>Names:</b> catena(bis(<math>\mu</math>2-Picrato-O,O',O',O')-(<math>\mu</math>2-dibenzo-24-crown-8)-potassium)</p> <p><b>Formula:</b> (C<sub>36</sub>H<sub>36</sub>K<sub>2</sub>N<sub>6</sub>O<sub>22</sub>)<sub>n</sub></p>	
<p><b>Refcode:</b> SOFKED<sup>13</sup></p> <p><b>Names:</b> catena(bis(<math>\mu</math>2-Picrato-O,O',O',O')-(<math>\mu</math>2-dibenzo-24-crown-8)-di-potassium)</p> <p><b>Formula:</b> (C<sub>36</sub>H<sub>36</sub>K<sub>2</sub>N<sub>6</sub>O<sub>22</sub>)<sub>n</sub></p>	

## 2.6 A CSD search for water associated with $[\text{PtCl}_6]^{2-}$ anions

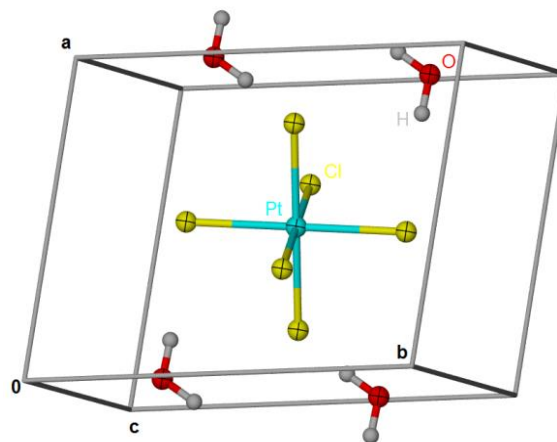
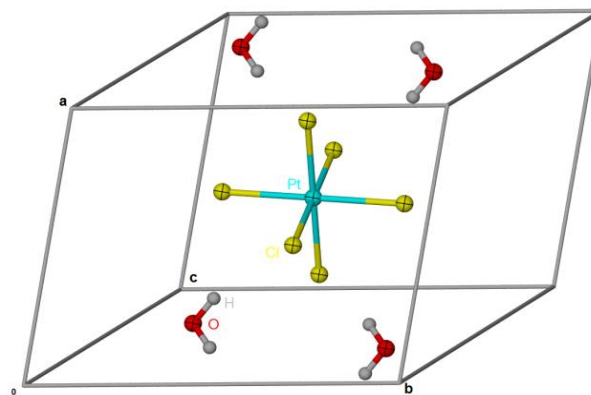
The CSD search for the  $[\text{PtCl}_6]^{2-}$  anion and water fragments resulted in 33 crystal structures (Appendix A). The subset of 33 structures was then searched with a contact restriction between the O atom of the water molecule to the  $\text{Cl}^-$  ion of the  $[\text{PtCl}_6]^{2-}$  anion  $\leq 5 \text{ \AA}$ . The  $\text{Cl}^-$  ion and O atom were selected to apply the restriction, since X-ray diffraction has some difficulty determining the position of hydrogen atoms.<sup>20</sup> This restriction reduced the 33 structures to 17 crystal structures that are illustrated below in Fig. 2.11. It is quite clear from these crystal structures that a water molecule (and in some cases more than one water molecule) crystallized in association with the *hexachloridoplatinate(IV)* anion. This implies that if the *hexachloridoplatinate(IV)* anion is crystallized in the presence of water or in a partially hydrated solvent, then there is a strong possibility that water would crystallize in close proximity of the  $[\text{PtCl}_6]^{2-}$  anion. The authors who obtained crystal structures showing the association of the water molecules with the  $[\text{PtCl}_6]^{2-}$  anion had no intention of forming these associated crystal structures. We cannot conclude that there is a high probability of forming these associated water molecules with the  $[\text{PtCl}_6]^{2-}$  anion but it gives us some indication the hydration of the anion in the solid state is possible.

The APPENDIX A, of this thesis document contains an Excel spreadsheet listing all the interatomic distances used to interpret the data shown below and a details list containing all the manually measured distances files. The  $\text{Cl}^-$  ion to O atom,  $\text{Cl}^-$  ion to H atom,  $\text{Pt}^{\text{IV}}$  ion to O atom, and  $\text{Pt}^{\text{IV}}$  ion to H atom inter atomic distances were all measured using Mercury 3.3 (2014) and they were compared to the calculated radial distribution functions  $3.22 \text{ \AA}$ ,  $2.49 \text{ \AA}$ ,  $4.15 \text{ \AA}$ , and  $3.29 \text{ \AA}$  respectively. Histograms were plotted from all the intramolecular distances, which was extracted from the crystal structures obtained from the CSD analysis. These histogram plots showed the interatomic distances in  $\text{\AA}$  on the x-axis and the number of interaction on the y-axis .

Fig. 2.11 The seventeen crystal structures that all have water crystallized around the  $[\text{PtCl}_6]^{2-}$  anion**Refcode:** BUPMAA01<sup>21</sup>**Names:** bis(9-Methylguaninium) hexachloro-  
platinum(IV) dihydrate**Formula:**  $2(\text{C}_6\text{H}_8\text{N}_5\text{O}^+)$ ,  $\text{Cl}_6\text{Pt}^{2-}$ ,  $2(\text{H}_2\text{O})$ **Refcode:** KURXAX<sup>22</sup>**Names:** Diacridinium hexachloro-  
platinum(IV) dihydrate**Formula:**  $2(\text{C}_{13}\text{H}_{10}\text{N}^+)$ ,  $\text{Cl}_6\text{Pt}^{2-}$ ,  $2(\text{H}_2\text{O})$ 

## Solid state hydration of hexachloroplatinate anion

## Chapter 2

**Refcode:** MARQUT<sup>23</sup>**Names:** bis(quinolinium) hexachloro  
platinum(IV) dihydrate**Formula:**  $2(\text{C}_9\text{H}_8\text{N}^+)$ ,  $\text{Cl}_6\text{Pt}^{2-}$ ,  $2(\text{H}_2\text{O})$ **Refcode:** MARRAA<sup>24</sup>**Names:** bis(7,8-benzoquinolinium)  
hexachloro-platinum(IV) dihydrate**Formula:**  $2(\text{C}_{13}\text{H}_{10}\text{N}^+)$ ,  $\text{Cl}_6\text{Pt}^{2-}$ ,  $2(\text{H}_2\text{O})$ 



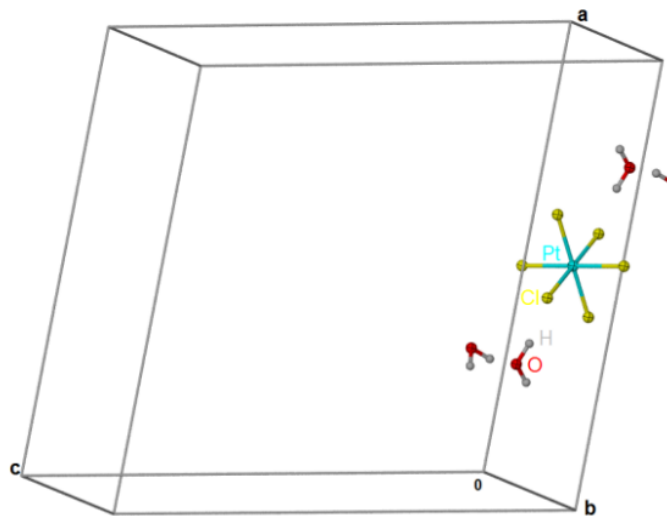
## Solid state hydration of hexachloroplatinate anion

## Chapter 2

**Refcode:** SOPFON<sup>25</sup>

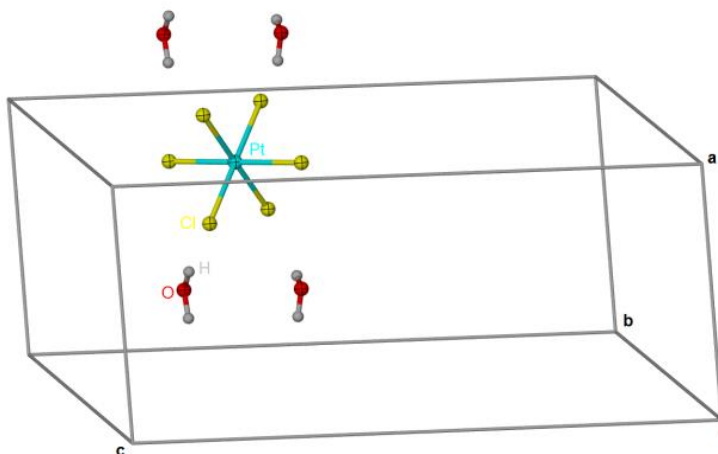
**Names:** bis(2-(R)-(1-1-Ethyl-2-hydroxyethylamino)-6-benzylamino-9-isopropylpurinium) hexachloroplatinum(IV)platinum(IV) dichloride tetrahydrate

**Formula:**  $2(\text{C}_{19}\text{H}_{28}\text{N}_6\text{O}_2^+)$ ,  $\text{Cl}_6\text{Pt}^{2-}$ ,  $2(\text{Cl}^-)$ ,  $4(\text{H}_2\text{O})$

**Refcode:** WUVZET<sup>26</sup>

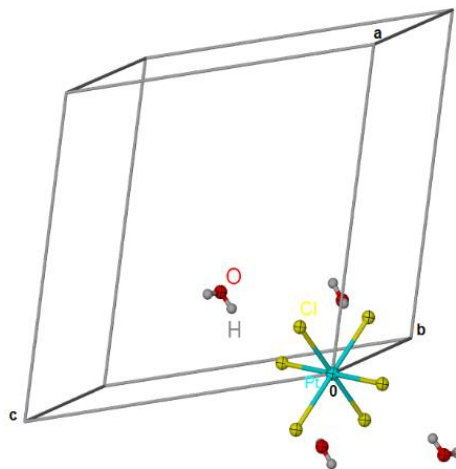
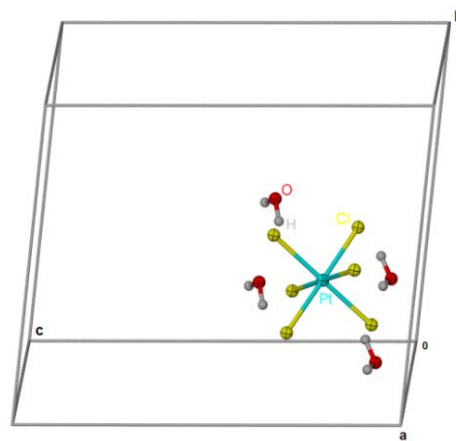
**Names:** 2-((4-Methylphenyl)diazenyl)-1H-imidazol-3-ium hexachloroplatinum(IV) dihydrate

**Formula:**  $2(\text{C}_{10}\text{H}_{11}\text{N}_4^+)$ ,  $\text{Cl}_6\text{Pt}^{2-}$ ,  $2(\text{H}_2\text{O})$



## Solid state hydration of hexachloroplatinate anion

## Chapter 2

**Refcode:** YAGXIO<sup>27</sup>**Names:** bis(3-Bromopyridinium) hexachloro-  
platinum(IV) dihydrate**Formula:** 2(C<sub>5</sub>H<sub>5</sub>BrN<sup>+</sup>), Cl<sub>6</sub>Pt<sup>2-</sup>, 2(H<sub>2</sub>O)**Refcode:** YAGXUA<sup>21</sup>**Names:** bis(3-Iodopyridinium) hexachloro-  
platinum(IV) dihydrate**Formula:** 2(C<sub>5</sub>H<sub>5</sub>IN<sup>+</sup>), Cl<sub>6</sub>Pt<sup>2-</sup>, 2(H<sub>2</sub>O)

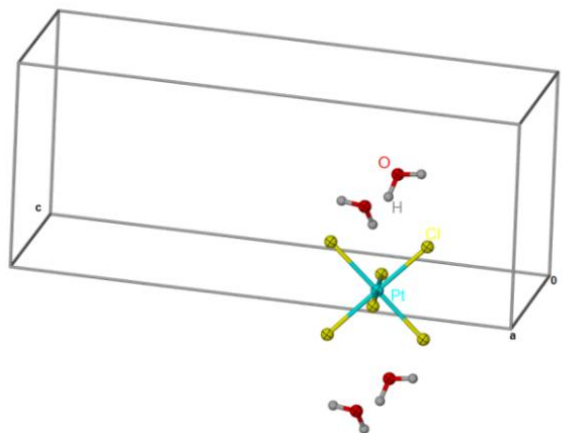
## Solid state hydration of hexachloroplatinate anion

## Chapter 2

**Refcode:** YAGXU001<sup>21</sup>

**Names:** bis(3-Iodopyridinium) hexachloro-  
platinum(IV) dihydrate

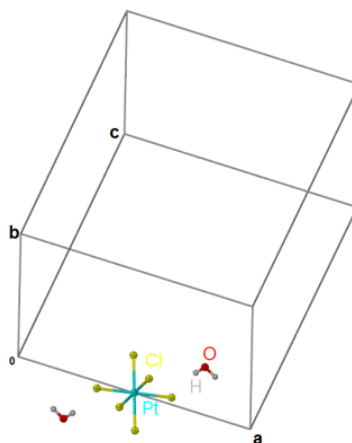
**Formula:**  $2(\text{C}_5\text{H}_5\text{IN}^+)$ ,  $\text{Cl}_6\text{Pt}^{2-}$ ,  $2(\text{H}_2\text{O})$



**Refcode:** FULZER<sup>28</sup>

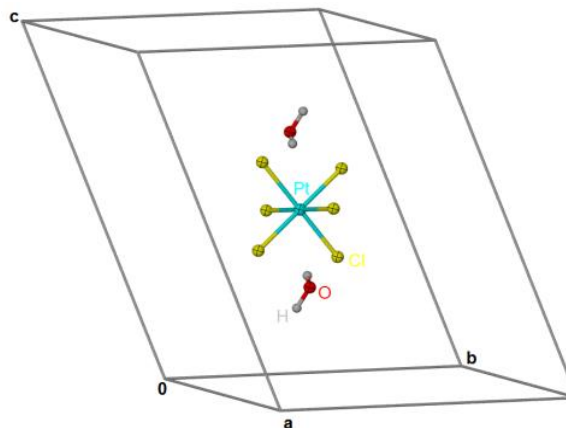
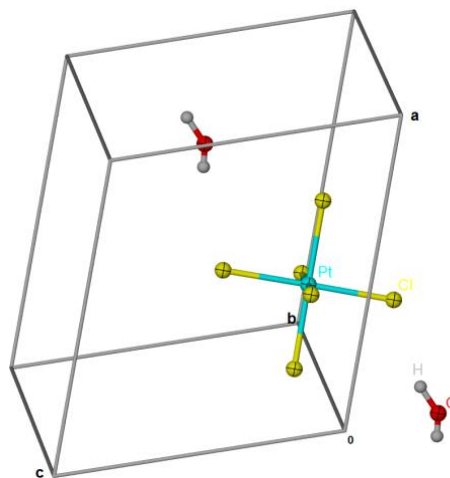
**Names:** tetrakis(1,3,5-Triammonio-1,3,5-  
trideoxy-cis-inositol) decachloride  
hexachloridoplatinate hexahydrate

**Formula:**  $4(\text{C}_6\text{H}_{18}\text{N}_3\text{O}_{33}^+)$ ,  $10(\text{Cl}^-)$ ,  $\text{Cl}_6\text{Pt}^{2-}$ ,  
 $6(\text{H}_2\text{O})$



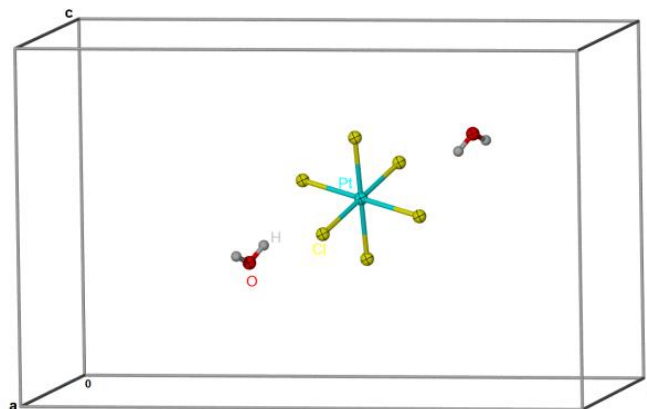
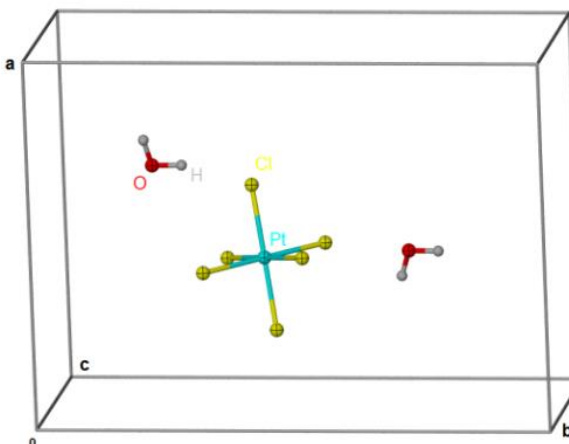
## Solid state hydration of hexachloroplatinate anion

## Chapter 2

**Refcode:** GEPCAF<sup>29</sup>**Names:** tetrakis(5,6-Dihydropyrimidino(5,4-c)carbazole) hexachloro-platinum(IV) dichloride tetrahydrate**Formula:**  $4(\text{C}_6\text{H}_{18}\text{N}_3\text{O}_{33}^+)$ ,  $10(\text{Cl}^-)$ ,  $\text{Cl}_6\text{Pt}^{2-}$ ,  $6(\text{H}_2\text{O})$ **Refcode:** KEDZIC<sup>30</sup>**Names:** bis(5,6-Dihydropyrimidino(5,4-c)carbazole) hexachloroplatinum(IV) monohydrate**Formula:**  $2(\text{C}_{14}\text{H}_{12}\text{N}_3^+)$ ,  $\text{Cl}_6|\text{Pt}^{2+}$ ,  $\text{H}_2\text{O}$ 

## Solid state hydration of hexachloroplatinate anion

## Chapter 2

**Refcode:** QOBYEM<sup>15</sup>**Names:** bis(1-Methylcytidinium) hexachloro-platinum(IV) dihydrate**Formula:**  $2(\text{C}_5\text{H}_8\text{N}_3\text{O}^+)$ ,  $\text{Cl}_6\text{Pt}^{2-}$ ,  $2(\text{H}_2\text{O})$ **Refcode:** SIPFIH<sup>31</sup>**Names:** 6-(Benzylamino)-2-((3-hydroxypropyl)amino)-9-isopropylpurinium hexachloro-platinum(IV)monohydrate**Formula:**  $\text{C}_{18}\text{H}_{26}\text{N}_6\text{O}_2^+$ ,  $\text{Cl}_6\text{Pt}^{2-}$ ,  $\text{H}_2\text{O}$ 

## Solid state hydration of hexachloroplatinate anion

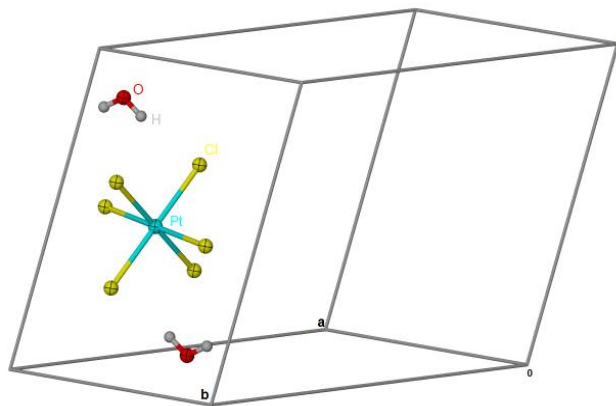
## Chapter 2

**Refcode:** XILXAS<sup>32</sup>

**Names:** 1,10-Diazonia-18-crown-6

hexachloridoplatinate(IV) dihydrate

**Formula:**  $C_{12}H_{28}N_2O_{42}^+$ ,  $Cl_6Pt^{2-}$ ,  $2(H_2O)$



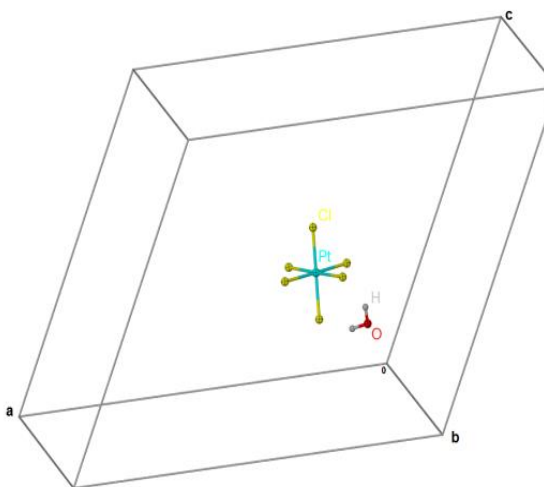
**Refcode:** EHAFOI<sup>33</sup>

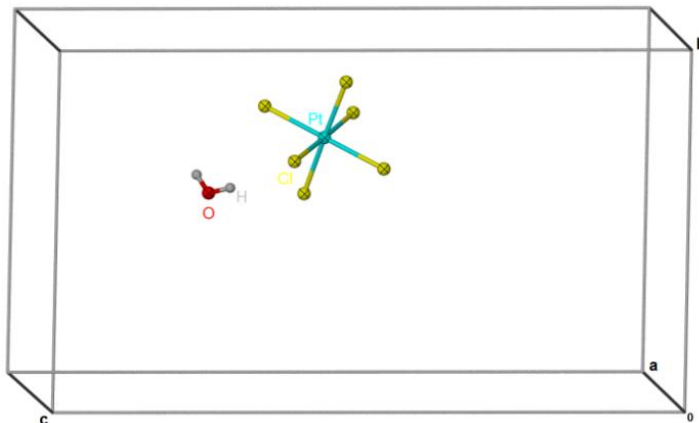
**Names:** bis(Benzyl(triphenyl)phosphonium)

hexachloro-platinum(IV)

hemihydrate

**Formula:**  $2(C_{25}H_{22}P^+)$ ,  $Cl_6Pt^{2-}$ ,  $0.5(H_2O)$



**Refcode:** NUZKEY<sup>34</sup>**Names:** tris(5-Bromocytosinium) hexachloro-  
platinum(IV) chloride monohydrate**Formula:**  $3(\text{C}_4\text{H}_5\text{BrN}_3\text{O}^+)$ ,  $\text{Cl}_6\text{Pt}^{2-}$ ,  $\text{Cl}^-$ ,  $\text{H}_2\text{O}$ 

---

## Discussion and Concluding remarks

---

The initial goal of  $\text{Na}^+$  and  $\text{K}^+$  cations crown ether salt formation with the  $[\text{PtCl}_6]^{2-}$  anion experiments was to allow for the association of water molecules with the  $[\text{PtCl}_6]^{2-}$  anion. However it did not turn out to be not as successful as hoped. It was observed that the *dibenzo-24-crown-8* molecule has a preferred structural conformation upon its complexation interactions with the  $\text{Na}^+$  and  $\text{K}^+$  cations (see Fig. 2.4 and Fig. 2.6). These preferred structural conformations were confirmed by conducting an additional CSD survey. The results from the CSD survey of the crystal structures obtained from our experiments and those from the CSD analyses showed that the *dibenzo-24-crown-8* molecules have a very distinct preferred structural conformation upon complexation with the  $\text{Na}^+$  cation (see Fig. 2.4 and Fig. 2.9). The  $\text{K}^+$  cation on the other hand has quite a different effect on the *dibenzo-24-crown-8* molecule (see Fig. 2.6 and Fig. 2.10). The structure obtained from our experiments and that of the CSD search showed that this crown ether has two  $\text{K}^+$  cations within the cavity.

The complexation interaction between the  $\text{Na}^+$  cation and the *dibenzo-24-crown-8* molecule has been studied by  $^{23}\text{Na}$  NMR by Popov *et al.*<sup>10</sup> and Detellier *et al.*<sup>11</sup> who postulate that the crown ether folds around the cation in solution. The six crystal structures (Fig. 2.9) obtained from the CSD survey all show the *dibenzo-24-crown-8-ether* having this preferred folding around the  $\text{Na}^+$  cation. This folding happens independently of the counter anion in all these structures. This can be seen in the crystal structure obtained by Fromm *et al.*<sup>12</sup> which has an iodide ( $\text{I}^-$ ) as a counter anion, a sterically smaller ion compared to that of the Goldberg *et al.*<sup>13</sup> structure which has a massive *tetra(carboxyphenyl)porphyrins counter anion*. Since our crown ether experiments did not result in any crystal structures with water molecules around the  $[\text{PtCl}_6]^{2-}$  anion,<sup>1</sup> an interesting observation is made based on *dibenzo-24-crown-8* preferred structural conformation upon complexation with the  $\text{Na}^+$  and  $\text{K}^+$  cations.

A CSD survey was carried out to look for crystal structures that have water molecule/s crystallized around the  $[\text{PtCl}_6]^{2-}$  anion. In 17 crystal structures water molecule/s are



associating with the  $[\text{PtCl}_6]^{2-}$  anion (see Fig.2.12). It should also be taken into account that the cation in these 17 crystal structures also interact with the water molecule and also compete sterically for the intermolecular interaction with the  $\text{Cl}^-$  ion on the  $[\text{PtCl}_6]^{2-}$  anion. Nevertheless, among the 17 crystal structures which make up 100% of the structures, 53% have four water molecules associating with the  $[\text{PtCl}_6]^{2-}$  anion<sup>14-21</sup>. 35% of the structures have two water molecules associating with the anion<sup>22-26</sup> and the remaining 12% of the structures have only one water molecule associating with the anion.<sup>27-28</sup> The average Pt-Cl bond lengths in all 17 structures fluctuate between  $2.315(3) \geq \text{Pt-Cl} \leq 2.328(3)$  with a  $0.013 \text{ \AA}$  difference. The results obtained from the computational simulation done by Naidoo *et al.*<sup>1</sup> suggest the following interatomic radial distribution function values for the association of the water molecule/s with the  $[\text{PtCl}_6]^{2-}$  anion and show that the  $\text{Cl}^-$  ion to O atom,  $\text{Cl}^-$  ion to H atom,  $\text{Pt}^{\text{IV}}$  ion to O atom, and  $\text{Pt}^{\text{IV}}$  ion to H atom interatomic distances to be  $3.22 \text{ \AA}$ ,  $2.49 \text{ \AA}$ ,  $4.15 \text{ \AA}$ , and  $3.29 \text{ \AA}$  respectively. The 17 crystal structures obtained from the CSD search were used to examine and validate the above-mentioned radial distribution function interatomic values ( $\text{Cl}^-$  ion to O atom,  $\text{Cl}^-$  ion to H atom,  $\text{Pt}^{\text{IV}}$  ion to O atom, and  $\text{Pt}^{\text{IV}}$  ion to H atom) by using experimental X-ray interatomic distances. The above mentioned interatomic distances were extracted from the 17 crystal structures and plotted as histograms displaying the maximum and minimum interatomic distances which are used to validate the computed interatomic radial distribution function values. These plots show the interatomic distance of two atoms on the x – axis and the number of distances on the y – axis. A list containing all of these distances can be found in the Appendix B.

The  $\text{Cl}^-$  ion to O atom interatomic distance ( $3.22 \text{ \AA}$ ) obtained from the radial distribution function of the hydration shell of  $[\text{PtCl}_6]^{2-}$  anion<sup>1</sup> is investigated using the data obtained from 17 crystal structures. In Figure (Fig. 2.12) the  $\text{Cl}^-$  ion to O atom are plotted against the number of  $\text{Cl}^-$  ion to O atom interatomic distances. The  $\text{Cl}^-$  to O atom interatomic distances that are higher than  $4.1 \text{ \AA}$  are water molecules interacting with the cation (counter ion) in addition to the  $\text{Cl}^-$  ion from the  $[\text{PtCl}_6]^{2-}$  anions which increases its distances.

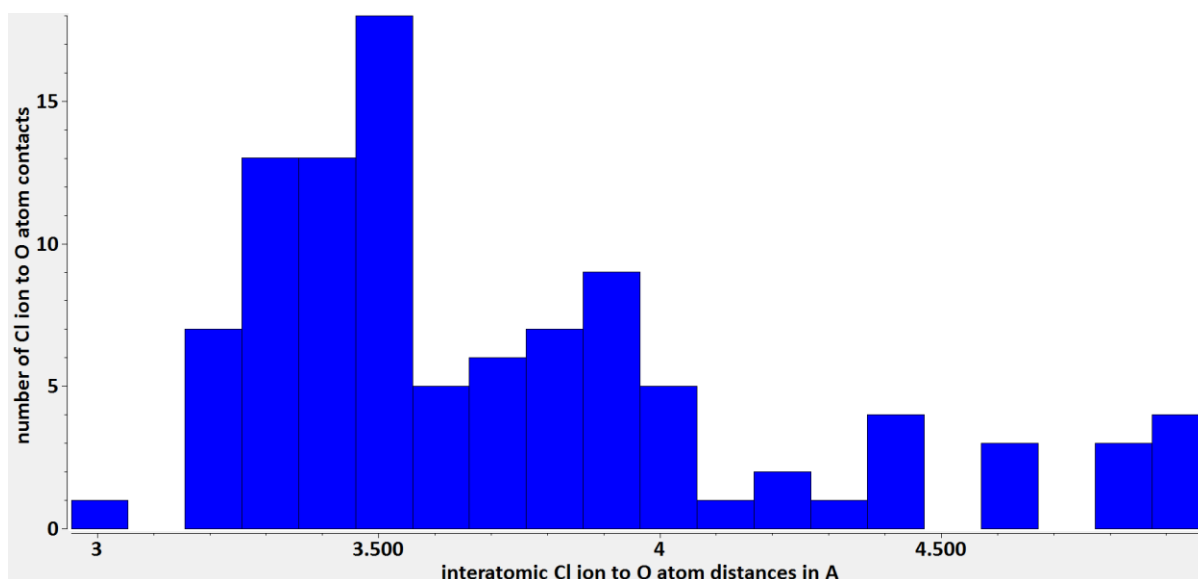


Figure 2.12 Histogram of the Cl<sup>-</sup> ion to O atom distance of the 17 crystal structures are plotted to validate the Cl<sup>-</sup> ion to O atom computed radial distribution function value (3.22 Å) obtained from the association of the water to the [PtCl<sub>6</sub>]<sup>2-</sup> anion simulation (

In Fig. 2.12 the interatomic Cl<sup>-</sup> ion to O atom radial distribution function value (3.22 Å) agrees well and is within the maximum (4.373 Å) and minimum value (2.983 Å), obtained from the distances in all crystal structures. This is a good indication of the validity of the computed radial distribution for the Cl to O atomic distance.

The computed radial distribution function values of the Cl<sup>-</sup> ion to H atom interatomic distance is 2.49 Å. The measurement obtained from the 17 crystal structures shows a wide range of distances ranging from 2.351 Å to 4.478 Å (Fig. 2.13). The reason for this wide distribution of interatomic distances could be due to the insensitivity of X-ray diffraction to locate the position of the H atom especially in the presence of atoms such as Pt, Cl and O, and is well demonstrated and discussed by Cotton *et al.*<sup>35</sup> Another factor which could influence this wide distribution of the interatomic distances between these two atoms are due to the water's interaction with the cations in the crystal structures. Nevertheless, the computed radial distribution function value of the Cl<sup>-</sup> ion to H atom distance (2.49 Å) is in good agreement with the experimental data.

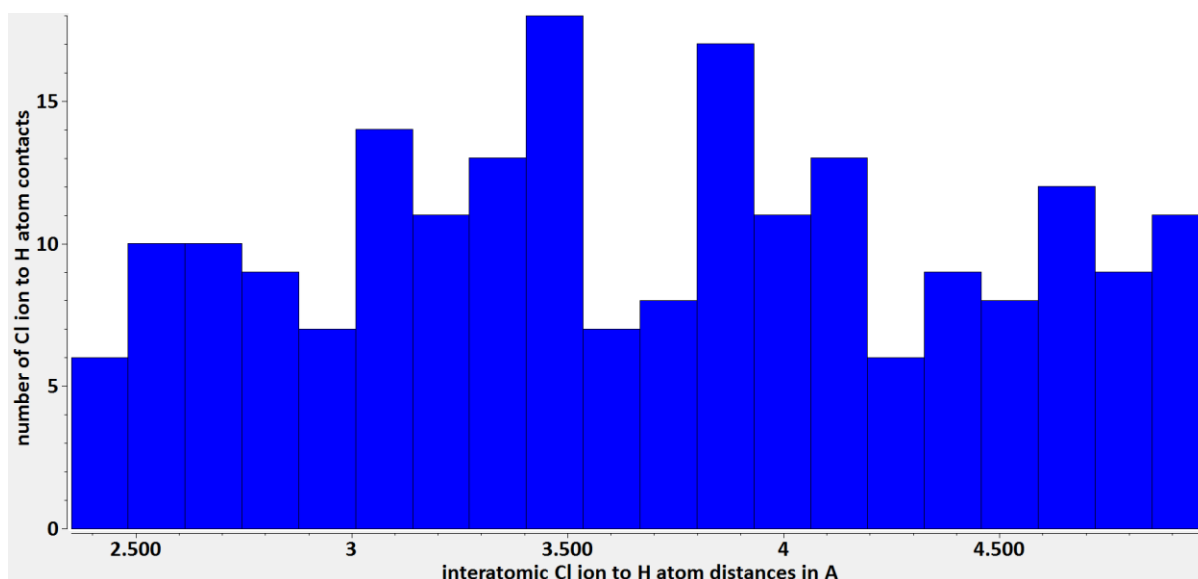


Figure 2.13 The  $\text{Cl}^-$  to H distance of the 17 crystal structures are plotted to validate the computed radial distribution function values (2.49 Å) obtained from the association of the water to the  $[\text{PtCl}_6]^{2-}$  anion simulation

The computed radial distribution function value of the  $\text{Pt}^{\text{IV}}$  ion to O distance is 4.15 Å. In Fig. 2.14 the  $\text{Pt}^{\text{IV}}$  ion to O atom distance in all 17 crystal structures shows that the computed radial distribution function value is close to the minimum (4.128 Å) values. This is a good indication of the validity of the computed radial distribution functions value of the  $\text{Pt}^{\text{IV}}$  ion to O atom distances, giving good evidence of the plausibility of the hydration shell structure around the  $[\text{PtCl}_6]^{2-}$  anion in solution.<sup>1</sup>

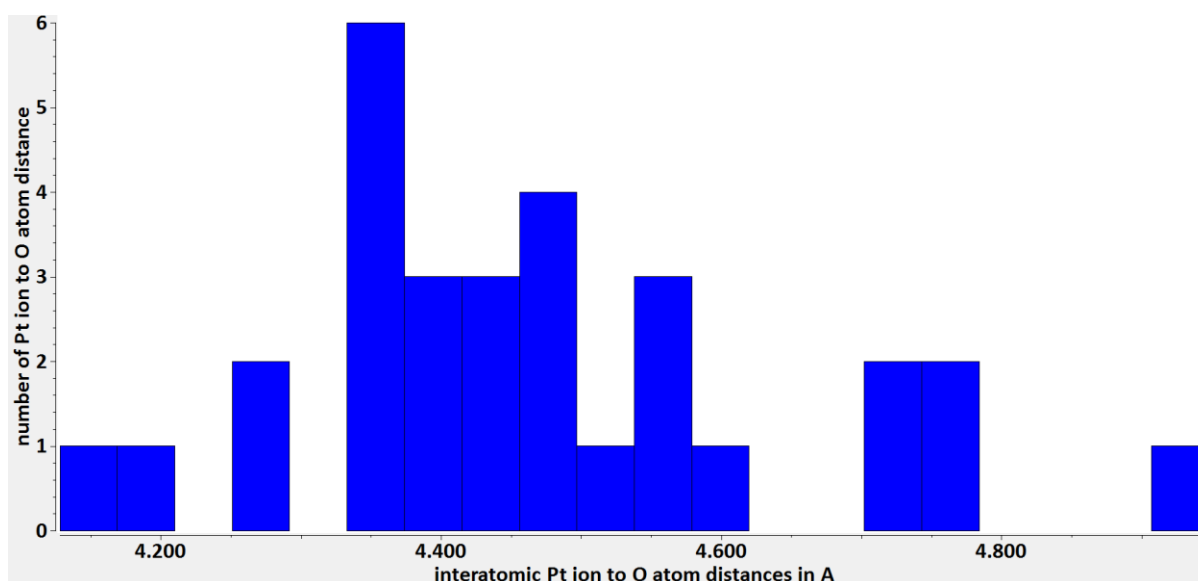


Figure 2.14 The  $\text{Pt}^{\text{IV}}$  ion to O atom distances of the 17 crystal structures are plotted to validate the computed radial distribution function values (4.15 Å) obtained from the association of the water to the  $[\text{PtCl}_6]^{2-}$  anion simulation

The computed interatomic  $\text{Pt}^{\text{IV}}$  ion to H atom radial distribution function value (3.29 Å) is the only distance which falls way below the minimum (3.443 Å) and maximum (5.118 Å) values (Fig. 2.15).

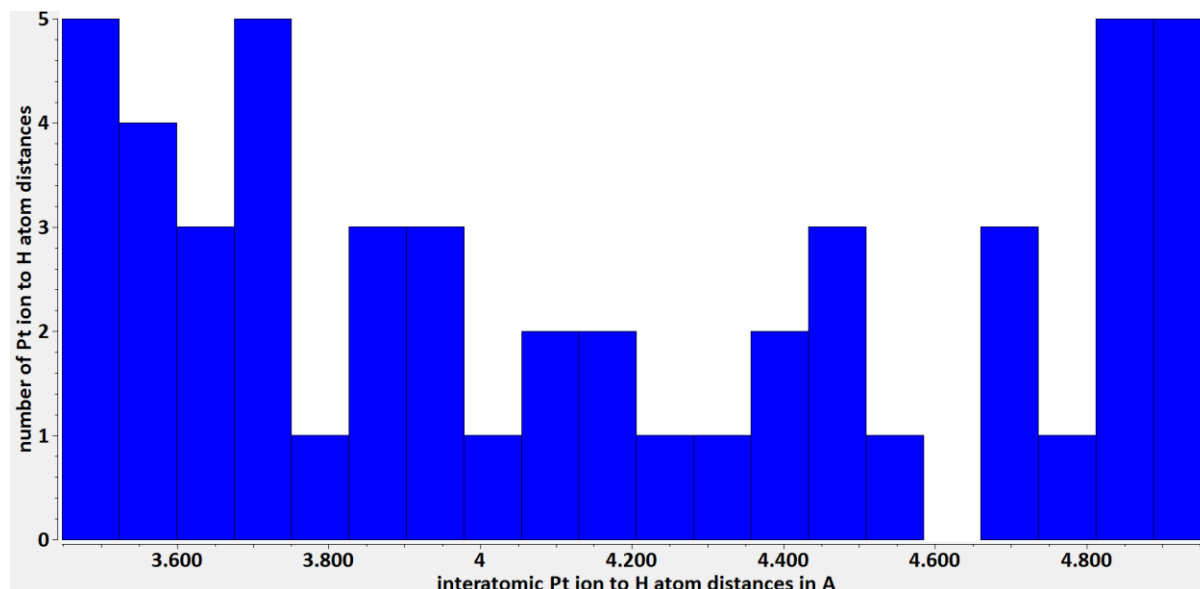


Figure 2.15 The  $\text{Pt}^{\text{IV}}$  ion to H distance of the 17 crystal structures are plotted to validate the computed radial distribution function values obtained from the association of the water to the  $[\text{PtCl}_6]^{2-}$  anion simulation

These plots (Fig. 2.12, 2.13, and 2.14) have shown that the computed radial distribution function values calculated for the association of the water to the  $[\text{PtCl}_6]^{2-}$  anion is a plausible solution structure for the hydration shell of the  $[\text{PtCl}_6]^{2-}$  anion.

The water molecules are located at approximately similar positions which correspond to those from the simulated solvation sphere calculations of water associated to the  $[\text{PtCl}_6]^{2-}$  anion. The calculation also suggests that the H atom of the water molecule points towards the triangular faces of the  $[\text{PtCl}_6]^{2-}$  anion octahedron<sup>1</sup> (see Fig. 2. 16). The cation (counter ion) in these crystal structures also interacts with the water molecules, influencing both the position and directionality of a hydrogen bond and how it interacts with the  $[\text{PtCl}_6]^{2-}$  anion.

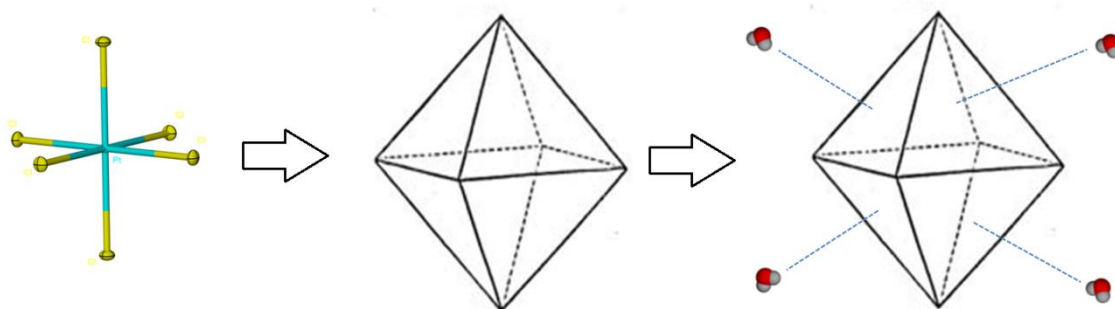


Figure 2.16 The water molecules interacting with the face of the octahedral  $[\text{PtCl}_6]^{2-}$  anion via hydrogen bonding

The work done by Bertani *et al.*<sup>36</sup> and Nyburg *et al.*<sup>37</sup> suggests that a halogen atom which is covalently bound to another, *i.e.* metal atom, has an anisotropic charge distribution (see Fig. 2.17). The figure shows that the halogen atom has a partially negative equatorial charge distribution ( $\delta^-$ ) with the head having a partially positive charge distribution ( $\delta^+$ ). This is unlike other atoms which have either a spherical or anisotropic charge distribution. This would surely influence the directionality of any interaction with this kind of atom.

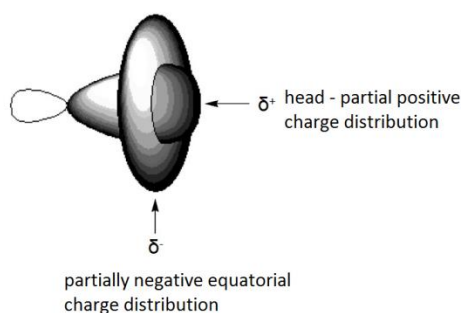


Fig. 2.17 Schematic representation of the electrostatic potential in covalently bound Cl, Br and I atoms.

The face of an octahedral  $[\text{PtCl}_6]^{2-}$  anion displays this unique electronic charge distribution (see Fig. 2.18). The chloride ions in the  $[\text{PtCl}_6]^{2-}$  anion are situated at the corners of the octahedral faces (see Fig. 2.18b), now also taking into account the anisotropic charge distribution of the chloride ion. The overall  $\delta^-$  would be greater in the centre of the octahedral face of the  $[\text{PtCl}_6]^{2-}$  anion since the contribution of the three  $\text{Cl}^-$  ions'  $\delta^-$  effect would make it more negative in the centre. The part of the octahedral face which is most likely to interact with water molecules via a hydrogen bond, would not be directed towards the edges but rather towards the centre of the octahedral face, as the H atom in water is  $\delta^+$ . This is also clear

from the crystal structures reported,<sup>38,39</sup> which have been modelled showing the hydrogen bonding interaction with the face of the  $[\text{PtCl}_6]^{2-}$  anion.

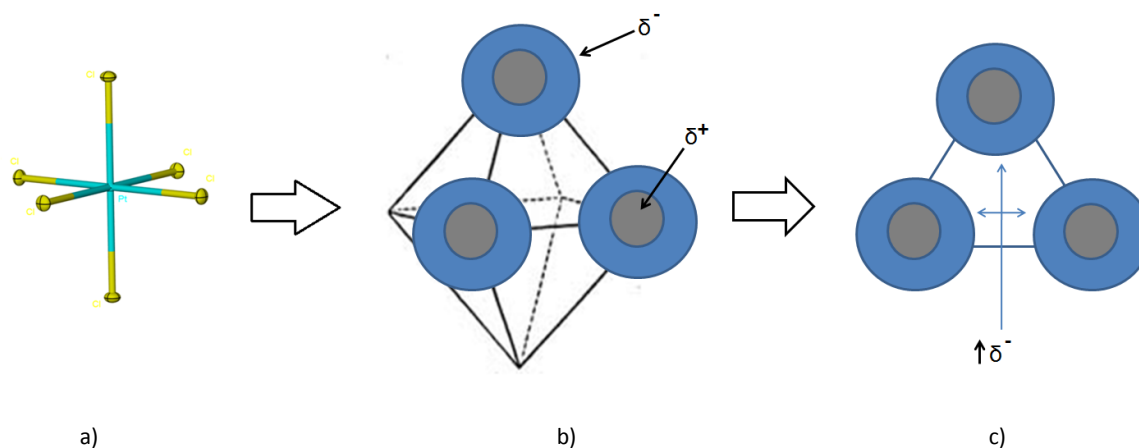


Fig. 2.18 The overall  $\delta^-$  would be greater in the centre of the octahedral face of the  $[\text{PtCl}_6]^{2-}$  since the contribution of the three Cl atoms'  $\delta^-$  effect would make it more negative in the centre.

As mentioned before, X-ray diffraction has some difficulty detecting the electron density of hydrogen atoms, especially in such close proximity to much heavier elements such as i.e. Pt, Cl, and O atoms. For this reason no assumptions can be made with respect to the hydrogen atoms' directionality towards the face of the octahedral  $[\text{PtCl}_6]^{2-}$  anion. A comment on the directionality of the hydrogen bonding interaction of the water molecule with the face of the octahedral  $[\text{PtCl}_6]^{2-}$  anion can be made, if additional computational geometry optimizations of the H atoms are carried out. The interaction of the cations (counter ions) with water molecule/s should also be taken into account. This could influence the directionality of the hydrogen bonding interaction with the face of the octahedral anion, as mentioned above.

In conclusion, this study has shown with existing crystallographic evidence that the  $[\text{PtCl}_6]^{2-}$  anion can be hydrated by up to four water molecules in the solid-state. This work also validates the solution structure of the association of water and the  $[\text{PtCl}_6]^{2-}$  anion by means of experimental X-ray.

Upon examination of the publications,<sup>21-34</sup> which contained the 17 crystal structures showing the association of water with the  $[\text{PtCl}_6]^{2-}$  anion, we found that none of the authors had any intention of crystallizing any water molecules around the  $[\text{PtCl}_6]^{2-}$  anion. This

therefore implies that there is a high probability of hydration of the  $[\text{PtCl}_6]^{2-}$  anion in the presence of water or if some water impurities are found in the solvent.

---

## References

---

1. K. J. Naidoo, G. Klatt, K. R. Koch, D. J. Robinson, *Inorg. Chem.*, **2002**, 41, 1845.
2. D. Steinborn, O. Gravenhorst, H. Hartung, U. Baumeister, *Inorg. Chem.*, **1997**, 36, 2195.
3. C. J. Jameson, A. K. Jameson, *J. Chem. Phys.*, **1986**, 85, 5448.
4. M. R. Burger, J. Kramer, H. Chermette, K. R. Koch, *Magn. Reson. Chem.*, **2010**, 48, S38.
5. I. J. Bruno, J. C. Cole, P. R. Edgington, M. Kessler, C. F. Macrae, P. McCabe, J. Pearson, R. Taylor, *Acta Crystallogr., Sect. B: Struct. Sci.*, **2002**, 58, 389.
6. *SMART Data Collection Software, Version 5.629*; Madison, WI, Bruker AXS Inc. **2003**.
7. *SAINT Data Collection Software, Version 6.45*; Madison, WI, Bruker AXS Inc. **2003**.
8. *SADABS, Version 2.05*; Madison, WI, Bruker AXS Inc. **2002**; R. H. Blessing, *Acta Crystallogr. Sect. A: Found. Crystallogr.*, **1995**, 51, 33.
9. L. J. Barbour, *J. Supramol. Chem.*, **2001**, 1, 189.
10. M. Shamsipur, G. Rounaghi, A. I. Popov, *J. Solution Chem.*, **1980**, 9, 9.
11. A. Delville, H. D. H. Stover, C. Detellier, *J. Am. Chem. Soc.*, **1987**, 109, 7293.
12. K. M. Fromm, E. D. Gueneau, J.-P. Rivera, G. Bernardinelli, H. Goesmann, *Z. Anorg. Allg. Chem.*, **2002**, 628, 171.
13. Y. Diskin-Posner, I. Goldberg, *New J. Chem.*, **2001**, 25, 899.
14. X. Gu, X. Lu, Sarula, Y. Deng, C. Ye, W. Xuebao, *Chin. Chin. J. Inorg. Chem.*, **2007**, 23, 669.
15. P. Dapporto, P. Paoli, I. Matijasic, L. Tusek-Bozic, *Inorg. Chim. Acta*, **1998**, 282, 76.
16. H. Zhang, X. Wang, D. E. Zelmon, B. K. Teo, *Inorg. Chem.*, **2001**, 40, 1501.
17. L. Xiao-Ming, L. Guo-Xiang, T. Shu-Jie, L. Shun-Cheng, J. HuaxueChin. *J. Struct. Chem.*, **1995**, 14, 157.
18. M. Mercer, M. R. Truter, *J. Chem. Soc., Dalton Trans.*, **1973**, 2469.
19. T. Gallagher, M. J. Taylor, S. R. Ernst, M. L. Hackert, *Acta Crystallogr., Sect. B: Struct. Sci.*, **1991**, 47, 362.
20. W.C. Hamilton, *Annu. Rev. Phys. Chem.*, **1962**, 13, 19.
21. A. S. Gaballa, H. Schmidt, C. Wagner, D. Steinborn, *Inorg. Chim. Acta.*, **2008**, 361, 2070.
22. K. Ha, *Acta Crystallogr. Sect. E Struct. Rep. Online*, **2010**, E66, m425.
23. K. Ha, *Z. Kristallogr. New Cryst. Struct.*, **2012**, 227, 31.
24. K. Ha, *Z. Kristallogr. New Cryst. Struct.*, **2012**, 227, 33.
25. Z. Travnicek, I. Popa, M. C. ajan, R. Herchel, J. Marek, *Polyhedron*, **2007**, 26, 5271.
26. S. Halder, G. Saha, B. G. Chand, A. D. Jana, G. Mostafa, J. Cheng, T. H. Lu, C. Sinha, *Inorg. Chim. Acta.*, **2010**, 363, 2080.
27. F. Zordan, L. Brammer, *Acta Crystallogr., Sect. B: Struct. Sci.*, **2004**, 60, 512.
28. G. Gencheva, P.R. Bontchev, J. Sander, K. Hegetschweiler, *Z. Kristallogr.-New Cryst. Struct.*, **2000**, 215, 183.
29. B. Viossat, N. Dung, J.C. Lancelot, M. Robba, *Inorg. Chim. Acta*, **1988**, 152, 189.
30. B. Viossat, N. Dung, J. C. Lancelot, M. Robba, *Inorg. Chim. Acta.*, **1989**, 161, 165.
31. Z. Travnicek, I. Popa, M. C. ajan, R. Herchel, J. Marek, *Polyhedron*, **2007**, 26, 5271.
32. M. Yousefi, S. Teimouri, V. Amani, H.R. Khavasi, *Acta Crystallogr., Sect. E: Struct. Rep. Online*, **2007**, 63, m2460.
33. N. A. Bokach, M. Haukka, A. J. L. Pombeiro, S. N. Morozkina, V. Yu. Kukushkin, *Inorg. Chim. Acta.*, **2002**, 336, 95.
34. G. Valle, R. Ettorre, *Z. Kristallogr.-New Cryst. Struct.*, **1998**, 213, 95.



- 
35. F. A. Cotton, R. L. Luck, *Inorg. Chem.*, **1989**, 28, 3210.
  36. R. Bertani, P. Sgarbossa, A. Venzo, F. Lelj, M. Amati, G. Resnati, T. Pilati, P. Metrangolo, G. Terraneo, *Coord. Chem. Rev.*, **2010**, 254, 677.
  37. S. C. Nyburg, C. H. Faerman, *Acta Cryst. Sect. B.*, **1985**, 41, 274.
  38. R. J. Warr, A. N. Westra, K. J. Bell, J. Chartres, R. Ellis, C. Tong, T. G. Simmance, A. Gadzhieva, A. J. Blake, P. A. Tasker, M. Schroder, *Chem. Eur. J.*, **2009**, 15, 4836.
  39. K. J. Bell, A. N. Westra, R. J. Warr, J. Chartres, R. Ellis, C. C. Tong, A. J. Blake, P. A. Tasker, M. Schroder, *Angew. Chem. Int. Ed.*, **2008**, 47, 1745.

# Chapter 3

## Single Crystal X-ray Diffraction Analysis of Dication Hexachloridoplatinate(IV) Salts as a Function of Temperature

### Synopsis

The single crystal X-ray diffraction (SCXRD) measurements of *dication hexachloridoplatinate(IV)* salts, *i.e.*  $\text{Rb}_2\text{PtCl}_6$ ,  $(\text{NH}_4)_2\text{PtCl}_6$  and  $[\text{N}(\text{CH}_3)_4]_2\text{PtCl}_6$ , were performed as a function of temperature and discussed with respect to the effect temperature has on atomic displacement upon lattice expansion. The Pt-Cl bond displacement of the  $[\text{PtCl}_6]^{2-}$  anion in all three salts were inspected to see whether weakening intramolecular interactions between the anion and cation induces any bond displacement upon lattice expansion as a function of temperature. The measured difference in Pt-Cl bond lengths in  $\text{Rb}_2\text{PtCl}_6$  and  $(\text{NH}_4)_2\text{PtCl}_6$  salts over a 100 K to 400 K temperature range are used to calculate the expected sensitivity of the  $^{195}\text{Pt}$  chemical shift in the solid state. The  $[\text{N}(\text{CH}_3)_4]_2\text{PtCl}_6$  salt displays multiple low and high temperature structural phase transitions which make it extremely difficult to compute the expected  $^{195}\text{Pt}$  chemical shift sensitivity over a similar temperature range. The results from SCXRD measurements would be used to study the atomic displacement in *dication hexachloridoplatinate(IV)* salts which would aid with the interpretation of our experimental  $^{195}\text{Pt}$  chemical shifts in the solid state. Quite some changes are occurring with respect to atomic displacement within these salts as a function of temperature. The interatomic distance between the cation and anion are increasing as function increasing temperature, which results in the weakening of intermolecular interaction between anion and cation in all three salts. We observed a small degree of change in Pt-Cl bond lengths in both  $(\text{NH}_4)_2\text{PtCl}_6$  and  $\text{Rb}_2\text{PtCl}_6$  as a function of temperature. The  $[\text{N}(\text{CH}_3)_4]_2\text{PtCl}_6$  salts has quite a large degree of Pt-Cl bond displacement due to structural phase transitions.

## Introduction

The theoretical and experimental work carried out by Jameson *et al.*<sup>1</sup>, looked at the sensitivity of the  $^{195}\text{Pt}$  chemical shift in solution. Their work correlates the bond displacement of the covalently bound Pt-Cl bond lengths in the octahedral  $[\text{PtCl}_6]^{2-}$  anion with the sensitivity of  $^{195}\text{Pt}$  chemical shift. The observations made by Jameson *et al.*<sup>1</sup> on the nature of the  $^{195}\text{Pt}$  nucleus in the  $[\text{PtCl}_6]^{2-}$  anion shows the  $^{195}\text{Pt}$  chemical shift to be extremely sensitive to subtle changes in Pt-Cl bond displacement in solution. This was recently confirmed by Koch *et al.*<sup>2</sup> using DFT calculations in which they correlate the sensitivity of  $^{195}\text{Pt}$  chemical shift to subtle changes in Pt-Cl bond displacement in the octahedral ( $O_h$  symmetry)  $[\text{PtX}_6]^{2-}$ , where X=Cl, Br, I, and F anions. The theoretical calculations carried out by Koch *et al.*<sup>2</sup> and Jameson *et al.*<sup>1</sup> were performed in the gas and solution phases, respectively. This study aims to investigate if the Pt-Cl bond displacement in the octahedral  $[\text{PtCl}_6]^{2-}$  anion also displays similar bond displacement effects in the solid state.

Using variable temperature SCXRD on the highly symmetrical inorganic *dication hexachloridoplatinate(IV)* salts  $\text{X}_2\text{PtCl}_6$  [X =  $\text{Rb}^+$ ,  $(\text{NH}_4)^+$  and  $[(\text{N}(\text{CH}_3)_4)^+]$ <sup>3,4</sup> makes it possible to probe the degree of atomic displacement upon lattice expansion. These three salt have distinctly different cations, the  $\text{Rb}^+$  cation has a purely electrostatic interaction to the  $[\text{PtCl}_6]^{2-}$  anion. The  $(\text{NH}_4)^+$  cation, on the other hand, has a partially electrostatic and highly directional hydrogen bonding interaction with the anion. The  $[(\text{N}(\text{CH}_3)_4)^+]$  cation is much larger and it is capable of having multiple hydrogen bonding interactions with the anion, which is quite different to that of the  $\text{Rb}^+$  and  $(\text{NH}_4)^+$  cations. These three cations are used as they would surely have a different interaction with the  $[\text{PtCl}_6]^{2-}$  anion, which would have a different influence on the degree of bond displacement within the  $[\text{PtCl}_6]^{2-}$  anion as a function of temperature. The SCXRD measurement on these salts would prove if bond displacement occurs within the Pt-Cl bond length as a function of temperature, which would extend the proposed hypothesis as set out by Jameson *et al.*<sup>1</sup> and Koch *et al.*<sup>2</sup> who postulated that the sensitivity of  $^{195}\text{Pt}$  chemical shift is due to changes in Pt-Cl bond length.

These salts were selected based on these crystal structures' high cubic symmetry. The  $[\text{PtCl}_6]^{2-}$  anion in these cubic salts adopts  $O_h$  symmetry, making all six Pt-Cl bond lengths equivalent. The  $\text{Rb}^+$  cation is spherical, whereas the  $(\text{NH}_4)^+$  adopts  $C_4$  symmetry which makes four N-H bond lengths equivalent. The cation of the  $[\text{N}(\text{CH}_3)_4]_2\text{PtCl}_6$  salt has multiple structural symmetry operators due to its known structural rotation, which causes phase transition at low and higher temperatures. These salts' high symmetry makes it easier to de-convolute the structural changes which occur during lattice expansion as a function of temperature.

The Pt-Cl bond displacements of  $\text{Rb}_2\text{PtCl}_6$  and  $(\text{NH}_4)_2\text{PtCl}_6$  salts measured by SCXRD as a function of temperature are used to calculate the expected  $^{195}\text{Pt}$  chemical shift sensitivity. The expected  $^{195}\text{Pt}$  chemical shift sensitivity is estimate by multiplying the measured difference in ( $\Delta\text{Pt-Cl}$ ) bond length by the calculated<sup>2</sup>  $\Delta(\delta^{195}\text{Pt})/\delta(\Delta\text{Pt-Cl}) = 18300 \text{ ppm}/\text{\AA}$ . The difference in Pt-Cl bond lengths are measured using variable temperature SCXRD measurements of the  $\text{Rb}_2\text{PtCl}_6$  and  $(\text{NH}_4)_2\text{PtCl}_6$  salts. These expected  $^{195}\text{Pt}$  chemical shift sensitivities will be compared with experimental solid state nuclear magnetic resonance (SSNMR) spectroscopy as a function of temperature to probe the  $^{195}\text{Pt}$  chemical shift (Chapter 4) in the solid state. The SCXRD analyses provide information on bond displacement within these specific crystal lattices and would help with the interpretation of the results obtained from variable temperature SSNMR measurements.

## Experimental

### 3.1 Synthesis of dication hexachloridoplatinate(IV) salts

It is well known that the morphology of a sample used during an SSNMR experiment has an influence on the spectral line width; an example of this is elegantly demonstrated in the paper of Horii *et al.*<sup>5</sup> They showed that the morphology of a sample directly influences the line width of spectra. The rate of nucleation had been reduced using two methods. The first method used the effect of temperature, which decreased the rate of nucleation during crystal growth. The second method used dilution, which decreased the rate of nucleation. These methods were initially used independently but gave the best results when used together and resulted in a crystalline salt.

#### 3.1.1 Synthesis of dication hexachloridoplatinate(IV) salt $[Rb_2PtCl_6]$ , $[(NH_4)_2PtCl_6]$ and $(N(CH_3)_4)^+_2PtCl_6$

A 20  $\mu$ l aliquot 0.2 M  $[PtCl_6]^{2-}$  solution was pipetted into a beaker from a 0.2 M  $[PtCl_6]^{2-}$  stock solution made up in 6 M HCl. To this solution was added 2 ml of  $dH_2O$  and 1 ml 6 M HCl. A 2 ml 0.5 M  $[Rb]^+$  solution was prepared separately. The two solutions were then separately heated on a standard temperature controlled magnetic stirrer and gradually heated to 70 °C. A 10 ml  $dH_2O$  solution was also heated to 70 °C and kept at this temperature for use throughout the experiment, where it was required. The reason for attempting this experiment at such an elevated temperature was to reduce the rate of nucleation. The 2 ml solution containing the aliquot of a 0.5 M  $[Rb]^+$ , 0.5 M  $[NH_4]^+$  and 0.5 M  $[(CH_3)_4N]^+$  was prepared separately. The solution was used to prepare all three salts and was systematically added at a rate of 0.5 ml per minute to the  $[PtCl_6]^{2-}$  anion containing solution. After the  $Rb^+$ ,  $[NH_4]^+$  and  $[(CH_3)_4N]^+$  solutions were separately added, the solutions were placed in the 90°C water bath. The solutions were then slowly cooled down to room temperature and left to stand for 24 h. This resulted in the formation of yellow crystals suitable for SCXRD measurement and SSNMR analysis (see Fig. 3.1.).

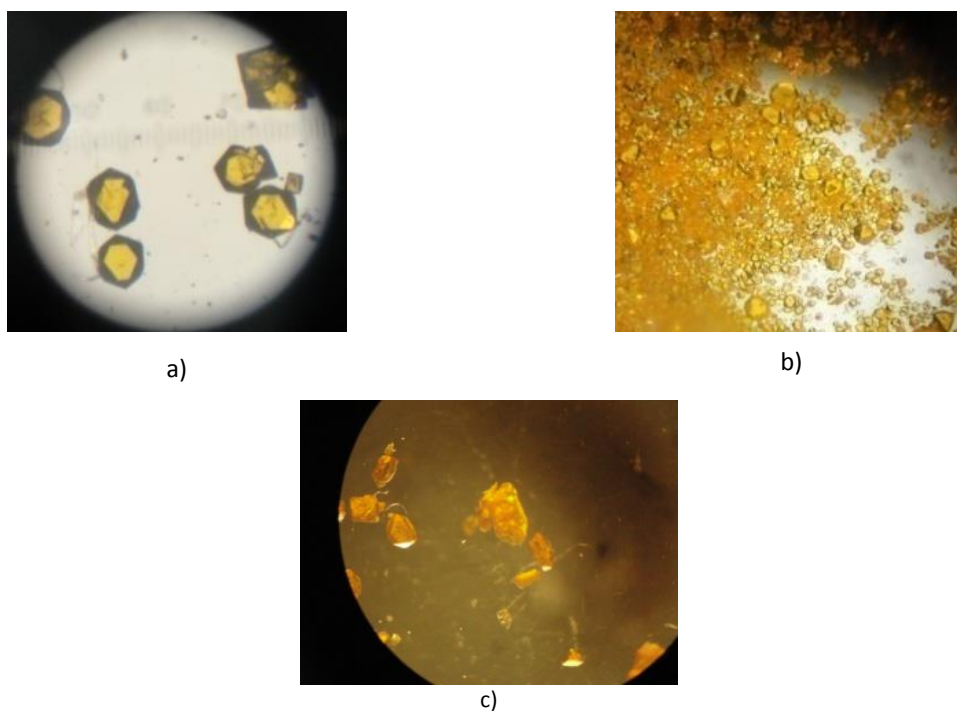


Figure 3.1 Crystals of a) *dirubidium hexachloridoplatinate(IV)*  $[\text{Rb}_2\text{PtCl}_6]$ , b) *diammonium hexachloridoplatinate(IV)*  $[(\text{NH}_4)_2\text{PtCl}_6]$  and *bis(tetramethylammoium hexachloridoplatinate(IV))*  $[(\text{N}(\text{CH}_3)_4)^+]_2\text{PtCl}_6$

The single crystals produced from these experiments were used to perform SCXRD measurements as a function of temperature. The same instrumentation was used (see Chapter 2, Section 2.3 for details).

## Results and Discussion

### 3.2 Single crystal X-ray diffraction characterization of dirubidium hexachloridoplatinate(IV) salt, $[Rb_2PtCl_6]$ as a function of temperature

The *dirubidium hexachloridoplatinate(IV)* salt crystallized in the space group  $Fm\bar{3}m$ , with three atoms in the asymmetric unit (see Fig. Fig. 3.2a). The  $[PtCl_6]^{2-}$  anion requires two  $Rb^+$  cations per  $[PtCl_6]^{2-}$  anion to result in the  $Rb_2PtCl_6$  salt (Fig. 3.2b). The  $[PtCl_6]^{2-}$  anion adopts  $O_h$  symmetry, which makes the Pt-Cl bond lengths equivalent. The  $Rb^+$  cation is situated within the 3-D cages (Fig. 3.3a) surrounded by twelve  $Cl^-$  ions forming twelve purely electrostatic interactions (Fig. 3.3b). The structural parameters of  $Rb_2PtCl_6$  crystal structure are tabulated and listed with the crystallographic parameter and the bond length can be obtained from the cif files in the Appendix B.

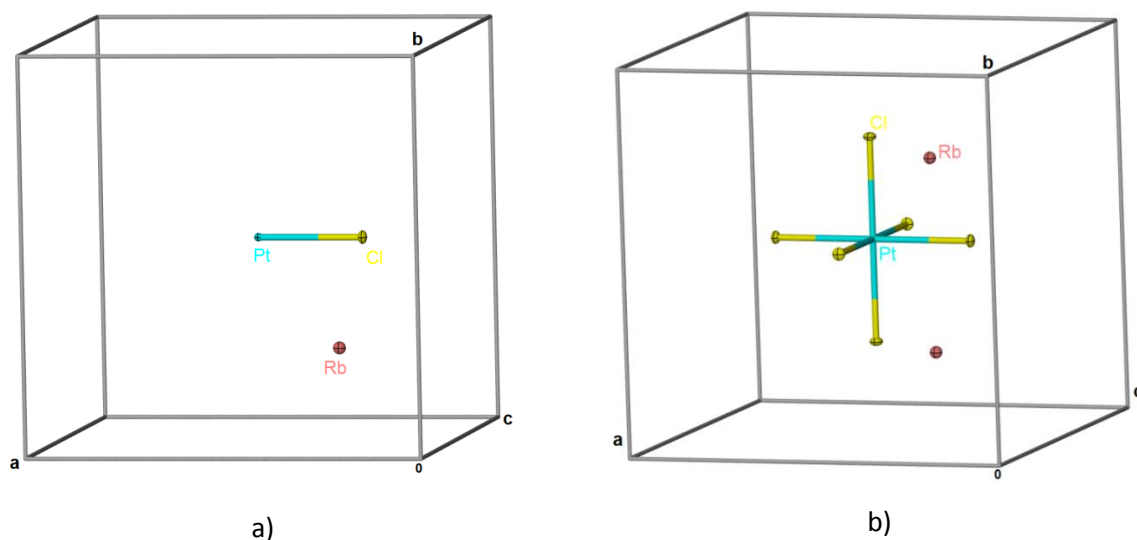


Figure 3.2 a) Three atoms in the asymmetric unit of  $Rb_2PtCl_6$  b) *Dirubidium hexachloridoplatinate(IV)* salt in unit cell

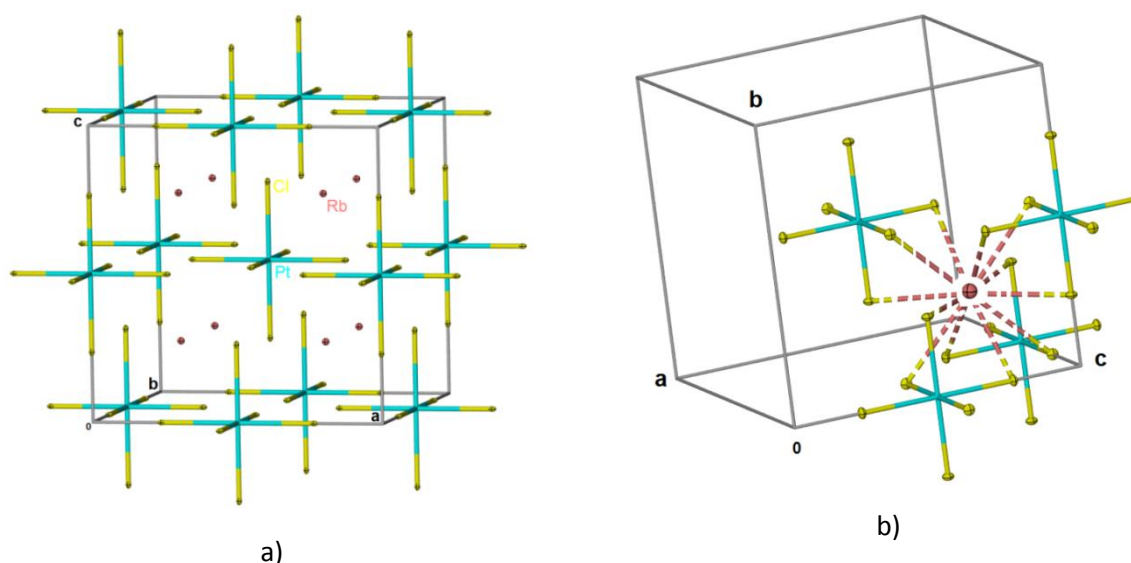


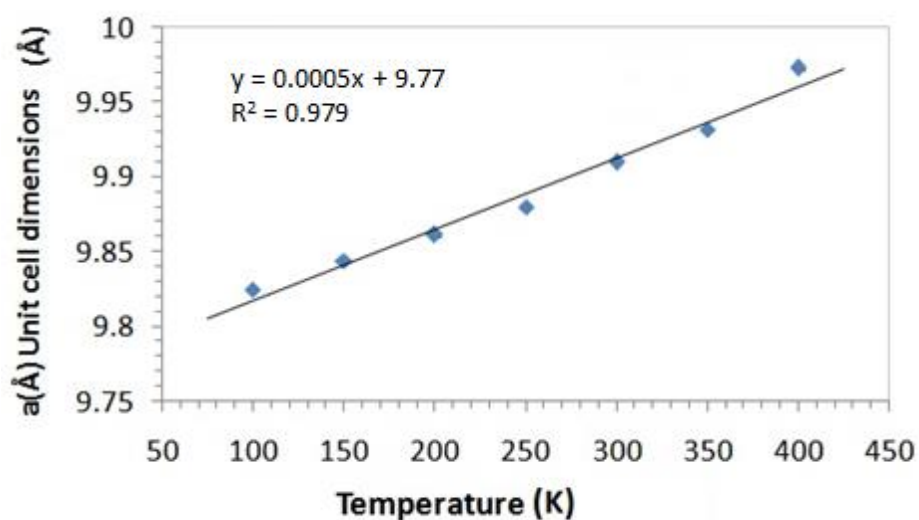
Figure 3.3 a) Packing diagram of  $\text{Rb}_2\text{PtCl}_6$  b) Electrostatic interaction of the Rb ion with twelve Cl ion  $\text{Pt-Cl}\cdots\text{Rb}^+$  in  $\text{Rb}_2\text{PtCl}_6$

The SCXRD measurements as a function of temperature were carried out from 100 K – 400 K with 50 K increments. The unit cell and unit volume parameters extracted from temperature dependence SCXRD measurements on the  $\text{Rb}_2\text{PtCl}_6$  salt are shown in Fig. 3.5 and Table 3.1. The slopes on both these plots Fig. 3.4 give an indication that this crystal structure does not undergo any structural phase transitions as a function of temperature. No other form of characterization was carried out on this crystal structure since all the lattice parameters obtained are consistent with what has already been reported for this crystal structure.

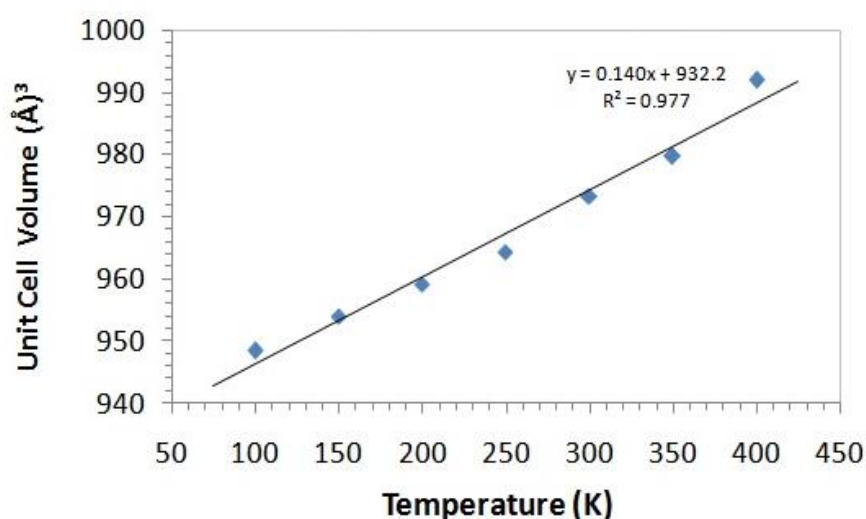
Table 3.1 The unit cell dimensions and unit cell volume obtained from SCXRD analysis of  $\text{Rb}_2\text{PtCl}_6$  change as a function of temperature

Temp K	Cell Dimensions of $a \text{ \AA}$	Cell Volume in $\text{\AA}^3$
100	9.825(2)	948.4(4)
150	9.844(2)	954.0(4)
200	9.8616(12)	959.1(2)
250	9.880(2)	964.4(4)
300	9.9100(17)	973.2(3)
350	9.932(3)	979.8(5)
400	9.973(7)	991.9(12)





a)



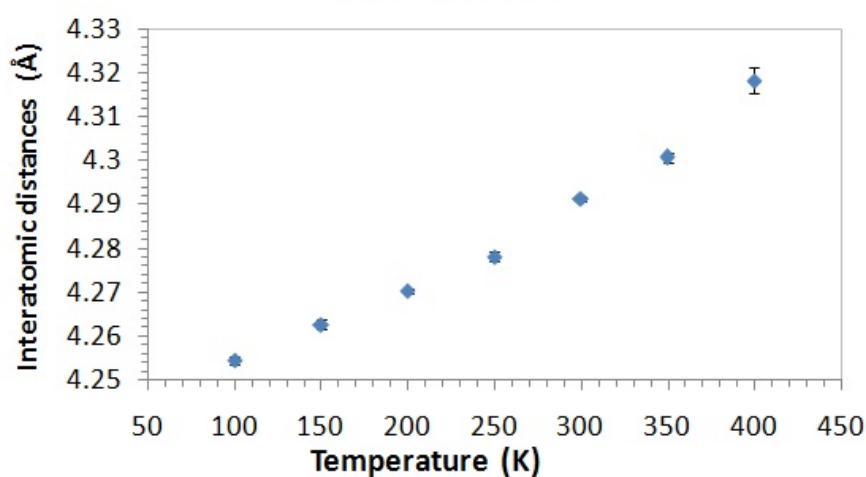
b)

Figure 3.4 The  $\text{Rb}_2\text{PtCl}_6$  showing how a) Unit cell dimensions ( $y=0.0005x + 9.77$ ,  $R^2=0.979$ ) and b) Unit cell volumes plots change as a function of temperature

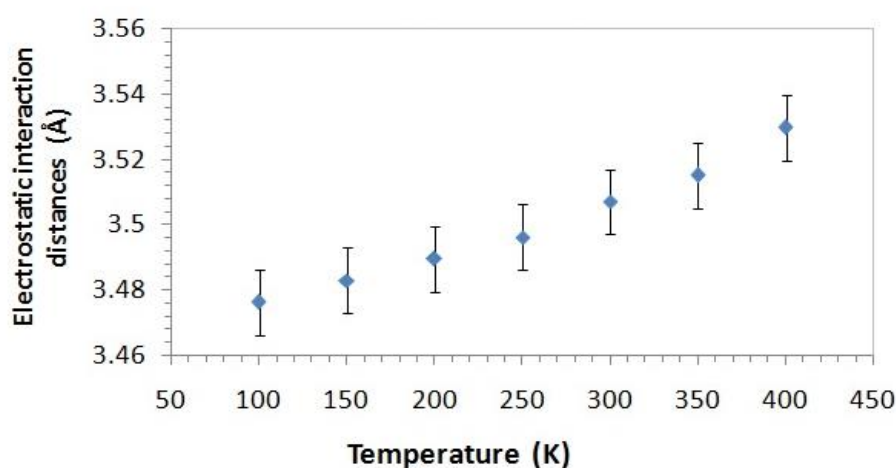
Additional information on the effect of temperature with respect to interatomic displacement between the  $\text{Pt}^{\text{IV}}$  ion in  $[\text{PtCl}_6]^{2-}$  and  $\text{Rb}^+$  cation is plotted in Fig. 3.5a and tabulated in Table 3.2. The effect on the electrostatic interaction between  $\text{Pt}-\text{Cl}\cdots\text{Rb}^+$  is also plotted in Fig. 3.5b and tabulated in Table 3.2. The covalent  $\text{Pt}-\text{Cl}$  bond displacements within the  $[\text{PtCl}_6]^{2-}$  are plotted in Fig. 3.6 and tabulated in Table 3.3.

Table 3.2 The interatomic distances between  $\text{Pt}^{\text{IV}}$  and  $\text{Rb}^+$  ions and the electrostatic interaction between the  $\text{Pt-Cl}\cdots\text{Rb}$  of  $\text{Rb}_2\text{PtCl}_6$  change as a function of temperature, measured directly from cif file using Mercury 3.3 (2014)

Temp in Kelvin	Pt to Rb interatomic in Å	Pt-Cl $\cdots$ Rb in Å
100	4.2544(9)	3.4762(7)
150	4.2626(10)	3.4830(8)
200	4.2702(5)	3.4895(4)
250	4.2781(10)	3.4962(8)
300	4.2912(7)	3.5070(6)
350	4.3007(12)	3.5151(10)
400	4.3183(30)	3.5297(24)



a)



b)

Figure 3.5 The interatomic distances a) Inter atomic distance between Pt to Rb ions (the difference in error is increasing since the degree of vibration is increasing as a function of temperature). b) Electrostatic interaction between the  $\text{Pt-Cl}\cdots\text{Rb}$  of  $\text{Rb}_2\text{PtCl}_6$  as a function of temperature

Table 3.3 The interatomic bond displacements in the covalent Pt-Cl bond of  $\text{Rb}_2\text{PtCl}_6$  obtained from SCXRD analysis measured as a function of temperature

Temp (K)	Pt-Cl Å
100	2.3236(9)
150	2.3230(9)
200	2.3222(7)
250	2.3212(9)
300	2.3247(9)
350	2.3240(10)
400	2.3293(19)

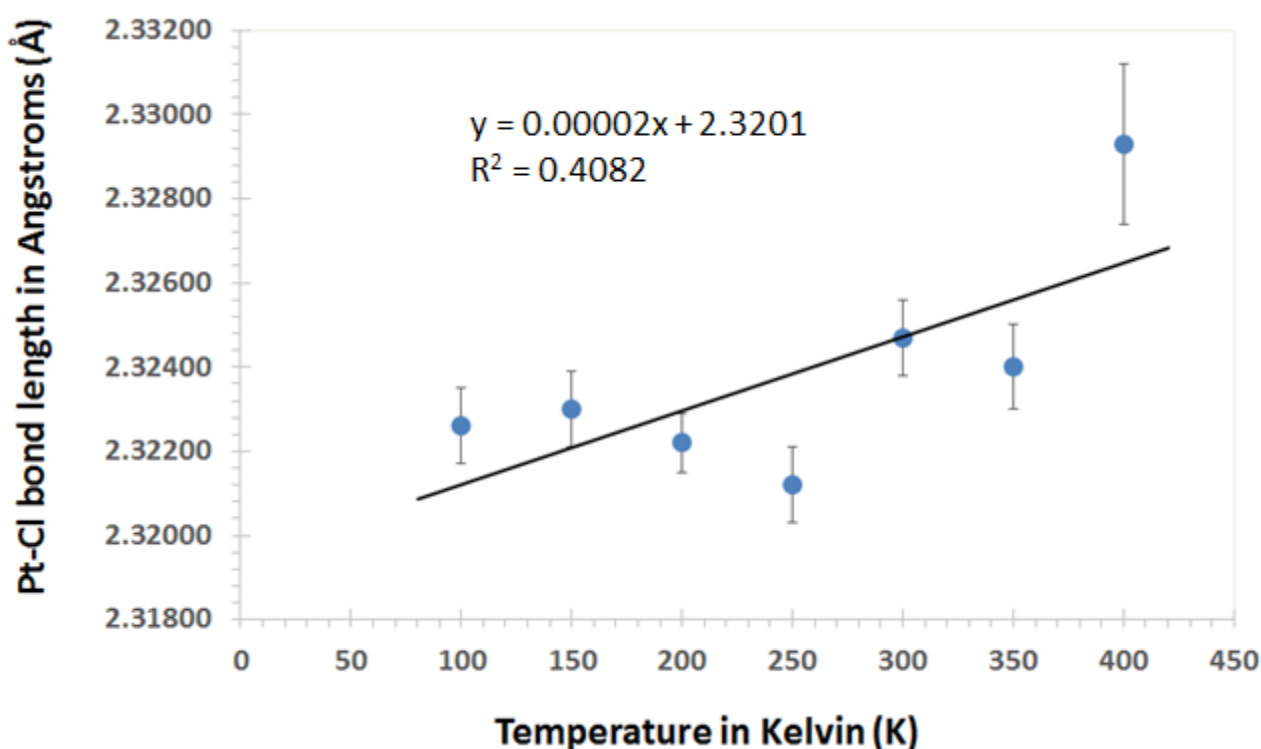


Figure 3.6 The SCXRD measurements of  $\text{Rb}_2\text{PtCl}_6$  as a function of temperature showing the Pt-Cl bond displacement, the ESD shows the degree of Pt-Cl displacement at a specific temperature. The slope was drawn to extract the average change in Pt-Cl bond displacement as a function of temperature

The *dirubidium hexachloridoplatinate(IV)*,  $\text{Rb}_2\text{PtCl}_6$  salt displayed no structural phase changes as a function of temperature, which is evident from the linear slopes showing the lattice parameter (Fig. 3.4a) and cell volume seen in Fig. 3.4a. The lattice expansion of  $\text{Rb}_2\text{PtCl}_6$  from 100 K to 400 K is 4.60 (0.05) %, which is quite low for lattice expansion of a crystal structure. The low lattice expansion in this salt also gives an indication of the structural rigidity and lattice dynamics which is elegantly

discussed by Armstong *et al.*<sup>6</sup> They point out that the rigid structural arrangement in the cubic lattice of these salts is due to the highly efficient face centred cubic packing arrangement of the atoms. Upon plotting the interatomic distance between the Pt<sup>IV</sup> ion in the [PtCl<sub>6</sub>]<sup>2-</sup> anion and Rb<sup>+</sup> cation, there is a systematic increase in the distance between the Rb<sup>+</sup> cation and [PtCl<sub>6</sub>]<sup>2-</sup> anion (see Fig. 3.5a) and similarly between Cl<sup>-</sup> ion in the [PtCl<sub>6</sub>]<sup>2-</sup> anion (Fig. 3.5b). This increase in distance would lead to a weakening of the purely electrostatic interaction (Pt-Cl...Rb<sup>+</sup>). The Pt-Cl bond displacement in the octahedral [PtCl<sub>6</sub>]<sup>2-</sup> anion, on the other hand, has a very small change over the entire temperature range (Fig. 3.6).

The conventional way of extracting average changes in bond length, if performed as a function of temperature, use the data showing the Pt-Cl bond displacement against temperature. From this data the slope was be estimated along with the standard deviation using linear regression statistics function, the calculation can be viewed in Appendix B. A slope (0.000015 Å/K) was extracted, which gives the average change in Pt-Cl bond length as a function of temperature. Using a linear regression the standard deviation on the slope was calculated (0.000008 Å/K), the temperature coefficient for Pt-Cl bond displacement is 0.000015 (0.000008) Å/K.

To estimate the expected <sup>195</sup>Pt chemical shift from X-ray diffraction data over a 100 K to 400 K range, the difference in Pt-Cl bond displacement from the highest to lowest temperature was taken as a reasonable estimate of the maximum Pt-Cl bond extension. The Pt-Cl bond length in Fig. 3.6 is initially increasing from 100 K to 200 K; it then decreases from 200 K to 300 K and from 300 K to 400 K it increases. There is, however, an overall increase in the Pt-Cl bond length from 100 K to 400 K, as seen from the positive slope (Fig. 3.6). If we assume that there is an overall increase in Pt-Cl bond length, we can take the highest temperature Pt-Cl bond length (400 K) and subtract it from the lowest temperature Pt-Cl bond length (100 K), which equates to 0.0057 (0.0021) Å. The error on the Pt-Cl bond length is calculated using the subtraction error propagation equation (see Appendix B). The sensitivity of <sup>195</sup>Pt chemical shift to changes in Pt-Cl bond displacement has been reported<sup>2</sup> to be large for a small change in Pt-Cl bond displacement; this change is used to calculate the expected sensitivity of <sup>195</sup>Pt chemical shift in the solid state. If we multiply the difference in Pt-Cl bond displacement 0.0057 (0.0021) Å with the computed <sup>195</sup>Pt chemical shift change with respect

to Pt-Cl bond length (18 300 ppm/ Å), it equates to  $104.3 \pm 38$  ppm over a 100 K to 400 K temperature range (estimated using equation 1).

$$\text{Expected } \delta^{195}\text{Pt difference}_{100\text{K to } 400\text{K}} = \text{Pt-Cl (bond length)}_{400\text{K}} - \text{Pt-Cl (bond length)}_{100\text{K}} \times (18300 \text{ Å/ppm}) \quad (1)$$

Table 3.4 Expected  $^{195}\text{Pt}$  chemical shift sensitivity and temperature coefficient over a 100 K to 400 K temperature range

	( $\Delta\text{Pt-Cl}$ ) 100K – 400 K range in Å	Expected $^{195}\text{Pt}$ chemical shift in ppm
<b>Rb<sub>2</sub>PtCl<sub>6</sub></b>	0.0057 (0.0021) Å	$104.3 \pm 38$ ppm

### 3.3 Single crystal X-ray diffraction characterization of diammonium hexachloridoplatinate(IV) salt, $[(\text{NH}_4)_2\text{PtCl}_6]$ as a function of temperature

The *diammonium hexachloridoplatinate(IV)* salt crystallized in the space group  $Fm\bar{3}m$ , with four atoms in the unit cell (see Fig. 3.7a and b). The  $[\text{PtCl}_6]^{2-}$  anion adopts  $O_h$  symmetry, which makes the Pt-Cl bond lengths equivalent. The  $\text{NH}_4^+$  cation is situated within the 3-D cages (Fig. 3.8a) and is surrounded by twelve  $\text{Cl}^-$  ion forming hydrogen bonds between the  $[\text{PtCl}_6]^{2-}$  anion and cation (Fig. 3.8b). The structural parameters of  $(\text{NH}_4)_2\text{PtCl}_6$  crystal structure are tabulated and listed with crystallographic parameters and bond length and can be obtained from cif files in the Appendix B.

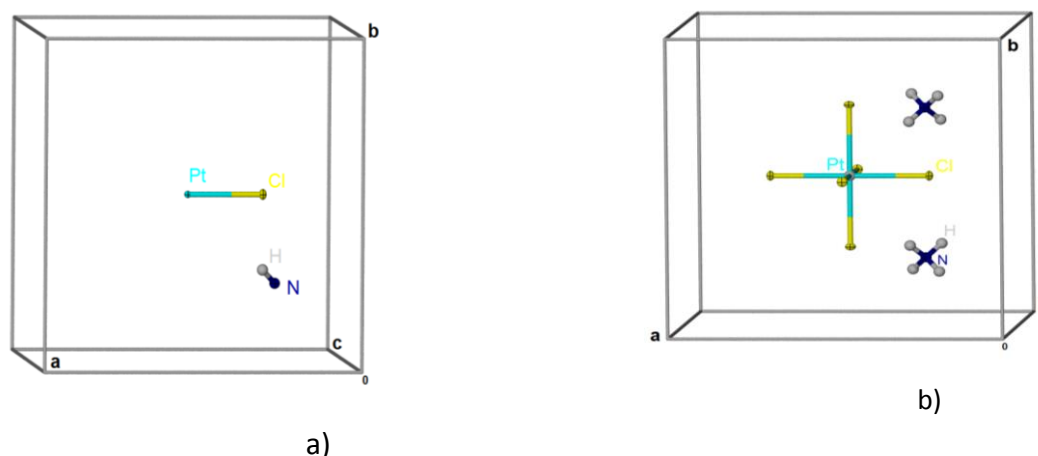


Figure 3.7 a) Four atoms in the asymmetric unit of  $(\text{NH}_4)_2\text{PtCl}_6$  b) *Diammonium hexachloridoplatinate(IV)* salt in unit cell

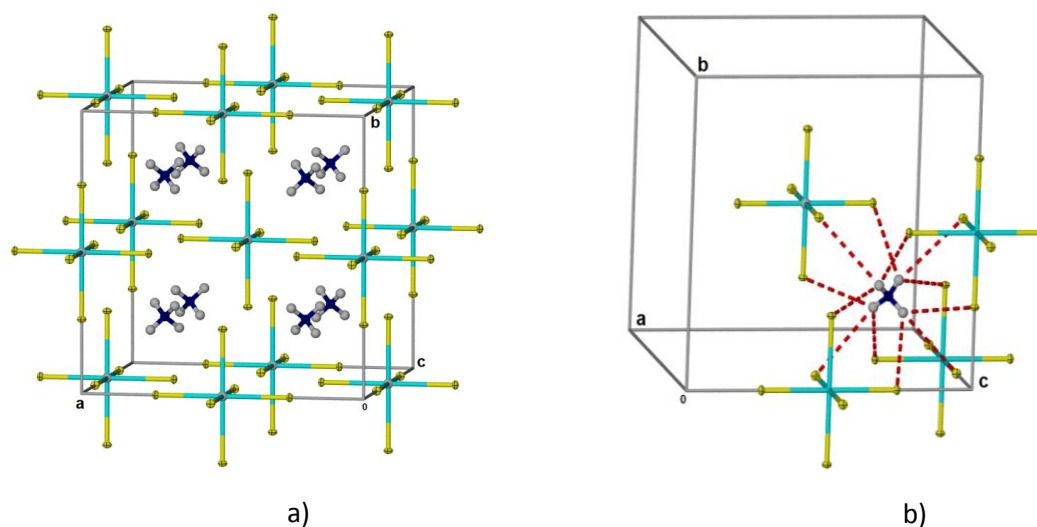
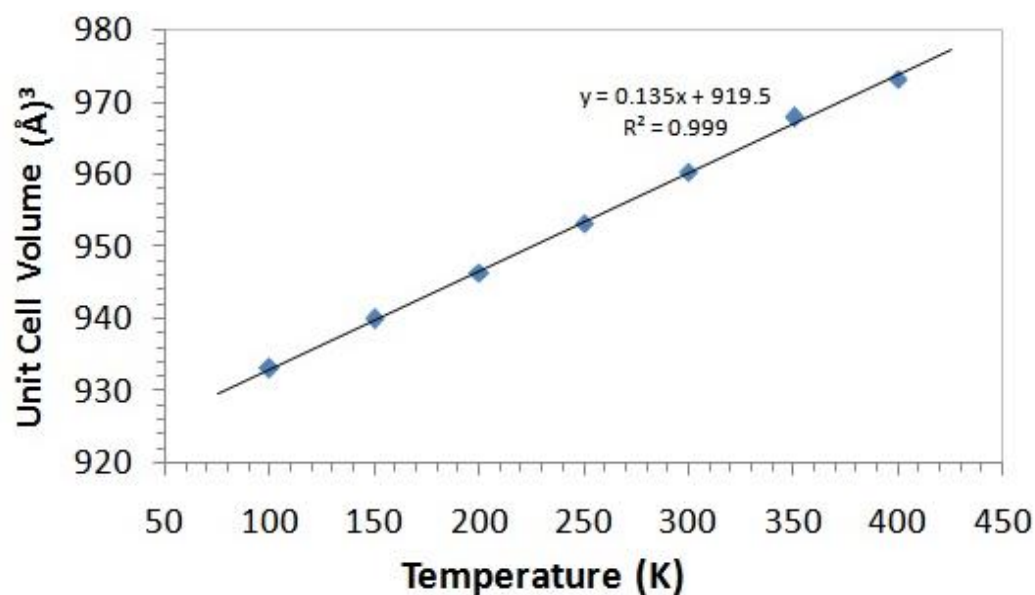


Figure 3.8 a) Packing diagram of  $(\text{NH}_4)_2\text{PtCl}_6$  b) hydrogen bonding interaction between  $[\text{PtCl}_6]^{2-}$  anion and  $\text{NH}_4^+$  cation ( $\text{Pt}-\text{Cl}\cdots\text{H}-\text{N}$ ) in the  $(\text{NH}_4)_2\text{PtCl}_6$  salt

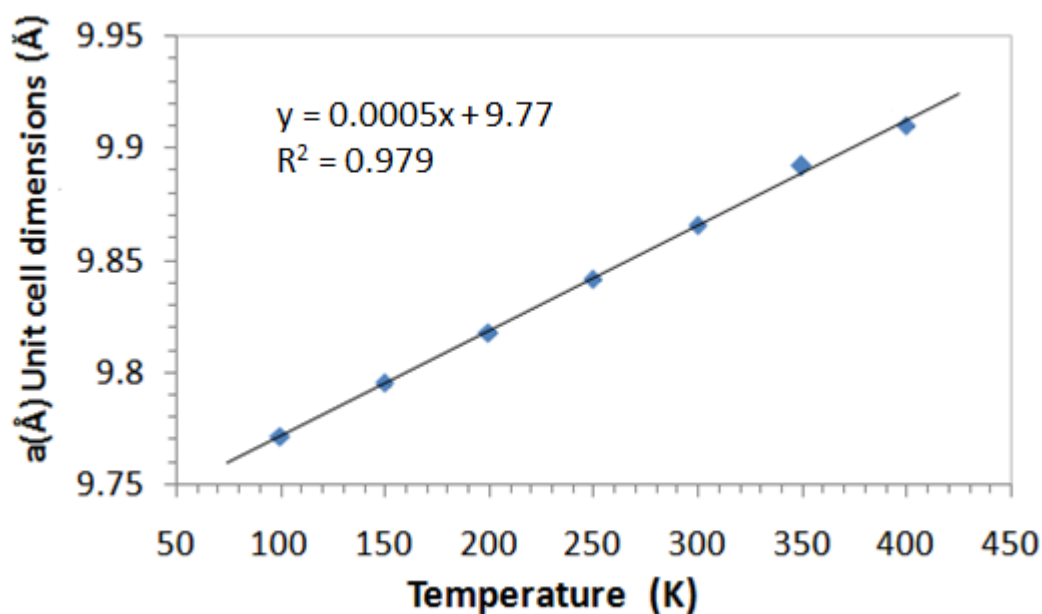
Table 3.5 The unit cell dimensions and unit cell volume obtained from SCXRD analysis of  $(\text{NH}_4)_2\text{PtCl}_6$  salt as a function of temperature

Temperature in K	Cell Dimensions distances in Å	Cell Volume in Å <sup>3</sup>
100	9.772(2)	933.2(2)
150	9.7957(15)	940.0(2)
200	9.8180(7)	946.39(12)
250	9.8416(7)	953.23(12)
300	9.8655(5)	960.5(9)
350	9.892(3)	968.1(4)
400	9.910(4)	973.1(6)

The SCXRD measurements of the  $(\text{NH}_4)_2\text{PtCl}_6$  salt were carried out from 100 K – 400 K temperature range with 50 K increments similar to that of the  $\text{Rb}_2\text{PtCl}_6$  salt. The unit cell and unit volume parameters extracted from temperature dependent XRD measurements on the  $(\text{NH}_4)_2\text{PtCl}_6$  salt are shown in Fig. 3.9 and in Table 3.5. The slopes from both of these plots (Fig. 3.9) give an indication that this crystal structure has no structural phase transitions as a function of temperature, which is similar to that of the  $\text{Rb}_2\text{PtCl}_6$ . The thermogravimetric analysis carried out on the  $(\text{NH}_4)_2\text{PtCl}_6$  salt<sup>7</sup> showed this structure to undergo no structural phase transitions as a function of temperature.



a)



b)

Figure 3.9 The  $(\text{NH}_4)_2\text{PtCl}_6$  salt a) Unit cell dimensions dimensions ( $y=0.0005x + 9.77$ ,  $R^2=0.979$ ) and b) Unit cell volumes change as a function of temperature

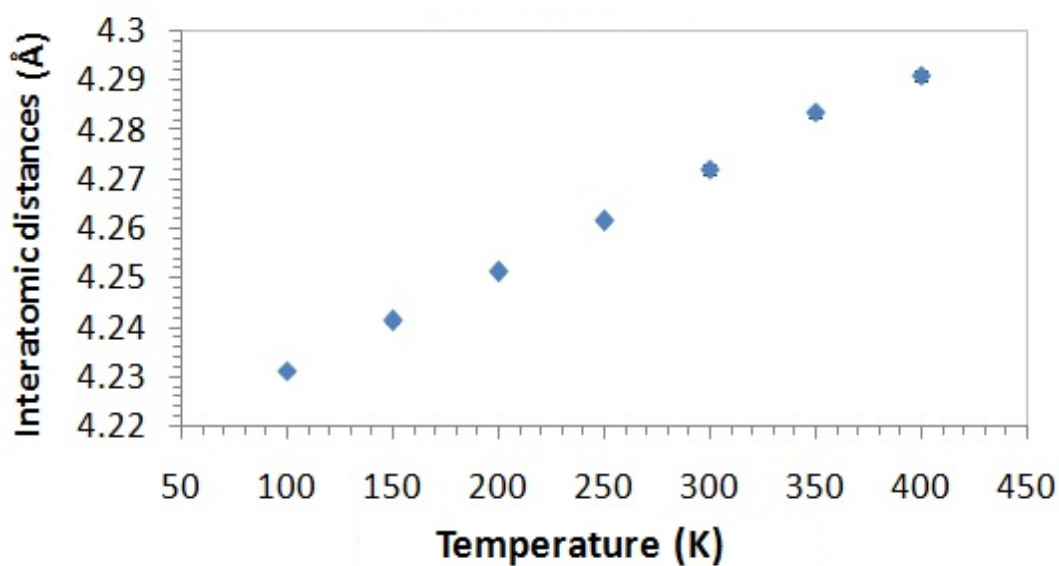
Additional information on the effect that temperature has on interatomic displacement between the  $\text{Pt}^{\text{IV}}$  ion in  $[\text{PtCl}_6]^{2-}$  and the  $\text{N}^+$  ion in  $(\text{NH}_4)^+$  is plotted in Fig. 3.10a and tabulated in Table 3.6. This shows that there is a systematic weakening of the interaction between the  $[\text{PtCl}_6]^{2-}$  anion and the

(NH<sub>4</sub>)<sup>+</sup> cation as a function of increasing temperature. This is further confirmed by the plot showing the increasing distances between the Cl<sup>-</sup> ion of the [PtCl<sub>6</sub>]<sup>2-</sup> anion and the N<sup>+</sup> ion of the (NH<sub>4</sub>)<sup>+</sup> cation plotted in Fig. 3.10b and tabulated in Table 3.5.

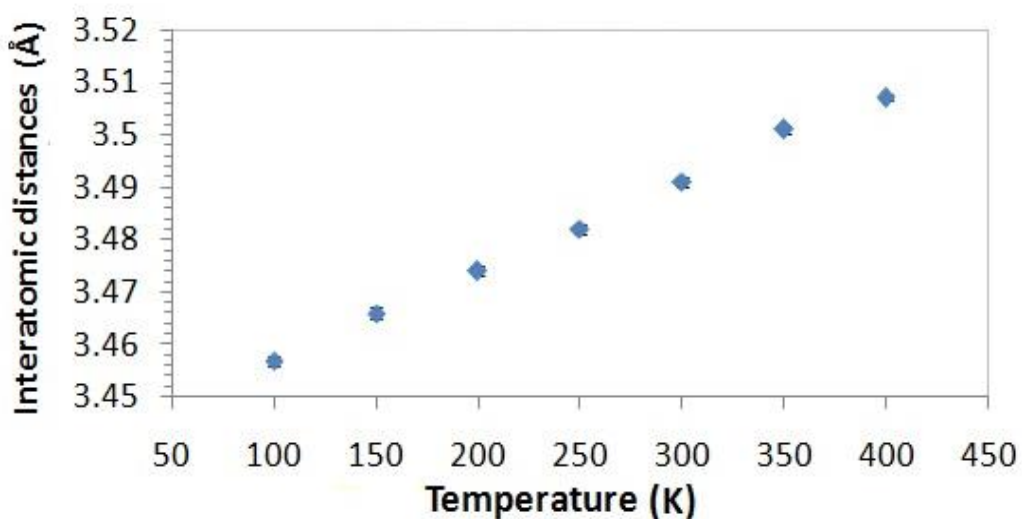
Table 3.6 The SCXRD of (NH<sub>4</sub>)<sub>2</sub>PtC<sub>6</sub> with respect to inter atomic distance between Pt<sup>IV</sup> and N<sup>+</sup> ions and the hydrogen bonding interaction Pt-Cl...H-N , measured directly from cif file using Mercury 3.3 (2014)

Temp in Kelvin	Pt to N interatomic distances in Å	Pt-Cl...N interatomic distances in Å
100	4.2314(5)	3.457(10)
150	4.2414(4)	3.466(12)
200	4.2513(2)	3.474(9)
250	4.2615(2)	3.482(11)
300	4.272(10)	3.491(10)
350	4.2834(8)	3.501(7)
400	4.291(10)	3.507(5)





a)



b)

Figure 3.10 The (NH<sub>4</sub>)<sub>2</sub>PtCl<sub>6</sub> salts a) Inter atomic distance between Pt<sup>4+</sup> and N atom b) Inter atomic distance between Cl<sup>-</sup> ion on the [PtCl<sub>6</sub>]<sup>2-</sup> anion and N atom of the (NH<sub>4</sub>)<sup>+</sup> cation obtained from SCXRD analysis of (NH<sub>4</sub>)<sub>2</sub>PtCl<sub>6</sub> salt as a function of temperature in

The covalent Pt-Cl bond displacements within the [PtCl<sub>6</sub>]<sup>2-</sup> anion are plotted in Fig. 3.11 and tabulated in Table 3.7.

Table 3.7 The Pt-Cl bond displacement in  $(\text{NH}_4)_2\text{PtCl}_6$  salt obtained from SCXRD analysis as a function of temperature in  $[\text{PtCl}_6]^{2-}$  anion as a function of temperature (there are two points at 250 K and 300 K which are outliers which are decreasing as temperature increases)

Temp in Kelvin	Pt-Cl
100	2.320(2)
150	2.3212(11)
200	2.3215(11)
250	2.3210(11)
300	2.321(2)
350	2.3225(11)
400	2.3240(14)

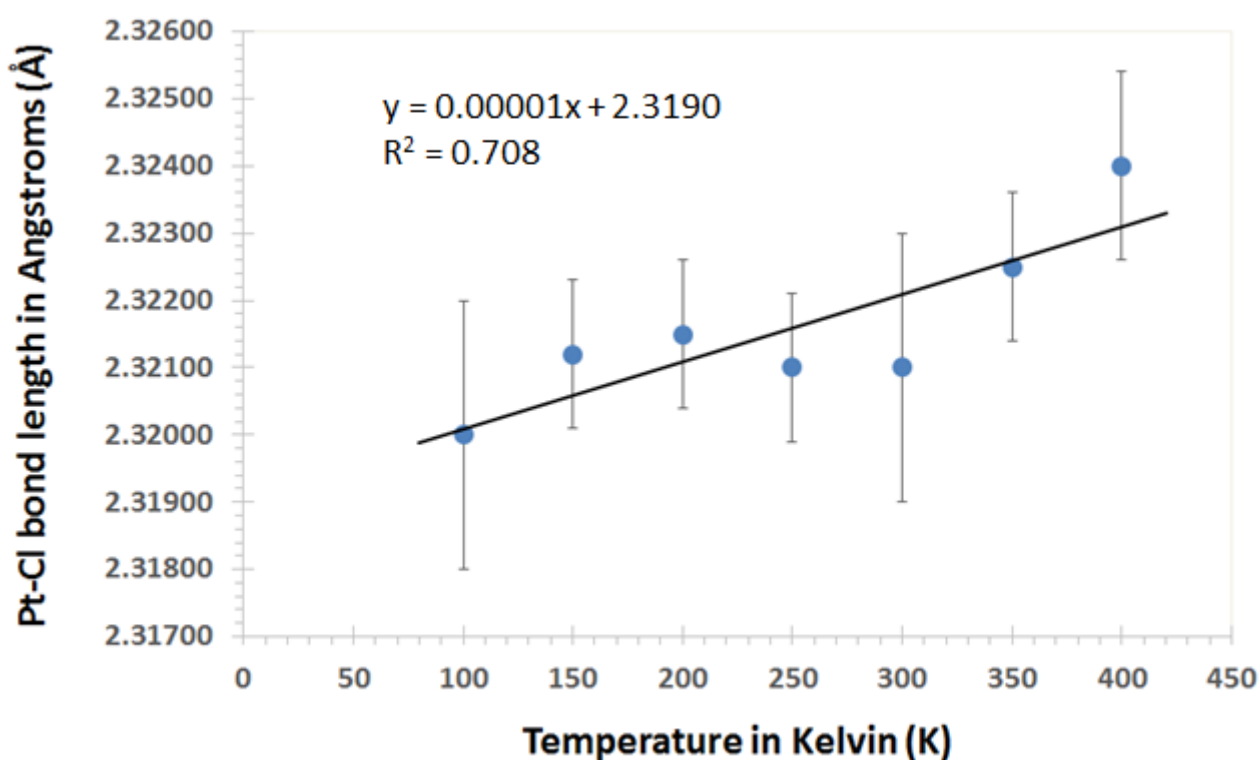


Figure. 3.11 The Pt-Cl bond displacement in  $(\text{NH}_4)_2\text{PtCl}_6$  salt obtained from SCXRD analysis as a function of temperature

The *diammonium hexachloridoplatinate(IV)*,  $(\text{NH}_4)_2\text{PtCl}_6$  salt is among the first crystal structures reported in the literature in the early 1920s.<sup>8</sup> The structure has a similar space group,  $Fm\bar{3}m$ , to that of the cubic  $\text{Rb}_2\text{PtCl}_6$  salt. This crystal structure does not undergo any phase transition (Fig. 3.9a & b) as a function of temperature. The extent of lattice expansion in this salt is 4.30 (0.05) %, which is slightly less than that of the  $\text{Rb}_2\text{PtCl}_6$  salt 4.60(0.05) % over similar temperature. The possible reason why the degree of lattice expansion is slightly less in this salt could be due to this structure having a

very strong directional hydrogen bond ( $\text{Pt-Cl}\cdots\text{H-N}$ ), which is a relatively stronger interaction than that of the purely electrostatic interaction ( $\text{Pt-Cl}\cdots\text{Rb}^+$ ) in the  $\text{Rb}_2\text{PtCl}_6$  salt based on the distances between the cation and anion in these two salts.

The average change in Pt-Cl bond displacement can be calculated by plotting the differences between the first (lowest temperature) value and the remainder, and plotting these against temperature. Then from this data the slope should be calculated along with the standard deviation using linear regression statistics. This was done and a slope ( $0.000010 \text{ \AA/K}$ ) was extracted, which gives an indication of the changing Pt-Cl bond length as a function of temperature. Using a linear regression the standard deviation from the slope value ( $0.000005 \text{ \AA/K}$ ) can be obtained at  $0.000010$  ( $0.000005$ )  $\text{\AA/K}$ . Please find details of the calculation in excel spreadsheet APPENDIX B.

The measured Pt-Cl difference obtained from SCXRD analyses performed as a function of temperature of the  $(\text{NH}_4)_2\text{PtCl}_6$  salt shows a slightly smaller degree of change of  $0.004(0.0024)$ . The error on the Pt-Cl bond length is calculated using the addition error propagation equation (see Appendix B). If we multiply this small change in Pt-Cl  $0.004$  ( $0.0024$ )  $\text{\AA}$  with the computed  $^{195}\text{Pt}$  chemical shift change of  $18\,300 \text{ ppm/\AA}$ , it equates to  $73.2 \pm 43 \text{ ppm}$  over the entire temperature range. This implies that the degree sensitivity of  $^{195}\text{Pt}$  chemical shift in the  $\text{Rb}_2\text{PtCl}_6$  salt is slightly higher than the  $(\text{NH}_4)_2\text{PtCl}_6$  salt over the same temperature range.

The standard deviations observed for the Pt-Cl bond length over the entire temperature range from  $100 \text{ K}$  to  $400 \text{ K}$  for the  $\text{Rb}_2\text{PtCl}_6$  salt [ $0.0057(0.0021) \text{ \AA}$ ] and the  $(\text{NH}_4)_2\text{PtCl}_6$  salt [ $0.004(0.0024) \text{ \AA}$ ]. One would assume that the hydrogen bonding in the  $(\text{NH}_4)_2\text{PtCl}_6$  salt between the  $[\text{PtCl}_6]^{2-}$  anion and  $\text{NH}_4^+$  cation would have a smaller standard deviation error in the Pt-Cl bond length due to the nature of the highly directional hydrogen bond, over that of the non-directional purely electrostatic interactions in the  $\text{Rb}_2\text{PtCl}_6$  salt. The difference may be attributed to an observation made by Svare *et al.*<sup>9</sup> and others<sup>10</sup> showing that the  $(\text{NH}_4)^+$  cation undergoes structural rotation within the in the  $(\text{NH}_4)_2\text{PtCl}_6$  salt, which they studied using inelastic neutron scattering. This could cause an uncertainty within the Pt-Cl bond length, which could explain the difference in error observed for this bond length to that of the error observed for the  $\text{Rb}_2\text{PtCl}_6$  salt. This error also

accounts for the differences between the deviation of the expected  $^{195}\text{Pt}$  chemical shift for the  $\text{Rb}_2\text{PtCl}_6$  salt  $104.3 \pm 38\text{ppm}$  and the  $[(\text{NH}_4)_2\text{PtCl}_6]$  salt  $73.2 \pm 43\text{ ppm}$

Table 3.8 Expected  $^{195}\text{Pt}$  chemical shift sensitivity and temperature coefficient over a 100 K to 400 K temperature range, based on lattice expansion and this small bond extension

	<b>(<math>\Delta\text{Pt-Cl}</math>) 100K – 400 K range in Å</b>	<b>Expected <math>^{195}\text{Pt}</math> chemical shift in ppm</b>
<b><math>(\text{NH}_4)_2\text{PtCl}_6</math></b>	0.004 (0.0024) Å	$73.2 \pm 43\text{ ppm}$

### 3.4 Single crystal X-ray diffraction characterization *bis(tetramethylammonium) hexachloridoplatinate(IV) salt $[\text{N}(\text{CH}_3)_4]_2\text{PtCl}_6$ as a function of temperature*

The *bis(tetramethylammonium) hexachloridoplatinate(IV)* salt was first studied by single crystal methods in 1926,<sup>11</sup> and was shown to undergo various low temperature phase transitions<sup>4,12</sup> as a function of temperature. The SCXRD measurements on this salt were done as a function of temperature ranging from 100 K – 500 K with 50 K increments. We found it of interest to reinvestigate this crystal structure in order to look at the intra- and interatomic displacement occurring during these phase transitions as a function of temperature. At 100 K the salt crystallizes in tetragonal *I*-4 space group with 13 atoms in the asymmetric unit (Fig. 3.12a). The extended packing is shown in Fig. 3.12a. The unit cell (Fig. 3.13a) contains two non-equivalent  $\text{Cl}^-$  ions which are both attached to the octahedral  $[\text{PtCl}_6]^{2-}$  anion, which has broken the  $\text{O}_h$  symmetry on the octahedral anion. At 150 K the crystal structure still remains in the tetragonal space group *I*-4 with slightly different hydrogen bonding interactions between  $[\text{PtCl}_6]^{2-}$  anion and  $[\text{N}(\text{CH}_3)_4]^+$  cation, to that of the structure collected at 100K (see Tables 3.7, 3.8 and 3.9). The structural parameters of *bis(tetramethylammonium) hexachloridoplatinate(IV)* crystal structure are tabulated and listed with crystallographic parameters and bond length and can be obtained from cif files in the Appendix B.

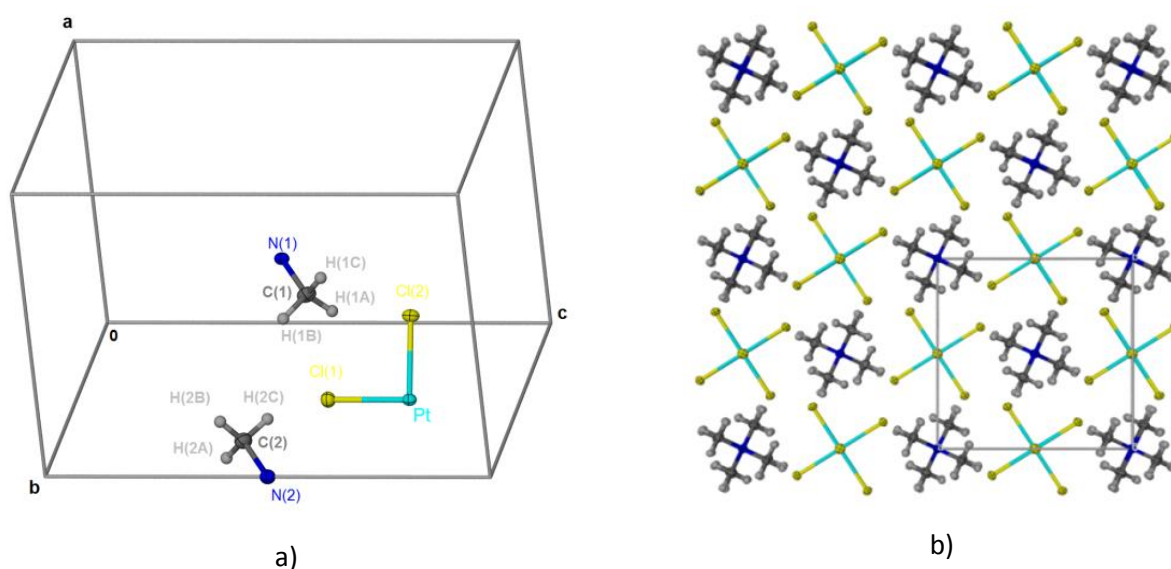


Figure 3.12 The  $[N(CH_3)_4]_2PtCl_6$  salt in tetragonal space group  $I-4$  at 100 K a) asymmetric unit b) Extended packing of the unit cell

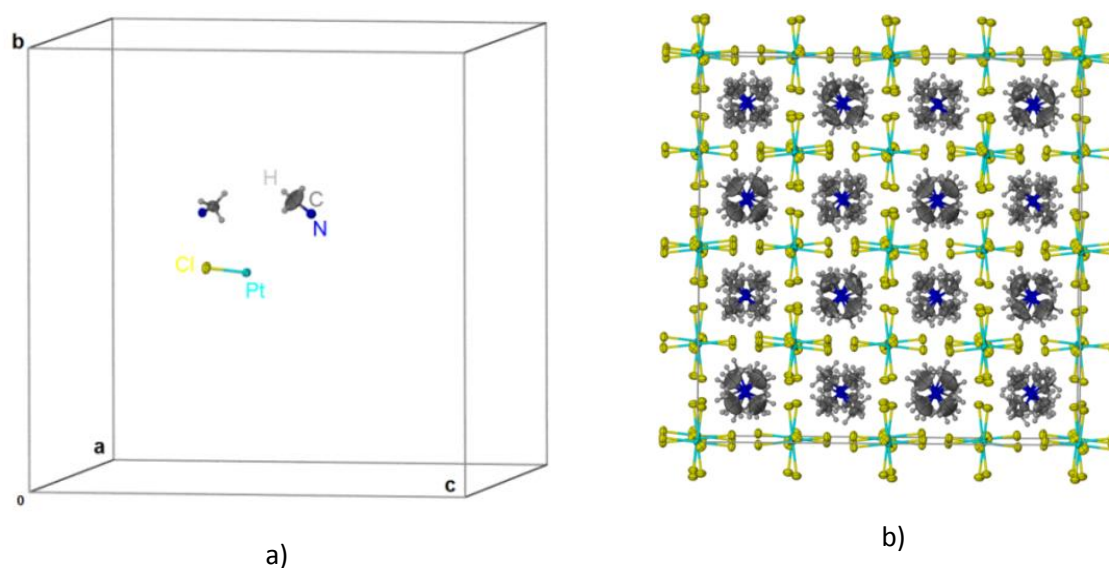


Figure 3.13 The  $[N(CH_3)_4]_2PtCl_6$  cubic supercell  $Fd-3c$  200 K a) asymmetric unit b) Extended packing of salt in super lattice

The crystal structure at 200 K converts via a first-order phase transition to a cubic super cell with space group  $Fd-3c$  (see Fig. 3.13a & b). At 250 K the crystal undergoes an additional phase transition to the cubic space group  $\alpha$ - to yield a disordered cubic structure (Fig. 3. 14a & b). At 400 K the crystal structure is already in cubic space group  $Fm\bar{3}m$  (Fig. 3. 15a & b). The differential scanning calorimetry (DSC) analysis on this salt<sup>13</sup> shows that the first phase transition occurs at  $153\text{ K} - 152\text{ K} \pm 2\text{ K}$ , where the space group goes from tetragonal  $I-4$  to cubic superlattice  $Fd-3c$ . The second phase transition detected is at  $181\text{ K} \pm 1\text{ K}$  which goes from cubic superlattice  $Fd-3c$  to a cubic  $\alpha\text{-}Fm\bar{3}m$  phase (see

.Fig. 3.19). The  $^{35}\text{Cl}$  nuclear quadrupolar resonance (NQR) spectroscopic measurements carried out as a function of temperature by Nakamura *et al.*<sup>14</sup> found an additional high temperature phase transition at 358 K. The paper, however, does not give such a detailed account on the effect that temperature has on intra- and intermolecular displacement occurring within this salt.

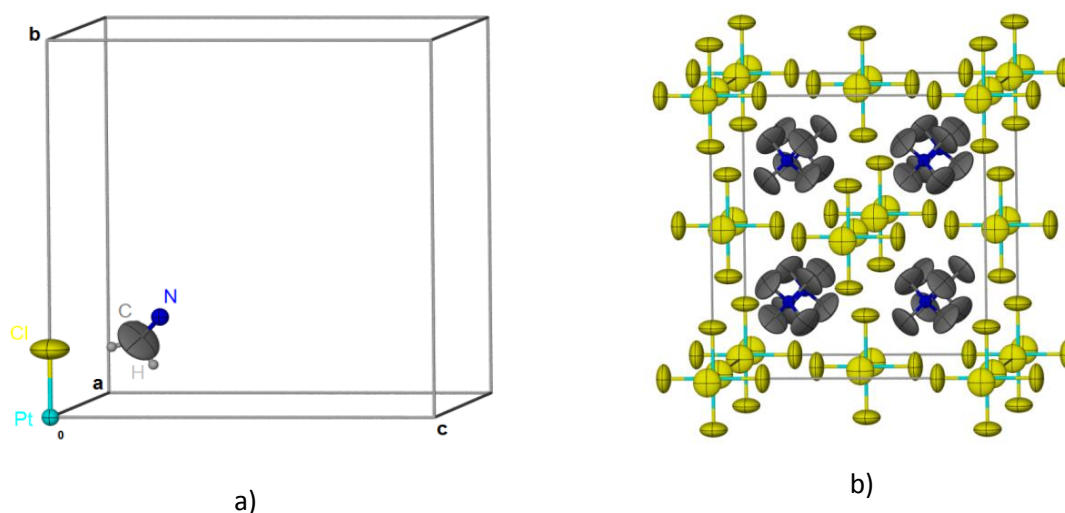


Figure 3.14 The  $[\text{N}(\text{CH}_3)_4]_2\text{PtCl}_6$  cubic supercell  $Fm\bar{3}m$  at 250 K a) asymmetric unit b) Extended packing of the salt

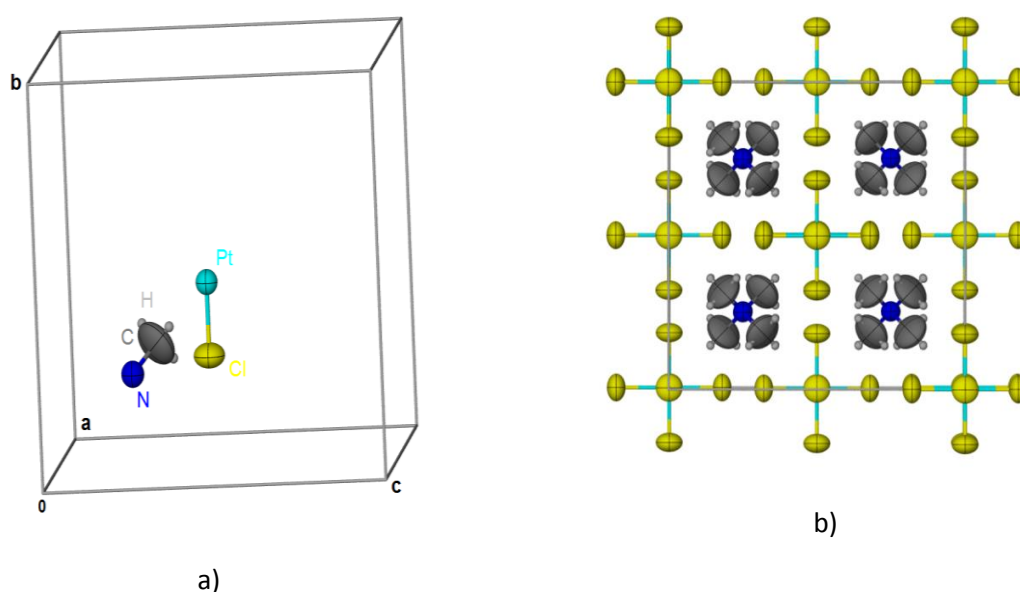
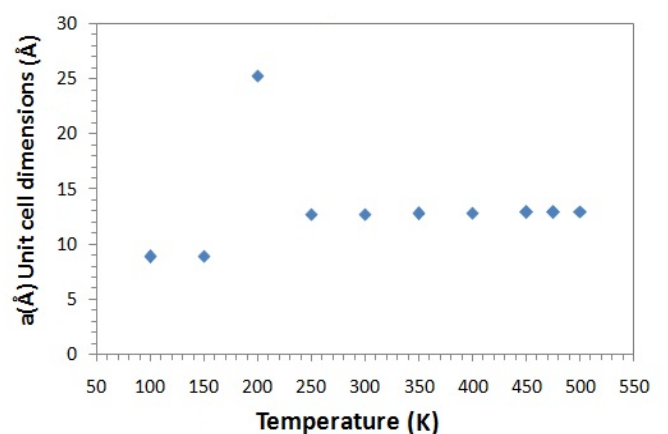


Figure 3.15 The  $[\text{N}(\text{CH}_3)_4]_2\text{PtCl}_6$  cubic supercell  $Fm\bar{3}m$  400 K a) asymmetric unit b) Extended packing of this salt

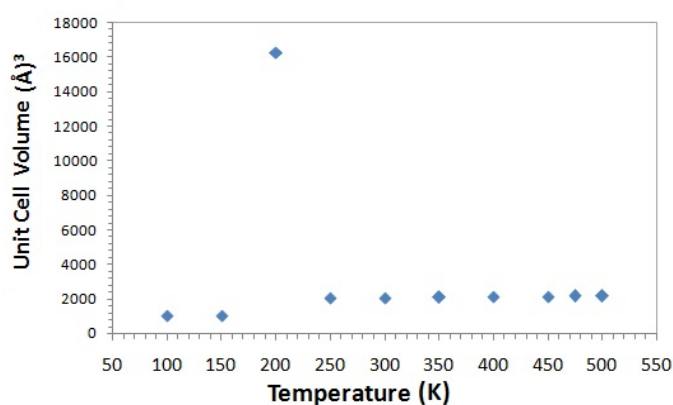
The effect that temperature has on the interatomic displacement between the  $\text{Pt}^{\text{IV}}$  ion in  $[\text{PtCl}_6]^{2-}$  anion and the  $\text{N}^+$  ion in  $[\text{N}(\text{CH}_3)_4]^+$  cation is plotted in Fig. 3.17a and tabulated in Table 3.10. This is a good indication that intra-molecular interaction between the  $[\text{PtCl}_6]^{2-}$  anion and  $[\text{N}(\text{CH}_3)_4]^+$  cation is becoming weaker as a function of increasing temperature. This is further confirmed with the plot

showing the systematic increasing in inter atomic distance between the  $\text{Cl}^-$  ions in  $[\text{PtCl}_6]^{2-}$  and  $\text{N}^+$  ion in  $[\text{N}(\text{CH}_3)_4]^+$  cation are in Fig. 3. 17b and tabulated in Table 3.10.

The unit cell and cell volume parameters extracted from the SCXRD measurements as a function of temperature on the  $[\text{N}(\text{CH}_3)_4]_2\text{PtCl}_6$  salt are shown below (see Fig. 3.16a & b) and in Table 3.9, which shows the effect that temperature has on the above mentioned parameters. These plots clearly shows the super lattice space group collected at 200 K. Unit cell and cell volume parameters are all systematically increasing as a function of increasing temperature from 250 K to 500 K (Table 3.9).



a)



b)

Figure. 3.16 The SCXRD of  $[(\text{CH}_3)_4\text{N}]_2\text{PtCl}_6$  salt showing how a) Unit cell dimensions and b) Unit cell volumes as a obtained from SCXRD analysis as a function of temperature, the outlier at 200 K is from the super lattice structure.



Table 3.9 The  $[\text{N}(\text{CH}_3)_4]_2\text{PtCl}_6$  salt a) Unit cell dimensions and b) Unit cell volumes both obtained from SCXRD analysis as a function of temperature

Temp in Kelvin	Cell Dimensions in Å	Cell Volume in Å <sup>3</sup>
100	8.8666(6)	997.58(12)
150	8.9031(4)	1005.06(13)
200	25.3219(16)	16236.4(18)
250	12.6990(15)	2047.9(4)
300	12.731(7)	2063.5(19)
350	12.787(3)	2090.6(8)
400	12.865(18)	2129(5)
450	12.878(9)	2136(3)
475	12.904(8)	2148(2)
500	12.929(11)	2161(13)

Table 3.10 The  $[\text{N}(\text{CH}_3)_4]_2\text{PtCl}_6$  salt with respect to inter atomic distance between a) Pt and N atom and the b) Distance between the Cl<sup>-</sup> ions in  $[\text{PtCl}_6]^{2-}$  the N atom  $[\text{N}(\text{CH}_3)_4]^+$  cation obtained from SCXRD analysis as a function of temperature, measured directly from cif file using Mercury 3.3 (2014)

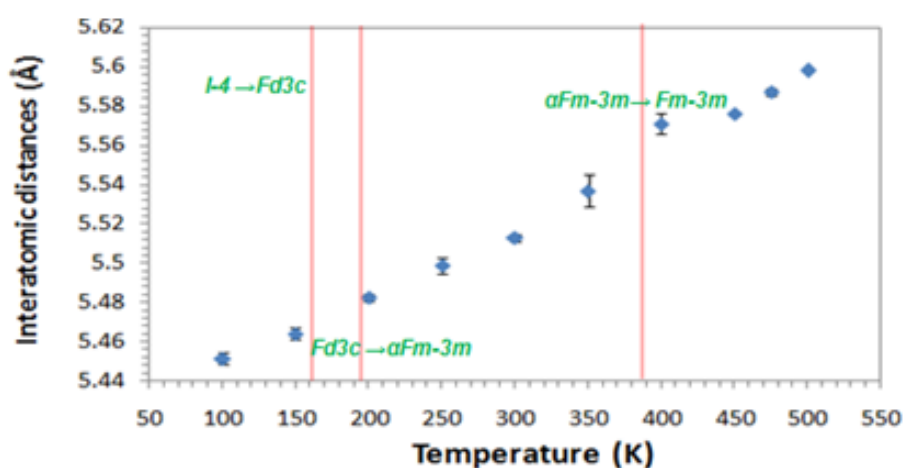
Temp in Kelvin	Pt to N distances in Å	Pt-Cl...N distances in Å	Pt-Cl...N distances in Å
100	5.451(30)	4.904(20)	
150	5.464(30)	4.536(20)	
200	5.482(20)	4.575(20)	4.193(20)
250	5.498(40)	3.717(30)	
300	5.513(20)	3.738(10)	
350	5.536(80)	3.761(50)	
400	5.571(50)	3.787(30)	
450	5.576(20)	4.644(20)	
475	5.587(20)	4.653(30)	
500	5.598(30)	4.663(30)	

The (*bis*)*tramethylammonium hexachloridoplatinate(IV)*,  $[\text{N}(\text{CH}_3)_4]_2\text{PtCl}_6$  salt, on the other hand, displays quite a variety of different structural phase transitions as a function of temperature. The room temperature crystal structure has been studied in 1926 by Huggins *et al.*<sup>15</sup> with single-crystal Laue methods. The same crystal structure was then studied by X-ray powder methods by the

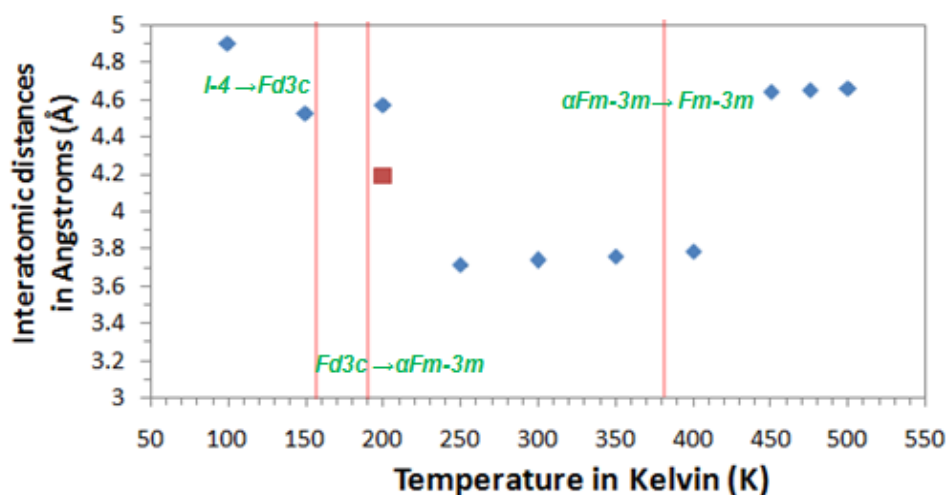


following authors: Vorlander *et al.*<sup>16</sup> Jorgensen *et al.*<sup>17</sup> and Morris *et al.*<sup>18,19,20</sup>. It was only in the later 1970s, that Berg and Sotofte *et al.*<sup>21</sup> used single crystal X-ray diffraction to study this crystal structure. The above mentioned authors showed how this compound crystallized in a face-centred cubic anti-fluorite structure with the space group  $Fm\bar{3}m$  at room temperature. The presence of several weak reflections from powder patterns was observed by the above-mentioned authors, which is not allowed if the structure obeys  $Fm\bar{3}m$  symmetry. These additional reflections were later investigated by Berg *et al.*<sup>22</sup> who discovered reflections that indicate the presence of the  $Fd-3c$  cubic super-lattice. This additional space group feature in the presence of the  $Fm\bar{3}m$  space group made it difficult to solve the super-lattice  $Fd-3c$  space group form of this crystal structure. Our measurements using SCXRD at 200 K resolved the super-lattice  $Fd-3c$  space group (see Fig. 3.13), which has twice the lattice parameters (see Fig. 3.16a & b).

At 200 K, there is an additional red spot on the plot showing two distances; the blue distance being greater than that of the red. The crystal structures at 250 K to 400 K have a slight increase in atomic displacement which drastically increases at 450 K to the last temperature at 500 K. The hydrogen bonding interactions between the  $\text{Pt-Cl}\cdots\text{H-N}$  are not plotted since XRD has some difficulty observing the positions of the H atoms. The atomic displacements in Fig. 3.20 clearly indicate that changes will occur with respect to hydrogen bonding interactions between the cations and anion since the hydrogen atom is situated in-between the  $\text{Cl}^-$  ions and the  $\text{N}^+$  ion Fig. 3.21.



a)



b)

Figure. 3.17 The  $[\text{N}(\text{CH}_3)_4]_2\text{PtCl}_6$  salt a) Pt and N atom distances b) Distance between the  $\text{Cl}^-$  ions in  $[\text{PtCl}_6]^{2-}$  anion and the N atom of the  $[(\text{CH}_3)_4\text{N}]^+$  cation obtained from SCXRD analysis as a function of temperature

The Pt-Cl bond displacements within the  $[\text{N}(\text{CH}_3)_4]_2\text{PtCl}_6$  salt (Fig. 3.18 and tabulated in Table 3.11), shows quite a large range of distances over a 100 K to 500 K temperature range, unlike the  $\text{Rb}_2\text{PtCl}_6$  and  $(\text{NH}_4)_2\text{PtCl}_6$  salts which have a small degree of bond displacement and show no structural phase transitions. This shows how the bond displacements change as the crystal structure undergoes multiple phase transitions. Initially, at 100 K and 150 K, the salt has two non-equivalent  $\text{Cl}^-$  ions (see Fig. 3.18). The crystal structure collected at 200 K to 500 K shows only one Pt-Cl bond length which indicates that all the  $\text{Cl}^-$  ions in  $[\text{PtCl}_6]^{2-}$  are in symmetrically equivalent environments.

Table 3.11 The bond displacement in Pt-Cl bond in  $[\text{N}(\text{CH}_3)_4]_2\text{PtCl}_6$  salt as obtained from SCXRD analysis as a function of temperature

Temp in Kelvin	Pt-Cl bond lengths in Å	Pt-Cl bond lengths in Å
100	2.3229(10)	2.3254(7)
150	2.3227(12)	2.3247(8)
200	2.3183(10)	
250	2.290(7)	
300	2.298(4)	
350	2.298(3)	
400	2.307(4)	
450	2.304(3)	
475	2.308(2)	
500	2.310(3)	

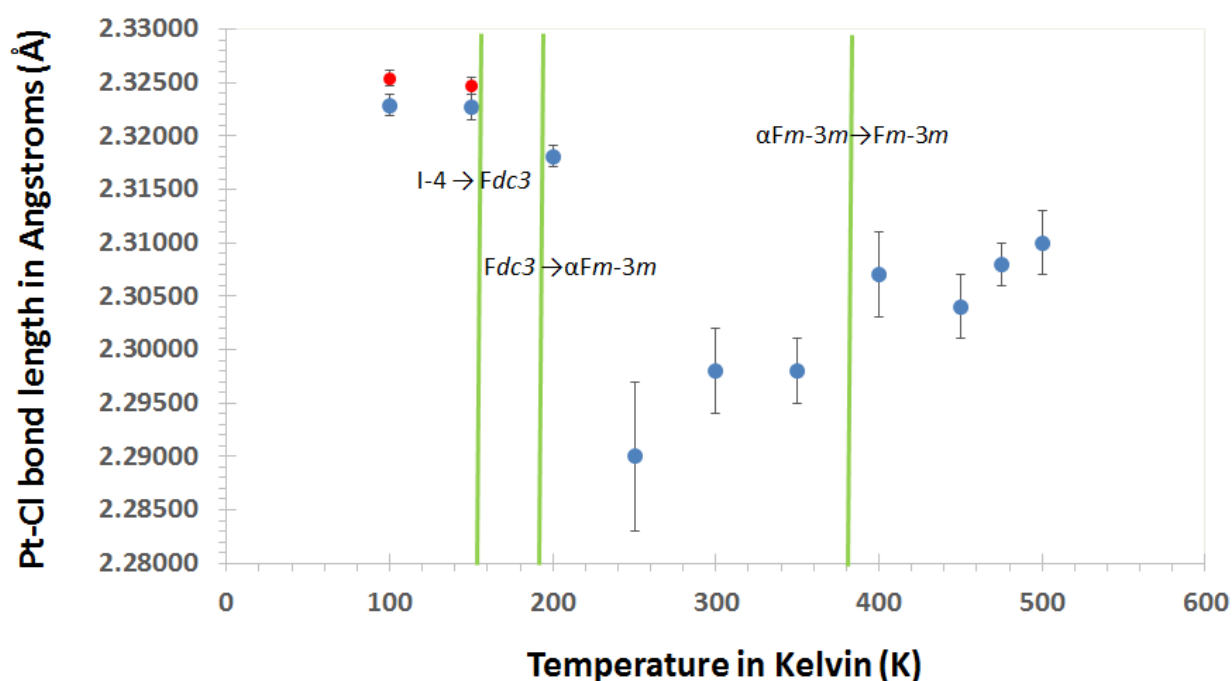


Figure. 3.18 The variation of the Pt-Cl bond displacement in  $[\text{N}(\text{CH}_3)_4]_2\text{PtCl}_6$  salts obtained from SCXRD analysis as a function of temperature, red spots are additional Pt-Cl bond lengths which arise due to the space group, green lines are the reported structural phase transitions.

Due to this  $[\text{N}(\text{CH}_3)_4]_2\text{PtCl}_6$  salt's undergoes multiple structural phase transitions as a function of temperature, these structural phase transition show large changes in Pt-Cl bond lengths which are

quite different from that of the  $(\text{NH}_4)_2\text{PtCl}_6$  and  $\text{Rb}_2\text{PtCl}_6$  salts. It is therefore not possible to apply the same calculation to predict the expected  $^{195}\text{Pt}$  chemical shift sensitivity using the Pt-Cl bond lengths due to the structure being in different crystallographic systems as a function of temperature.

This study has proven a detailed account on the effect that temperature has on lattice expansion and the intra- and intermolecular interactions in *dirubidium hexachloridoplatinate(IV)*,  $\text{Rb}_2\text{PtCl}_6$ , *diammonium hexachloridoplatinate(IV)* and  $(\text{NH}_4)_2\text{PtCl}_6$  *(bis)tramethylammonium hexachloridoplatinate(IV)*,  $[\text{N}(\text{CH}_3)_4]_2\text{PtCl}_6$  salts. These salts will be used to conduct temperature dependent  $^{195}\text{Pt}$  chemical shift solid state nuclear magnetic resonance (SSNMR) experiments which will be discussed at length in the following chapter. The expected  $^{195}\text{Pt}$  chemical shift calculated from the crystallographic data in this chapter will be compared with the experimental  $^{195}\text{Pt}$  chemical shift sensitivity using SSNMR measurement as a function of temperature. The experimental  $^{195}\text{Pt}$  chemical shift temperature coefficient's from these three salts will be compared to that of the previously reported  $^{195}\text{Pt}$  chemical shift temperature coefficients.

In the work by Jameson *et al.*<sup>1</sup> an estimated temperature coefficient is given from  $^{195}\text{Pt}$  chemical shift to be -0.53 ppm/degree based on the average vibrational frequencies and from isotope effects due to  $^{35}\text{Cl}$  and  $^{37}\text{Cl}$  -0,167 ppm per  $^{35}\text{Cl}$ . The  $^{195}\text{Pt}$  temperature coefficient for the  $[\text{PtCl}_6]^{2-}$  anion has not yet been measured experimentally, so we will be the first to measure and investigate in the solid state. It is not advisable to measure  $^{195}\text{Pt}$  chemical shift temperature coefficient in solution, since you would have to take into account the solvent effects and the hydrations sphere, which is even more difficult. Moreover, if we look at the -0.53 ppm/K coefficient over temperature range 100 K to 400 K which is a 300 K range one gets *ca* 159 ppm/K even with the small degree of lattice expansion observed from the data above. The negative sign in -0.53 ppm/K also indicates that the chemical shift become more negative at lower temperatures (or shifts to more positive fields relative to a real reference at room temperature, as the  $^{195}\text{Pt}$  nucleus becomes less shielding as the average Pt-Cl bond length increases with temperature.

---

## References

---

1. C. J. Jameson, A. K. Jameson, *J.Chem.Phys.*, **1986**, 85, 5484.
2. M. R. Burger, J. Kramer, H. Chermette , K. R. Koch. *Magn. Reson. Chem.*, **2010**, 41, S38.
3. R. W. G. Wyckoff, E. W. Posnjak, *J. Amer. Chem. Soc.*, **1921**, 43, 2292.
4. R. W. Berg, I. Sotofte, *Acta. Chem. Scand.*, A. **1978**, 32, 3.
5. K. Kuwabara, H. Kaji, M. Tsuji, F. Horii, *Macromolecules*, **2000**, 33, 7093.
6. R. L. Armstrong, *Phys. Lett.*, **1980**, 57, 343.
7. Y. Verde-Gomez, G. Alonso-Nuneza, F. Cervantes, A. Keer, *Mater. Lett.*, **2003**, 57, 4667.
8. R. W. G. Wyckoff , E. Posnjak, *J. Am. Chem. Soc.*, **1921**, 2292.
9. Z. K. Otnest, I Svarex, *J. Phys. C: Solid State Phys.*, **1979**, 12, 3899.
10. T. Lalowicz, M. Punkkinen, E. E. Ylinen *J. Phys. C: Solid St. Phys.*, **1979**, 12, 4051.
11. M.L. Huggins, *Phys. Rev.*, **1926**, 27, 638.
12. D. M. Adams , D. M. J. Morris, *J. Chem. Soc.(A)*, **1967**, 2076.
13. R. W. Berg, *J. Chem. Phys.*, **1978**, 69, 1325.
14. Y. Furukawa, L. S. Prabhumirashi, R. Ikeda, D. Nakamura, *Bull. Chem. Soc. Japan*. **1982**, 55, 995.
15. M.L. Huggins, *Phys. Rev.* **1926**, 27, 638.
16. C. K. Jorgensen, *Acta. Chem. Scand.*, **1963**, 17, 1034.
17. D. Vorlander, *Ber. Dtsch. Chem. Ges.*, **1931**, 64, 1763.
18. D. M. Adams, D. M. Morris, *J. Chem. Soc. A.*, **1967**, 1666.
19. D. M. Adams, D. M. Morris, *J. Chem. Soc. A.*, **1967**, 1669.
20. D. M. Adams, D. M. Morris, *J. Chem. Soc. A.*, **1967**, 2067.
21. R. W. Berg, I. Sotofte, *Acta. Chem. Scand. Ser. A*, **1978**, 32, 241.
22. R. W. Berg, K. Nielsen, *Acta. Chem. Scand. Ser. A*, **1979**, 33, 157.

# Chapter 4

## Solid State Nuclear Magnetic Resonance Spectroscopy of $\text{C}_2\text{PtCl}_6$ Salts to Probe the Temperature Dependence of the $^{195}\text{Pt}$ NMR Shielding

### Introduction

This study aims to use variable temperature  $^{195}\text{Pt}$  SSNMR measurements as a potential probe for Pt-Cl bond lengths in simple  $(\text{Rb}_2\text{PtCl}_6)$ ,  $(\text{NH}_4)_2\text{PtCl}_6$  and  $[\text{N}(\text{CH}_3)_4]_2\text{PtCl}_6$  salts. The experimental and computational work carried out by Koch *et al.*<sup>1</sup> and Jameson *et al.*<sup>2</sup> both suggest that the sensitivity of  $^{195}\text{Pt}$  chemical shift in  $[\text{PtCl}_6]^{2-}$  anion type complexes are directly dependent on the degree of Pt-Cl bond displacement within the octahedral  $[\text{PtCl}_6]^{2-}$  anion. The crystallographic data obtained from single crystal X-ray diffraction (SCXRD) measurement performed as a function of temperature (see Chapter 3) on  $(\text{Rb}_2\text{PtCl}_6)$ ,  $(\text{NH}_4)_2\text{PtCl}_6$  and  $[\text{N}(\text{CH}_3)_4]_2\text{PtCl}_6$  is used to interpret and give additional insight in order to account for the temperature dependence  $^{195}\text{Pt}$  MAS SSNMR measurements on the same salts. In Chapter 3, predictions of the expected  $^{195}\text{Pt}$  chemical shift sensitivity of  $\text{Rb}_2\text{PtCl}_6$  ( $104.3 \pm 38$  ppm) and  $(\text{NH}_4)_2\text{PtCl}_6$  ( $73.2 \pm 43$  ppm) are calculated from the Pt-Cl bond displacement over a 100 K – 400 K temperature range. The experimental  $^{195}\text{Pt}$  chemical shift measurements are compared with the expected  $^{195}\text{Pt}$  chemical shift sensitivity. The results from  $^{195}\text{Pt}$  SSNMR measurements performed, as a function of temperature on these salts would prove if these predicted  $^{195}\text{Pt}$  chemical shift sensitivity were indeed correct.

Physicists first described the concept of nuclear magnetic resonance (NMR) in 1938 from molecular beams,<sup>3</sup> and later reported the first proton NMR spectra of water<sup>4</sup> and solid wax paraffin.<sup>5</sup>

This analytical technique has served the international research community as one of the central approaches for structural elucidation of liquids and solids. Although this technique has its origin in a physics laboratory, it has been popularised and developed mainly due to its enormous importance in the fields of chemistry, biochemistry, physiology, medicine, pharmacy and material science research.

The development of SSNMR ran in parallel to that of solution-state NMR.<sup>6</sup> In solution, a NMR spectrum usually consists of a series of very sharp transitions; this is due to the averaging of anisotropic NMR interactions, which is a consequence of rapid random molecular tumbling. By contrast, some SSNMR spectra have very broad spectral lineshapes, which are attributed to the anisotropic or orientation-dependent interactions that cannot be averaged out in solids. The presence of these broad NMR lineshapes in SSNMR was first thought to be a hindrance for the principle investigator, but it has been shown to provide much more information on chemical structure and dynamics of solids.

The NMR active spin  $\frac{1}{2}$   $^{195}\text{Pt}$  nucleus, has a relatively high natural abundance of 33.8%, together with a large magnetogyric ratio ( $5.768 \times 10^7 \text{ rad T}^{-1} \text{ s}^{-1}$ ). This nucleus has an absolute sensitivity twenty times higher than that of  $^{13}\text{C}$  but is still among the least documented NMR active nuclei in the literature. Although  $^{195}\text{Pt}$  NMR studies exist, they are mainly of coordination compounds or organometallic complexes.<sup>7,8,9</sup> Usually these were of Pt(0) and Pt(II) compounds where they were mainly studied in solution.<sup>10</sup> In the solid-state, square-planar Pt(II) complexes have quite a large chemical shielding anisotropy<sup>11,12,13</sup> resulting in numerous spinning sidebands in the  $^{195}\text{Pt}$  NMR spectra. The spinning sidebands cause some complication upon interpretation of the spectrum as it might overlap with some with the actual isotropic chemical shift ( $\sigma_{\text{iso}}$ ) peaks, not making Pt(II) measurements not as useful. By contrast, octahedral Pt(IV) complexes give rise to relatively sharp spectral lines in  $^{195}\text{Pt}$  SSNMR spectra<sup>14</sup> which is quite useful.

An SSNMR spectrum can provide similar to even identical structural information to that of solution-state NMR. The extraction of some of this information requires highly specialised experimental procedures that include magic angle spinning (MAS), cross polarization (CP), special 2D experiments and enhanced probe electronics experiments. Solid state NMR has quite a large

library of various different experimental procedures, like pulse sequencing, that are enhancing spectral resolution. This introduction focuses on some of these techniques namely Static, MAS, CP, and CP/MAS experiments.

## 4.1 Solid-state Nuclear Magnetic Resonance Theory\*

### 4.1.1 Nuclei in a static uniform field

The most simplistic spin system is that of an isolated spin in a static uniform magnetic field at which an NMR experiment is usually conducted and this involves no other interaction. The Hamiltonian  $\hat{H}$  for a nuclear spin in a static field can be written as follows

$$\hat{H} = -\hat{\mu} \cdot B_0 \quad 4.1$$

where  $\hat{\mu}$  is the nuclear magnetic moment operator and  $B_0$  is the magnetic field applied in the NMR. This Hamiltonian is referred to as the Zeeman Hamiltonian, where  $\hat{\mu}$  can be written in terms of the nuclear spin operator  $\hat{I}$  of the system.

$$\hat{\mu} = \gamma \hbar \hat{I} \quad 4.2$$

where  $\gamma$  is the gyromagnetic ratio and  $\hbar$  is the Planck constant. The applied field is taken to be along  $z$  direction if you combine Equations 3.1 and 3.2

$$\hat{H} = -\gamma \hbar \hat{I}_z B_0 \quad 4.3$$

The eigenfunctions of  $\hat{H}$  are the wavefunctions which are used to describe the conceivable states of the spin systems in the presence of an external magnetic  $B_0$  field.  $\hat{H}$  eigenfunction is directly proportional to the operator  $\hat{I}_z$ , in this case, the eigenfunctions  $\hat{H}$  are the eigenfunctions of  $\hat{I}_z$ , written as  $|I, m\rangle$  in bracket notation, or otherwise as  $\Psi_{Im}$ , where  $I$  is the nuclear spin quantum number of the system. The quantum number  $m$  can take  $2I + 1$  values:  $I, I - 1, I - 2, \dots, -I$ . The eigenvalues of  $\hat{H}$  describe the energy associated with the different possible states of the spin. The eigenvalues are obtained by operating with  $\hat{H}$  on the spin wave functions:

$$\hat{H} |I, m\rangle = E_{I,m} |I, m\rangle \quad 4.4$$

where  $E_{I,m}$  is the energy of the eigenstate  $|I, m\rangle$ . Substituting the Equation 3.3 of the  $\hat{H}$  in Equation 4.4 gives the following

---

\* M. J. Duer, Introduction to Solid-state NMR spectroscopy, 2004, Wiley-Blackwell, (The mathematic theory for this section is taken directly 4.1.1 to 4.1.4).



$$\hat{H}|I, m\rangle = -(\gamma\hbar B_0)\hat{I}_z|I, m\rangle = -(\gamma\hbar B_0)m|I, m\rangle \quad 4.5$$

since  $|I, m\rangle$  is an eigenfunction of  $\hat{I}_z$ , with eigenvalue  $m$ , i.e.

$$\hat{I}_z|I, m\rangle = m|I, m\rangle \quad 4.6$$

The energy level of the eigenstates is obtained from comparing Equations 3.4 and 3.5:

$$E_{l,m} = -\gamma\hbar B_0 m \quad 4.7$$

If we now consider a spin with  $I = \frac{1}{2}$ ,  $m = \pm \frac{1}{2}$  there are two possible eigenstates with energy  $E_{\frac{1}{2}, \pm \frac{1}{2}} = \pm \frac{1}{2} \gamma\hbar B_0$ . This is illustrated in (Fig. 4.1). These states are called the Zeeman states. The transition energy  $\Delta E$  between the spin states can be written as  $\gamma\hbar B_0$ . This is expressed in frequency units, which corresponds to  $\omega_0 (= \gamma B_0)$ , the Larmor frequency in the vector model, that corresponds to the rotation of the net nuclear magnetization vector about  $B_0$  and not to a transition frequency.

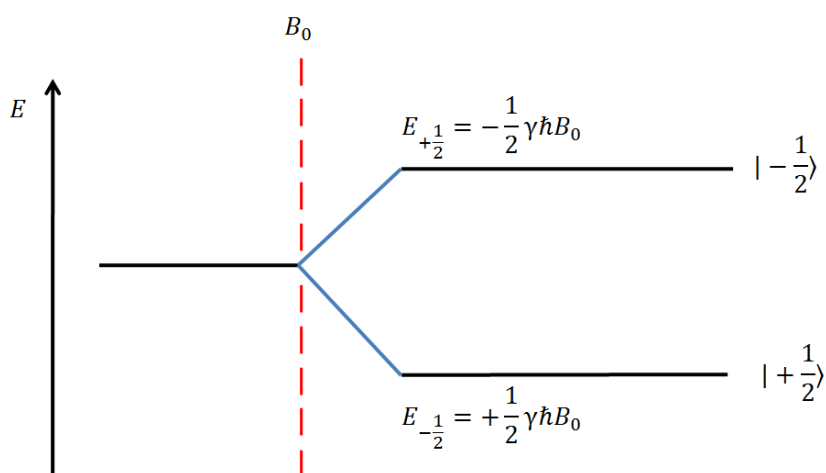


Figure 4. 1 The energy level (Zeeman levels) for spin  $= -\frac{1}{2}$  nucleus in an applied magnetic field  $B_0$  (positive  $\gamma$ ). The levels are labelled according to their magnetic quantum number,  $m$ .

The most simplistic of non-interacting spin  $= -\frac{1}{2}$  nuclei, each spin system has one or two possible eigenstates. At equilibrium, there is a Boltzmann distribution of nuclear spin over these two states, each eigenstate  $\Psi$  the population  $\rho_\Psi$  can be written

$$\rho_\Psi = \frac{\exp\left(-\frac{E_\Psi}{kT}\right)}{\sum_{\Psi'} \exp\left(-\frac{E_{\Psi'}}{kT}\right)} \quad 4.8$$

where  $E_\Psi$  is the energy of the  $\Psi$  eigenstate. For spin  $-\frac{1}{2}$  nuclei,

$$\sum_{m=\pm\frac{1}{2}} \exp\left(-E_m/kT\right) \approx 2$$

The eigenstates and their respective populations determine the properties of the spin systems and hence determine the outcome of any NMR experiment of the sample.

#### 4.1.2 Nuclear spin interaction

The various sources of magnetic fields that are internal to the sample also affect the nuclear spin system. In solid samples this can cause extensive line broadening. The Hamiltonian operator describes the most significant of these interactions, namely chemical shielding, dipole coupling, and quadrupolar coupling.

In an NMR experiment, an applied static field  $B_0$  is generally orders of magnitude greater than any molecular local fields arising within a sample as a result of the other nuclear magnetic dipoles and chemical shielding interactions. As a consequence,  $B_0$  remains as the quantization axis for the nuclear spins in a sample and many of these local fields have little effect on the spin state (at equilibrium). The only part of local fields with any noteworthy effect on spin states are the components parallel or antiparallel to the applied magnetic field  $B_0$  and that of the components precessing in the plane perpendicular to the applied field  $B_0$  at the frequency at or near the Larmor frequency.

The Hamiltonian that describes the interaction between any local field  $B_{loc}$  and a nuclear spin  $I$  can be written as

$$\begin{aligned}\hat{H} &= -\gamma \hat{I} B_{loc} \\ &= -\gamma (\hat{I}_x B_x^{loc} + \hat{I}_y B_y^{loc} + \hat{I}_z B_z^{loc})\end{aligned}\quad 4.9$$

It is also possible to express the local magnetic field  $B_{loc}$  in the interaction as

$$B_{loc} = A_{loc} \cdot J \quad 4.10$$

where  $A_{loc}$  is a second-rank Cartesian tensor, referred to as the coupling tensor, that describes the nuclear spin interaction and the interactions' orientation dependence in an applied field. The vector  $J$  is the decisive source of the  $B_{loc}$  magnetic field at a nucleus, another nuclear spin in the case of dipole-dipole coupling, or  $B_0$  field itself in the case of chemical shielding. This can now be written as a general contribution to the nuclear spin Hamiltonian form and interaction  $A$  by reference to Equation 3.9 and 3.10 (frequency units)

$$\hat{H}_A = -\gamma \hat{I} B_{loc} = \hat{I} \cdot A_{loc} \cdot J \quad 4.11$$

Where the factor of  $-\gamma$  has been combined into  $A_{loc} \cdot J$ .

Chemical shielding is the source of the chemical shift, the interaction Hamiltonian is given by frequency units

$$\hat{H}_{cs} = \gamma \hat{I} \cdot \sigma \cdot B_0 \quad 4.12$$

where  $\sigma$  is the shielding tensor and  $B_0$  is the applied magnetic field in an NMR experiment. The perturbation of electrons around the nuclear spin  $I$  by applied field  $B_0$  gives rise to the shielding effects. The shielding tensor describes the extent of the effect and how it relates to the molecule's orientation. In an NMR experiment the orientation dependence arises due to the applied magnetic field  $B_0$  effectively orientating the spin vector,  $I$ , and also determines the shielding field (strength and direction) from the electrons that interact with the spin  $I$ . The strength of the interaction between the spin  $I$  and the shielding field is highly dependent on the relative position of the spin  $I$  and the electrons giving rise to the shielding field with respect to the applied field.

For dipolar-dipole coupling/dipolar coupling Hamiltonian in frequency units can be written as follows:

$$\hat{H}_{dd} = -2\hat{I} \cdot D \cdot \hat{S}$$

where the dipolar-coupled spin  $S$  is the local magnetic field acting on the spin  $I$ ,  $D$  is the dipolar-coupling tensor describing the strength and orientation dependence of the interaction between  $I$  and  $S$  spin systems. This interaction arises by virtue of the magnetic field that each creates around itself. The orientation dependence is due to the applied magnetic field in the NMR experiment,  $B_0$ , effectively orientates both spin  $I$  and  $S$ , therefore creating the two fields. The interaction between these two spin systems are dependent on the relative position of the two spins in space with respect to the applied field.

Three quarters of all NMR active nuclei on the periodic table have a spin greater than  $\frac{1}{2}$  and these nuclei are termed quadrupolar nuclei. These nuclei own a nuclear electric quadrupole moment ( $Q$ ), with a non-spherical nuclear charge distribution. These nuclei have an ability to form quadrupole-coupling interactions, which is different to the previously mentioned interactions. The quadrupole moments of these nuclei interact with their own electric field gradients (EFG). The Hamiltonian describing the quadrupolar interaction is a similar form to those for the chemical shielding (4.13).

$$\hat{H}_Q = \frac{eQ}{2I(2I-1)\hbar} I \cdot V \cdot I \quad 4.13$$

where  $V$  is the electric field gradient tensor and  $Q$  is the nuclear electric quadrupolar moment. The quadrupolar coupling interaction affects the nuclear spin energy levels in addition to the other magnetic interactions of a spin system. The strength of this interaction is directly dependent on the magnitude of the nuclear quadrupole moment and the strength of the electric field gradient of the atom.

#### 4.1.3 Interaction tensors in solid-state NMR

Nuclear spin interaction, for example NMR shielding, depends on molecular orientation and therefore its size cannot be described by a single number, but by a mathematical second-rank tensor. A nuclear spin system can be described using Cartesian second-rank spin operators, such as  $\hat{I}_x, \hat{I}_y, \hat{I}_z$ .

A second-rank Cartesian tensor, such as the shielding tensor  $\sigma$  is represented by a  $3 \times 3$  matrix:

$$\sigma = \begin{pmatrix} \sigma_{xx} & \sigma_{xy} & \sigma_{xz} \\ \sigma_{yx} & \sigma_{yy} & \sigma_{yz} \\ \sigma_{zx} & \sigma_{zy} & \sigma_{zz} \end{pmatrix} \quad 4.14$$

where  $x, y, z$  is unspecified axis frame. Describing the shielding tensor using this system becomes more clear when expressed in a laboratory frame (which is defined by  $B_0$  being along  $z$ ). The local

magnetic field  $B_{loc}$  at a nucleus with a shielding tensor  $\sigma^{lab}$  i.e. a shielding tensor expressed  $B_0 = \sigma^{lab} \cdot B_0$

$$\begin{aligned}
 &= \begin{pmatrix} \sigma_{xx}^{lab} & \sigma_{xy}^{lab} & \sigma_{xz}^{lab} \\ \sigma_{yx}^{lab} & \sigma_{yy}^{lab} & \sigma_{yz}^{lab} \\ \sigma_{zx}^{lab} & \sigma_{zy}^{lab} & \sigma_{zz}^{lab} \end{pmatrix} \cdot \begin{pmatrix} 0 \\ 0 \\ B_0 \end{pmatrix} \\
 &= \begin{pmatrix} \sigma_{xz}^{lab} B_0 \\ \sigma_{yz}^{lab} B_0 \\ \sigma_{zz}^{lab} B_0 \end{pmatrix}
 \end{aligned} \tag{4.15}$$

for an applied magnetic field  $B_0$  in the laboratory along the  $z$  direction. The  $\sigma_{xz}^{lab} B_0$  is the local shielding field in the laboratory  $x$ -direction, when  $B_0$  is applied along  $z$ . The dipolar- and quadrupole-coupling tensor is described using a similar explanation. The  $D_{xz}^{lab} \hat{S}_z$  (where  $D$  is the dipolar coupling tensor for the interaction between the two spin  $I$  and  $S$ ) is the local magnetic field at spin  $I$  in the laboratory  $x$ -direction arising from the  $z$  component of the spin. This is why it is necessary to use a second-rank tensor to describe the strength of the nuclear spin interaction with locally arising magnetic fields. The extra local field is itself a vector quantity, i.e.  $B_0$  in the case of shielding;  $S$  in the case of dipolar local field it causes is another three-component Cartesian vector. This requires a  $3 \times 3$  matrix which is a second-rank tensor. The axis frame is the *principal axis frame*, designated 'PAF', or  $x^{PAF}, y^{PAF}, z^{PAF}$ . The numbers along the resulting diagonal of  $\sigma^{PAF}$  are the *principle values* of the shielding tensor, so, for instance,  $\sigma_{xx}^{PAF}$  is the principle value associated with the principle axis frame  $x$ -axis. The local environment of the nucleus, to which the interaction pertains, determines the orientation of the principle axis. The shielding tensor principle axis frame is determined by the electronic structure of the molecule. This makes it possible to now visualise an interaction tensor as being represented by an ellipsoid fixed within the molecule and centred on the nucleus as it applies to Fig. 4.2. The shielding tensor consist of two parts; a symmetric ( $\sigma^s$ ) and antisymmetric ( $\sigma^{as}$ ) component and from this one can clearly see why it is important to use a second rank tensor to describe these interactions.

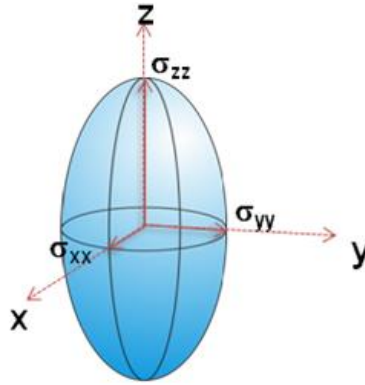


Figure 4. 2 Illustrating the ellipsoid representation of an interaction tensor using shielding tensor as an example

The principle axes of the ellipse match with the principle frame of the shielding tensor. The lengths of each principle axis are directly proportional to the magnitude of the principal value of the interaction tensor associated with that principal axis. A nucleus at a specific crystallographic site of symmetry can be described using an interaction tensor. It will also reflect this system's specific symmetry. For example, the chemical shielding tensor for a nucleus at a site of axial symmetry has a principle axis frame in which the  $z^{PAF}$ -axis coincides with the symmetry axis and the principle values as such are  $\sigma_{xx}^{PAF} = \sigma_{yy}^{PAF} \neq \sigma_{zz}^{PAF}$ . The three principle values of these interaction tensors  $\sigma_{\alpha\alpha}^{PAF}$  are used to express, instead of isotropic value  $\sigma_{iso}$ , the anisotropy  $\Delta_A$ , and asymmetry  $\eta_A$  of the interaction. These quantities are defined from the principle values as follows.

$$\sigma_{iso} = \frac{1}{3} (\sigma_{xx}^{PAF} + \sigma_{yy}^{PAF} + \sigma_{zz}^{PAF}) \quad 4.16$$

$$\Delta_A = \sigma_{zz}^{PAF} - \sigma_{iso} \quad 4.17$$

$$\eta_A = \frac{\sigma_{xx}^{PAF} - \sigma_{yy}^{PAF}}{\Delta_A} \quad 4.18$$

The anisotropy is related to the length of the ellipsoid that is used to describe the interaction tensor. The asymmetry parameters are described by measuring how far a cross-section through the ellipsoid (parallel to the  $x^{PAF} - y^{PAF}$  plane) deviates from circular. The unique NMR parameters provided by SSNMR studies on quadrupolar nuclei are the nuclear quadrupolar coupling constant  $C_Q$  and the symmetry parameter  $\eta_Q$ . The nuclear quadrupolar coupling constants are directly proportional to the principle component of the electric field gradient (EFG) tensor at a given nucleus and is given by the following equation

$$C_Q = \frac{eQV_{zz}}{h} = \frac{e^2 q_{zz}Q}{h} \quad 4.20$$

where  $V_{zz} = eq_{zz}$ , and the nuclear quadrupole moment  $eQ$ ,  $h$  is the Planck constant and  $C_Q$  is in Hertz. To date the best known values for nuclear quadrupolar moment ( $Qm$ ) were done by Pyykkö *et al.*<sup>15</sup> in 2008. The quadrupolar asymmetry parameter  $\eta_Q$  is defined in equation 3.21

$$\eta_Q = \frac{V_{xx} - V_{yy}}{V_{zz}} \quad 4.21$$

where  $|V_{zz}| \geq |V_{yy}| \geq |V_{xx}|$ . It should be noted that the trace of the EFG tensor is 0, thus  $0 \leq \eta_Q \leq 1$ .<sup>16</sup>

#### 4.1.4 Graphical Summary of Internal spin interactions<sup>17</sup>

**Chemical shielding term:** This represents the direct magnetic interaction of the external magnetic field and the nuclear spins, through the involvement of the electrons (Figure 4.3).

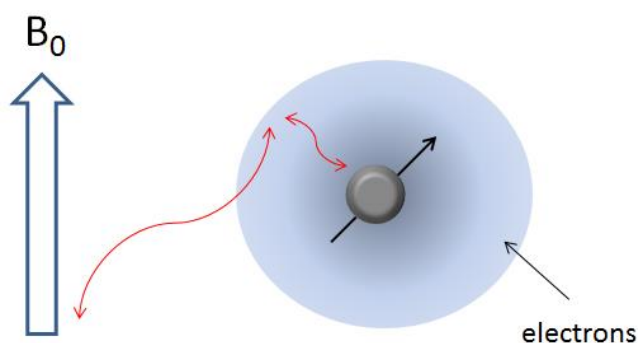


Figure 4. 3 The chemical shielding interaction, the electrons are depicted by the light blue cloud

**Quadrupolar coupling interaction:** These represent the electric interactions of the spin  $> \frac{1}{2}$  nuclei with the surrounding electric fields. This arises due to the nucleus having a non-spherical charge distribution of the nuclear charge. The nucleus has an orientation-dependent electrostatic interaction with its environment i.e. electric field gradient (Figure 4.4).

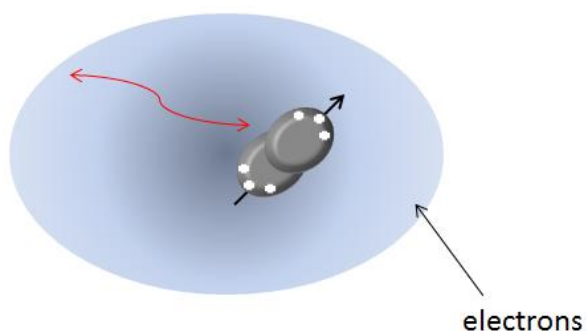


Figure 4. 4 The quadrupole coupling interaction

**Direct dipole-dipole coupling:** These represent the direct magnetic interactions of the nuclear spin with each other (Figure 4.5).



Figure 4. 5 The direct dipole-dipole coupling

**J-coupling:** This interaction is mediated through chemical bonds connecting two spins. It is an indirect interaction between two nuclear spins, which arises from hyperfine interaction between the nuclei and local electrons (Figure 4.6).



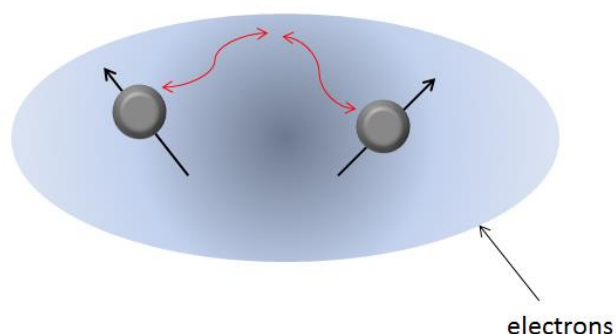


Figure 4. 6 The indirect dipole-dipole coupling (J-coupling)

The circles in Figure 4.7 display the typical relative size of these internal spin interactions terms and their contribution to the experimentally observed NMR chemical shielding, in the absence of molecular motion. For spin  $> \frac{1}{2}$ , the quadrupole coupling term is usually the largest term. However, this term vanishes for spin  $= \frac{1}{2}$ . The direct dipole-dipole coupling and chemical shift terms are usually the next largest, followed by the  $J$  coupling and the spin-rotation interactions

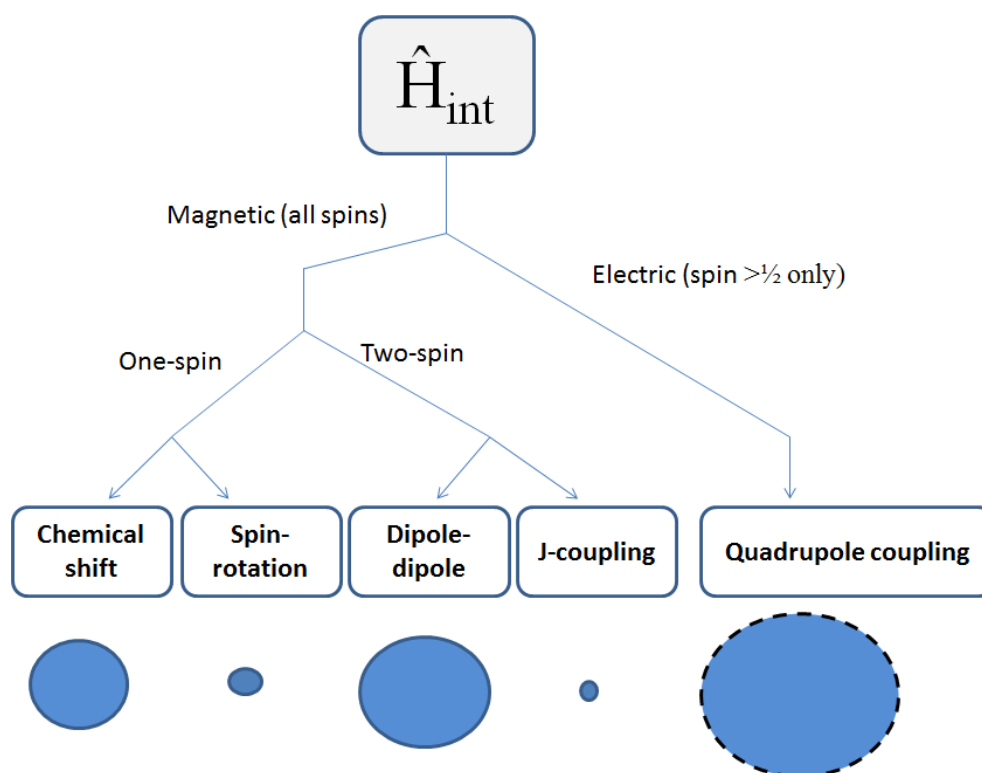


Figure 4. 7 Organization of the internal spin interaction terms, and their rough relative magnitudes. The quadrupolar coupling vanishes for spin  $= \frac{1}{2}$ .

#### 4.1.5 Magic-angle Spinning (MAS)

One of the most widely used SSNMR techniques is MAS. The unique angle of  $54.47^\circ$  called the “magic angle”, introduced by Andrew and Louw *et al.*<sup>18,19</sup> in 1958 and has been a groundbreaking discovery. It was found to have the ability to both theoretically and experimentally remove spectral broadening.<sup>20</sup> The remarkable ability of this experiment to enhance the spectral resolution by removing magnetic dipolar interactions, anisotropy of chemical shift, dipolar interactions, and quadrupolar interactions gives onus to its popularity. The removal of these above-mentioned interactions in the SSNMR experiment gives this technique quite a unique ability to determine, similarly to that of solution, the isotropic chemical shift and  $J$  coupling. In Fig. 4.8 the diagram illustrates the magic-angle spinning experiment. The sample is spun in a cylindrical rotor about the spinning axis orientated at the magic angle ( $\theta_R = 54.74^\circ$ ) with respect to the applied magnetic field  $B_0$ .

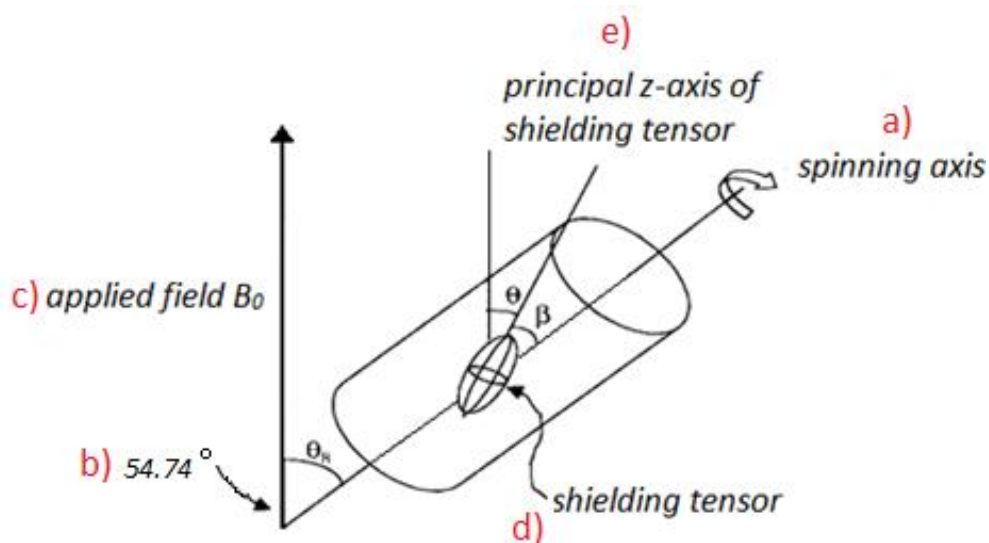


Figure 4.8 Schematic representation of the magic-angle spinning experiment where the sample is spun rapidly in a cylindrical rotor about the a) spinning axis orientated at the b) magic angle  $\theta_R = 54.74^\circ$  with respect to the c) applied magnetic field  $B_0$ . The d) chemical shielding tensor is represented here by an ellipsoid which is fixed at the molecule to which it applies and so rotates with the sample. The angle  $\theta$  is the angle between  $B_0$  and e) principle z-axis of the shielding tensor,  $\beta$  is the angle between the z-axis of the shielding tensor principle axis frame and the spinning axis.

If a sample is spun about the axis inclined at an angle  $\theta_R$  to the applied field, then  $\theta$  varies with time as the molecule rotates with the sample. The average of the orientation dependence of the nuclear spin interactions ( $3\cos\theta^2 - 1$ ), under these circumstances, can be shown as follows

$$\langle 3 \cos^2 \theta - 1 \rangle = \frac{1}{2} (3 \cos^2 \theta_R - 1) (3 \cos^2 \beta - 1) \quad 4.19$$

where the angles  $\beta$  and  $\theta_R$  are defined in Fig. 3.3. The angle  $\beta$  is between the principle z-axis of the shielding tensor and the spinning axis,  $\theta_R$  is the angle between the applied field and the spinning axis and  $\theta$  is the angle between the principle z-axis of the interaction tensor and the applied field  $B_0$ . The angle  $\beta$  is obviously a fixed value for a given nucleus in a rigid solid, but like  $\theta$ , takes on all possible values in a powder sample. The angle  $\theta_R$  is under control of the experiment. If the angle  $\theta_R$  is set at  $54.74^\circ$ , then  $(3 \cos^2 \theta_R - 1) = 0$ , and so the average,  $\langle 3 \cos^2 \theta - 1 \rangle$ , is zero as well. If the experimental spinning rate is fast so that  $\theta$  is averaged rapidly compared with the anisotropy of the interaction, the interaction anisotropy averages to zero.

This technique averages the anisotropy associated with any interaction which causes a shift in the energies of the Zeeman spin functions, but no mixing between the Zeeman function (to first order), such as chemical shift, anisotropy, heteronuclear dipolar coupling and quadrupolar coupling.

#### 4.1.6 Cross-polarization (CP) Techniques

The Cross-polarization<sup>21</sup> method is used to enhance dilute spins such as  $^{13}\text{C}$  nuclei, which are of low absolute sensitivity. After the MAS technique, cross-polarization is one of the most widely used techniques in solid-state NMR. The NMR active nuclei with a low natural abundance usually have a relatively poor signal-to-noise ratio. The beauty of this experiment is to enhance the magnetization of the nuclei with very low natural abundance. This is done via cross-polarization mediated by the dipolar interaction between a  $^1\text{H}$  and X spin, where X = low natural abundant nuclei.

#### 4.1.7 Cross-polarization Magic Angle Spinning (CPMAS)

Since Scheafer and Stejskal<sup>22</sup> first reported on the use of the combined CP and MAS technique in a SSNMR experiment, it has revolutionised the resolution possible in SSNMR spectra. Their results showed that you could obtain similar resolution in a solid to that of high-resolution NMR in solution. The CP technique increased the signal-to-noise ratio and bypasses the  $T_1$  relaxation process of observed nuclei, with relatively low natural abundance. It also removes dipolar coupling interactions during high power proton decoupling during acquisition, in addition to the continuous magic-angle

sample spinning which reduces the chemical shift anisotropy interactions. This is why this technique has become one of the most popular used techniques to enhance spectral resolution of  $^1\text{H}$  complexes.

## Experimental

### *4.2 Instrument information*

The temperature dependence of  $^{87}\text{Rb}$  and  $^{195}\text{Pt}$  SSNMR experiments were conducted on a Varian VNMRS 500, Wide Bore 500 MHz Solid State Nuclear Magnetic Resonance Spectrometer using a 4.0 mm HX MAS probe. The  $^{87}\text{Rb}$  chemical shift was referenced with  $\text{RbCl}$ ,  $\text{D}_2\text{O}$  0.001 M and  $^{195}\text{Pt}$  with 1.2 M solution in acidic  $\text{D}_2\text{O}$   $\text{Na}_2\text{PtCl}_6$ . All experiments used standard MAS conditions; with spinning rate set to 5 kHz. A recycle delay of 40 seconds was used for all measurements. The CP technique and  $^1\text{H}$  decoupling were utilized for the hydrogen containing the  $(\text{NH}_4)_2\text{PtCl}_6$  salt. All SSNMR spectra were deconvoluted using Dmfit software.<sup>23</sup> The temperature dependence SSNMR measurements were conducted from 153 K – 413 K for  $\text{Rb}_2\text{PtCl}_6$ ,  $(\text{NH}_4)_2\text{PtCl}_6$  and  $[(\text{CH}_3)_4\text{N}]_2\text{PtCl}_6$  salts.

### *4.3 Synthesis of dication hexachloroplatinate(IV) $[\text{X}_2\text{PtCl}_6]$ salts*

The same procedures have been used as in Chapter 3 to produce the  $\text{Rb}_2\text{PtCl}_6$ ,  $(\text{NH}_4)_2\text{PtCl}_6$  and  $[\text{N}(\text{CH}_3)_4]_2\text{PtCl}_6$  salts, used to conduct the SSNMR experiments.

### *4.4 $^{195}\text{Pt}$ and $^{87}\text{Rb}$ MAS SSNMR of $\text{Rb}_2\text{PtCl}_6$ , $^{195}\text{Pt}$ for $(\text{NH}_4)_2\text{PtCl}_6$ and, $^{195}\text{Pt}$ for $[\text{N}(\text{CH}_3)_4]_2\text{PtCl}_6$*

The temperature dependence SSNMR of both  $^{87}\text{Rb}$  and  $^{195}\text{Pt}$  chemical shifts were obtained from the  $\text{Rb}_2\text{PtCl}_6$  salt, using the MAS technique. The Rb atom has two NMR active isotopes, which are both relatively sensitive in an NMR experiment.<sup>24,25,26</sup> We opted to use the  $^{87}\text{Rb}$  isotope over that of  $^{85}\text{Rb}$

isotope, even though the  $^{85}\text{Rb}$  nucleus has a higher relative abundance. The  $^{87}\text{Rb}$  isotope, on the other hand, has a higher absolute sensitivity to that of the  $^{85}\text{Rb}$  isotope making this a better nucleus with which to conduct our experiments. We attempted to perform SSNMR experiments with the  $^{85}\text{Rb}$  isotope but better resolution was observed with  $^{87}\text{Rb}$  isotope. The temperature dependence  $^{195}\text{Pt}$  SSNMR spectra were collected on the  $(\text{NH}_4)_2\text{PtCl}_6$  salt, using the CP/MAS techniques. We could not obtain a good signal for the  $^{15}\text{N}$  nucleus from the  $(\text{NH}_4)_2\text{PtCl}_6$  salt due to it having such fast relaxation in the solid-state; even with the CP/MAS techniques, our attempts to observe this nucleus were futile. The results from all the SSNMR experiments are presented.

## Results and Discussion

### 4.5.1 $^{195}\text{Pt}$ CP MAS SSNMR of $(\text{NH}_4)_2\text{PtCl}_6$

A room temperature 25 °C  $^{195}\text{Pt}$  chemical shift measurement using CP/MAS methods the of  $(\text{NH}_4)_2\text{PtCl}_6$  (see Fig. 4.9) shows some splitting of the  $^{195}\text{Pt}$  chemical shift signal; similar observations were made by Hayashi *et al.*<sup>14</sup> and Sebald *et al.*<sup>27</sup> in which they extracted J coupling parameters  $J$  ( $^{195}\text{Pt}$ - $^{35/37}\text{Cl}$ ). The  $^{195}\text{Pt}$  spectra show clear signs of dipole-dipole interaction, indirect spin coupling, quadrupolar coupling and we propose an additional isotope effect of the  $^{35}\text{Cl}/^{37}\text{Cl}$  nuclei to the  $^{195}\text{Pt}$  nucleus. The temperature dependence of  $^{195}\text{Pt}$  chemical shift measured using CP/MAS conditions of the  $(\text{NH}_4)_2\text{PtCl}_6$  is moving more downfield relative to the 1.2 M  $[\text{PtCl}_6]^{2-}$  solution reference at 0 = ppm (Figure 4.10a & b). Generally, the  $^{195}\text{Pt}$  chemical shift in solution is referred to as the resonance frequency of  $^{195}\text{Pt}$  relative to tetramethyl silane (TMS) at 100.0 MHz at any given field.<sup>28</sup> The reason we use the 1.2 M  $[\text{PtCl}_6]^{2-}$  in  $\text{D}_2\text{O}$  at 0 = ppm is because it is an easier reference with which to compare our  $^{195}\text{Pt}$  chemical shifts measurements, other than to convert our chemical shift relative to the strength of the magnetic field.

The  $^{195}\text{Pt}$  chemical shift measurements performed using CP/MAS SSNMR experiments carried out by Hayashi *et al.*<sup>14</sup> on the  $(\text{NH}_4)_2\text{PtCl}_6$  fails to mention the influence of isotope effects on the  $^{195}\text{Pt}$  chemical shift signal. Sadler *et al.*<sup>29</sup> was the first to report  $^{35/37}\text{Cl}$  isotope shifts visible on  $^{195}\text{Pt}$

chemical shift (Figure 4.11), and later similar isotopes effects were reported by Preezt *et al.*<sup>30</sup> The  $^{195}\text{Pt}$  chemical shift of 0.2 M  $[\text{PtCl}_6]^{2-}$  anion (Figure 4.11), very closely resembles the solid state  $^{195}\text{Pt}$  chemical shift signal (Figure 4.9).

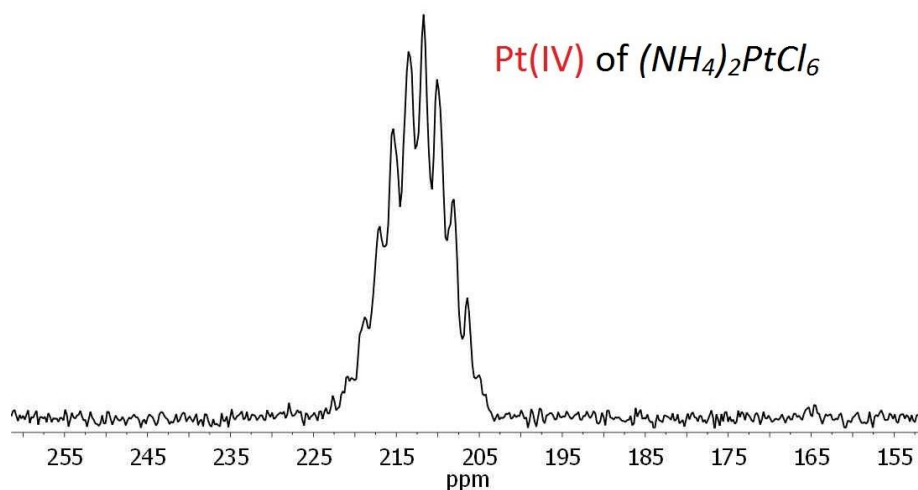
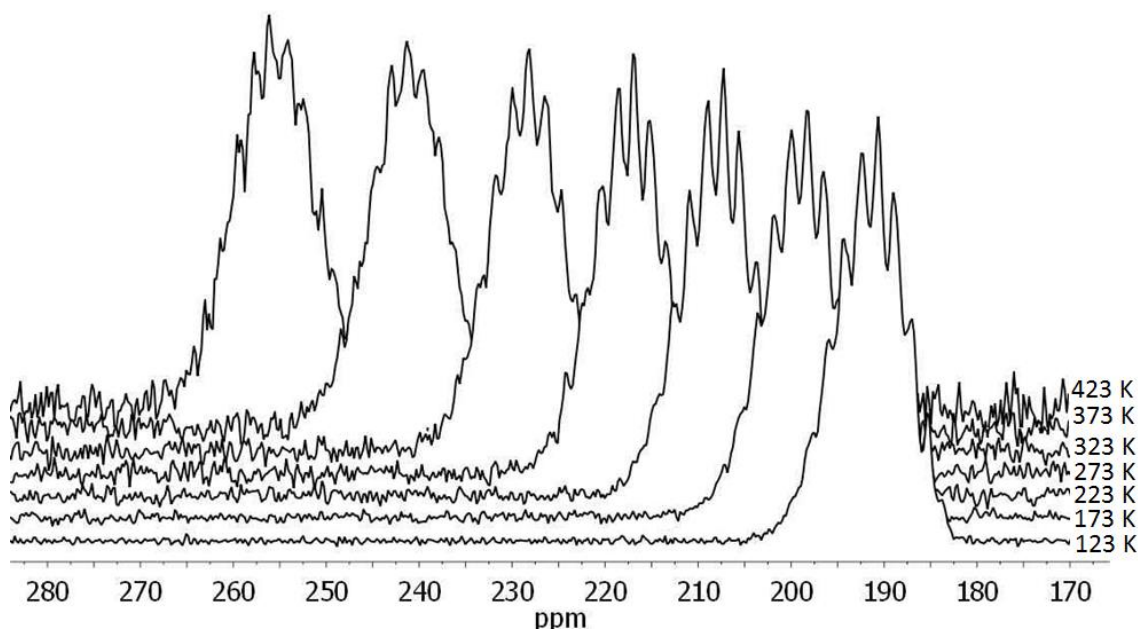
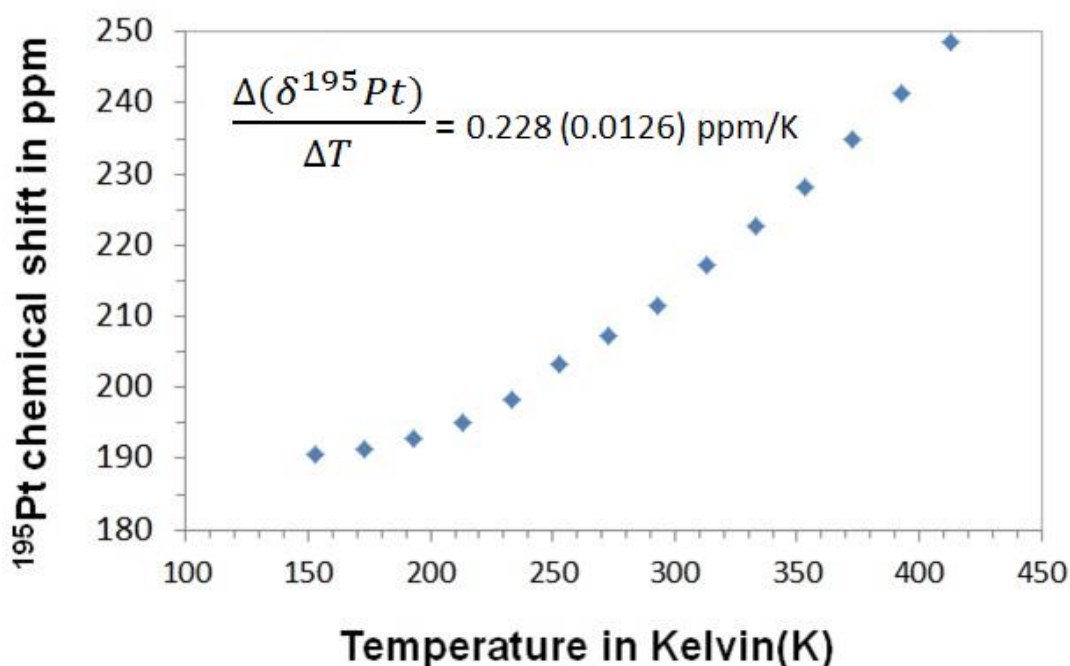


Figure 4. 9 Room temperature  $^{195}\text{Pt}$  chemical shift using MAS SSNMR of  $(\text{NH}_4)_2\text{PtCl}_6$



a)



b)

Figure 4. 10 a)  $^{195}\text{Pt}$  MAS SSNMR chemical shift variation of  $\text{Rb}_2\text{PtCl}_6$  as a function of temperature from 123 K to 423 K (spun at 5kHz) b) Plot of  $\delta(^{195}\text{Pt})$  against temperature relative to a reference of a solution 1.2 M  $(\text{PtCl}_6)^{2-}$   $\delta(^{195}\text{Pt}) = 0$  ppm at 25°C

A more fundamental understanding on the isotope effects on chemical shift are elegantly discussed in the work carried out by Jameson *et al.*<sup>2,31,32</sup> in which they propose isotope shifts to be due to differences in molecular masses between  $^{35}\text{Cl}/^{37}\text{Cl}$  isotopes, which would in turn have different Pt- $^{35}/^{37}\text{Cl}$  bond lengths in an octahedral  $[\text{PtCl}_6]^{2-}$  anion. The difference in mass would result in difference in  $^{195}\text{Pt}$  chemical shifts for the Pt- $^{35}\text{Cl}$  and Pt- $^{37}\text{Cl}$  respectively.

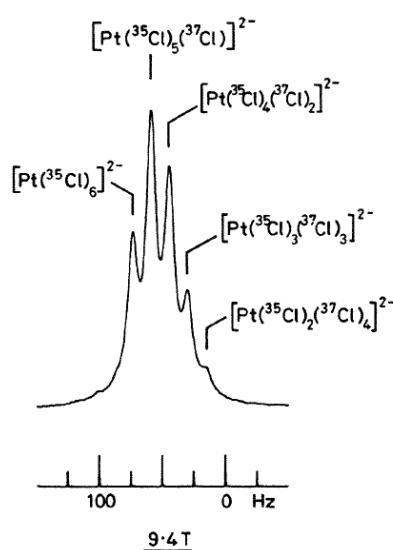


Figure 4. 11  $^{195}\text{Pt}$  NMR spectrum of  $[\text{PtCl}_6]^{2-}$  in a 2 mol. $\text{dm}^{-3}$  solution of  $\text{Na}_2\text{PtCl}_6$  salt in  $\text{D}_2\text{O}$  collected at 294 K at 1.4, 4.7 and 9.4 T fields. (Image reproduced from Sadler<sup>29</sup>)

The development of high-resolution solution NMR gave Koch *et al.*<sup>33</sup> the means to unambiguously assign both the isotopologue and isotopomer using  $^{195}\text{Pt}$  NMR. These spectra clearly show the isotope effects from  $^{35}\text{Cl}/^{37}\text{Cl}$  on the  $^{195}\text{Pt}$  chemical shift spectra. The  $^{195}\text{Pt}$  chemical shift measured using CP/MAS method of the  $(\text{NH}_4)_2\text{PtCl}_6$  salt clearly shows some resemblance to the solution spectra but since the quadrupolar coupling interaction in solution is almost non-existent due to rapid molecular tumbling and fast relaxation of the  $\text{Cl}^-$  ion. The dipole interaction and spin coupling, isotope effects, and quadrupolar coupling cause a multitude of effects, responsible for the observed  $^{195}\text{Pt}$  chemical shift spectra of  $(\text{NH}_4)_2\text{PtCl}_6$  salt in the solid state. We assume that the isotope effects are present in the  $^{195}\text{Pt}$  chemical shift signal among other effects, as mentioned above.

At low temperature the hydrogen bonding interaction between the  $[\text{NH}_4]^+$  cation and  $[\text{PtCl}_6]^{2-}$  anion is expected to be the strongest, this is assumed based on the distance obtained from single crystal X-ray diffraction measurements on these salts (see Chapter 3). The hydrogen bonding interaction is a directional interaction and is a much stronger interaction than that of the purely electrostatic interaction in  $(\text{Rb})_2\text{PtCl}_6$ . If the temperature increases, it would increase lattice vibration, which would promote lattice expansion (see Chapter 3, Section 3.3). As the lattice expands the displacement between the  $[\text{PtCl}_6]^{2-}$  and  $[\text{NH}_4]^+$  ions would increase and result in the weakening of the hydrogen bonding interaction between the  $\text{Pt}-\text{Cl}\cdots\text{H}-\text{N}$ . The  $\text{Cl}^-$  ion in the  $(\text{NH}_4)_2\text{PtCl}_6$  salt has a partially negative charge as a result of its interaction with  $\text{Pt}^{\text{IV}}$  ion forming the  $[\text{PtCl}_6]^{2-}$  anion, which has two additional electrons. These two electrons are evenly distributed between six  $\text{Cl}^-$  ions. If the hydrogen bonding interaction weakens due to lattice expansion, this would mean that this partial negative charge on the  $\text{Cl}^-$  ion would increase. Since  $\text{Cl}^-$  ion no longer has to share that electron so closely with the H ion it will increase the electron charge distribution on the  $\text{Cl}^-$  ion. Since the electronegativity of the  $\text{Cl}^-$  ion is higher than that of the H ion, the electronic charge density would have a higher affinity for the  $\text{Cl}^-$  ion, which would in turn also increase the electron negativity of the ion. If we look at the electronegativity of the Cl atom (2.8) relative to that of Pt atom (1.4), based on the the  $\text{Cl}^-$  ion electronegativity, as it is becoming more negative it would then draw electron density from the  $\text{Pt}^{\text{IV}}$  ion, as the hydrogen bonding interaction is becomes weaker due to lattice expansion. This could account for the observed upfield  $^{195}\text{Pt}$  chemical shift in our temperature dependent  $^{195}\text{Pt}$  MAS SSNMR experiments.



The equation (1) looks at the interaction of an  $I$  spin interacting with an  $S$  spin, which can be expressed as follows.<sup>34</sup>

$$V_m = -mJ_{iso} + C_m K \quad (1)$$

where  $V_m$  is the frequency deviation from the isotropic position,  $m$  is the sub-quantum number of the  $S$  spin and  $J_{iso}$  is the isotropic indirect spin coupling constant. The first term of the equation accounts for the contribution from the isotropic part of the indirect spin coupling. The second term includes the dipole-dipole interactions and the anisotropic part of the indirect spin coupling. The terms  $C_m$  and  $K$  are given by

$$C_m = \frac{3}{20} \frac{S(S+1)-3m^2}{S(2S-1)} \quad (2)$$

$$K = \frac{\chi}{Z_S} \left( -\frac{\Delta J}{3} C_J + D C_D \right) \quad (3)$$

where  $\chi$  is the quadrupolar coupling constant ( $\chi = e^2 Q q / h$ ),  $Z_S$  is the Zeeman frequency of the  $S$  spin ( $Z_S = \gamma_S H_0 / 2\pi$ ) and  $\Delta J$  is the anisotropy of the indirect spin coupling. An axially symmetric  $J$  tensor is assumed.  $D$  expresses the magnitude of the dipole-dipole interaction:

$$D = \frac{\gamma_I \gamma_S h}{4\pi^2 r_{IS}^3} \quad (4)$$

where  $r_{IS}$  is the distance between the  $I$  and  $S$  spins.

The above equation shows how the interatomic distance between the two interaction spins plays a key role in the determination of coupling interactions. In equation (4) the term  $D \propto \frac{1}{r_{IS}^3}$  implies that with an increase in distance/displacement the term  $D$  would decrease. The Pt-Cl bond lengths in the  $[\text{PtCl}_6]^{2-}$  anion over the entire temperature range, shows a small change which would imply that any change in the Pt-Cl bond length would affect dipole-dipole interactions, indirect spin coupling and isotope shifts. It is still extremely difficult to assess how all the individual solids state NMR shielding terms such as quadrupolar coupling, dipole-dipole, indirect spin coupling interactions and isotope effects from  $^{35}\text{Cl}/^{37}\text{Cl}$  atoms contribute to the splitting of the  $^{195}\text{Pt}$  chemical shift signal. This makes it difficult to assess to what extent each of these above mentioned interactions and effects have on the influence have on the  $^{195}\text{Pt}$  chemical shift.

The  $^{195}\text{Pt}$  chemical shift measurements performed using the CP/MAS method as a function of temperature of the  $(\text{NH}_4)_2\text{PtCl}_6$  salt, show a change of 57.8 ppm in  $^{195}\text{Pt}$  chemical shift as the temperature increases from 153 K to 413 K. It is not possible to extract a standard deviation from the experimental  $^{195}\text{Pt}$  chemical shift signal, since this spectra is displaying a multitude of different interactions such as dipole-dipole interaction, indirect spin coupling, quadrupolar coupling and isotope effect. This value is close to that of the expected  $^{195}\text{Pt}$  chemical shift sensitivity of  $73.2 \pm 43$  ppm calculated from variable temperature SCXRD data. The experimental  $^{195}\text{Pt}$  chemical shift of the  $(\text{NH}_4)_2\text{PtCl}_6$  salts measured as a function temperature moves more downfield as a function of increasing temperature. The temperature coefficients obtained by means of NMR measurements as a function of temperature can be rationalized by the assumption that heating causes an increase in thermal motion, which increases bond displacement. The  $^{195}\text{Pt}$  chemical shift of the  $(\text{NH}_4)_2\text{PtCl}_6$  salts moves more downfield as a function of increasing temperature (Fig. 4.12) and it is conventionally signed as a positive temperature coefficient.<sup>35</sup> This image illustrates the chemical shift relative to the solution reference at 0 = ppm, if the atom is becoming more de-shielded (downfield) it has a positive sign and therefore has a positive temperature coefficient and vice versa if it is becoming more shielded. If one assigns a reference to this system, for example if one uses tetramethyl silane (TMS) as a reference and lock it at 0 ppm. The term de-shielding become downfield and shielding becomes upfield.

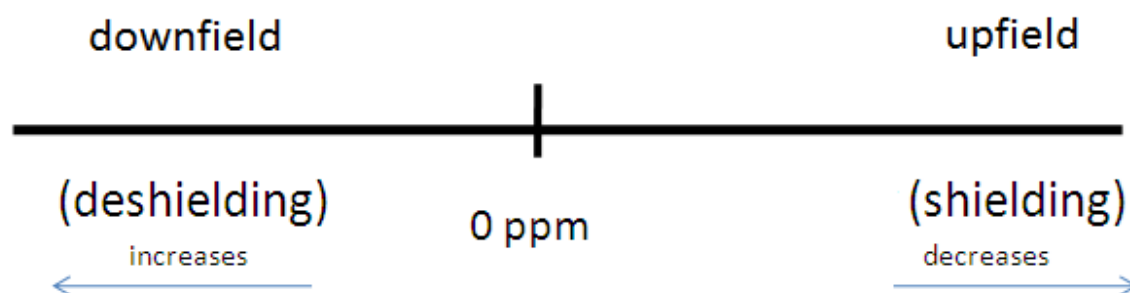


Figure 4. 12  $^{195}\text{Pt}$  chemical shift as a function of temperature illustrating the sign convention for the calculation of temperature coefficients

Although the  $^{195}\text{Pt}$  chemical shift as a function of temperature of the  $(\text{NH}_4)_2\text{PtCl}_6$  salt shows non-linear behaviour particularly at low temperature, an overall positive temperature coefficient can be estimated over a wide temperature range.

$$\text{Expected } \delta^{195}\text{Pt difference}_{100\text{K to } 400\text{K}} = \text{Pt-Cl (bond length)}_{400\text{K}} - \text{Pt-Cl (bond length)}_{100\text{K}} \times 18300 \text{ Å/ppm} \quad (5)$$

The experimental temperature coefficient was calculated using linear regression statistics to be  $0.228 (0.0126) \text{ ppm/K}$ , calculation can be found in Appendix C. This is the first reported temperature coefficient for  $^{195}\text{Pt}$  chemical shift in the solid state. Although Jameson *et al.*<sup>2</sup> commented on what the expected temperature coefficient of the  $^{195}\text{Pt}$  chemical shift for the  $[\text{PtCl}_6]^{2-}$  anion would be, we report the first temperature coefficient for  $^{195}\text{Pt}$  chemical shift of *dication hexachloroplatinate(IV)* salts in the solid state as a function of temperature. This would imply that the hypotheses put out by Koch *et al.*<sup>1</sup> and Jameson *et al.*<sup>2</sup> are correct with respect to the extent of Pt-Cl bond displacements and its influence on the sensitivity of  $^{195}\text{Pt}$  chemical shift in  $[\text{PtCl}_6]^{2-}$  anion. The experimental and theoretical work carried out by these authors were done in gaseous and solution phase using a conductor-like screening model (COSMO) respectively. With the aid of SCXRD and SSNMR measurements performed as a function of temperature, it was possible to probe the  $^{195}\text{Pt}$  chemical shift sensitivity to changing Pt-Cl bond lengths (Figure 4.13). This plot shows that with increase in Pt-Cl bond lengths there is a more downfield shift of the  $^{195}\text{Pt}$  chemical shift signal. This study extends  $^{195}\text{Pt}$  chemical shift sensitivity to Pt-Cl bond displacement in the solid state in deceptively simple *dication hexachloridoplatinate(IV)* salts.

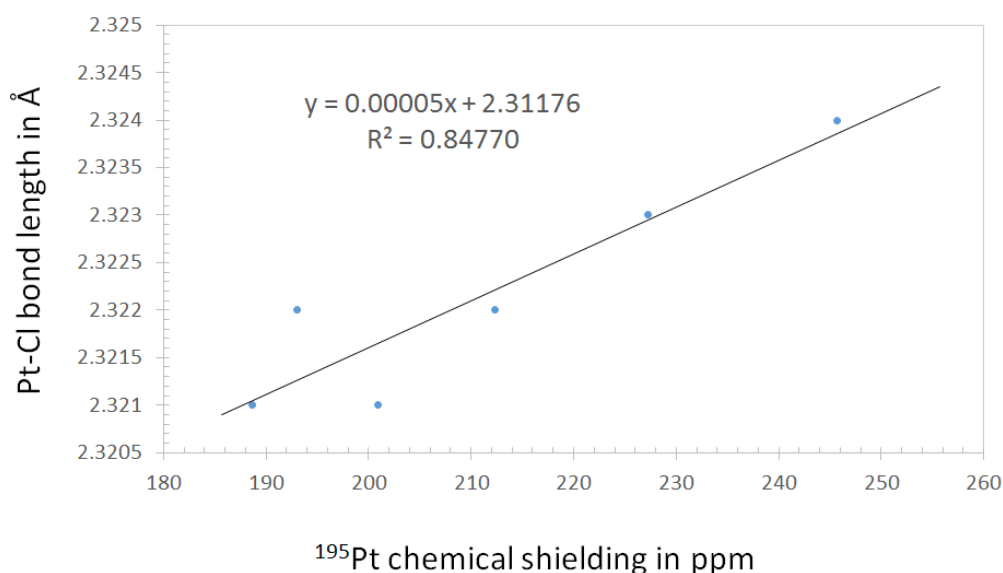


Figure 4. 13 This plot shows the relationship between the Pt-Cl bond displacement and  $^{195}\text{Pt}$  chemical shift as a function of temperature.

#### 4.5.2 $^{195}\text{Pt}$ CP MAS SSNMR $\text{Rb}_2\text{PtCl}_6$

Upon first glance the room temperature 25 °C  $^{195}\text{Pt}$  chemical shift signal obtained from MAS methods of  $(\text{Rb})_2\text{PtCl}_6$  salt (see Fig. 4.14) seems not to be well resolved. On the contrary, it is displaying in a similar manner to the  $(\text{NH}_4)_2\text{PtCl}_6$  salt, very rear dipole-dipole interaction, spin coupling and isotope effects in the solid-state. The splitting of the  $^{195}\text{Pt}$  chemical shift signal has been reported in similar cubic crystal structures by Hayashi *et al.*<sup>14</sup> and Sebald *et al.*,<sup>27</sup> these authors have also ignored to mention the isotope effects from the  $^{35}\text{Cl}/^{37}\text{Cl}$  isotopies contribution to the  $^{195}\text{Pt}$  chemical shift signal. These authors all used CP/MAS conditions upon performing  $^{195}\text{Pt}$  SSNMR experiments since these conditions require the complex being measured to have protons. This made the  $(\text{NH}_4)_2\text{PtCl}_6$  a better candidate over that of  $(\text{Rb})_2\text{PtCl}_6$ , which contains no protons. This is clear upon comparing the  $(\text{NH}_4)_2\text{PtCl}_6$  (Fig. 4.9) to that of  $(\text{Rb})_2\text{PtCl}_6$  (Fig. 4.14) salt.

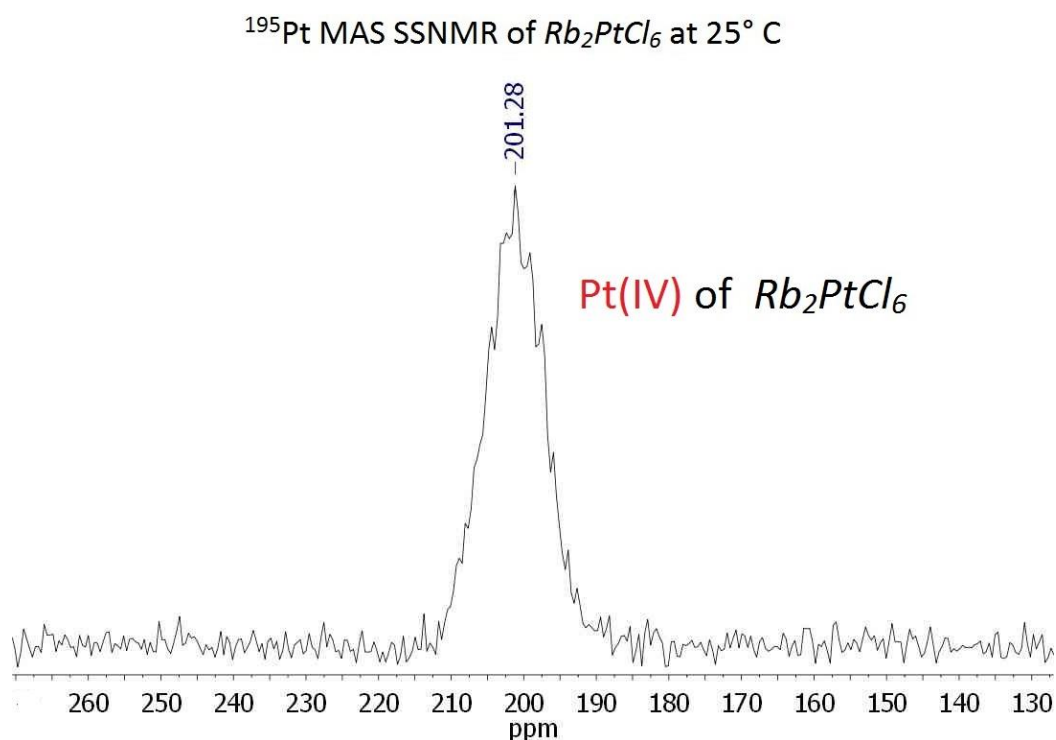
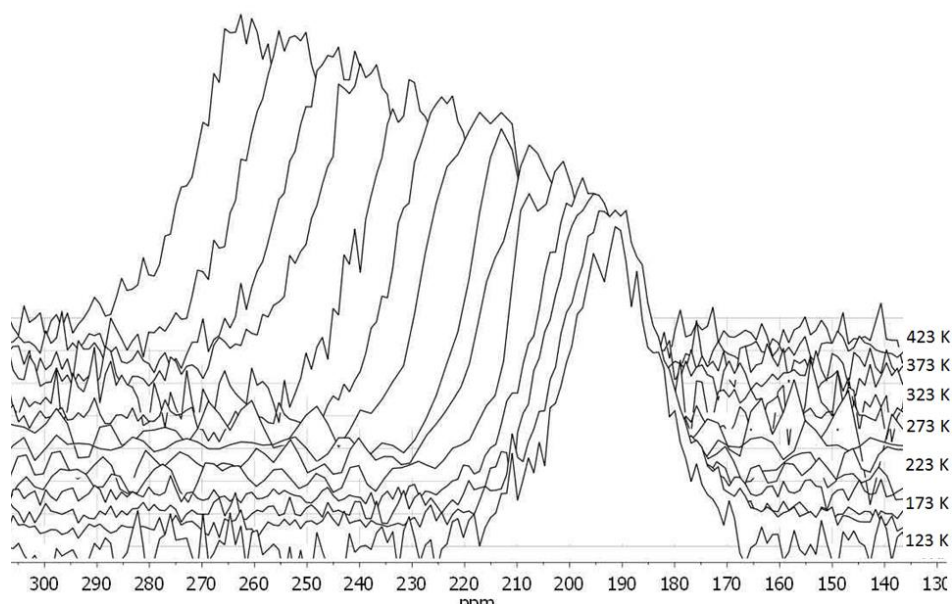


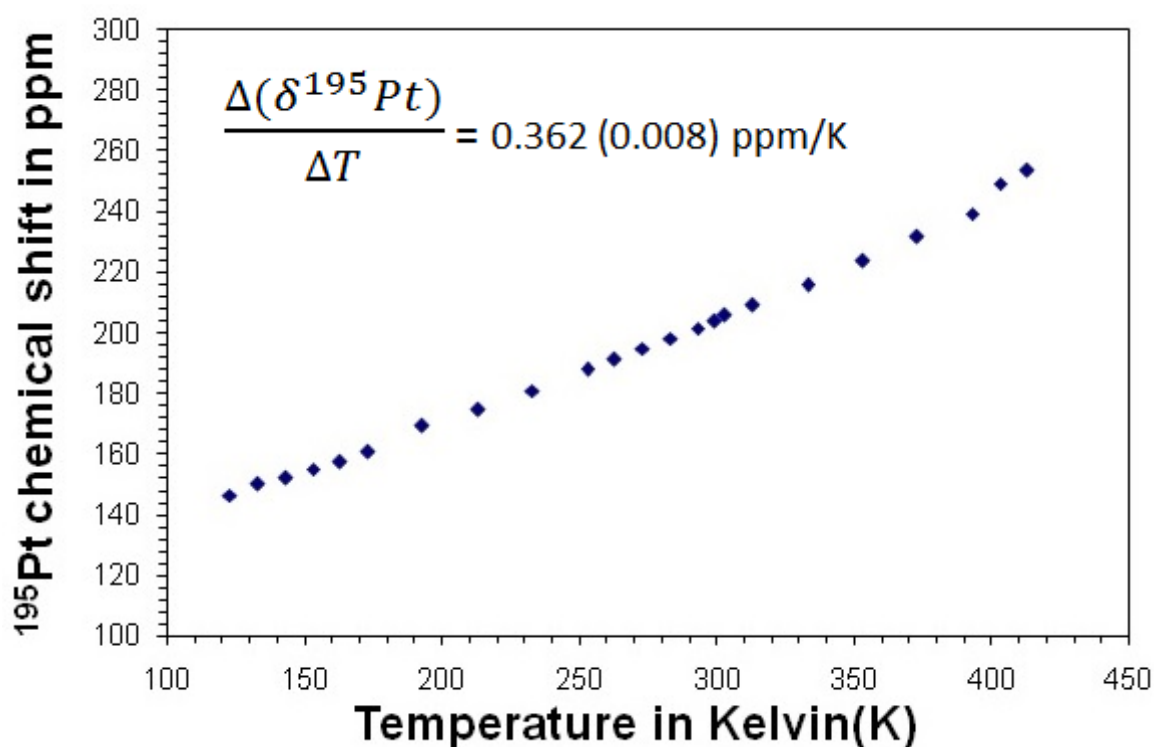
Figure 4. 14 Room temperature (25 °C)  $^{195}\text{Pt}$  chemical shift using MAS SSNMR of  $\text{Rb}_2\text{PtCl}_6$  spun at 5 kHz

The  $^{195}\text{Pt}$  MAS SSNMR measurements conducted as a function of temperature on the  $(\text{Rb})_2\text{PtCl}_6$  salt were done within a temperature range of -150 °C (123.15 K) and 150 °C (423.15 K) as seen in Fig.

4.15a. This clearly illustrates how the  $^{195}\text{Pt}$  chemical shift signal is moving more downfield relative to the 1.2 M  $[\text{PtCl}_6]^{2-}$  reference solution at 0 ppm. This is clearer from the plot shown in Fig. 4.15b



a)



b)

Figure 4. 15a)  $^{195}\text{Pt}$  chemical shift measurements using MAS method show the  $^{195}\text{Pt}$  chemical shift variation of  $\text{Rb}_2\text{PtCl}_6$  as a function of temperature from 123 K to 423 K (spun at 5kHz) b) Plot of  $\delta(^{195}\text{Pt})$  against temperature relative to a reference of a solution 1.2 M  $(\text{PtCl}_6)^{2-}$   $\delta(^{195}\text{Pt}) = 0$  ppm at 25°C)

The  $(\text{Rb})_2\text{PtCl}_6$  salt adopts a cubic ( $F\bar{3}m\bar{3}$ ) symmetry and the octahedral  $[\text{PtCl}_6]^{2-}$  anion adopts the  $O_h$  symmetry with  $C_4$  axial symmetry for the Pt-Cl bond. This cubic symmetry makes the Pt-Cl bond lengths in  $[\text{PtCl}_6]^{2-}$  all equivalent. At lower temperatures the purely electrostatic interaction between the  $\text{Rb}^+$  and  $[\text{PtCl}_6]^{2-}$  ions would be strongest. If the temperature is increased this would increase the lattice vibration and lattice expansion together with an increase in bond displacement within the crystal lattice (see Section 3.2, Chapter 3). In Chapter 3 the temperature dependence SCXRD measurements of the  $(\text{Rb})_2\text{PtCl}_6$ , shows an increase in lattice parameters by 4.3% for both the unit cell dimension and unit cell volume over a 100 K to 400 K temperature range.

Let us consider the electrostatic interaction between the  $\text{Cl}^-$  ion and the  $\text{Rb}^+$  ion for a moment. The  $\text{Cl}^-$  ion has a partially negative charge as a result of its interaction with  $\text{Pt}^{\text{IV}}$  ion forming the  $[\text{PtCl}_6]^{2-}$  anion, which has two additional electrons. The two electronic charges are evenly distributed between six  $\text{Cl}^-$  ions giving it this partial negative charge. Similarly to that of the  $(\text{NH}_4)_2\text{PtCl}_6$  salt, it requires two opposing  $[\text{Rb}]^+$  ion charges to make a neutral  $(\text{Rb})_2\text{PtCl}_6$  complex. The two  $\text{Rb}^+$  cations therefore neutralize the anion, hence forming the  $(\text{Rb})_2\text{PtCl}_6$  complex. The weakening of the electrostatic interaction between the  $\text{Pt-Cl}\cdots\text{Rb}$ , would mean that this partial negative charge on the  $\text{Cl}^-$  ion would increase. Since the electronegativity of the  $\text{Cl}^-$  ion is higher than that of the  $\text{Rb}^+$  ion, it has a higher affinity for electronic charge, as the interaction between anion and cation weakens the electronic charge, the density on the  $\text{Cl}^-$  ion would increase. If we look at the electronegativity of the Cl atom (2.8) relative to that of Pt atom (1.4), the Cl ion is becoming more negative and it would draw electron density from the  $\text{Pt}^{\text{IV}}$  ion in the  $[\text{PtCl}_6]^{2-}$  anion as the electrostatic interaction is becoming weaker. This could account for the observed downfield shift observed in  $^{195}\text{Pt}$  chemical shift experiments performed as a function of temperature. A very interesting observation is made up on investigating the covalent Pt-Cl bond displacement in  $(\text{Rb})_2\text{PtCl}_6$  salt as a function of temperature. It is generally assumed that the interatomic bond displacement in the covalent bond would increase because of lattice expansion brought on by an increase in temperature. The SCXRD measurements performed as a function of temperature show a small difference within the covalent Pt-Cl bond in  $(\text{Rb})_2\text{PtCl}_6$  salt. (see Fig. 4. 15).

The  $(\text{Rb})_2\text{PtCl}_6$  salt  $^{195}\text{Pt}$  chemical shift measurement performed using MAS SSNMR method as a function of temperature, show a 98.5 ppm difference over a 153 K – 413 K range. This value is close to that of the expected  $^{195}\text{Pt}$  chemical shift sensitivity of  $104.3 \pm 38$  ppm obtained from variable temperature SCXRD analysis of the  $(\text{Rb})_2\text{PtCl}_6$  salts. The temperature coefficient was extracted from  $^{195}\text{Pt}$  chemical shift measurement on the  $(\text{Rb})_2\text{PtCl}_6$  salts as a function of temperature is  $0.362$  ( $0.008$ ) ppm/K, which is higher than that of the  $(\text{NH}_4)_2\text{PtCl}_6$  salt of is  $0.228$  ( $0.0126$ ) ppm/K. The temperature coefficient for the  $(\text{NH}_4)_2\text{PtCl}_6$  salt was calculated from data that has a different  $^{195}\text{Pt}$  chemical shift trend to that of the  $(\text{Rb})_2\text{PtCl}_6$  salts trend. The  $(\text{NH}_4)_2\text{PtCl}_6$  salts  $^{195}\text{Pt}$  chemical shift measurements as a function of temperature tended towards a quadratic trend whereas the  $(\text{Rb})_2\text{PtCl}_6$  tends to be more linear.

These results appear to confirm the hypothesis set out by Jameson *et al.*<sup>2</sup> and others,<sup>1</sup> which correlates the sensitivity of the  $^{195}\text{Pt}$  chemical shift to changes in Pt-Cl bond displacement in the  $[\text{PtCl}_6]^{2-}$  anion. With the aid of SCXRD and SSNMR measurements performed as a function of temperature, it was possible to probe the extent of bond displacement in the solid state (Figure 4.16). This plot show with increase in Pt-Cl bond lengths there is an increase in the  $^{195}\text{Pt}$  chemical shift. This study extends  $^{195}\text{Pt}$  chemical shift sensitivity to Pt-Cl bond displacement in the solid state. This study has found some evidence in support of this hypothesis using SSNMR.

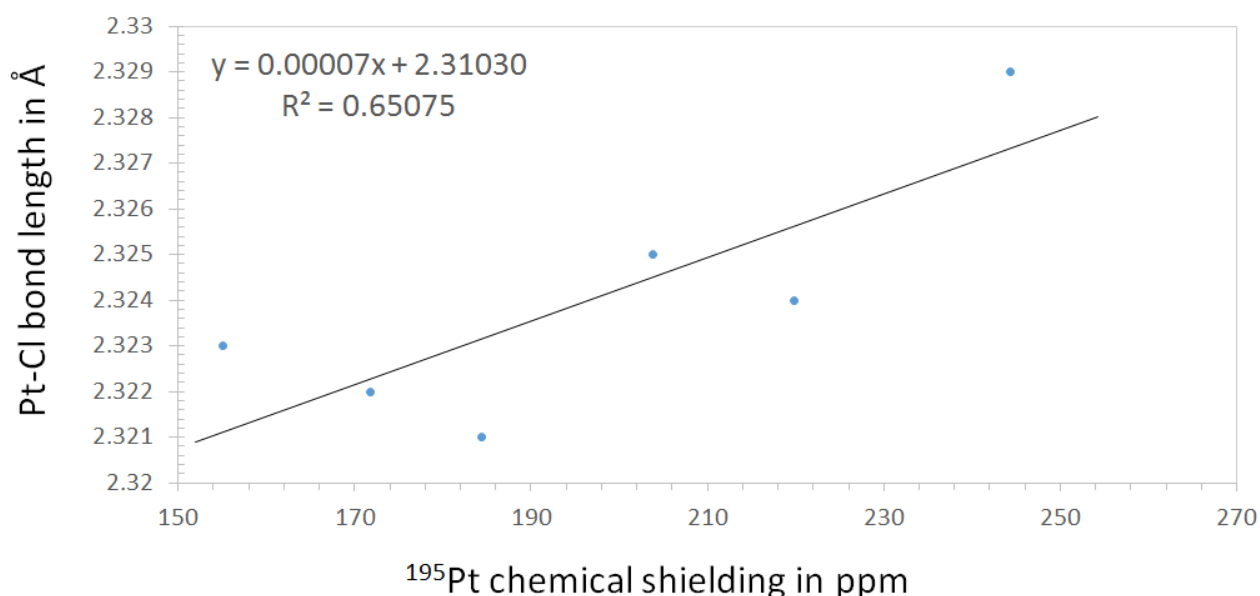


Figure 4. 16 The plot shows the relationship between Pt-Cl bond lengths and  $^{195}\text{Pt}$  chemical shielding of the  $\text{Rb}_2\text{PtCl}_6$  salt as a function of increasing temperature

4.5.3  $^{87}\text{Rb}$  MAS SSNMR experimental analysis of  $\text{Rb}_2\text{PtCl}_6$ 

A room temperature (25 °C)  $^{87}\text{Rb}$  chemical shift measured using MAS method of precipitated  $\text{Rb}_2\text{PtCl}_6$  (see Fig. 4.17) indicates that the sample still contains some  $\text{RbCl}$  as a contaminant. This was as a result of using an excess of  $\text{RbCl}$  during the crystallization process in forming the  $\text{Rb}_2\text{PtCl}_6$  salt. Nevertheless, a clear and observable  $^{87}\text{Rb}$  chemical shift signal is obtained for the  $\text{Rb}^+$  cation in the  $\text{Rb}_2\text{PtCl}_6$  salt. Also noticeable from Fig. 4.18 are the spinning sidebands from both the  $\text{RbCl}$  and  $\text{Rb}^+$  ion. Upon changing the spinning speed during the MAS experiment, it was clear that the  $^{87}\text{Rb}$  chemical shift ( $\sigma_{\text{iso}}$ ) remained the same, hence confirming the minor peaks to be spinning sidebands. The temperature dependence of  $^{87}\text{Rb}$  chemical shift measured with MAS method were done over a temperature range of -150 °C (123.15 K) and 150 °C (423.15 K) as shown in Fig. 4.17.

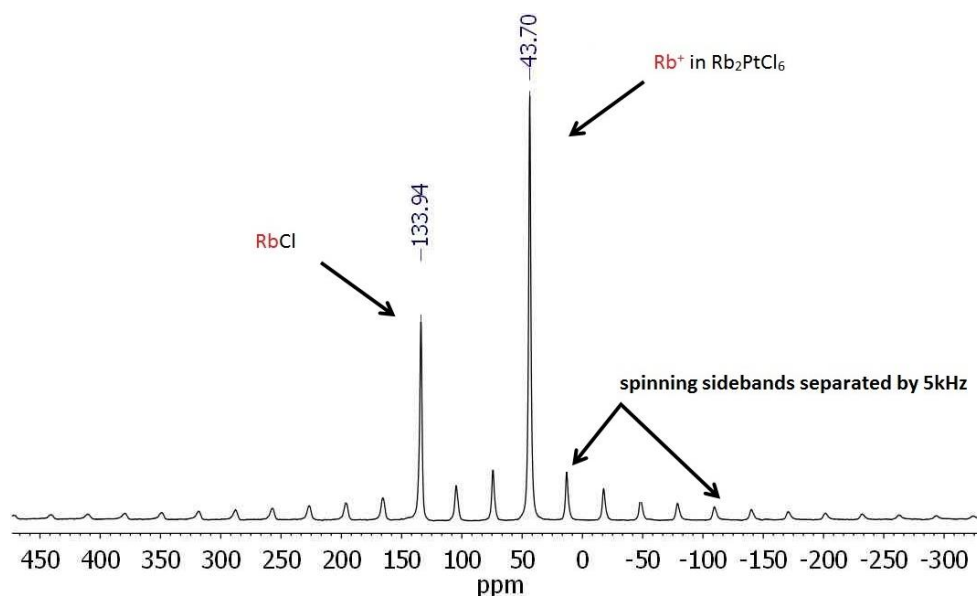


Figure 4. 17 Room temperature  $^{87}\text{Rb}$  MAS SSNMR of  $\text{Rb}_2\text{PtCl}_6$  spun at 5 kHz and  $\text{RbCl}$  impurity

It is clear from Fig. 4.18 that with an increase in temperature the  $^{87}\text{Rb}$  chemical shift signal of the  $^{87}\text{Rb}$  nucleus in  $\text{RbCl}$  become more upfield from the magnetic field relative to the reference sample  $\text{RbCl}$  0.01 M at 0 ppm. In Fig 4.19a this is even more distinct in addition to the plotted data 4.20a. The  $\text{Rb}^+$  cation in  $\text{Rb}_2\text{PtCl}_6$  on the other hand is downfield relative to the reference sample  $\text{RbCl}$  0.01 M, which can be observed in Fig. 4.18, Fig.4.19b and Fig. 4.20b.



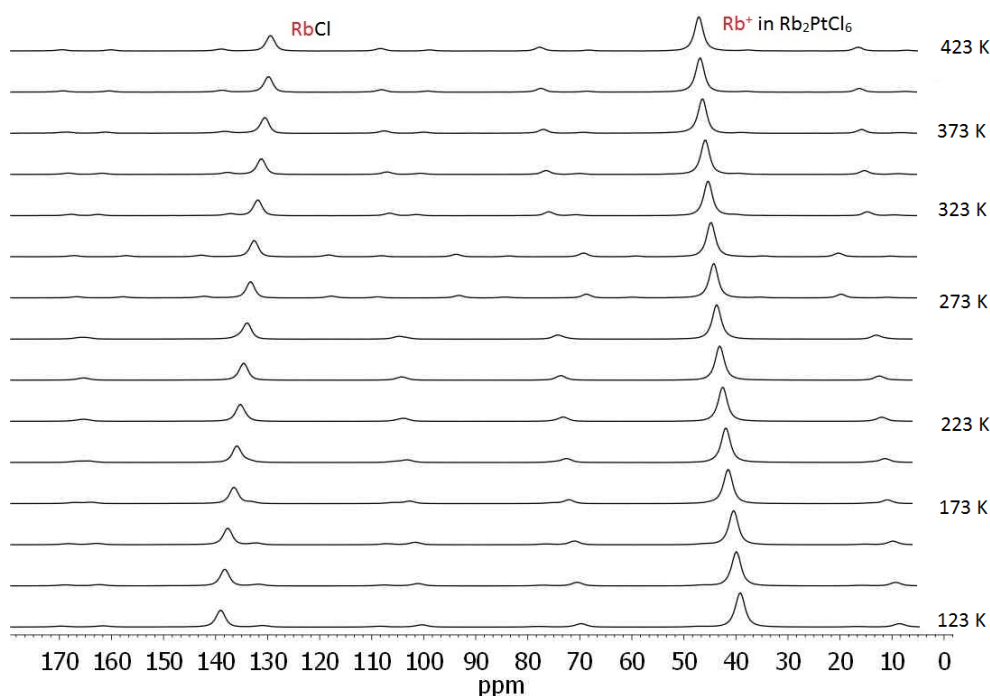


Figure 4. 18 The  $^{87}\text{Rb}$  MAS SSNMR of  $\text{Rb}_2\text{PtCl}_6$  and  $\text{RbCl}$  spun at 5kHz as a function of temperature

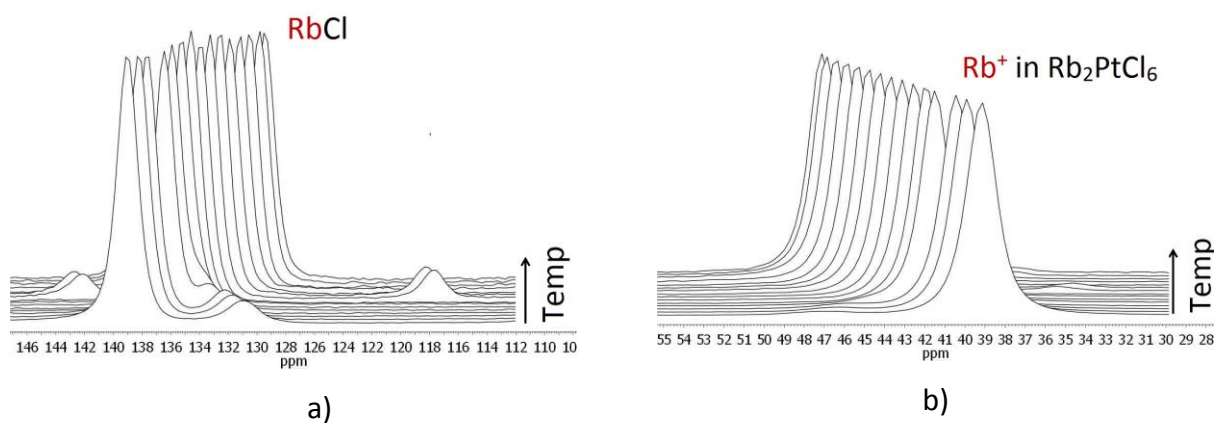
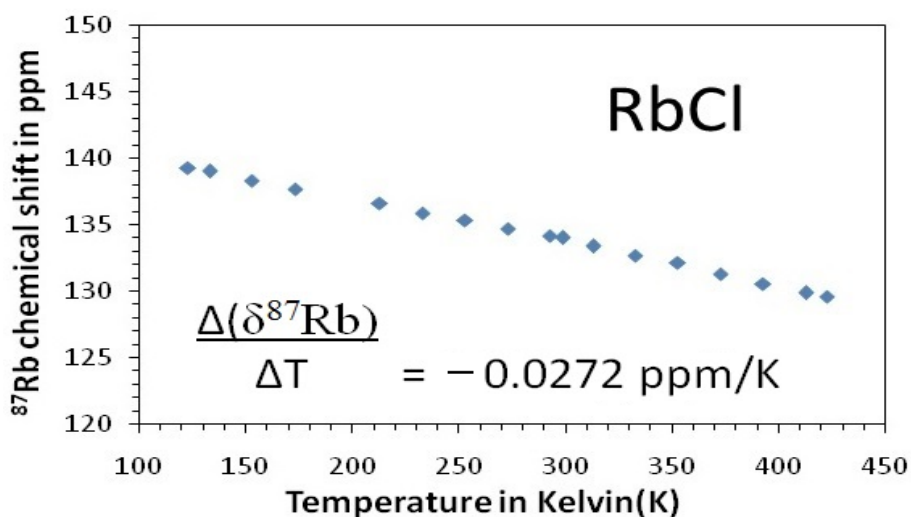
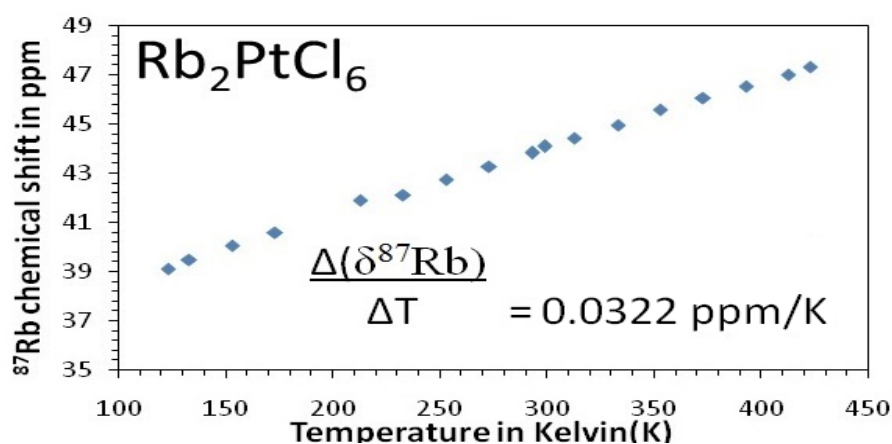


Figure 4. 19a) The  $^{87}\text{Rb}$  chemical shift of a)  $\text{RbCl}$  showing the  $^{87}\text{Rb}$  nucleus becoming more shielding as a function of increasing temperature and b) The  $^{87}\text{Rb}$  chemical shielding of the  $\text{Rb}_2\text{PtCl}_6$  salt as function of increasing temperature using MAS SSNMR spun at 5 kHz.



a)



b)

Figure 4. 20a) <sup>85</sup>Rb MAS SSNMR chemical shift variation of RbCl as a function of temperature from 123 K to 423 K (spun at 5kHz) b) <sup>85</sup>Rb MAS SSNMR shielding variation of Rb<sub>2</sub>PtCl<sub>6</sub> as a function of temperature from 123 K to 423 K (spun at 5kHz)

The experimental temperature coefficient obtained from temperature dependence <sup>87</sup>Rb chemical shift measurements using MAS SSNMR of the RbCl (0,0322 ppm/K) and Rb<sub>2</sub>PtCl<sub>6</sub> salts (-0,0272 ppm/K) were calculated from the slopes of these trends. These temperature coefficients are smaller by a factor of ten, relative to that of the <sup>195</sup>Pt temperature coefficients of Rb<sub>2</sub>PtCl<sub>6</sub> and (NH<sub>4</sub>)<sub>2</sub>PtCl<sub>6</sub> salts, highlighting the sensitivity of <sup>195</sup>Pt nucleus over that of the <sup>87</sup>Rb nucleus.

The <sup>87</sup>Rb chemical shift signal of the Rb<sup>+</sup> ion in RbCl resonates fairly upfield relative to that of the Rb<sup>+</sup> ion in (Rb)<sub>2</sub>PtCl<sub>6</sub> salt. In solid RbCl the Cl<sup>-</sup> ion is bound to the Rb<sup>+</sup> ion through an ionic bond; relative to that of the free Rb<sup>+</sup> cation in (Rb)<sub>2</sub>PtCl<sub>6</sub> salt, therefore making the <sup>87</sup>Rb nucleus in RbCl more de-shielded from the magnetic field to that of the free Rb<sup>+</sup> cation in (Rb)<sub>2</sub>PtCl<sub>6</sub> salt relative to

the reference of  $\text{D}_2\text{O}$ , 0.01 M  $\text{RbCl}$  0 = ppm at 25 °C. It is for this reason that the  $^{87}\text{Rb}$  chemical shift of the  $\text{Rb}^+$  cation in the  $\text{RbCl}$  salt appears more downfield relative to that of the  $\text{Rb}^+$  cation in the  $(\text{Rb})_2\text{PtCl}_6$  salt

The  $^{87}\text{Rb}$  chemical shift measurements using the MAS method performed as function of temperature on the  $(\text{Rb})_2\text{PtCl}_6$  and  $\text{RbCl}$  salts (see Fig. 4.20a & b) show the  $^{87}\text{Rb}$  chemical shift to have a very low sensitivity to temperature variation. In the case of the  $\text{Rb}^+$  ion in  $(\text{Rb})_2\text{PtCl}_6$ , this could be due to the rigidity of the salt. If we consider the  $\text{Rb}^+$  ion in the  $(\text{Rb})_2\text{PtCl}_6$  salt, the cation is situated within the cage of a cubic anti-fluorite structure (see Fig. 4.21). A review written by Armstrong *et al.*<sup>36</sup> about these anti-fluorite structures gives some insights into similar structures' rigidity due to the cations and anions efficient face-centred-cubic packing arrangements in these salts.

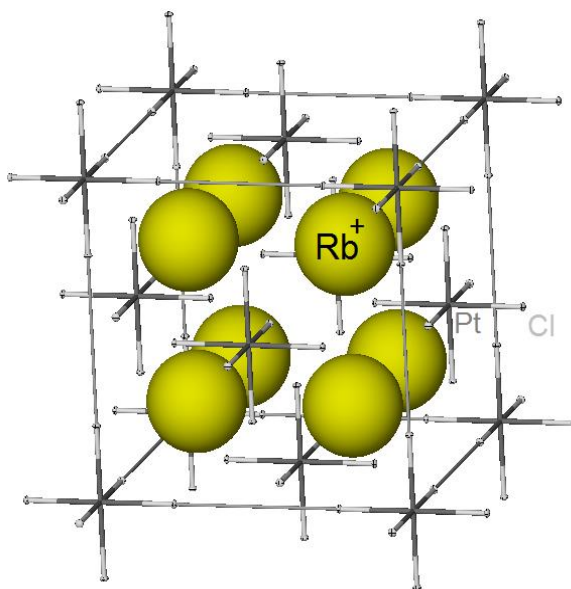


Figure 4. 21 Cubic anti-fluorite crystal structure of  $(\text{Rb})_2\text{PtCl}_6$

If one looks at the diagram of the  $\text{Rb}^+$  cation in  $(\text{Rb})_2\text{PtCl}_6$  illustrating the anti-fluorite type structure, the cations are trapped within a cage. The rigid packing arrangement in anti-fluorite type structure is said to be one of the main reasons for the small extent of lattice expansion.<sup>37,38</sup> This would lead to a limited space within which the cation could be displaced/move. The  $\text{Rb}^+$  cation would, as a result of lattice expansion, also move further away from the  $\text{Cl}^-$  ion in the  $[\text{PtCl}_6]^{2-}$  anion weakening the electrostatic interaction between the cation and anion by 0.0528 Å from 100 K to 400 K. The electron negativity of the Cl atom is 2.8 and 0.9 for Rb atom, which means the electron from the  $\text{Rb}^+$  ion would have a higher affinity for the  $\text{Cl}^-$  ion. These are the factors which could influence the shielding of a nucleus during lattice expansion and could account for some of the experimentally

observed  $^{87}\text{Rb}$  chemical shift in both the free  $\text{Rb}^+$  cation in  $(\text{Rb})_2\text{PtCl}_6$  and ionically bound  $\text{Rb}^+$  ion  $\text{RbCl}$  salt. This simple use of electronegativity of the atoms is not an adequate explanation; it serves only as a preliminary explanation. To account for effects such as conjugation and polarizability in molecules, in conjunction to what is happening with these charges when molecules are interacting with one another, is not so straightforward. This requires more quantum mechanically derived charges, which are more reliable.

The difference in interaction between the  $(\text{NH}_4)_2\text{PtCl}_6$  and  $(\text{Rb})_2\text{PtCl}_6$  salts could give an account as to why we are observing such differences in experimental  $^{195}\text{Pt}$  chemical shift trends in both these salts. In the  $(\text{Rb})_2\text{PtCl}_6$  salt we have a purely electrostatic interaction, which is a non-direction interaction, whereas hydrogen bonding in the  $(\text{NH}_4)_2\text{PtCl}_6$  salt is a more directional interaction. If we look at how these two distinct and different, interactions could affect the  $\text{Cl}^-$  ion and in turn the  $\text{Pt}^{\text{IV}}$  ion, it could give some insight as to why we are observing such a difference in the  $^{195}\text{Pt}$  chemical shift trends as a function of temperature. The average temperature coefficients derived from the  $^{35}\text{Cl}$  Nuclear Quadrupolar Resonance (NQR)<sup>39</sup> frequencies performed as a function of temperature of  $(\text{Rb})_2\text{PtCl}_6$  and  $(\text{NH}_4)_2\text{PtCl}_6$  salts are both decreasing absolute negative temperature coefficients with increasing temperature. The NQR measurement is a measure of the deviation of the nuclear charge distribution from spherical symmetry. This means both the  $(\text{Rb})_2\text{PtCl}_6$  and  $(\text{NH}_4)_2\text{PtCl}_6$  salts measure a decrease in the  $^{35}\text{Cl}$  NQR frequencies as a function of decreasing temperature. This is surely giving some indication that something is happening around the electron density of the  $\text{Cl}^-$  ion in these salts. We investigate in Chapter 5, the effects changing inter-and intramolecular interactions have on the electrostatic potential of  $(\text{Rb})_2\text{PtCl}_6$  and  $(\text{NH}_4)_2\text{PtCl}_6$  salt crystal structures as a function of temperature using semi-empirical quantum mechanical calculations.

#### 4. 5.4 $^{195}\text{Pt}$ CP MAS SSNMR of $[\text{N}(\text{CH}_3)_4]_2\text{PtCl}_6$

The  $^{195}\text{Pt}$  chemical shift measurements performed with CP/MAS method of  $[\text{N}(\text{CH}_3)_4]_2\text{PtCl}_6$  at 30 °C (see Fig. 4.22) shows some splitting of the  $^{195}\text{Pt}$  chemical shift signal. The resolution of this spectrum is not as well resolved as that of the ammonium derivative, as shown in Fig. 4.9. The splitting observed in the spectra is due to dipole-dipole interaction, indirect spin coupling, and isotope effects from the  $^{35}\text{Cl}/^{37}\text{Cl}$  nucleus to the  $^{195}\text{Pt}$  nucleus.<sup>14</sup> The  $^{195}\text{Pt}$  chemical shift measurements

performed as a function of temperature were done within a temperature range of  $-125\text{ }^{\circ}\text{C}$  (148.15 K) and  $160\text{ }^{\circ}\text{C}$  (433.15 K). The  $^{195}\text{Pt}$  chemical shifts are moving more downfield relative to the 1.2 M  $[\text{PtCl}_6]^{2-}$  reference solution at 0 ppm (Figure 4.23). It is not possible to extract temperature coefficients from the  $^{195}\text{Pt}$  chemical shift trends as this structure undergoes several structural phase transitions as a function of temperature.

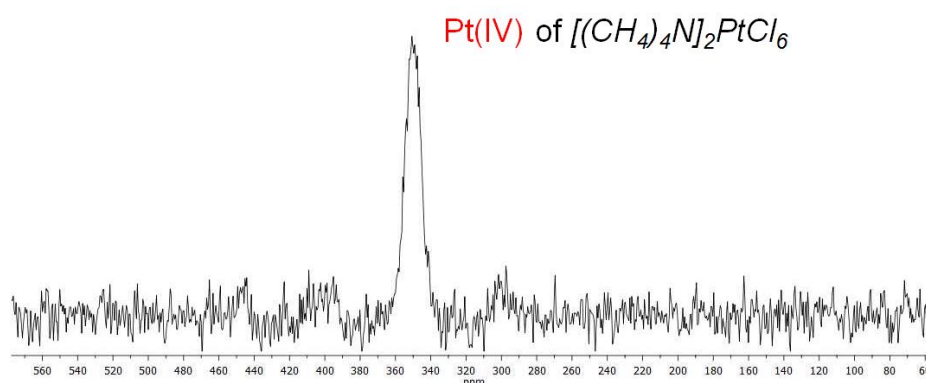


Figure 4.22  $^{195}\text{Pt}$  chemical shift signal measured using CP/MAS SSNMR of  $[(\text{CH}_3)_4\text{N}]_2\text{PtCl}_6$  spun at 5 kHz.

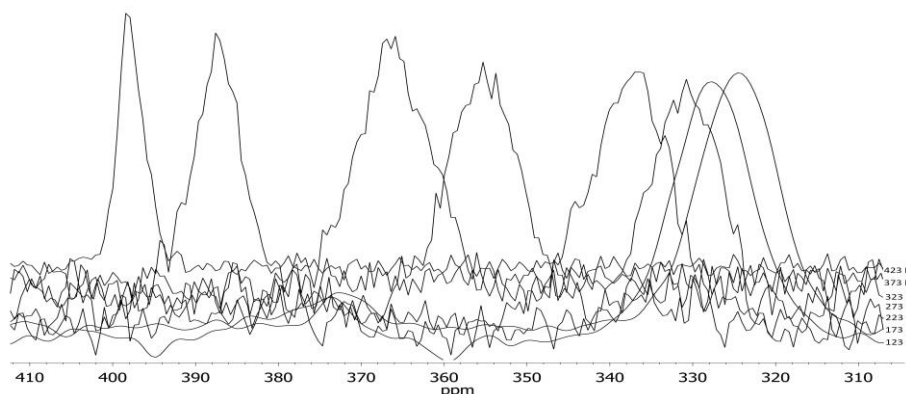


Figure 4.23  $^{195}\text{Pt}$  chemical shift measurements using MAS SSNMR showing the shielding variation of  $[\text{N}(\text{CH}_3)_4]_2\text{PtCl}_6$  as a function of temperature from 123 K to 423 K (spun at 5 kHz)

The  $[\text{N}(\text{CH}_3)_4]_2\text{PtCl}_6$  salt undergoes quite a few structural phase transitions as a function of temperature as discussed in Section 3.3, Chapter 3. This salt has previously been studied by variable temperature  $^1\text{H}$  NMR. These  $^1\text{H}$  NMR measurements<sup>40</sup> on the *bis(tetramethylammonium) hexachloroplatinate(IV)* confirms the molecular motion in the *tetramethylammonium* cation to be one of the main contributions to the structural phase transition. The  $^{35}\text{Cl}$  (NQR) Spectroscopy studies carried out on the  $[\text{N}(\text{CH}_3)_4]_2\text{PtCl}_6$  salt<sup>41</sup> show the salt structural phase transition based on the disappearance of two  $^{35}\text{Cl}$  frequencies merging into a single  $^{35}\text{Cl}$  frequency as the temperature

increases. This shows that at a lower temperature, the salt has two non-equivalent  $\text{Cl}^-$  ions and as the temperature increases it only has one equivalent  $\text{Cl}^-$  ion in the  $[\text{N}(\text{CH}_3)_4]_2\text{PtCl}_6$  salt. This is also clear from our single crystal X-ray diffraction measurement on this salt in Chapter 3 (Table 3.11 and Fig. 3:18).

In this study we measure the  $^{195}\text{Pt}$  chemical shift measurements as a function of temperature using CP/MAS conditions on the  $[\text{N}(\text{CH}_3)_4]_2\text{PtCl}_6$  salt. If we start investigating our nuclei independently, starting with the  $^{195}\text{Pt}$  nucleus it is quite clear from the experiment results that the  $^{195}\text{Pt}$  chemical shift signal is moving more downfield as a function of increasing temperature (see Fig. 4.23). This is indicative of a loss of electron charge density from the nucleus. Although the  $^{195}\text{Pt}$  chemical shift trend show outliers at different temperatures from that of previously reported temperature at which the structure phase transition occurs it is still remarkable that the nucleus can pick up these changes.

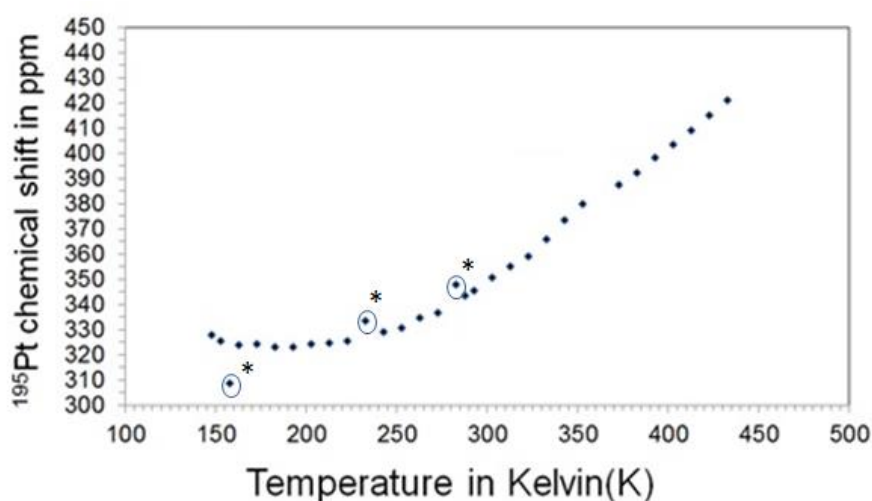


Figure 4. 23 Temperature dependence of  $^{195}\text{Pt}$  chemical shift using CP/MAS method of  $[\text{N}(\text{CH}_3)_4]_2\text{PtCl}_6$  spun at 5 kHz, the circles marked with mark starts are the outliers from the trends possible. It marks the possible temperature at which the phase transitions occurs.

The  $\text{Cl}^-$  ions in this salt are covalently bound to the  $\text{Pt}^{\text{IV}}$  ion, which means that both the  $^{35/37}\text{Cl}$  NMR active nuclei have extremely large chemical shielding anisotropy. This extremely large chemical shielding anisotropy is attributed to the atom's large non-spherical electric field gradient. It is for this reason that  $^{35/37}\text{Cl}$  NQR spectroscopy is preferred over  $^{35/37}\text{Cl}$  SSNMR measurement, as it is the only means to measure the electronic environment of a Cl atom with such large quadrupolar coupling constants. The work done by Nakamura *et al.*<sup>40,41</sup> on this salt shows how the  $\text{Cl}^-$  ions electric

field gradient (EFG) is affected by a change in temperature. The  $^{35}\text{Cl}$  NQR frequency measured as a function of temperature of the  $[(\text{CH}_3)_4\text{N}]_2\text{PtCl}_6$  salt decreases, which indicates a change of the  $\text{Cl}^-$  ions electric field gradient. This decreasing in the  $^{35}\text{Cl}$  frequency has been postulated to be a direct result of lattice expansion.

It is difficult to make an assumption on how the  $\text{Cl}^-$  ions of the  $[\text{PtCl}_6]^{2-}$  anion in all three *dication hexachloroplatinate* salts influences our experimentally observed  $^{195}\text{Pt}$  chemical shielding as a function of temperature. The results from  $^{35}\text{Cl}$  NQR spectroscopy of these salts show that changing temperature influence the electric field gradients of the  $\text{Cl}^-$  ions in all three these salts.<sup>39,40,41</sup> This would be enough evidence to investigate how the electronic environment changes, using computational methods since there is such limitation using nuclear magnetic resonance techniques.

## Concluding remarks

The experimental results highlight the sensitivity of the  $^{195}\text{Pt}$  chemical shift in the solid-state. The  $^{195}\text{Pt}$  chemical shielding measurements of the  $(\text{Rb})_2\text{PtCl}_6$ ,  $(\text{NH}_4)_2\text{PtCl}_6$  and  $[\text{N}(\text{CH}_3)_4]_2\text{PtCl}_6$  salts, performed as a function of temperature display unique variation trends upon changing the cation in the *dication hexachloroplatinate(IV)* salts (see Figures 4.10b, 4.15b and 4.23). The Pt-Cl bond lengths obtained from the SCXRD measurements performed as a function of temperature on the  $(\text{Rb})_2\text{PtCl}_6$  and  $(\text{NH}_4)_2\text{PtCl}_6$  salts were used to predict the expected  $^{195}\text{Pt}$  chemical shift sensitivity. The expected  $^{195}\text{Pt}$  chemical shielding calculated from SCXRD analysis were in good agreement to that of the experimental  $^{195}\text{Pt}$  chemical shift sensitivity of the  $(\text{Rb})_2\text{PtCl}_6$  and  $(\text{NH}_4)_2\text{PtCl}_6$  salts over the experimental temperature range at which these SSNMR experiments were conducted. In gas-phase<sup>1</sup> and solution<sup>2,42-43</sup> the Pt-Cl bond displacement within the  $[\text{PtCl}_6]^{2-}$  anion have been shown to have a significant impact on the  $^{195}\text{Pt}$  chemical shift. This study has shown that Pt-Cl bond displacement is one of the key factors responsible for the sensitivity of  $^{195}\text{Pt}$  chemical shielding in the solid state. The experimental temperature coefficients for  $\text{Rb}_2\text{PtCl}_6$  (0.362 (0.008) ppm/K) and  $(\text{NH}_4)_2\text{PtCl}_6$



(0.228 (0.0126) ppm/K) are very different from one another, nevertheless, these are the first reported temperature coefficients for  $^{195}\text{Pt}$  chemical shifts in the solid state.

The quadrupolar coupling from  $^{35}\text{Cl}/^{37}\text{Cl}$  nuclei affecting the  $^{195}\text{Pt}$  and neighbouring nuclei in these *dication hexachloridoplatinate(IV)* is the dominant interaction contributing to the overall chemical shielding (see Figure 4.7). To date, nuclei with such large quadrupolar coupling are experimentally difficult or sometimes impossible to measure using SSNMR with nuclei having quadrupolar coupling constants of  $< 10\text{MHz}$ . Even measuring  $^{35}\text{Cl}$  quadrupolar nuclei with  $< 10\text{MHz}$  requires large non-commercial magnetic fields in the giga-Hertz range. This makes the computation of such large quadrupolar nuclei quite attractive in addition to computing how subtle changes in the electronic structures of a crystal lattice can influence chemical shielding. These subtle effects are difficult to investigate by means of SSNMR alone, so the use of quantum mechanical calculations might shed some light on this matter.

In Chapter 3, we discussed the SCXRD measurements as a function of temperature for the  $(\text{Rb})_2\text{PtCl}_6$ ,  $(\text{NH}_4)_2\text{PtCl}_6$  and  $[\text{N}(\text{CH}_3)_4]_2\text{PtCl}_6$  salts. The atomic coordinates obtained from SCXRD measurements performed as a function of temperature can now be imported into a solid state Density Functional Theory (DFT) computational software interface. The quantum mechanical properties can be calculated from the atomic coordinates, which would give additional insights into the quantum mechanical properties and how they are affected upon lattice expansion as a function of temperature. The following chapter will deal with the quantum mechanical changes happening within a crystal lattice during lattice expansion. The following chapter will only look at the quantum mechanical properties of the  $(\text{Rb})_2\text{PtCl}_6$  and  $(\text{NH}_4)_2\text{PtCl}_6$  salts since the  $[\text{N}(\text{CH}_3)_4]_2\text{PtCl}_6$  salts undergoes multiple structural phase transitions as a function of temperature. The solid state NMR parameters of these salts will also be computed and compared with the experimental measurements done in this chapter.

The chapter that follows examines computed SSNMR chemical shielding tensors and electrostatic potentials of  $\text{Rb}_2\text{PtCl}_6$  and  $(\text{NH}_4)_2\text{PtCl}_6$  salts as a function of increasing temperature. The experimental solid state nuclear magnetic resonance (SSNMR) measurement performed in Chapter 4 gives the overall isotropic chemical shielding, which does not include individual chemical shielding



parameters *i.e.* chemical shift, spin-rotation, dipole-dipole, J-coupling and quadrupolar coupling. The three *dication hexachloridoplatinate (IV)* salts,  $\text{Rb}_2\text{PtCl}_6$ ,  $(\text{NH}_4)_2\text{PtCl}_6$  and  $[\text{N}(\text{CH}_3)_4]_2\text{PtCl}_6$  contain all of the above mentioned chemical shielding parameters, making it difficult to extract individual parameters from experimentally performed SSNMR measurement. In this chapter, a DFT approach is taken to extract isotropic shielding parameters and quadrupolar coupling parameters from single crystal X-ray diffraction (SCXRD) data. The software cannot account for all shielding parameters such as spin-rotation, dipole-dipole and J-coupling as the functionals have not yet been developed in this DFT software. This chapter also investigates the electrostatic potentials in these salts, giving insight into the electronic charge distribution of the atoms in these salts as a function of increasing temperature using semi-empirical quantum mechanical formulism.

## References

1. M. R. Burger, J. Kramer, H. Chermette, K. R. Koch, *Magn. Reson. Chem.*, **2010**, 48, S38.
2. C. J. Jameson, A. K. Jameson, *J. Phys. Chem.* **1986**, 85, 5484.
3. I. I. Rabi, J. R. Zacharias, S. Millman, P. Kusch, *Phys. Rev.*, **1938**, 53, 318.
4. F. Bloch, W. W. Hansen, M. Packard, *Phys. Rev.*, **1946**, 70, 474.
5. E. M. Purcell, H. C. Torrey, R. V. Pound, *Phys. Rev.*, **1946**, 69, 37.
6. B. V. Rollin, *Nature*, **1946**, 158, 669.
7. S. A. O'Reilly, P. S. White, J. L. Templeton, *J. Am. Chem. Soc.*, **1996**, 118, 5684.
8. R. K. Harris, I. J. McNaught, P. Reams, K. J. Packer, *Magn. Reson. Chem.*, **1991**, 29, S60.
9. L. Reven, *J. Mol. Catal.* **1994**, 86, 447.
10. H. Rüegger, D. Moskau, *Magn. Reson. Chem.*, **1991**, 29, S11.
11. W. P. Power, R. E. Wasylshen, *Inorg. Chem.*, **1992**, 31, 2176.
12. J. Herzfeld, A. E. Berger, *J. Chem. Phys.*, **1980**, 73, 6021.
13. B. A. Demko, R. E. Wasylshen, *Inorg. Chem.*, **2008**, 47, 2786.
14. S. Hayashi, K. Hayamizu, *Magn. Reson. Chem.*, **1992**, 30, 658.
15. P. Pyykkö, *Mol. Phys.*, **2008**, 106, 1965.
16. P. P. Man, in 'Encyclopedia of Magnetic Resonance', eds D. M. Grant and R. K. Harris, Wiley: Chichester, **1996**, pp. 3838.
17. M. H. Levitt, *Spin Dynamics, Basics of Nuclear Magnetic Resonance*, **2008**, Wiley.
18. E. R. Andrew, A. Bradbury, R. G. Eades, *Nature*, **1958**, 182, 1659.
19. I. J. Lowe, *Phys. Rev. Lett.*, **1959**, 2, 285.
20. E. R. Andrew, *Philos. Trans. R. Soc. London Ser. A*, **1981**, 299, 505.
21. A. Pines, M. G. Gibby, J. Schaefer, J. S. Waugh, *J. Chem. Phys.*, **1973**, 59, 569.
22. J. Schaefer, E. O. Stejskal, *J. Amer. Chem. Soc.*, **1976**, 98, 1031.

- 
23. D. Massiot, F. Fayon, M. Capron, I. King, S. Le Calvé, B. Alonso, J. O. Durand, B. Bujoli, Z. Gan, G. Hoatson, *Magn. Reson. Chem.*, **2002**, 40, 70.
  24. L. A. O'Dell, K. J. Harris, R. W. Schurko, *J. Magn. Reson.*, **2010**, 203, 156 P. K. Madhu, K. J. Pike, R. Dupree, M. H. Levitt, M. E. Smith, *Chem. Phys. Lett.*, **2003**, 367, 150.
  25. M. J. Thrippleton, T. J. Ball, and S. Wimperis, *J. Chem. Phys.*, **2008**, 128, 34507.
  26. P. K. Madhu, K. J. Pike, R. Dupree, M. H. Levitt, M. E. Smith, *Chem. Phys. Lett.*, **2003**, 367, 150.
  27. G. Peters, W. Preetz, T. Schaller, A. Sebald, *J. Magn. Reson. Series A*, **1996**, 120, 121.
  28. R. K. Harris, E. D. Beckers, S. M. Cabral de Menezes, R. Goodfellow, P. Granger, *Pure Appl. Chem.*, **2001**, 78, 1759.
  29. I. M. Ismail, S. J. S. Kerrison, P. J. Sadler, *J. Chem. Soc., Chem. Commun.*, **1980**, 1175.
  30. W. Preetz, G. Peters, D. Bubltz, *Chem. Rev.*, **1996**, 96, 977.
  31. C. J. Jameson, A. K. Jameson, D. Oppusunggu, *J. Chem. Phys.*, 1986, **85**, 5480.
  32. C. J. Jameson, D. Rehder, M. Hoch, *J. Am. Chem. Soc.*, **1987**, 109, 2589.
  33. W. J. Gerber, P. Murray, K. R. Koch, *Dalton. Trans.*, **2008**, 4113.
  34. A. C. Olivieri, *J. Magn. Reson.*, **1989**, 81, 201.
  35. N. J. Baxter, M. P. Williamson, *J. Biomol. NMR*, **1997**, 9, 359.
  36. R. L. Armstrong, *Phys. Letters*, **1980**, 57, 343.
  37. J.O. Hernandez, E. A. Choren, *Thermochim. Acta*, **1983**, 71, 265.
  38. R. D. Weir, E. F. Westrum JR, *J. Chem. Thermodynamics*, **1991**, 23, 653.
  39. D. Borchers, A. Weiss, *Ber. Bunsenges. Phys. Chem.*, **1989**, 93, 559.
  40. L. S. Prabhumirashi, R. Ikeda, D. Nakamura, *Ber. Bunsenges. Phys. Chem.*, **1981**, 85, 1142.
  41. Y. Furukawa, L. Prabhumirashi, R. Ikeda, D. Nakamura, *Bull. Chem. Soc. Jpn.*, **1982**, 55, 995.
  42. J. C. Davis, M. Bühl, K. R. Koch, *J. Chem. Theory Comput.*, **2012**, 345, 2380.
  43. J. C. Davis, M. Bühl, K. R. Koch, *J. Phys. Chem. A.*, **2013**, 117, 8054.

# Chapter 5

## A DFT computational Assessment of the Possible Origin of the Temperature Dependence of the $^{195}\text{Pt}$ shielding in the solid state in $\text{X}_2[\text{PtCl}_6]$ ( $\text{X} = \text{Rb}^+$ and $\text{NH}_4^+$ )

### Synopsis

The recent development of density functional theory (DFT) based first principle computational methods now allows for accurate calculation of solid state nuclear magnetic resonance (SSNMR) parameters from crystallographic data. This chapter entails DFT SSNMR parameters and Hartree-Fock electrostatic potential analyses of  $\text{Rb}_2\text{PtCl}_6$  and  $(\text{NH}_4)_2\text{PtCl}_6$  salt crystal structures as a function of temperature. The gauge-including projector augmented wave (GIPAW) method incorporated in CASTEP software is used to compute all SSNMR parameters. The VAMP computational software uses semi-empirical quantum chemistry methods to compute atomic electrostatic potentials charges of  $\text{Rb}_2\text{PtCl}_6$  and  $(\text{NH}_4)_2\text{PtCl}_6$  crystal structures. The calculated NMR parameters give a detailed account on the behaviour of NMR active nuclei in  $\text{Rb}_2\text{PtCl}_6$  and  $(\text{NH}_4)_2\text{PtCl}_6$  salts upon lattice expansion as a function of temperature. This computational study gives a quantum mechanical account on the origins of experimentally observed temperature dependent  $^{195}\text{Pt}$  chemical shifts in *dication hexachloridoplatinate(IV)* salt. The results from VAMP analyses shed light on the effect that lattice expansion has on electrostatic potentials charges in these salts as a function of temperature. The combined computational methods give a detailed account on the effect temperature has on computed NMR parameters and electrostatic potentials charges from experimental temperature dependent single crystal X-ray diffraction data.

---

## Introduction

---

Nuclear magnetic resonance (NMR) spectroscopy is a phenomenon which occurs when a nucleus with a non-zero spin ( $I \neq 0$ ) is placed within a static magnetic field and subjected to a second oscillating magnetic field. This results in a nuclear spin transition between the Zeeman energy levels. It is the relaxation from the excitation state energy level back to the Zeeman ground state energy level that is detected during a NMR experiment.<sup>1</sup> While NMR techniques are mostly sensitive to local atomic environments, there are situations where long range effects such as atomic ring currents and changes in electrostatic effects can have an influence on experimentally observed NMR spectra. The influence of these effects cannot be extracted by means of conventional SSNMR experiments, which make the use of *ab initio* calculations quite useful to account for additional shielding and magnetic interactions between nuclei in solid state systems.<sup>2,3</sup>

The computational estimation of NMR parameters in large non-crystalline systems can be quite expensive computationally. The inherent properties of a crystalline system on the other hand are symmetry and translational repetition. This means that the environment of the atoms represented within the asymmetric unit are usually repeated throughout the entire crystal structure by a symmetry operator. This property makes it possible to develop relatively computationally inexpensive methods to predict NMR parameters using periodic boundary conditions.<sup>4</sup> The goal of accurate computational predictions of NMR shielding parameters is an ongoing computational challenge but there has been relatively good progress in chemical systems such as molecular crystals,<sup>5</sup> supramolecular assemblies<sup>6</sup> and organometallic compounds.<sup>7</sup>

The computational code in the NMR-CASTEP program (Accelrys, Inc.)<sup>8,9</sup> makes use of a density functional theory (DFT) approach called gauge including projector augmented wave (GIPAW).<sup>2,10</sup> to calculate shielding parameters in molecular crystals. The GIPAW method uses two approaches. The first deals with the quantum mechanical response of electrons to an external applied uniform magnetic field.<sup>9</sup> The second approach used in the GIPAW method makes use of

pseudo-potentials,<sup>11</sup> which represent an interaction between core and valence states orbitals. The pseudo-potentials used in the GIPAW methods remove the core electrons from the calculation, together with “smoothing” of valence electron wave functions at the nucleus of the atoms in question.<sup>12</sup> The group of Car *et al.*<sup>13</sup> demonstrated that core electron wave functions are not significantly altered by changes in chemical bonding, therefore do not contribute significantly to the shielding of nuclei in an externally applied magnetic field. They propose that the behaviour of the outer valence wave functions which are relatively close to the nucleus are essential in describing chemical shielding. The projected augmented wave (PAW) method developed by van der Walle and Blochl<sup>14</sup> allows for the reconstruction of all electron wave functions from their pseudo wave function equivalents, which accounts for the removal of core electrons from the calculation. The GIPAW method is an extension of the PAW<sup>13</sup> method for calculating NMR shielding parameters and is widely used by the experimental community.

One of the main reasons for using the DFT-GIPAW periodic approach in this study is because all NMR parameters can be obtained from a single calculation. All the atomic sites within the crystal structure are taken into account. Effects such as delocalization of the electronic states and electrostatic effects are accounted for, allowing for the reasonably accurate extraction of SSNMR parameters such as isotropic shielding, chemical shielding anisotropic, and quadrupolar coupling. Although electrostatic effects can also be extracted using very specialized pulse sequences in SSNMR experiments, they require the nuclei in question to have a quadrupole moment ( $Qm$ ) with a nuclear spin  $I > \frac{1}{2}$ . Such quadrupolar nuclei interact with their electric field gradients (EFG), an interaction known as quadrupolar coupling ( $C_Q$ ). The quadrupolar coupling interaction measures the change which occurs around an atom's electric field gradient. It is not possible to obtain any information on electrostatic effects of non-quadrupolar nuclei by means of SSNMR spectroscopy. The  $H$  atom with nuclear spin  $\frac{1}{2}$  is unique as it interacts with its EFG in a way that is similar to quadrupolar nuclei. The first to report this was Russian physicist Berestetski<sup>15</sup> and various other authors,<sup>16,17,18,19</sup> who calculated the  $H$  atom quadrupolar coupling interaction.

The electrostatic atomic potential calculations performed in this study were carried out with Material Studio, VAMP<sup>20</sup> (Accelrys, Inc.) which incorporates VESRPA<sup>21</sup> software; a semi-empirical quantum chemistry method based on the Hartree-Fock formalism. This method was used in combination with the NDDO<sup>22</sup> and PM6<sup>23</sup> Hamiltonians to calculate electrostatic potentials charges of *dication hexachloridoplatinate(IV)* salts. The electrostatic potentials charges of all atoms within these salts were computed to investigate the origin of the effect that temperature has on these crystal structures, as a function of temperature.

The crystallographic coordinates obtained from variable temperature SCXRD measurements on  $\text{Rb}_2\text{PtCl}_6$  and  $(\text{NH}_4)_2\text{PtCl}_6$ , discussed in Chapter 3, were used as inputs for the DFT computations. The NMR-CASTEP and VAMP code implemented in *Material Studio 6.0* (Accelrys, Inc) were used to calculate the quantum mechanically derived electrostatic of the atoms and NMR parameters which show how the *dication hexachloridoplatinate(IV)* salt's crystal structures are affected upon lattice expansion with an increase in temperature. The calculated NMR parameters such as nuclear shielding, electric field gradient (EFG) tensors and electrostatic potentials charges are presented. All the calculated NMR parameters and electrostatic potentials charges of these fourteen crystal structures are presented.<sup>8</sup>

### 5.1 Background definitions of the NMR parameters

The calculation of SSNMR parameters such as chemical shielding anisotropy (CSA) and quadrupolar interactions can be obtained by performing NMR-CASTEP using DFT-GIPAW methods. These calculations allow for the determination of physical tensors elements which are related to NMR interactions (i.e. CSA and EFG). These two tensors can be used to determine a variety of different NMR parameters.

Using the Heaberlen convention<sup>24</sup> the CSA tensor is characterized by 3 parameters, isotropic chemical shielding ( $\sigma_{\text{iso}}$ ) equations (1), the reduced anisotropy ( $\Delta_{\text{CS}}$ ) equations (2) and asymmetry ( $\eta_{\text{CS}}$ ) equations (3), forming the 3 principle components of the CSA tensors

$$\sigma_{\text{iso}} = \frac{1}{3}(\sigma_{11} + \sigma_{22} + \sigma_{33}) \quad (1)$$

$$\Delta_{CS} = \sigma_{33} - \sigma_{iso} \quad (2)$$

$$\eta_{CS} = \frac{\sigma_{22} - \sigma_{11}}{\Delta_{CS}} \quad (3)$$

where the components  $\sigma_{ii}$  are sorted in the following way  $|\sigma_{33} - \sigma_{iso}| \geq |\sigma_{22} - \sigma_{iso}| \geq |\sigma_{11} - \sigma_{iso}|$ ,

The EFG tensor is fully characterized with 2 parameters. Using the Heaberlen convention, we define the 2 parameters of quadrupolar interactions as the quadrupolar coupling constant,  $C_Q$ , and the quadrupolar asymmetry,  $\eta_Q$  (see equation 4 & 5 respectively). These are the 2 principle components which describe the quadrupolar nuclei's interaction with the EFG where ( $V_{\alpha\alpha}$ ,  $\alpha=x, y, z$ ) with  $|V_{zz}| \geq |V_{yy}| \geq |V_{xx}|$  are the dimension of the EFG tensor components.

$$C_Q = \frac{e|QV_{zz}|}{h} \quad (4)$$

$$\eta_Q = \frac{V_{xx} - V_{yy}}{V_{zz}} \quad (5)$$

We present a density functional based method for calculating NMR shielding tensors for 5d Pt, 4p Rb, Cl 3p, N 2p and 1s H nuclei using periodic boundary conditions.

### 5.2 Identification of NMR parameters from SSNMR spectra

This section will not cover the entire breadth of examples but will focus on the type of characteristics relevant to this particular study. The isotropic shielding ( $\sigma_{iso}$ ) parameters are often not so easy to identify with static SSNMR experiments. Even under magic angle spinning (MAS) conditions, the  $\sigma_{iso}$  spectral line could be among various spinning sidebands (see Fig. 5.1). Conventionally, upon varying the spinning speed at which a MAS experiment is conducted, the positions of the spinning sidebands change to the adjusted spinning speeds relative to the  $\sigma_{iso}$  position. The  $\sigma_{iso}$  parameter will stay unchanged, which usually serves as a good method for identification of the  $\sigma_{iso}$  parameter. This method usually works well in systems where the nucleus under investigation does not have large chemical shift anisotropy.

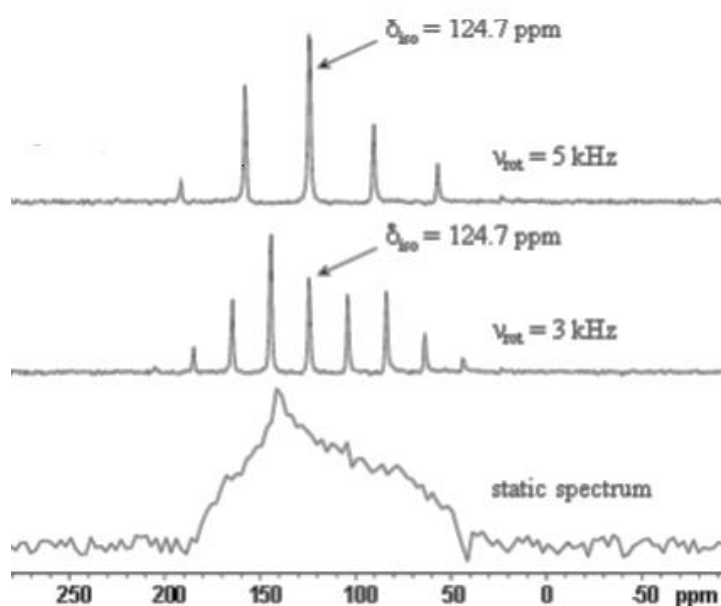


Figure 5. 1 Isotropic chemical shift of  $^{85}\text{Rb}$  isotope at difference spinning speeds illustrating that increase in spinning speed increases spectral resolution.

In the solid state  $^{35/37}\text{Cl}$  nuclei are well known to have large chemical shift anisotropy making the identification of the  $\sigma_{\text{iso}}$  parameter somewhat problematic. One of the advantages in this study is the fact that the *dication hexachloridoplatinate(IV)* salts under investigation adopt a cubic symmetry which makes the asymmetry ( $\eta_{\text{CS}}$ ) parameter of this nuclei equate to zero. This makes the identification of the  $\sigma_{\text{iso}}$  parameter easier to identify in  $^{35}\text{Cl}$  spectra (Fig. 5.2) of this nature. The reduced anisotropy parameter ( $\Delta_{\text{CS}}$ ) and the quadrupolar coupling interaction is shown on the  $^{35}\text{Cl}$  SSNMR spectra of a *dication hexachloridoplatinate(IV)* salts (Fig. 5.2).

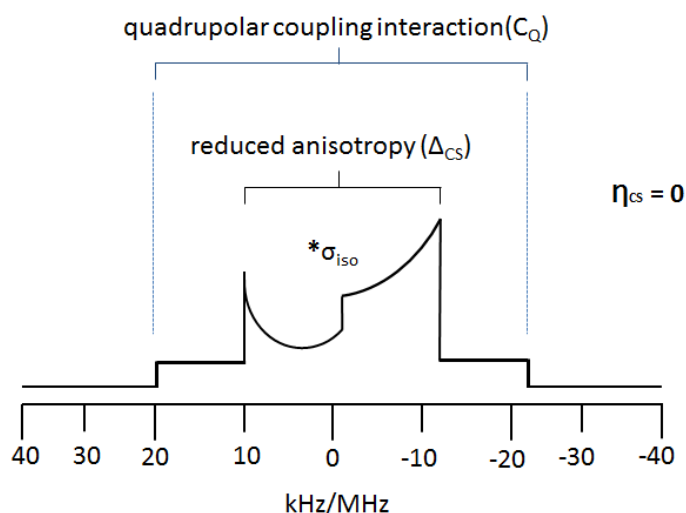


Figure 5. 2 Displaying isotropic chemical shielding ( $\sigma_{\text{iso}}$ ) and reduced anisotropy parameter ( $\Delta_{\text{CS}}$ ) quadrupolar interaction from a  $^{35}\text{Cl}$  SSNMR spectra of a dication hexachloroplatinte salts with ( $\eta_{\text{CS}}$ )=0.



The quadrupolar coupling ( $C_Q$ ) interaction can be quantified by measuring the entire width of the spectra (see Fig. 5.2.). It is quite clear from Fig. 5.3 how the quadrupolar coupling interaction increases and how this is affecting the line broadening of this spectrum.

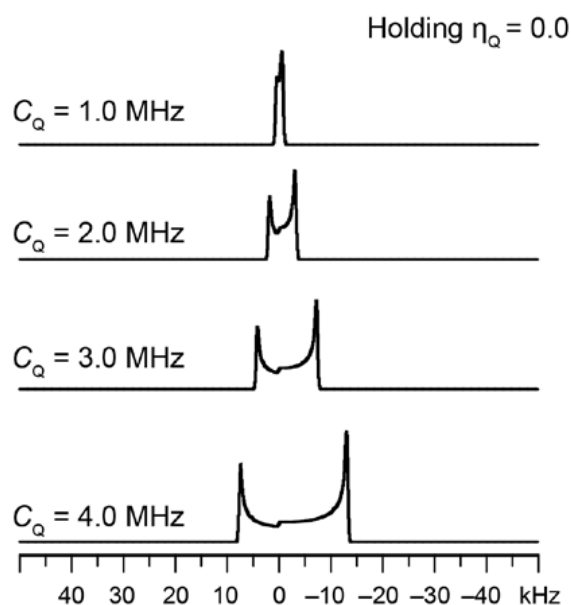


Figure 5.3 Increasing the quadrupolar coupling interaction have an effect on the reduced anisotropy of the spectra

## Experimental

The  $\text{Rb}_2\text{PtCl}_6$  and  $(\text{NH}_4)_2\text{PtCl}_6$  salts were synthesized as described in Chapter 3 and the crystal structures of  $\text{Rb}_2\text{PtCl}_6$  and  $(\text{NH}_4)_2\text{PtCl}_6$  salts were determined at various temperatures using single crystal X-ray diffraction (SCXRD). The atomic coordinates of fourteen crystal structures collected over a 100 K to 400 K with 50 K intervals were used to perform the DFT quantum mechanical calculations. The atomic positions in the seven  $\text{Rb}_2\text{PtCl}_6$  crystal structures were not geometrically optimized. Since H atoms cannot reliably be located using X-ray diffraction,<sup>25</sup> geometry optimizations were performed on all seven  $(\text{NH}_4)_2\text{PtCl}_6$  crystal structures using the NMR-CASTEP program. The crystallographic positions of the heavier atoms in these structures e.g. Pt, Cl and N ions were fixed and only the hydrogen ions were geometrically optimized. The coordinates and

method of geometric optimization performed on these crystal structures together with the optimized structure can be found in the Appendix D.

It is importance to be aware that computational simulations are usually carried out for a static molecular situation at 0 K, which is clearly not entirely realistic for comparison to experimental NMR and XRD measurements in this study. The CASTEP computations allows for the adjustment of the unit cell dimensions, which in this study is of utmost importance since SSNMR and SCXRD measurement were performed as a function of temperature. This compensation accounts for the difference in degree of vibration at different temperatures in the crystal lattice. The results obtained from SCXRD measurements performed as a function of temperature of the  $\text{Rb}_2\text{PtCl}_6$  salts (Chapter 3, Figure 3.4a) and  $(\text{NH}_4)_2\text{PtCl}_6$  (Chapter 3, Figure 3.9a) showing the lattice expansion of the unit cells, produced two reasonable linear slope equations ( $y = 0.0005x + 9.77$ ,  $R^2 = 0.979$  and ( $y = 0.0005x + 9.7253$ ,  $R^2 = 0.999$ ) respectively. These equations can be used to adjust the unit cell parameters in the CASTEP program, in order to correct the unit cell dimensions to that of the experimental temperature at which the experiments were conducted. If we take the  $(\text{NH}_4)_2\text{PtCl}_6$  structure collected at 100 K and use the equation obtained from the plotted unit cell dimension ( $y = 0.0005x + 9.7253$ ,  $R^2 = 0.999$ ), the equation can take on a new form  $(y_{(100\text{ K})} - y_{(0\text{ K})}) = 0.0005(x_{(100\text{ K})} - x_{(0\text{ K})}) + 9.7253$ . Using this equation we could now adjust the computational lattice parameters to that at which the experimental parameters were collected, allowing for the computational simulation of lattice vibration to that of the experimental conditions (see Appendix D for full details on all unit cell adjustments).

### 5.3 Convergence of computed NMR parameters

The convergence of any computational calculation is of utmost importance. The NMR parameters such as isotropic chemical shielding ( $\sigma_{\text{iso}}$ ), chemical shielding anisotropy ( $\Delta_{\text{CS}}$ ) and quadrupolar coupling ( $C_Q$ ) are checked if these parameters converge. The atomic coordinates obtained from the  $\text{Rb}_2\text{PtCl}_6$  crystal structure collected at 100 K are used to test the computational convergence of NMR parameters. The results obtained from these convergence optimization calculations can be applied to the  $(\text{NH}_4)_2\text{PtCl}_6$  crystal structures, since it has the same space group and similar to the  $\text{Rb}_2\text{PtCl}_6$  salt, it is an anti-fluorite type crystal structure.

The convergences of computed NMR parameters were tested using generalized gradient approximation (GGA)<sup>26,27</sup> with Perdew, Burke and Ernzerhof (PBE)<sup>28</sup> functional for solid state systems. The convergence of NMR parameters mainly depends on the kinetic energy cutoff ( $E_{\text{cut}}$ ) and Monkhorst–Pack k-point mesh.<sup>29</sup> The  $E_{\text{cut}}$  determines the size of the basis set used for expansion of the electronic wave function. The  $E_{\text{cut}}$  value is strongly related to the atomic composition of the system in question. The  $E_{\text{cut}}$  value used during the convergence of our chemical system is  $E_{\text{cut}} = 800\text{eV}$ . The reason for selecting this value is because the  $^{195}\text{Pt}$  nucleus has not been computed with CASTEP-NMR calculations to date. The  $^{95}\text{Mo}$  nucleus has recently been studied by CASTEP-NMR computational methods and these results have shown excellent agreement to experimentally observed SSNMR measurements.<sup>30</sup> They used an  $E_{\text{cut}} = 600\text{eV}$  to perform the calculations for the  $^{95}\text{Mo}$  nucleus. Since the  $^{195}\text{Pt}$  nucleus is a much heavier atom than the  $^{95}\text{Mo}$  nucleus, the  $E_{\text{cut}} = 800\text{eV}$  was used to perform our experiments. It could be possible that the NMR parameters could converge at  $E_{\text{cut}} < 800\text{ eV}$ , which can decrease the computational cost but we opted to use this value at  $800\text{eV}$ .

The Monkhorst–Pack k-point mesh relies on the integration of the Brillouin zone. We use seven different k-point mesh values ranging from  $(1 \times 1 \times 1)$  to  $(7 \times 7 \times 7)$  to check for convergence at  $E_{\text{cut}} = 800\text{eV}$  for all nuclei ( $^{195}\text{Pt}$ ,  $^{85}\text{Rb}$  and  $^{35}\text{Cl}$ ). The NMR parameters have fully converged from k-point mesh  $(4 \times 4 \times 4)$  onward for  $^{195}\text{Pt}$   $\sigma_{\text{iso}}$ ,  $^{85}\text{Rb}$   $\sigma_{\text{iso}}$ ,  $^{35}\text{Cl}$   $\sigma_{\text{iso}}$  and  $^{35}\text{Cl}$  ( $\Delta_{\text{CS}}$ ) (see Fig. 5.4, a, b and c respectively). The quadrupolar coupling ( $C_Q$ ) parameter fully converged from  $(4 \times 4 \times 4)$  (see Fig. 5.4d). The NMR parameters all fully converge from  $(4 \times 4 \times 4)$  k-point mesh. Even though the convergence of the NMR parameters at  $E_{\text{cut}} = 800\text{ eV}$  and  $(4 \times 4 \times 4)$  k-point mesh were reached, a higher  $(7 \times 7 \times 7)$  k-point mesh was used for the  $\text{Rb}_2\text{PtCl}_6$ . This was mainly done since the NMR parameters for the  $^{195}\text{Pt}$  nucleus have not previously been computed using CASTEP. Another point of reference used when considering increasing the k-point mesh for our system was from the work done by Hanna *et al.*<sup>31</sup> They computed  $^{93}\text{Nb}$  SSNMR parameters for the  $\text{LiNbO}_3$  crystal structure and used a  $(6 \times 6 \times 6)$  k-point mesh; since the  $^{195}\text{Pt}$  nucleus is considerably heavier atom  $(7 \times 7 \times 7)$  k-point mesh were used.

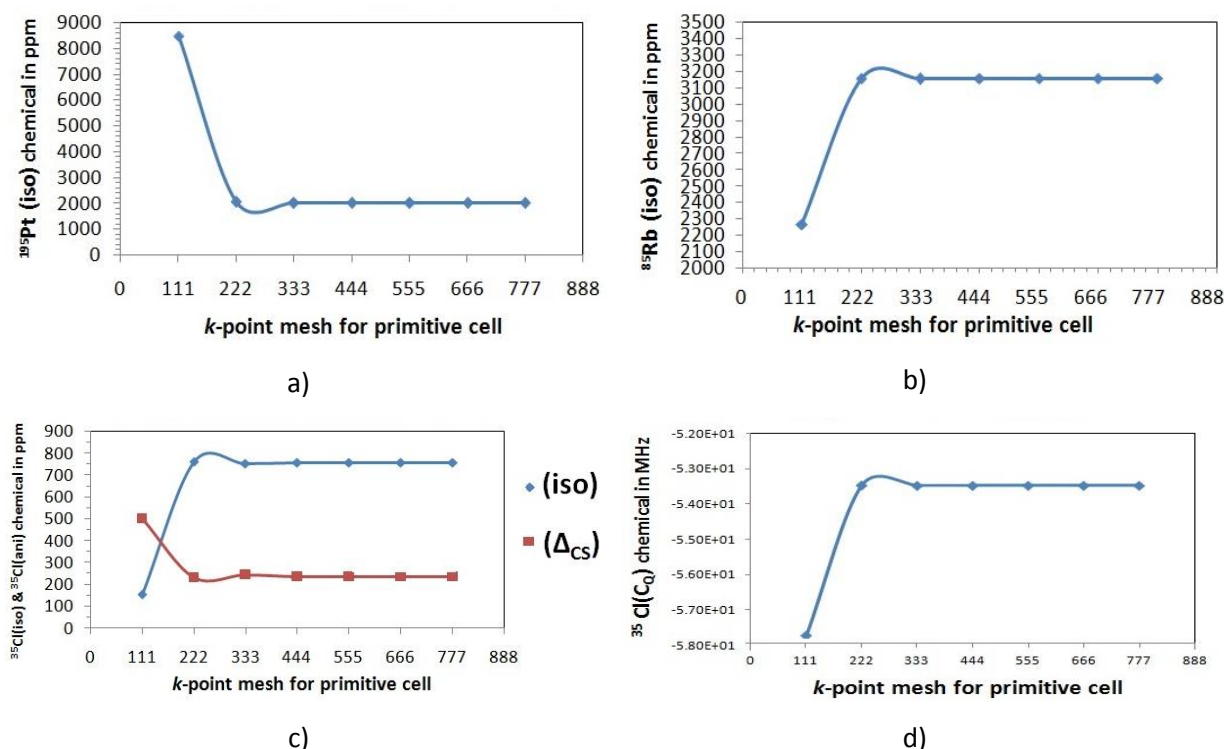


Figure 5. 4 Convergence NMR parameters a)  $^{195}\text{Pt}\sigma_{\text{iso}}$  chemical shift in ppm, b)  $^{85}\text{Rb}\sigma_{\text{iso}}$  chemical shift in ppm c)  $^{35}\text{Cl}\sigma_{\text{iso}}$  and  $^{35}\text{Cl}(\Delta_{\text{CS}})$  chemical shift in ppm and d)  $^{35}\text{Cl}(C_Q)$  quadrupolar coupling in MHz

The optimum convergence parameters selected for first principle DFT-NMR calculations for  $\text{Rb}_2\text{PtCl}_6$  and  $(\text{NH}_4)_2\text{PtCl}_6$  crystal structures were at  $E_{\text{cut}} = 800$  eV and k-point mesh (7 x 7 x 7). The NMR-CASTEP computations used GGA functional, PBE, revised Perdew Burke and Ernzerhof (RPBE),<sup>32</sup> Perdew and Wand 1991 (PW91),<sup>33</sup> Wu-Cohen (WC)<sup>34</sup> and revised Perdew Burke and Ernzerhof for solids (PBESOL)<sup>35</sup> to compute SSNMR parameters. The calculation would also be a good test to monitor the suitability of these functionals on a system containing  $^{195}\text{Pt}$  nuclei.

## Results and Discussions

### 5. 4 NMR-CASTEP Computational results of $^{195}\text{Pt}$ shielding of $(\text{NH}_4)_2\text{PtCl}_6$ and $\text{Rb}_2\text{PtCl}_6$

The computed  $^{195}\text{Pt}$  ( $\sigma_{\text{iso}}$ ) shielding tensor of  $(\text{NH}_4)_2\text{PtCl}_6$  salt (Fig. 5.5) is increases as a function of temperature between 100 K and 150 K, it then decreases to 350 K. The  $^{195}\text{Pt}$  ( $\sigma_{\text{iso}}$ ) shielding tensor

at 400 K is drastically increases in its calculated  $^{195}\text{Pt}$  ( $\sigma_{\text{iso}}$ ) shielding tensor. The overall performance of the various GGA functionals have similar behaving  $^{195}\text{Pt}$  ( $\sigma_{\text{iso}}$ ) shielding trends over the entire temperature range (Fig. 5.5).

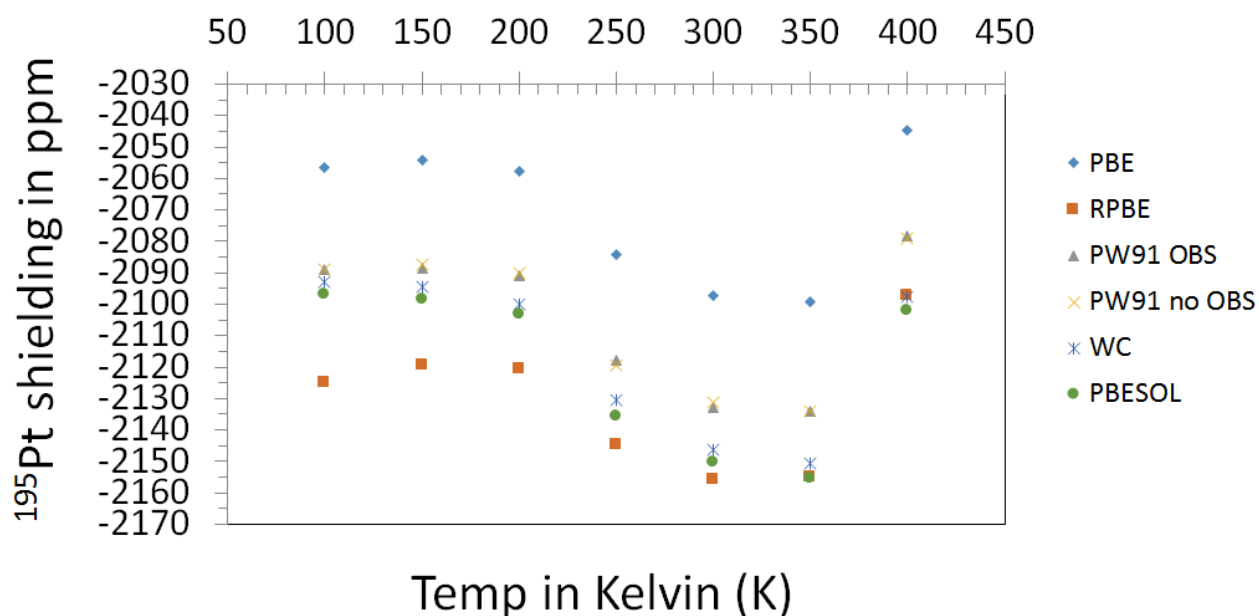


Figure 5. 5 The  $^{195}\text{Pt}$  ( $\sigma_{\text{iso}}$ ) shielding trends of  $(\text{NH}_4)_2\text{PtCl}_6$  salts as a function of temperature

The computed  $^{195}\text{Pt}$  ( $\sigma_{\text{iso}}$ ) shielding tensor (Fig. 5.6) of the  $\text{Rb}_2\text{PtCl}_6$  salt performed as a function of temperature shows that the tensor is increasing as a function of increasing temperature. All the various GGA functionals employed to calculate the  $^{195}\text{Pt}$  ( $\sigma_{\text{iso}}$ ) shielding show similar trends over the entire temperature range. The  $^{195}\text{Pt}$  ( $\sigma_{\text{iso}}$ ) shielding trends of the  $\text{Rb}_2\text{PtCl}_6$  salt (Fig. 5.6) have much less discrepancies between the calculated  $^{195}\text{Pt}$  ( $\sigma_{\text{iso}}$ ) shielding trends relative to what GGA functional was used compared to that of the of  $(\text{NH}_4)_2\text{PtCl}_6$  salts (Fig. 5.5).

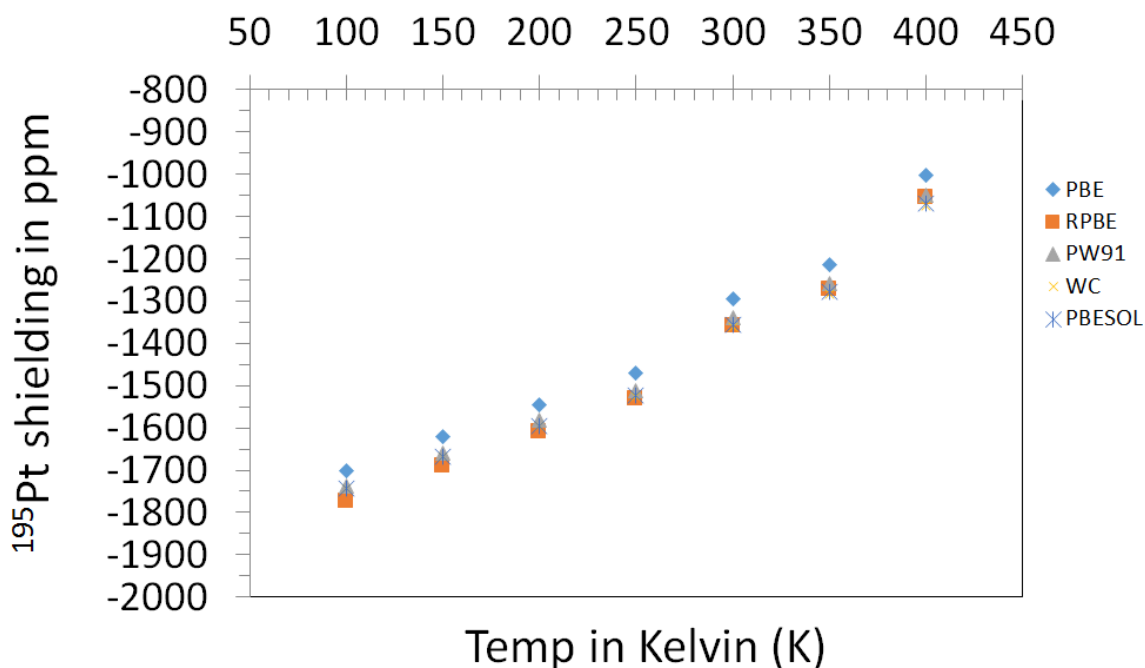


Figure 5. 6 The  $^{195}\text{Pt}$  ( $\sigma_{\text{iso}}$ ) shielding trends of  $\text{Rb}_2\text{PtCl}_6$  ( $\text{NH}_4$ )<sub>2</sub> $\text{PtCl}_6$  salts as a function of temperature

One thing to note before discussing DFT-NMR computational data is the subject of selecting a suitable reference with which one can compare experimentally observed chemical shift parameters to computed shielding parameters. In our SSNMR experiments we used solutions as a reference for the  $^{195}\text{Pt}$  nucleus (1.2 M  $\text{Na}_2\text{PtCl}_6$  in  $\text{D}_2\text{O}$ )<sup>36</sup> and  $^{85}\text{Rb}$  nucleus (0.01 M  $\text{RbCl}$  in  $\text{D}_2\text{O}$ )<sup>36</sup>. Since we use a chemical reference our experimental shielding in an external magnetic field are termed the chemical shielding (chemical shift).

In our computational model we do not use an external reference, the NMR-CASTEP software calculates the nucleus overall shielding in an externally applied magnetic field resulting in the overall isotropic shielding of this nucleus. Our experimental  $^{195}\text{Pt}$  chemical shift measurements are relative to a reference at 0 = ppm. The computed  $^{195}\text{Pt}$  isotropic shielding parameters are measured as the overall shielding of  $^{195}\text{Pt}$  nucleus which is a sign independent measurement as it could be of a positive or a negative value. If we assume the calculated  $^{195}\text{Pt}$  isotropic shielding as a function of temperature to be negative value, then the  $^{195}\text{Pt}$  isotropic shielding of the  $\text{Rb}_2\text{PtCl}_6$  salt is becoming more positive as a function of increasing temperature. The computed  $^{195}\text{Pt}$  isotropic shielding parameters of the  $(\text{NH}_4)_2\text{PtCl}_6$  salt have quite a different trends the  $^{195}\text{Pt}$  isotropic shielding initially increasing from 100 K – 150 K, it then decreases from

200 K – 350 K and at 400 K a sudden increase is observed. This was quite a puzzling observation as many factors could influence the  $^{195}\text{Pt}$  isotropic shielding in the  $(\text{NH}_4)_2\text{PtCl}_6$  salt in the solid state. One of the main factors is the influence of the computed quadrupolar coupling constants ( $C_Q$ ) from both  $^{37/37}\text{Cl}$  isotopes and its influence on the computed  $^{195}\text{Pt}$  isotropic shielding. This is a factor that cannot be excluded since the contribution of the quadrupolar coupling of covalently bound  $\text{Cl}^-$  ion to the  $\text{Pt}^{\text{IV}}$  ion is  $> 50 \text{ MHz}$ .<sup>37</sup> This is among the highest known quadrupolar coupling constants and it is well known that this has the greatest influence on the overall observed NMR shielding if it is in close proximity to other SSNMR active nuclei. This topic is discussed at length later in this chapter. The other factor is the geometrical optimization of the hydrogen ion of the  $(\text{NH}_4)^+$  cation. If these hydrogen ions are not correctly geometrically optimized in all seven  $(\text{NH}_4)_2\text{PtCl}_6$  salt crystal structures it will surely influence the end result of computed SSNMR parameters. It is well known that dispersion correction functionals also influence accuracy of calculations containing hydrogen atom/ions as it accounts for long range London forces which play a subtle but important role in a huge variety of hydrogen atoms/ion systems. The selection of a suitable dispersion correctional functional that would account for the influence of long range hydrogen bonding interaction in systems such as the  $(\text{NH}_4)_2\text{PtCl}_6$  salt is therefore of utmost importance.

There is quite a difference in  $^{195}\text{Pt}$  ( $\sigma_{\text{iso}}$ ) shielding sensitivity observed in computed temperature dependent trends of  $\text{Rb}_2\text{PtCl}_6$  salt relative to that of  $(\text{NH}_4)_2\text{PtCl}_6$  salt. Comparing the calculations done with the GGA, PBE functional within the temperature range of 100 K to 400 K. The computed  $^{195}\text{Pt}$  ( $\sigma_{\text{iso}}$ ) shielding sensitivity of the  $\text{Rb}_2\text{PtCl}_6$  salt is 701.24 ppm whereas the  $(\text{NH}_4)_2\text{PtCl}_6$  salt is 12.0 ppm. The experimental temperature dependence  $^{195}\text{Pt}$  chemical shift sensitivity in the  $(\text{NH}_4)_2\text{PtCl}_6$  salt (57.8 ppm) was lower than that of the  $\text{Rb}_2\text{PtCl}_6$  salts (98.5 ppm). The calculated temperature dependence  $^{195}\text{Pt}$  ( $\sigma_{\text{iso}}$ ) shielding trends of the  $\text{Rb}_2\text{PtCl}_6$  salts resemble that of the experimental observed temperature dependence  $^{195}\text{Pt}$  ( $\sigma_{\text{iso}}$ ) chemical shift trend. The computed temperature dependence  $^{195}\text{Pt}$  ( $\sigma_{\text{iso}}$ ) shielding trend of the  $(\text{NH}_4)_2\text{PtCl}_6$  salt is quite different to that of the experimentally observed  $^{195}\text{Pt}$  ( $\sigma_{\text{iso}}$ ) chemical shift trends. Upon close examination of the  $(\text{NH}_4)_2\text{PtCl}_6$  crystal structure at 400 K, it is clear that the hydrogen bond ( $\text{Pt}-\text{Cl}\cdots\text{H}-\text{N}$ ) is much weaker than that at 100 K, which is as a result of lattice expansion with an increase in temperature. If we assume that the hydrogen bonding ( $\text{Pt}-\text{Cl}\cdots\text{H}-\text{N}$ ) interaction has an influence on the  $^{195}\text{Pt}$  isotropic shielding via the  $\text{Cl}^-$  ion, then surely the effect that hydrogen

bonding has on the  $\text{Cl}^-$  ion, which is translated to the  $\text{Pt}^{\text{IV}}$  ion, can be affected as the interaction is weakened. An attempt was made to investigate the average cut-off distance of hydrogen bonding interactions between metal chlorides and ammonium fragments ( $\text{M}-\text{Cl}\cdots\text{H}-\text{N}$ ) using CSD database. It was, however, difficult to compare hydrogen bonding distances using CSD data, which were collected at different temperatures, since lower temperature is usually preferred over high temperatures for doing single crystal X-ray diffraction data collections. The DFT-NMR calculations done on the  $(\text{NH}_4)_2\text{PtCl}_6$  salt used a dispersion correction Ortmann, Bechstedt and Schmidt (OBS)<sup>38</sup> which has been shown<sup>39</sup> not to be so effective over a long range especially for a heavier metal atom. This could be one reason why, after a certain distance the effect with which hydrogen bonding to the  $\text{Cl}^-$  ion, which is translated to the  $\text{Pt}^{\text{IV}}$  ion in  $(\text{NH}_4)_2\text{PtCl}_6$  cannot be taken into account when computing the  $^{195}\text{Pt}$  ( $\sigma_{\text{iso}}$ ) shielding at 400 K.

The efficiency of computational calculations is conventionally tested by plotting computed against experimental NMR parameters.<sup>40,41</sup> If the plot is linear related it is usually a good indication of the accuracy and plausibility of the computational results and method. The computed  $^{195}\text{Pt}$  ( $\sigma_{\text{iso}}$ ) shielding of the GGA, PBE functional is plotted against the experimental  $^{195}\text{Pt}$  chemical shift of the  $\text{Rb}_2\text{PtCl}_6$  (Fig. 5.7) and  $(\text{NH}_4)_2\text{PtCl}_6$  (Fig. 5.8) salts. The plot of the  $\text{Rb}_2\text{PtCl}_6$  salts shows that experimental  $^{195}\text{Pt}$  chemical shift and computed  $^{195}\text{Pt}$  ( $\sigma_{\text{iso}}$ ) shielding are increasing as a function of increasing temperature. The experimental  $^{195}\text{Pt}$  chemical shift of the  $(\text{NH}_4)_2\text{PtCl}_6$  is increasing as a function of increasing temperature but the computed  $^{195}\text{Pt}$  ( $\sigma_{\text{iso}}$ ) shielding parameters is displaying quite unusual trends, which is not reflecting what is observed from experimentally trends. The above discussed influences of quadrupolar coupling, geometric optimization of H atoms/ions, and dispersion correctional functional are thought to be some contributing to these unusual computed  $^{195}\text{Pt}$  ( $\sigma_{\text{iso}}$ ) shielding trends of the  $(\text{NH}_4)_2\text{PtCl}_6$  salt as a function of temperature.



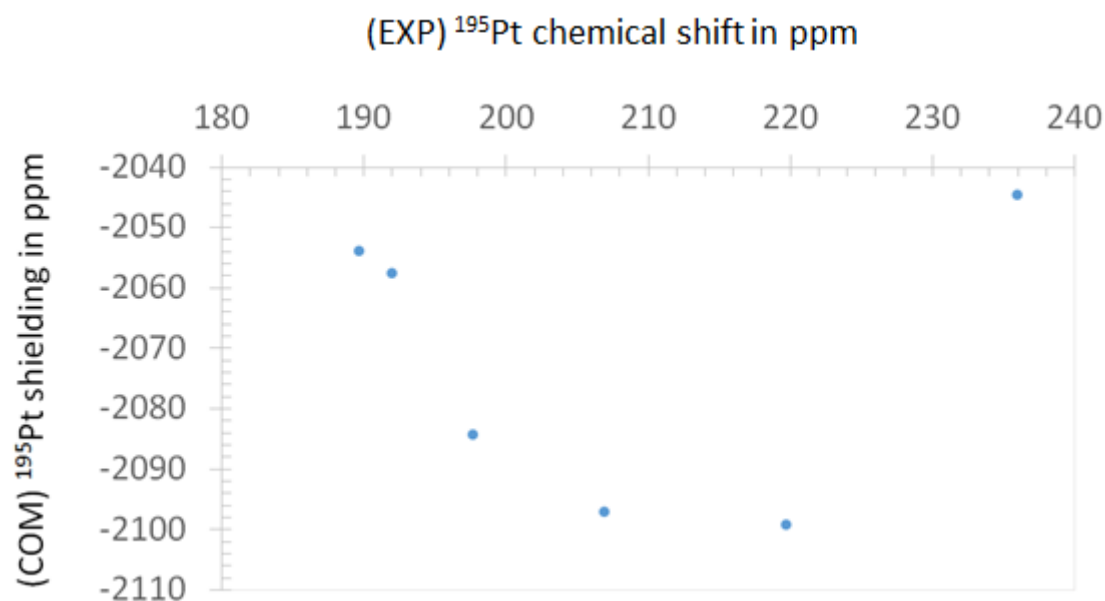


Figure 5. 7 Plot of Computed  $^{195}\text{Pt}$  ( $\sigma_{\text{iso}}$ ) shielding (PBE) vs. experimental  $^{195}\text{Pt}$  chemical shift trends of  $(\text{NH}_4)_2\text{PtCl}_6$  salt (150 K to 400 K), our SSNMR experiments could not be performed at 100 K so we therefore used the SSNMR parameters from 150 K to 400 K.

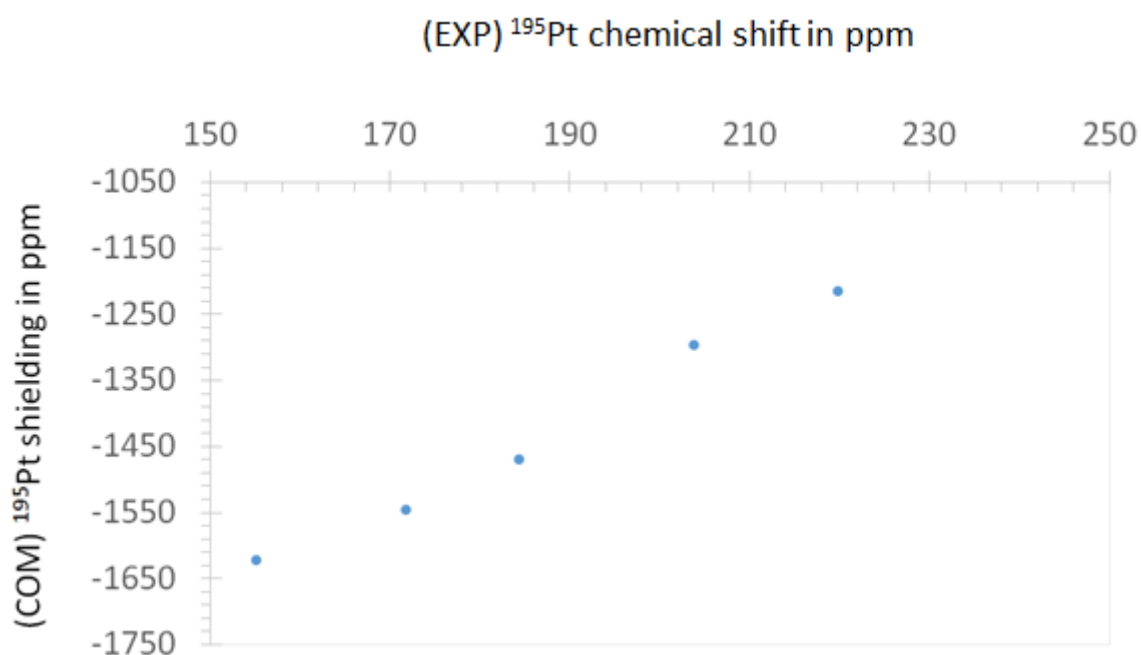


Figure 5. 8 Plot of computed C  $^{195}\text{Pt}$  ( $\sigma_{\text{iso}}$ ) shielding (PBE) vs. experimental  $^{195}\text{Pt}$  chemical shift trends of  $\text{Rb}_2\text{PtCl}_6$  salt as a function of temperature (150 K to 400 K), our SSNMR experiments could not be performed at 100 K so we therefore used the SSNMR parameters from 150 K to 400 K.

The experimental temperature dependence  $^{195}\text{Pt}$  chemical shift shows that the  $\text{Rb}_2\text{PtCl}_6$  and  $(\text{NH}_4)_2\text{PtCl}_6$  salts are both moving more downfield with an increase in temperature. If the Pt nucleus is becoming moving more downfield, which indicates a loss of electronic charge distribution on the  $\text{Pt}^{\text{IV}}$  ion, then surely this density has to be transferred to another neighbouring atom? We perform electrostatic potential charge calculations of the  $\text{Rb}_2\text{PtCl}_6$  and  $(\text{NH}_4)_2\text{PtCl}_6$  salts crystal structures to investigate the influence that changing temperature has on electrostatic potential charges in these salts.

### *5.5 The Pt ion electrostatic potential calculations by VAMP of $(\text{NH}_4)_2\text{PtCl}_6$ and $\text{Rb}_2\text{PtCl}_6$*

The computed electrostatic potentials which are calculated as atomic charges shows that the charge of the  $\text{Pt}^{\text{IV}}$  ion in the  $(\text{NH}_4)_2\text{PtCl}_6$  salt (Fig. 5.9) are increasing as a function of increasing temperature. The same increase is observed for the  $\text{Pt}^{\text{IV}}$  ion charges in the  $\text{Rb}_2\text{PtCl}_6$  salt (Fig. 5.10). The difference in calculated charges (400 K and 100 K) of the  $\text{Pt}^{\text{IV}}$  ion in  $(\text{NH}_4)_2\text{PtCl}_6$  is 0.0009e and 0.004e for the  $\text{Rb}_2\text{PtCl}_6$  salts. The increase of the  $\text{Pt}^{\text{IV}}$  ion charge is indicative of a loss of electron charge density from the  $\text{Pt}^{\text{IV}}$  ion (Fig. 5.10). These computed temperature dependence  $\text{Pt}^{\text{IV}}$  ion electrostatic potential charges results coincide with the experimentally observed  $^{195}\text{Pt}$  chemical shift measurements, which show that the  $^{195}\text{Pt}$  nuclei are becoming de-shielding as a function of temperature due to the loss of electronic charge from this ion. The difference in sensitivity of  $\text{Pt}^{\text{IV}}$  ion fitted electrostatic potentials charges also reflects the sensitivity of the experimental temperature dependence  $^{195}\text{Pt}$  chemical shift of these salts, where the  $(\text{NH}_4)_2\text{PtCl}_6$  salt is less sensitive than that of the  $\text{Rb}_2\text{PtCl}_6$  salt.

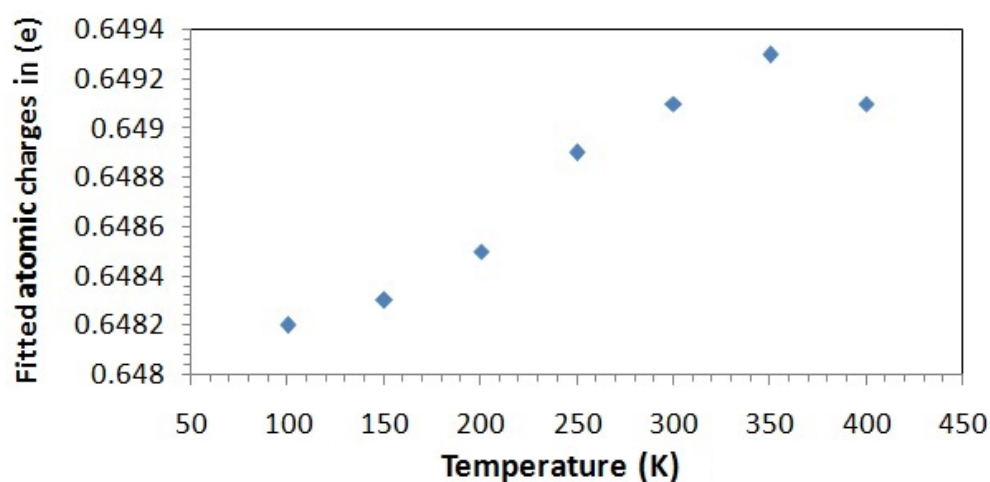


Figure 5. 9 Electrostatic potential charges of the  $\text{Pt}^{\text{IV}}$  ion in  $(\text{NH}_4)_2\text{PtCl}_6$  salts as a function of temperature

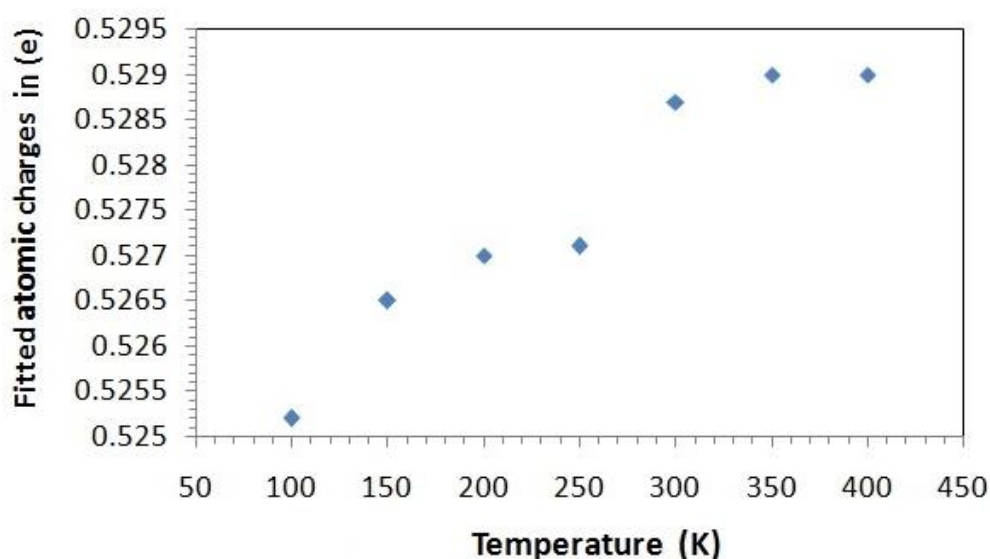


Figure 5. 10 Electrostatic potential charges of the  $\text{Pt}^{\text{IV}}$  ion in  $\text{Rb}_2\text{PtCl}_6$  salts as a function of temperature

### 5. 6 NMR-CASTEP Computational results of $^{35}\text{Cl}$ isotropic, anisotropic shielding and quadrupolar coupling of $(\text{NH}_4)_2\text{PtCl}_6$ and $\text{Rb}_2\text{PtCl}_6$

The computed  $^{35}\text{Cl}$  ( $\sigma_{\text{iso}}$ ) shielding tensor of the  $(\text{NH}_4)_2\text{PtCl}_6$  salt decreases as a function of increasing temperature (Fig. 5.11). The computed  $^{35}\text{Cl}$  ( $\Delta_{\text{CS}}$ ) shielding tensor is increasing (Fig. 5.12). The functionals all seem to behave very similarly with respect to the observed  $^{35}\text{Cl}$  ( $\sigma_{\text{iso}}$ ) trends, the relative agreement of the  $^{35}\text{Cl}$  ( $\Delta_{\text{CS}}$ ) shielding tensors are better than that obtained for the  $^{35}\text{Cl}$  ( $\sigma_{\text{iso}}$ ) tensors trends.

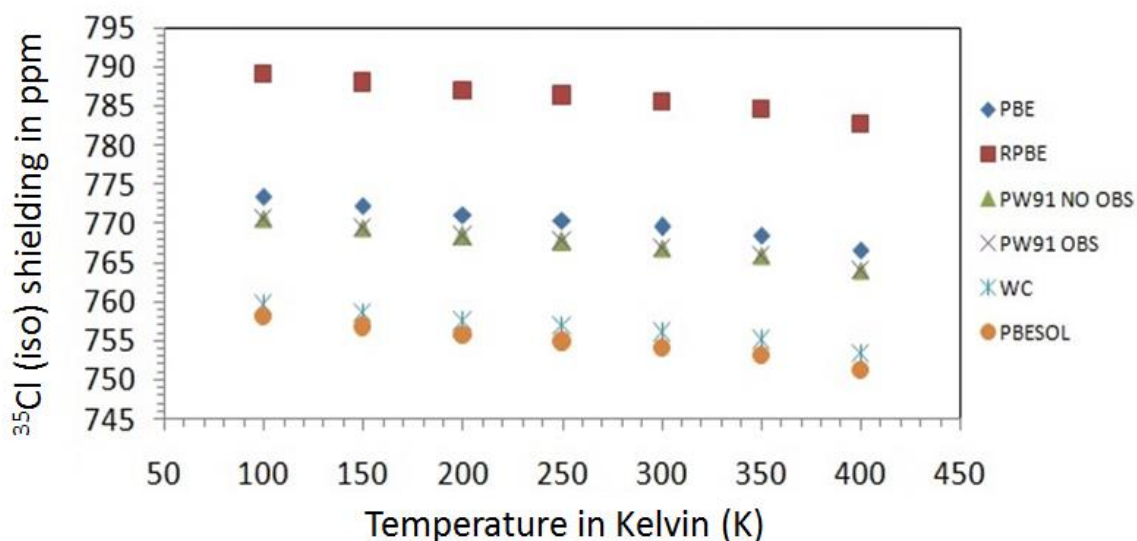


Figure 5.11 The  $^{35}\text{Cl}$  ( $\sigma_{\text{iso}}$ ) shielding of  $(\text{NH}_4)_2\text{PtCl}_6$  salt as a function of temperature

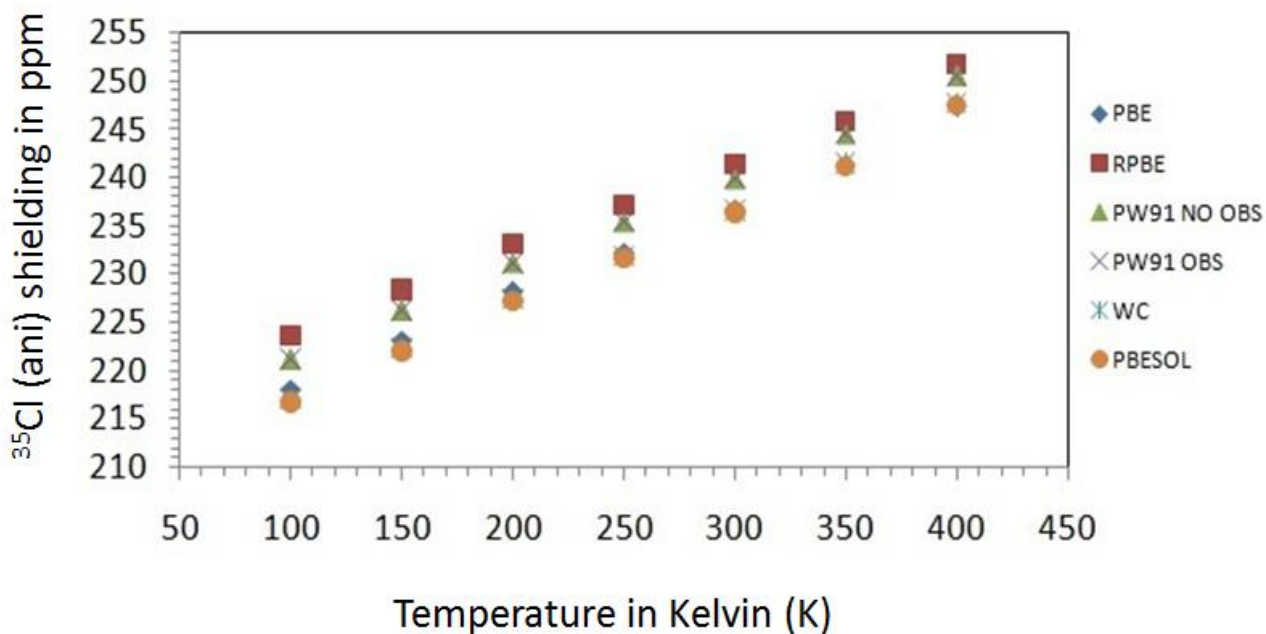


Figure 5.12 The  $^{35}\text{Cl}$  ( $\Delta_{\text{CS}}$ ) shielding of  $(\text{NH}_4)_2\text{PtCl}_6$  salts as a function of temperature

The computed  $^{35}\text{Cl}$  ( $C_Q$ ) tensors from 100 K to 150 K are slightly increasing as a function of increasing temperature (Fig. 5.13). The  $^{35}\text{Cl}$  ( $C_Q$ ) from 200 K to 350 K all seem to be decreasing as a function of temperature with the exception of the structure at 400 K. The GGA functionals have similar trends for the  $^{35}\text{Cl}$  ( $C_Q$ ) quadrupolar coupling tensor as a function of increasing temperature.

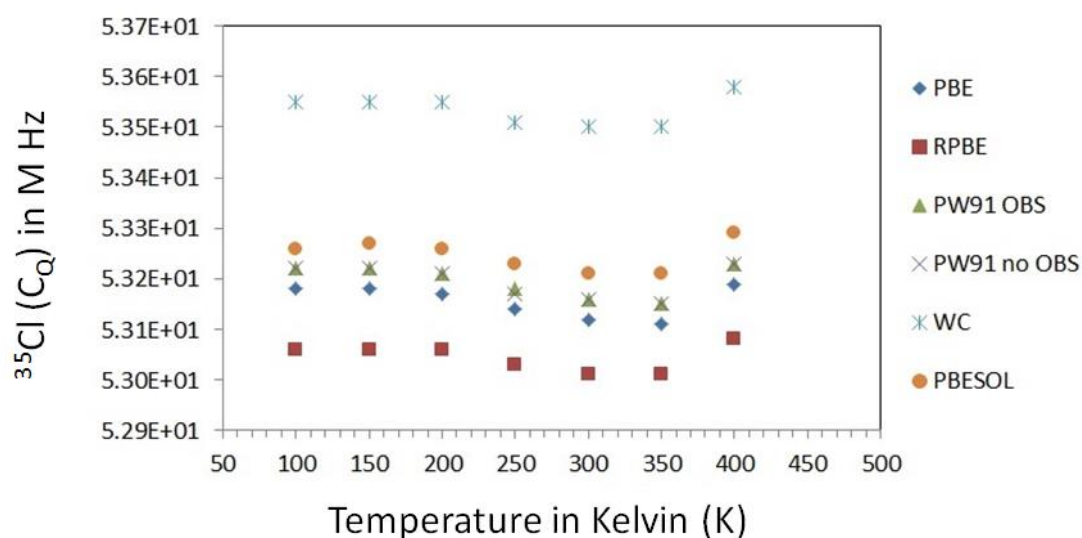


Figure 5. 13 The  $^{35}\text{Cl}$  ( $C_Q$ ) parameter of  $(\text{NH}_4)_2\text{PtCl}_6$  salt as a function of temperature

The computed  $^{35}\text{Cl}$  ( $\sigma_{\text{iso}}$ ) shielding tensor of the  $\text{Rb}_2\text{PtCl}_6$  salt is decreasing as a function of increasing temperature (Fig. 5.14). The GGA functionals all indicate that the  $^{35}\text{Cl}$  ( $\sigma_{\text{iso}}$ ) shielding decreases. The calculated  $^{35}\text{Cl}$  ( $\Delta C_S$ ) shielding tensor shows an increase as a function of temperature (Fig. 5.15). The computed  $^{35}\text{Cl}$  ( $\Delta C_S$ ) shielding tensor shows an increase (Fig. 5.12). The GGA functionals all seem to behave very similarly with respect to the observed  $^{35}\text{Cl}$  ( $\Delta C_S$ ) shielding trends. The relative agreement of the computed  $^{35}\text{Cl}$  ( $\Delta C_S$ ) shielding tensor values obtained from using different GGA functional is in better agreement than that obtained for the  $^{35}\text{Cl}$  ( $\sigma_{\text{iso}}$ ) shielding trends. A similar observation is made for the  $(\text{NH}_4)_2\text{PtCl}_6$  salt. The computed  $^{35}\text{Cl}$  quadrupolar coupling ( $C_Q$ ) tensor increasing as a function of temperature (Fig. 5.16).

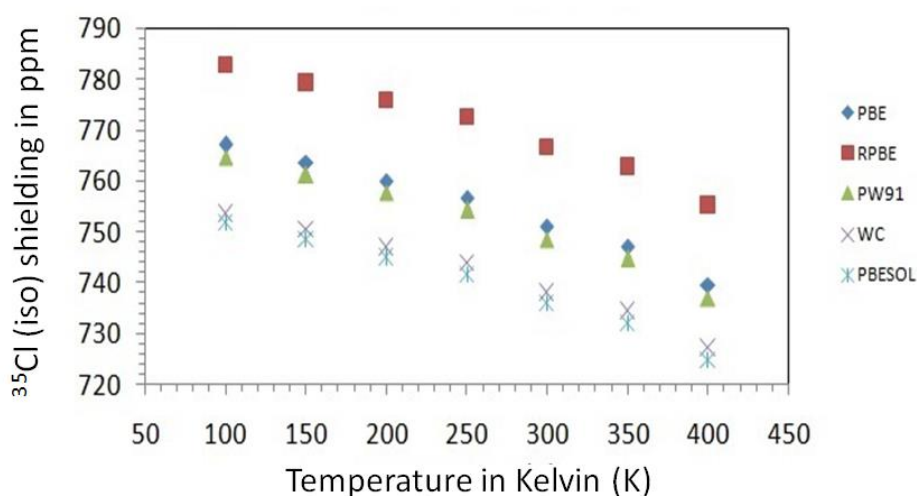


Figure 5. 14 The  $^{35}\text{Cl}$   $\sigma_{\text{iso}}$  shielding tensor of  $\text{Rb}_2\text{PtCl}_6$  salts as a function of temperature

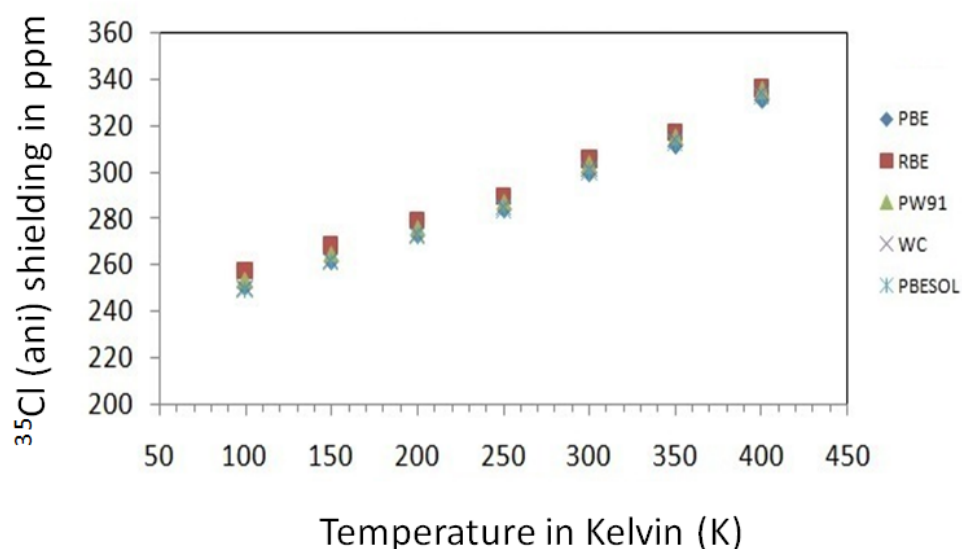


Figure 5. 15 The  $^{35}\text{Cl}$  ( $\Delta_{\text{Cs}}$ ) shielding of  $\text{Rb}_2\text{PtCl}_6$  salt as a function of temperature

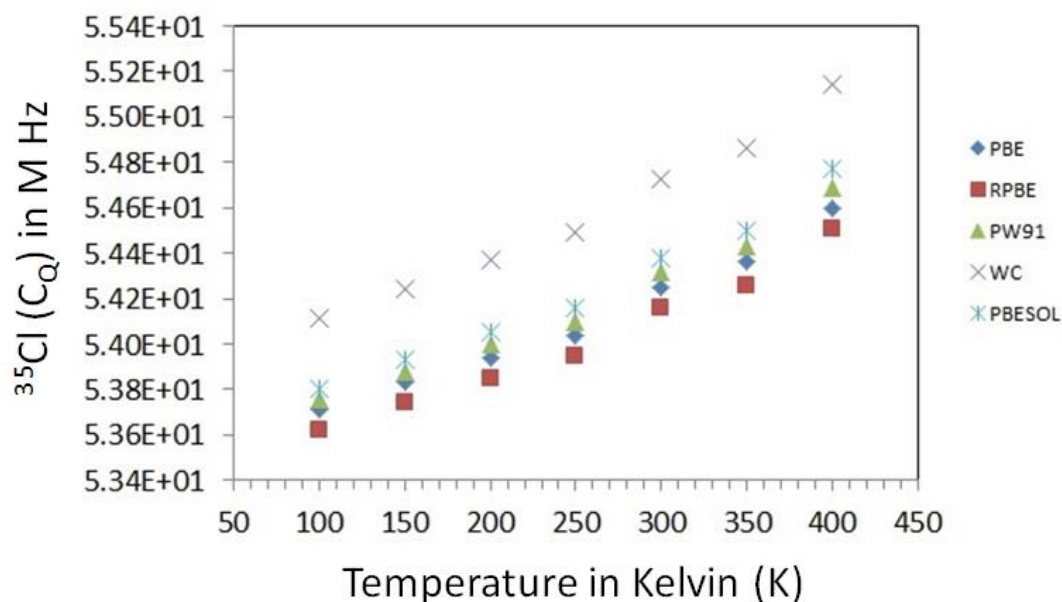


Figure 5. 16 The  $^{35}\text{Cl}$  ( $C_Q$ ) chemical shift of  $\text{Rb}_2\text{PtCl}_6$  salt as a function of temperature

The computed  $^{35}\text{Cl}$  ( $\sigma_{\text{iso}}$ ) shielding trends of  $(\text{NH}_4)_2\text{PtCl}_6$  salts (Fig. 5.11) and  $\text{Rb}_2\text{PtCl}_6$  (Fig. 5.14) salts are both decreasing as a function of increasing temperature. The  $^{35}\text{Cl}$  ( $\sigma_{\text{iso}}$ ) sensitivity of these salts over the entire temperature range (100 K – 400 K) is quite different. Using the GGA, PBE functional the sensitivity range of the  $^{35}\text{Cl}$  ( $\sigma_{\text{iso}}$ ) shielding parameter in  $(\text{NH}_4)_2\text{PtCl}_6$  salt is 6.91 ppm, which is less sensitive than the  $\text{Rb}_2\text{PtCl}_6$  of 29.47 ppm. The computed  $^{35}\text{Cl}$  ( $\Delta_{\text{Cs}}$ ) shielding trends for  $(\text{NH}_4)_2\text{PtCl}_6$  (Fig. 5.12) and  $\text{Rb}_2\text{PtCl}_6$  (Fig. 5.15) salts both show an increase as a function of increasing temperature. The computed  $^{35}\text{Cl}$  ( $\Delta_{\text{Cs}}$ ) shielding sensitivity in both these salts is quite

different. The  $^{35}\text{Cl}$  ( $\Delta_{\text{CS}}$ ) shielding range in  $(\text{NH}_4)_2\text{PtCl}_6$  is 29.47 ppm, which is almost three times less than that of the  $^{35}\text{Cl}$  ( $\Delta_{\text{CS}}$ ) shielding range of 81.21 ppm of  $\text{Rb}_2\text{PtCl}_6$ . These changing parameters can be viewed on the proposed  $^{35}\text{Cl}$  SSNMR spectra of these salts Fig. 5.2. The differences with respect to the shielding sensitivity of the  $\text{Cl}^-$  ions in  $(\text{NH}_4)_2\text{PtCl}_6$  and  $\text{Rb}_2\text{PtCl}_6$  salts are due to the nature of the  $\text{Cl}^-$  ion interaction with the cation. It has been shown that hydrogen bonding interactions to a Cl atom/ion influence the EFG around of this atom differently, relative to a system in which the Cl atom/ion is not involved in H bonding interactions.<sup>42,43</sup>

The computed  $^{35}\text{Cl}$   $C_Q$  trends of the  $(\text{NH}_4)_2\text{PtCl}_6$  salts (Fig. 5.13) are quite different to that of the  $\text{Rb}_2\text{PtCl}_6$  (Fig. 5.16) salt. A change in  $C_Q$  parameters in these salts is a good indication that the EFG around  $\text{Cl}^-$  ion in these salts are changing. The  $^{35}\text{Cl}$   $C_Q$  tensor in  $\text{Rb}_2\text{PtCl}_6$  is increasing as a function of increasing temperature. This means that there would be an increase in line broadening in the  $^{35}\text{Cl}$  spectra as a function of increasing temperature (Fig. 5.3).

These changing  $^{35}\text{Cl}$  SSNMR parameters in both  $(\text{NH}_4)_2\text{PtCl}_6$  and  $\text{Rb}_2\text{PtCl}_6$  salts are giving some indication that the electronic environments (EFG) of these  $\text{Cl}^-$  ions are changing at different rates. These changes are brought upon by the weakening intramolecular interactions between the anion and cation as a function of increasing temperature. We investigate the changing effects on these  $\text{Cl}^-$  ions by investigating the electrostatic potentials charges of these ions as a function of increasing temperature.

### *5.7 The $\text{Cl}^-$ ion electrostatic potential calculations by VAMP for $(\text{NH}_4)_2\text{PtCl}_6$ and $\text{Rb}_2\text{PtCl}_6$*

The  $\text{Cl}^-$  ion in the  $(\text{NH}_4)_2\text{PtCl}_6$  salt crystal structures shows a decrease of its electrostatic potential charge as a function of increasing temperature (Fig. 5.17). The overall charge on the  $\text{Cl}^-$  ion in the  $(\text{NH}_4)_2\text{PtCl}_6$  salts is negative and a decrease in electrostatic charge on this ion is indicative of an increase of electron charge density. The  $\text{Cl}^-$  ion in the  $\text{Rb}_2\text{PtCl}_6$  salt (Fig. 5.18) also shows an increase in its electrostatic potential charge. The difference in the calculated electrostatic potential charge of the  $\text{Cl}^-$  ion in  $(\text{NH}_4)_2\text{PtCl}_6$  is 0.0004e and 0.002e for the  $\text{Rb}_2\text{PtCl}_6$  salt over the entire temperature range (100 K to 400 K). This is another indication of the influence that a



hydrogen bonding interaction has on the  $\text{Cl}^-$  ion electronic charge distribution is quite different if compared to that of the purely electrostatic interaction. The calculated electrostatic potential charges of the  $\text{Cl}^-$  ion in both the  $(\text{NH}_4)_2\text{PtCl}_6$  (Fig. 5.17) and  $\text{Rb}_2\text{PtCl}_6$  (Fig. 5.18) salts decrease as the temperature increases. These findings suggest that the electronic charge distribution of the  $\text{Pt}^{\text{IV}}$  ion is polarized towards the  $\text{Cl}^-$  ion as a result of the weakening interaction between the cation and anion due to lattice expansion, as a function of increasing temperature.

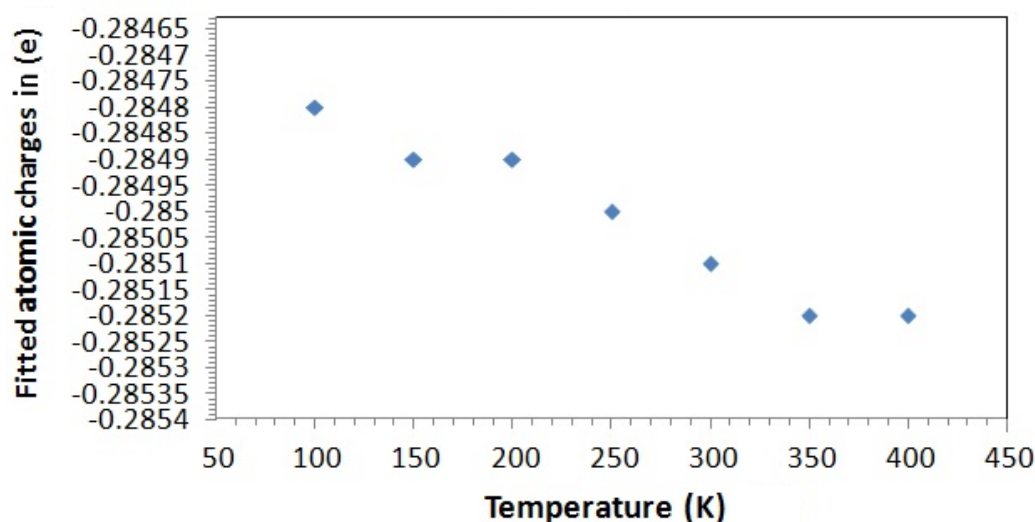


Figure 5. 17 Electrostatic potential atomic charges of the  $\text{Cl}^-$  ion in  $(\text{NH}_4)_2\text{PtCl}_6$  salts as a function of increasing temperature

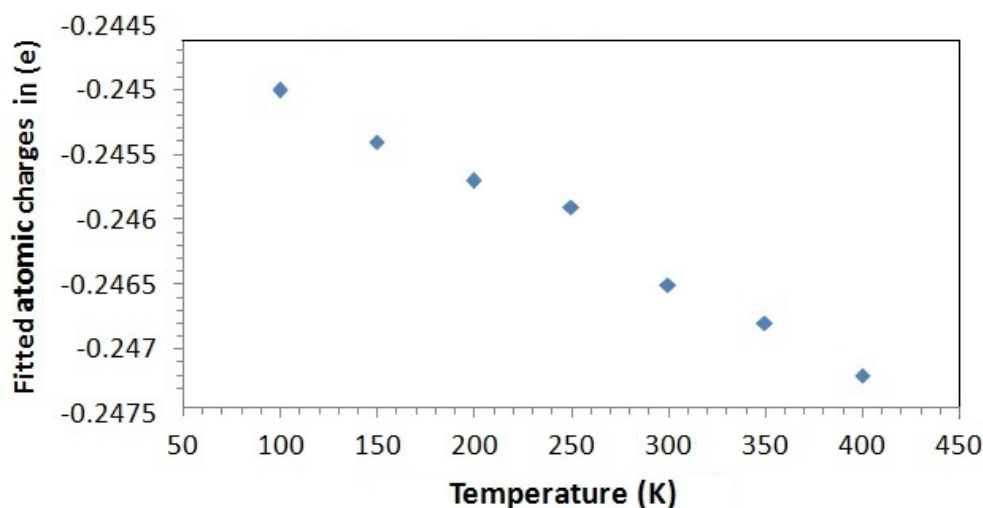


Figure 5. 18 Electrostatic potential atomic charges of the  $\text{Cl}^-$  ion in  $\text{Rb}_2\text{PtCl}_6$  salts as a function of increasing temperature



### 5. 8 NMR-CASTEP Computational results of $^{87}\text{Rb}$ isotropic shielding tensors of $\text{Rb}_2\text{PtCl}_6$ and $^{14}\text{N}$ isotropic, $^1\text{H}$ isotropic anisotropic shielding tensors and quadrupolar coupling of $(\text{NH}_4)_2\text{PtCl}_6$

The calculated  $^{87}\text{Rb}$  ( $\sigma_{\text{iso}}$ ) shielding tensor increases as a function of increasing temperature (Fig. 5.19). The GGA functionals all show that the  $^{87}\text{Rb}$  ( $\sigma_{\text{iso}}$ ) shielding tensor is increasing as a function of increasing temperature. The computed  $^{85}\text{Rb}$  ( $\sigma_{\text{iso}}$ ) shielding trends are very similar to the linear trends of the experimental  $^{87}\text{Rb}$  ( $\sigma_{\text{iso}}$ ) chemical shielding trend as a function of increasing temperature.

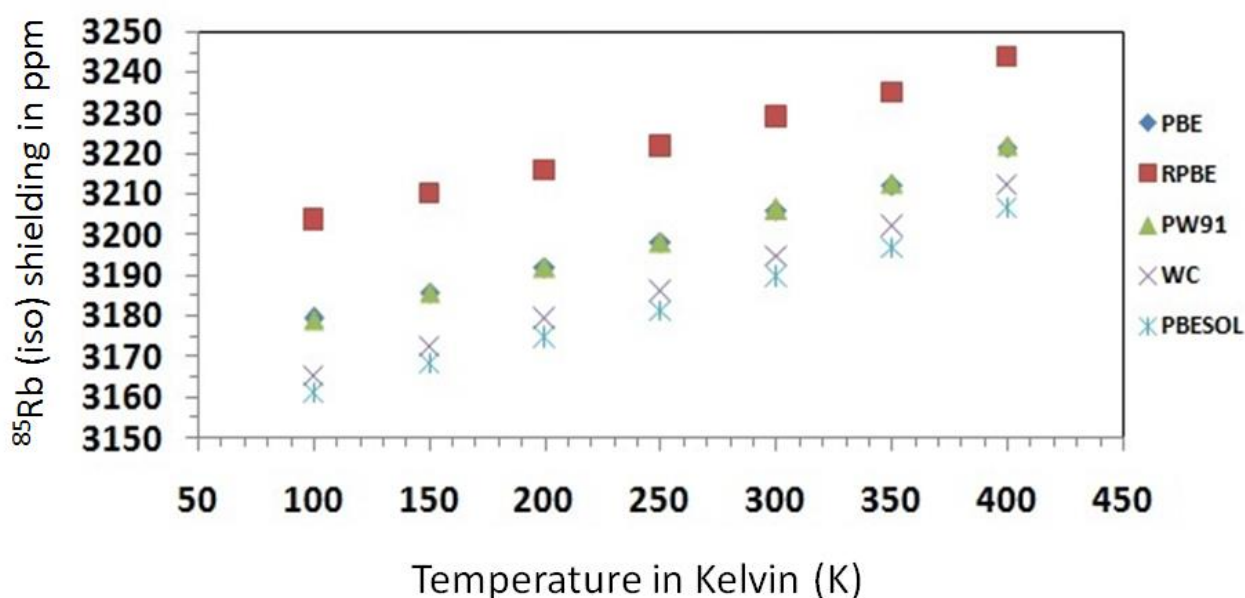


Figure 5. 19 The  $^{85}\text{Rb}$   $\sigma_{\text{iso}}$  shielding of  $\text{Rb}_2\text{PtCl}_6$  salt as a function of temperature

The experimental  $^{85}\text{Rb}$  MAS SSNMR experiments performed as a function of temperature showed that this nucleus is becoming more de-shielded and therefore we assume the computed  $^{87}\text{Rb}$  shielding trends to represent de-shielding. The  $\text{Rb}^+$  cation is a spherical ion involved in an electrostatic interaction ( $\text{Pt-Cl}\cdots\text{Rb}$ ) with a partially negative  $\text{Cl}^-$  ion of the  $[\text{PtCl}_6]^{2-}$ . The weakening of the electrostatic interaction between the anion and cation would cause the  $\text{Rb}^+$  cation to be a bit more positively charged since it does not have to share its electronic charge with the  $\text{Cl}^-$  ion, which in return causes the  $^{85}\text{Rb}$  nucleus to experience de-shielding as a function of increasing temperature. The computed  $^{85}\text{Rb}$  ( $\sigma_{\text{iso}}$ ) shielding tensor is plotted against experimental  $^{85}\text{Rb}$  ( $\sigma_{\text{iso}}$ ) chemical shielding tensors as a function of temperature are linearly related (Figure 5.20). This confirms and validates the accuracy of our computational method showing that both these salts

are showing in increase of its computed  $^{85}\text{Rb}$  shielding and experimental  $^{85}\text{Rb}$  chemical shielding parameters.

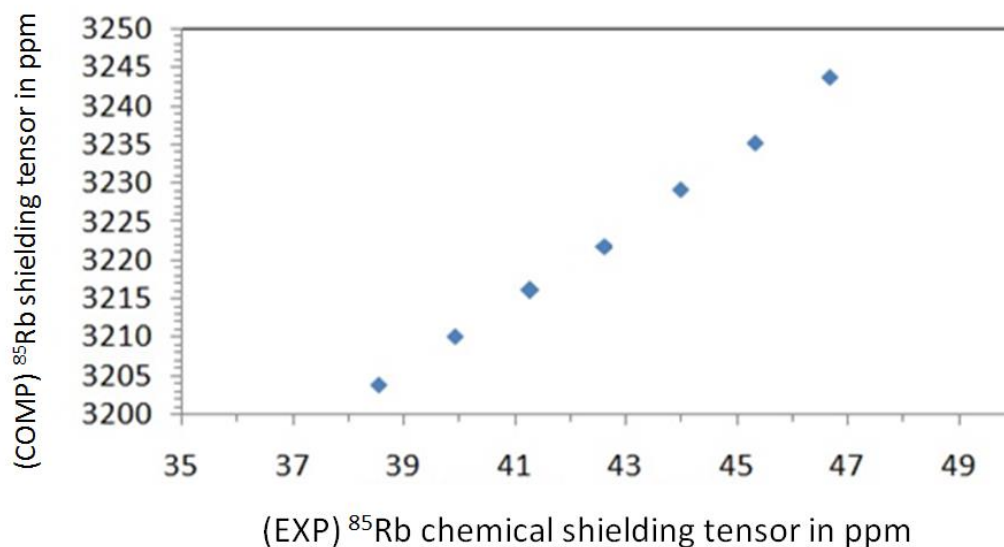


Figure 5. 20 Plot of computed  $^{85}\text{Rb}$  shielding against the experimental  $^{85}\text{Rb}$  chemical shielding trends of  $\text{Rb}_2\text{PtCl}_6$  salt as a function of increasing temperature

The computed  $^{14}\text{N}$  ( $\sigma_{\text{iso}}$ ) shielding tensors are increasing as a function of increasing temperature (Fig. 5.21). All GGA functionals for this nucleus seem to indicate an overall increase with respect to the  $^{14}\text{N}$  ( $\sigma_{\text{iso}}$ ) shielding tensor as temperature increases.

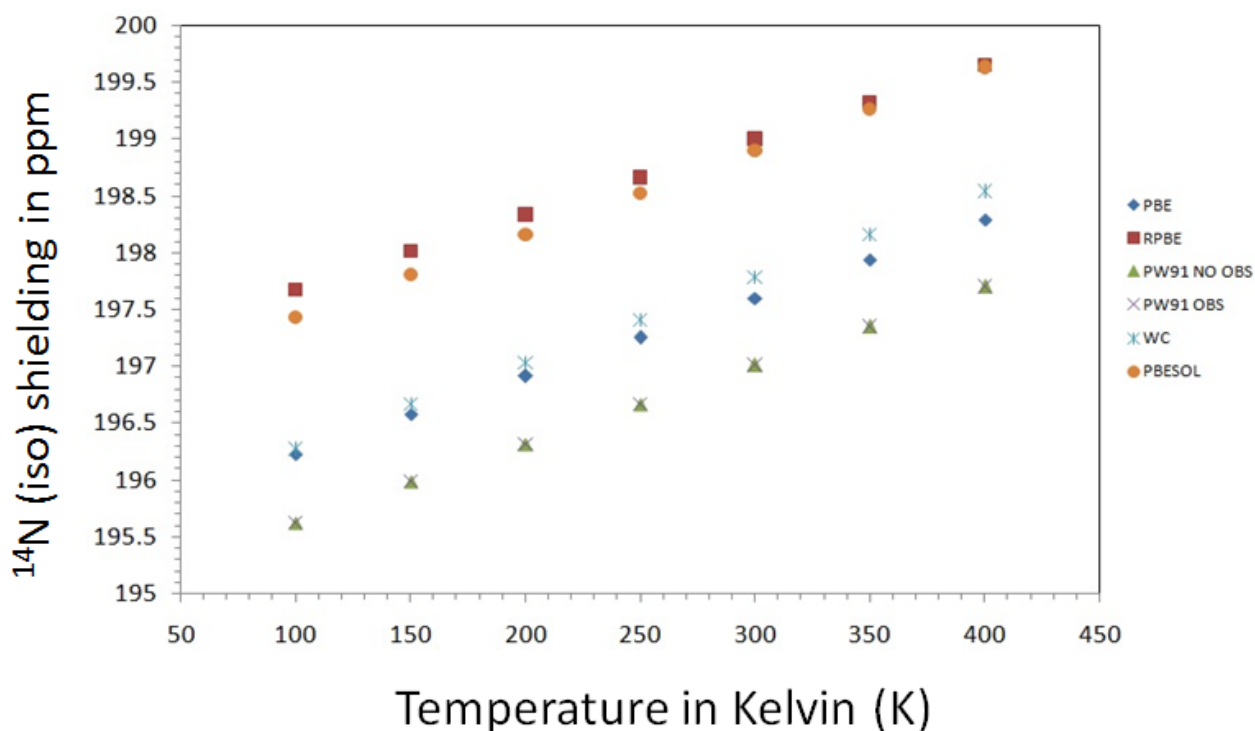


Figure 5. 21 The computed  $^{14}\text{N}$  ( $\sigma_{\text{iso}}$ ) shielding tensor of  $(\text{NH}_4)_2\text{PtCl}_6$  as a function of temperature

Experimental  $^{14}\text{N}$  SSNMR measurements were attempted, but since this nucleus has such fast relaxation times in the solid state, it was very difficult to obtain a good resonance signal. Although a few attempts were made to obtain good spectra, even with CP/MAS methods it required more than 24 hours to collect a spectrum. Therefore we did not attempt to perform temperature dependent measurement of this nucleus. The computed  $^{14}\text{N}$  SSNMR parameters as a function of temperature shed some light on the behaviour of the  $^{14}\text{N}$  nucleus upon lattice expansion. The computed  $^{14}\text{N}$  SSNMR parameters of the  $(\text{NH}_4)_2\text{PtCl}_6$  salt (Fig. 5.21) show an increasing  $^{14}\text{N}$  ( $\sigma_{\text{iso}}$ ) shielding parameter.

The computed  $^1\text{H}$  ( $\sigma_{\text{iso}}$ ) shielding (Fig. 5.22) and  $^1\text{H}$  ( $\Delta_{\text{CS}}$ ) shielding (Fig. 5.23) tensors are increasing as a function of increasing temperature. The computed  $^1\text{H}$  ( $\Delta_{\text{CS}}$ ) shielding tensor at 400 K show a slight decrease.

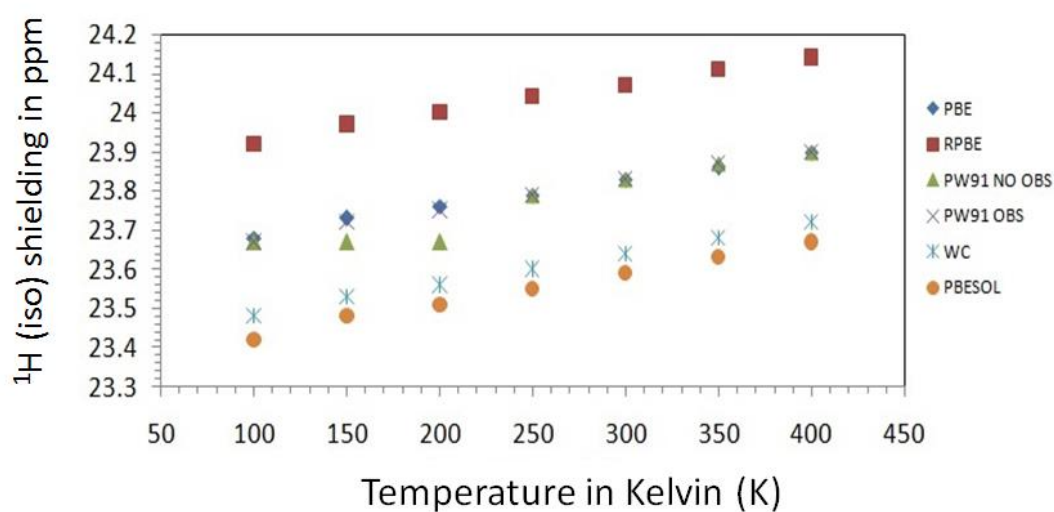


Figure 5. 22 The  $^1\text{H}$   $\sigma_{\text{iso}}$  shielding of the  $(\text{NH}_4)_2\text{PtCl}_6$  salts as a function of temperature

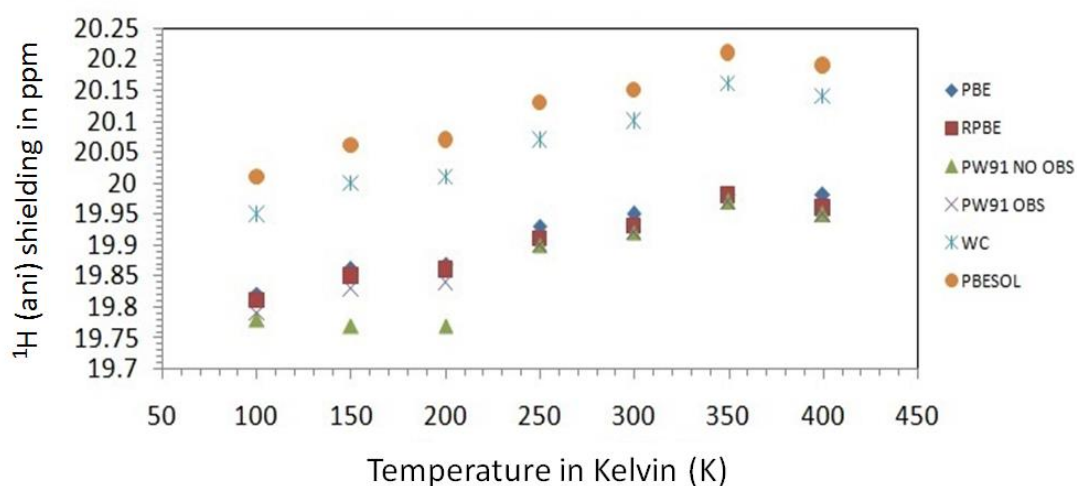


Figure 5. 23 The  $^1\text{H}$  ( $\Delta_{\text{CS}}$ ) chemical shift of  $(\text{NH}_4)_2\text{PtCl}_6$  salts as a function of temperature

The computed temperature dependence  $^1\text{H}$  ( $C_Q$ ) quadrupolar coupling tensors are decreasing as a function of temperature (see Fig. 5.24). The GGA functionals all indicate a decrease in the  $^1\text{H}$  ( $C_Q$ ) quadrupolar coupling tensor as a function of increasing temperature.

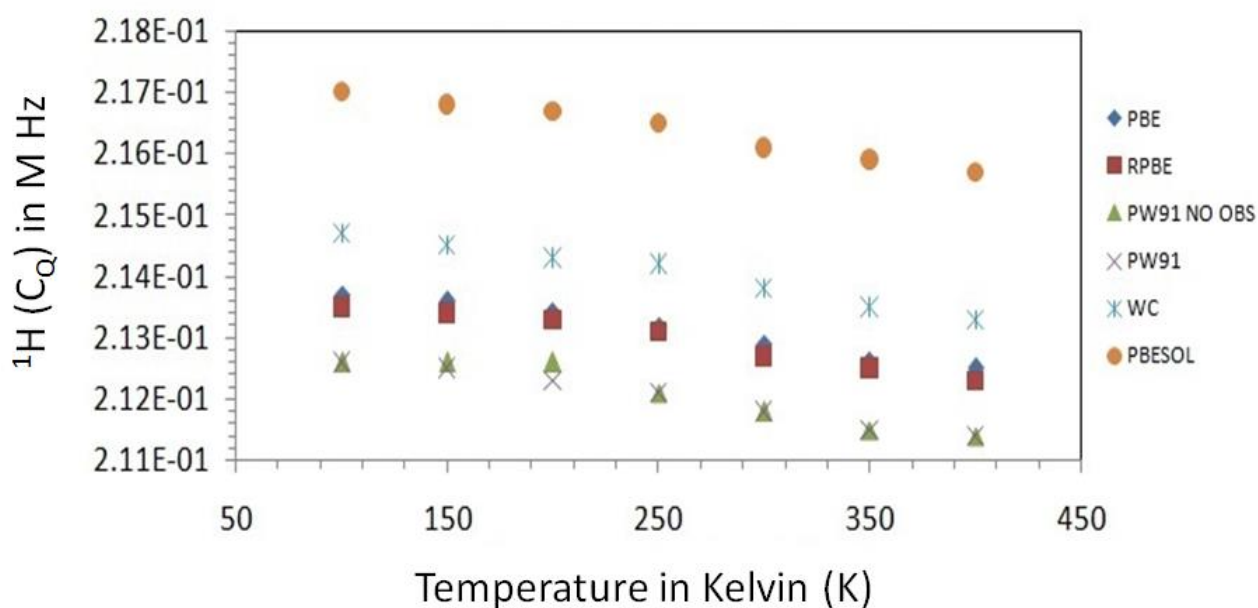


Figure 5. 24 The  $^1\text{H}$  ( $C_Q$ ) parameter of  $(\text{NH}_4)_2\text{PtCl}_6$  salt as a function of temperature

The computed  $^1\text{H}$  ( $\sigma_{\text{iso}}$ ) shielding (Fig. 5.22) and  $^1\text{H}$  ( $\Delta C_s$ ) shielding (Fig. 5.23) parameters of the  $(\text{NH}_4)_2\text{PtCl}_6$  salt performed as a function of temperature shows an increase in both  $\sigma_{\text{iso}}$  and  $\Delta C_s$  parameters. A good example of the importance of applying a dispersion correction is with the GGA with PW91 functional (Fig. 5.22 & 5.23). The OBS dispersion correction is turned on (PW91 OBS) and turned off (PW91 no OBS) in order to observe the effect that it has on the computed temperature dependence  $^1\text{H}$  ( $\sigma_{\text{iso}}$ ) and  $^1\text{H}$  ( $\Delta C_s$ ) shielding parameters over the entire temperature range. The  $^1\text{H}$  ( $\sigma_{\text{iso}}$ ) and  $^1\text{H}$  ( $\Delta C_s$ ) shielding trends show some deviation from the linear trends from 100 K to 200 K. This shows the importance of having a dispersion correction, which accounts for subtle long range London forces, especially at low and high temperatures. The temperature dependence  $^1\text{H}$  quadrupolar coupling ( $C_Q$ ) tensor is decreasing as a function of increasing temperature. This implies that the electronic environment of the H ion is changing with increasing temperature (Fig. 5.24). The fact that the  $C_Q$  interaction is decreasing as the temperature is increased shows that the interaction between  $^1\text{H}$  nucleus and its EFG is becoming weaker, i.e. the electronic charge distribution on the H ion is changing with increasing temperature. In all three of these Fig. 5.22, 5.23, and 5.24 it is clear that the dispersion correction is affecting the calculated parameters at temperatures between 100 K to 200 K, and at higher temperature 250 K to 400 K the dispersion corrections seem to produce similar results.

### 5.9 The electrostatic potential calculations by VAMP of the cations: Rb ion in $\text{Rb}_2\text{PtCl}_6$ and N and H ions in $(\text{NH}_4)_2\text{PtCl}_6$

The calculated electrostatic potential charge of the  $\text{Rb}^+$  ion in the  $\text{Rb}_2\text{PtCl}_6$  salt performed as a function of temperature is increasing (Fig. 5.25). The overall charge of the  $\text{Rb}^+$  ion in the  $\text{Rb}_2\text{PtCl}_6$  salts are positive and an increase of electrostatic charge on this atom is indicative of a decrease of electron density on this atom. This is why we are observing a more downfield shift of our experimental  $^{85}\text{Rb}$  MAS SSNMR experiments of the  $\text{Rb}_2\text{PtCl}_6$  salt as a function of temperature.

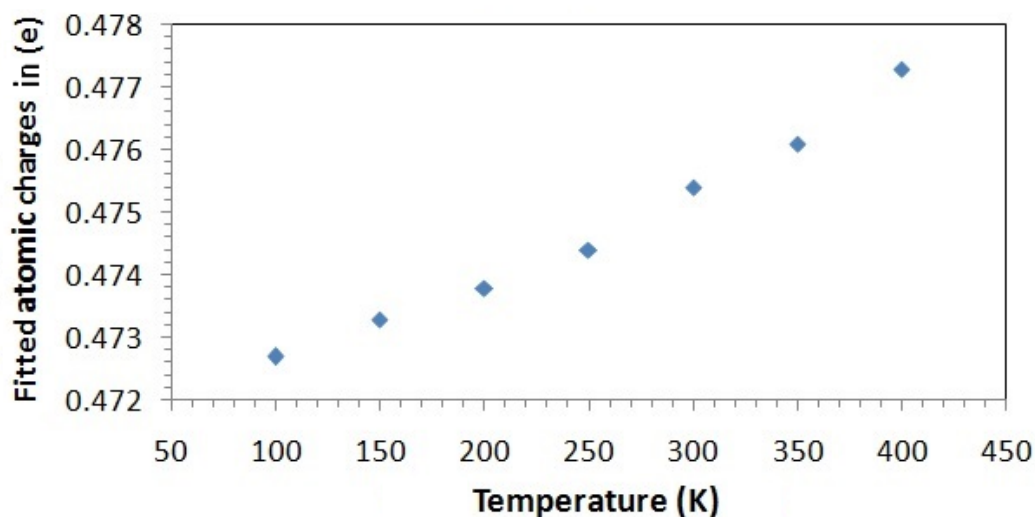


Figure 5. 25 The electrostatic potential atomic charges of the  $\text{Rb}^+$  ion in  $\text{Rb}_2\text{PtCl}_6$  salts as a function of temperature

The computed electrostatic potential charges of the  $\text{N}^+$  ion (Fig. 5.26) is increasing. This is a good indication that the electronic charge distribution on the  $\text{N}^+$  ion is decreasing upon lattice expansion.

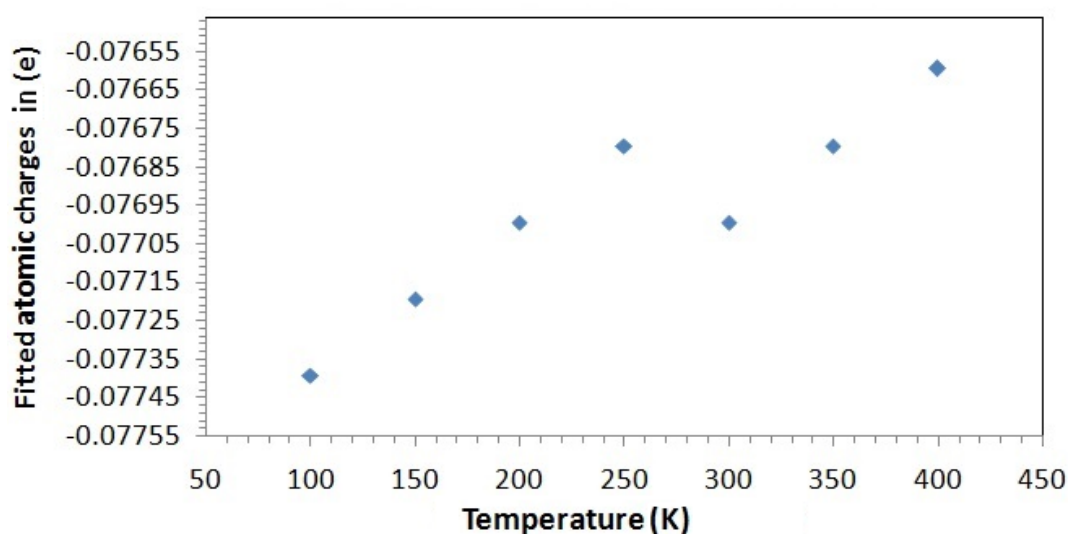


Figure 5. 26 The electrostatic potential atomic charges of the N ion in  $(\text{NH}_4)_2\text{PtCl}_6$  salts as a function of temperature

In Fig. 5.27 the  $\text{H}^+$  ion electrostatic potential atomic charges are decreasing as a function of increasing temperature. The decrease in this  $\text{H}^+$  ion atomic charge is associated with an increase of electron density on this  $\text{H}^+$  ion.

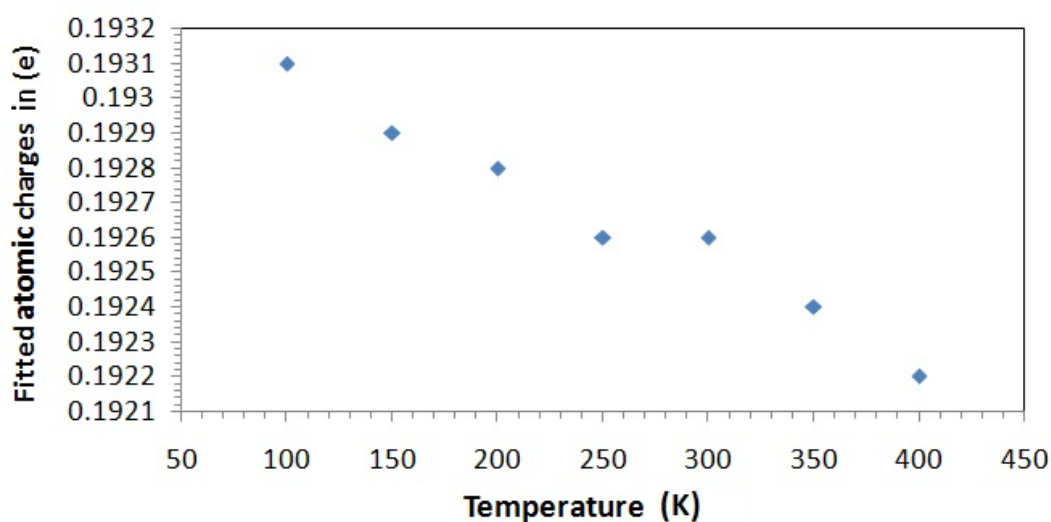


Figure 5. 27 The electrostatic potential of the H atom in  $(\text{NH}_4)_2\text{PtCl}_6$  salts as a function of temperature

The calculated electrostatic potential charge of the  $\text{N}^+$  ion in  $(\text{NH}_4)_2\text{PtCl}_6$  (Fig. 5.26) crystal structures is increasing as a function of increasing temperature. This increase of atomic charge is

associated with a loss of electron density on this atom. The atomic charge on the H ion is increasing (Fig. 5.27)

In a study carried out by Penner *et al.*<sup>44</sup> they performed a multitude of multinuclear NMR and quantum chemical studies of solid tetramethylammonium chloride. They investigated the effects that atomic displacement of the H<sup>+</sup> ion in the N-H...Cl hydrogen bonding interaction has on various SSNMR parameters. The computational results show that the N-H inter-nuclear distance is highly dependent on the computational methods used, which would directly influence the outcome of the computed NMR parameters. Their study shows that the computed shielding parameters and quadrupolar coupling parameters of <sup>1</sup>/<sub>2</sub>H and <sup>35</sup>Cl are extremely sensitive to the position of the H atom within a 1 – 1.2 Å range of the hydrogen bonding interaction. The <sup>1</sup>H ( $\Delta_{CS}$ ) parameter in their computational calculation seems to be unaffected by the position of the hydrogen atom. Their results also show the <sup>14</sup>N ( $\sigma_{iso}$ ) parameter is much less dependent on the H atom position. They conclude that it is not possible to compute the exact position of the H atom to match their experimentally observed chemical shielding parameters. The study showed that the <sup>1</sup>H C<sub>Q</sub> and <sup>35</sup>Cl C<sub>Q</sub> parameters show irregular values compared to literature values due to uncertainty of the H atom's position. This is exactly what we are observing in our computational SSNMR measurements, which showed an irregular behaviour of <sup>35</sup>Cl C<sub>Q</sub> (Fig. 5.13) trends, even though the H ions positions were geometrically optimized before performing the SSNMR and electrostatic potential charge calculations. In a more recent study on the computation of <sup>35</sup>Cl SSNMR parameters where the Cl atom/ions are involved in hydrogen bonding,<sup>45</sup> they show that if the Cl atom/ion is interacting with H atom/ion via hydrogen bonding, it is one most difficult systems with which to compute the C<sub>Q</sub> parameters. This is due to the obtaining of an accurate position of the hydrogen atom in such close proximity to the Cl atom. They have shown, with countless calculations, that it is extremely difficult to obtain close to accurate C<sub>Q</sub> parameters, which can be compared to experimental measurements. This is why we are observing such strange trends for our computed <sup>195</sup>Pt ( $\sigma_{iso}$ ) shielding tensors trends as a function of temperature. The quadrupolar coupling interactions dominate the shielding trends in both the (NH<sub>4</sub>)<sub>2</sub>PtCl<sub>6</sub> and Rb<sub>2</sub>PtCl<sub>6</sub> salts. If this parameter cannot be accurately computed in the (NH<sub>4</sub>)<sub>2</sub>PtCl<sub>6</sub> salts it will produce incorrect quadrupolar coupling values, which will influence the other computational SSNMR parameters,



which is evident from our computational  $^{195}\text{Pt}$  ( $\sigma_{\text{iso}}$ ) shielding tensor trends as a function of temperature. This could explain why we are observing the strange trends for our  $^{195}\text{Pt}$  ( $\sigma_{\text{iso}}$ ) shielding tensor in the  $(\text{NH}_4)_2\text{PtCl}_6$  salts.

The Pt-Cl bond displacement observed within the octahedral  $[\text{PtCl}_6]^{2-}$  anion from the SCXRD of the  $(\text{NH}_4)_2\text{PtCl}_6$  and  $\text{Rb}_2\text{PtCl}_6$  salt (Chapter 3) performed as a function of temperature, might be due to the polarization of electron charge density from the  $\text{Pt}^{\text{IV}}$  ion toward the  $\text{Cl}^-$  ion. This is clear from our semi-empirical quantum mechanically derived electrostatic potentials charges and SSNMR parameters calculated using DFT.

## Concluding remarks

The results from the NMR-CASTEP calculations shed light on the behaviour of the NMR active nuclei in  $\text{Rb}_2\text{PtCl}_6$  and  $(\text{NH}_4)_2\text{PtCl}_6$  salts crystal structure as a function of increasing temperature. The semi-empirical quantum mechanically derived electrostatic potentials charges show how these two salts' electrostatics are influenced with an increase in temperature. This computational study gives insight into the bonding and non-bonding interactions within a crystal lattice and how they are quantum mechanically affected upon lattice expansion. The computed electrostatic potentials charges and NMR parameters complement each other and strengthen our hypothesis of an electron density polarization from the  $\text{Pt}^{\text{IV}}$  ion towards the  $\text{Cl}^-$  ion. These results have demonstrated why de-shielding is observed in experimental  $^{195}\text{Pt}$  chemical shift trends in  $\text{Rb}_2\text{PtCl}_6$  and  $(\text{NH}_4)_2\text{PtCl}_6$  salts as a function of temperature. It also illustrates how the electron density on the  $\text{Pt}^{\text{IV}}$  ion is polarized towards the  $\text{Cl}^-$  ion as the interactions between the cation and anion are weakened in both the  $\text{Rb}_2\text{PtCl}_6$  and  $(\text{NH}_4)_2\text{PtCl}_6$  salts crystal structures.

This study suggests that a multi-faceted solid-state analytical approach is central to the understanding of experimental temperature dependence  $^{195}\text{Pt}$  chemical shift SSNMR measurements of  $\text{Rb}_2\text{PtCl}_6$  and  $(\text{NH}_4)_2\text{PtCl}_6$  salts. This research shows how the combination of

usually independently performed solid-state analytical techniques, i.e. temperature dependent SCXRD, SSNMR and DFT calculations, is crucial for the interpretation and understanding of temperature dependent SSNMR spectra. This study uses these independent solid-state techniques to paint a 3D picture using crystallographic, magnetic resonance and quantum mechanical paint brushes in order to illustrate how lattice expansion influences the  $^{195}\text{Pt}$  isotropic shielding in *dication hexachloroplatinate(IV)* salts. These results were used to formulate a “polarization of electronic charge densities theory” whereby the  $\text{Pt}^{\text{IV}}$  ions’ electronic charge density is polarized towards the  $\text{Cl}^-$  ion due to the weakening intermolecular interaction between the cation and anion. This is the first contribution which takes this approach in the understanding and interpretation of temperature dependence SSNMR spectra.

The calculated SSNMR parameters can reveal new information which is sometimes inaccessible by means of conventional experimental SSNMR procedures. The computational data reputed in this chapter has proven to enhance the understanding of experimentally observed  $^{195}\text{Pt}$  shift trends using SSNMR as a function of increasing temperature.

## References

1. E. M. Purcell, H. C. Torrey, R. V. Pound, *Phys. Rev.*, **1946**, 69, 37.
2. T. Helgaker, M. Jaszuski, K. Ruud, *Chem. Rev.*, **1999**, 99, 293.
3. J. Gauss, J. F. Stanton, *Adv. Chem. Phys.*, **2002**, 123, 355.
4. C.J. Pickard, F. Mauri, *Phys. Rev.B.*, **2001**, 63, 245101.
5. J. Gauss, S. F. Stanton, *Adv. Chem. Phys.*, **2002**, 123, 355.
6. J. C. Facelli, D. M. Grant, *Nature*, **1993**, 365, 325.
7. C. Ochsenfeld, S. P. Brown, I. Schnell, J. Gauss, H. W. Spiess, *J. Am. Chem. Soc.*, **2001**, 123, 2597.
8. S. J. Clark, M. D. Segall, C.J. Pickard, P. J. Hasnip, M. J. Probert, K. Refson, M. C. Payne, *Z. Kristallogr.*, **2005**, 220, 567.
9. M. Profeta, F. Mauri, C. J. Pickard, *J. Am. Chem. Soc.*, **2003**, 125, 541.
10. F. Mauri, B. G. Pfommer, S. G. Louie, *Phys. Rev. Lett.*, **1996**, 77, 5300.
11. D. Vanderbilt, *Phys. Rev. B.*, **1990**, 41, 7892.
12. R. K. Harris, P. Hodgkinson, C. J. Pickard, J. R. Yates, V. Zorin, *Magn. Reson. Chem.*, **2007**, 45, S174.
13. T. Gregor, F. Mauri, R. J. Car, *J. Chem. Phys.*, **1999**, 111, 1815.
14. C. G. van der Walle, P. E. Blochl, *Phys. Rev. B*, **1993**, 47, 4244.
15. A. I. Akhiezer, V. B. Berestetskii, **1969**, *Quantum Electrodynamics* (Moscow: Nauka) (in Russian)

16. V. G. Baryshevskii, *Nuclear Optics of Polarized Media*, (Minsk – Byelorussian State University Press) **1976**, pg. 139 (in Russian); V. G. Baryshevskii and S. A. Kuten, *Theory of Atomic Nucleus*, (Leningrad, Leningrad Nuclear Physics Institute Press), **1978**, pg. 95 (in Russian).
17. D. S. Beder, *Nucl. Phys. A*, **1978**, 305, 411.
18. S. A. Kuten, *Phys. Lett.* **1987**, 67A, 355.
19. I. B. Kuriplovich, *J. Phys. B. At. Mol. Phys.*, **1984**, 17, L803.
20. T. Clark, *A Handbook of Computational Chemistry*, Wiley, New York, **1985**, T. Clark, A. Alex, B. Beck, F. Burkhardt, J. Chandrasekhar, P. Gedeck, A. Horn, M. Hutter, B. Martin, G. Rauhut, W. Sauer, T. Schindler, T. Steinke, Erlangen **2003**.
21. B. Beck, T. Clark, R. C. Glen, *J. Comp. Chem.*, **1996**, 16, 744.
22. J. A. Pople, D. P. Santry, G. A. Segal, *J. Chem. Phys.*, **1965**, 43, S129.
23. C. R. Cramer, *Essentials of Computational Chemistry*, Wiley, Chichester, **2002**, p 126 – 131.
24. U. Heaberlen, *High Resolution NMR in solids*, Acedemic Press: New York, **1976**.
25. W.C. Hamilton, *Annu. Rev. Phys. Chem.*, **1962**, 13, 19.
26. J. P. Perdew, K. Burke, M. Ernzerhof, *Phys. Rev. Lett.* **1996**, 77.
27. J. P. Perdew, K. Burke, M. Ernzerhof, *M. Phys. Rev. Lett.*, **1998**, 80.
28. J. P. Perdew, K. Burke, M. Ernzerhof, *Phys. Rev. Lett*, **1996**, 77, 18.
29. H. J. Monkhorst, J. D. Pack, *Phys. Rev.*, **1976**, 13, 12, 5188.
30. J. Cuny, S. Cordier, C. Perrin, C. J. Pickard, L. Delevoye, J. Trébosc, Z. Gan, L. Le Pollès, R. Gautier, *Inorg. Chem.*, **2013**, 52, 617.
31. J. V. Hanna, K. J. Pike, T. Charpentier, T. F. Kemp, M. E. Smith, B. E. G. Lucier, R. W. Schurko, Lindsay S. Cahill, *Chem. Eur. J.*, **2010**, 16, 3222.
32. B. Hammer, L. B. Hansen and J. K. Norskov, *Phys. Rev. B.*, **1999**, 59, 11.
33. J. P. Perdew, J. A. Chevary, S. H. Vosko, K. A. Jackson, M. R. Pederson, D. J. Singh, *Phys. Rev.B.*, **1992**, 46, 11.
34. Z. Wu, R. E. Cohen, *Phys. Rev. B.*, **2006**, 73, 235116.
35. J. P. Perdew, A. Ruzsinszky, G. I. Csonka, O. A. Vydrov, G. E. Scuseria, L. A. Constantin, X. Zhou, K. Burke, *Phys. Rev. Lett.*, **2008**, 100, 136406.
36. R. K. Harris, E. D. Becker, S. M. Cabral De Menezes, R. Goodfellow, P. Granger, *Pure Appl. Chem.*, **2001**, 73, 1795.
37. L. S. Prabhumirashi, R. Ikeda, D. Nakamura, *Ber. Bunsenges. Phys. Chem.*, **1981**, 85, 1142, Y. Furukawa, L. Prabhumirashi, R. Ikeda, D. Nakamura, *Bull. Chem. Soc. Jpn.*, **1982**, 55, 995.
38. F. Ortmann, F. Bechstedt, W. G. Schmidt, *Phys. Rev. B.*, **2006**, 73, 205101.
39. Y. Liu, W. G. Gooddards III, *Mater. Trans.*, **2009**, 7, 1664.
40. V. K. Michealis, S. Kroeker *J. Phys. Chem. C*, **2010**, 114, 21736.
41. J. V. Hanna, K. J. Pike, T. Charpentier, T. F. Kemp, M. E. Smith, B. E. G. Lucier, R. W. Schurko, Lindsay S. Cahill, *Chem. Eur. J.* **2010**, 16, 3222.
42. J. P. Yesinowski, M. L. Buess, A. N. Garroway, *Anal. Chem.*, **1995**, 67, 2256.
43. D. L. Bryce, M. Gee, R. E. Wasylshen, *J. Phys. Chem. A.*, **2001**, 105, 10413.
44. G. H. Penner, R. Webber, L. A. O'Dell, *Can. J. Chem*, **2011**, 89, 1036.
45. M. Hildebrand, H. Hamaed, A. M. Namespetra, J. M. Donohue, R. Fu, b I. Hung, Z. Ganb, Robert W. Schurko, *CrystEngComm*, **2014**, 16, 7334.

# Chapter 6

## Conclusions and recommendation for future work

### Conclusions

The aims set out for this project were twofold. The first was to investigate the hypothesis that  $[\text{PtCl}_6]^{2-}$  anions are hydrated and establish the nature of the interaction of water molecules with the  $[\text{PtCl}_6]^{2-}$  anion salts. This involved the investigation of a hydration shell of the  $[\text{PtCl}_6]^{2-}$  anions in the solid state using single crystal diffraction studies. We attempted to develop cation chelated crown-ether with the  $[\text{PtCl}_6]^{2-}$  anions crystal systems with the aim of crystalizing water in the vicinity of the  $[\text{PtCl}_6]^{2-}$  anion. The variable temperature single crystal x-ray diffraction data obtained from these experiments will be used to investigate the effect weakening intramolecular interactions between the  $[\text{PtCl}_6]^{2-}$  anion and surrounding water molecules would have on the Pt-Cl bond displacement within the  $[\text{PtCl}_6]^{2-}$  anion. The hydration shell around the  $[\text{PtCl}_6]^{2-}$  anion will be investigated using an addition Cambridge Structural Database (CSD) analysis to search the current literature for crystal structures that may exhibit similar features to the computed hydration shell around the  $[\text{PtCl}_6]^{2-}$  anion. The combination of these two investigation is used to give some insight into the degree of hydration of the  $[\text{PtCl}_6]^{2-}$  anion in the solid-state.

Although it was not possible to obtain a crystal structure, which crystalized water around the  $[\text{PtCl}_6]^{2-}$  anion in a similar manner as suggested by the computational simulations performed by Naidoo *et al.*,<sup>1</sup> the CSD analysis showed that 17 crystal structures exist that have water molecules associated with the  $[\text{PtCl}_6]^{2-}$  anion in their crystal structures. The crystal structures obtained from the CSD analysis were used to validate the proposed hydrations sphere structure of the association of water with  $[\text{PtCl}_6]^{2-}$  anion in solution using X-ray diffraction studies. The analysis done on these structures confirmed the legitimacy of the

hydration shell by comparing the radial distribution function values from the simulation to those of the experimental values obtained from the 17 crystal structures displaying the association of the water with the  $[\text{PtCl}_6]^{2-}$  anion. The CSD analysis on these crystal structures show that from the 17 structures, nine have four waters associated to the  $[\text{PtCl}_6]^{2-}$  anion. In six of the crystal structures there are two water associated with the  $[\text{PtCl}_6]^{2-}$  anion and the remaining two structures only had one water associated to the anion.

Interestingly, the cation chelated crown ether experiments which were initially designed to crystallize water which associated to the  $[\text{PtCl}_6]^{2-}$  anion were not successful. Nevertheless, they showed that the *dibenzo-24-crown-8-ether* has a preferred structural confirmation upon its interaction with  $\text{Na}^+$  and  $\text{K}^+$  cations in the solid state. The *dibenzo-24-crown-8-ether* is folded (wrapped) around the  $\text{Na}^+$  cation. A similar observation was made upon doing a CSD analysis of the *dibenzo-24-crown-8-ether* and  $\text{Na}^+$  cation which showed that six crystal structures displayed similar features to our experiment, which showed the crown ether folded around the cation. The chelated crown ether experiments of the *dibenzo-24-crown-8-ether* and  $\text{K}^+$  cation showed that two  $\text{K}^+$  cations are situated within the cavity of the crown ether. It is not quite clear why we could not obtain any crystal structures, with which water crystalized around the  $[\text{PtCl}_6]^{2-}$  anion. It could be that the crown ether reduces the solvation shell of the  $[\text{PtCl}_6]^{2-}$  anion therefore, resulting in weak hydration energies around the anion.

Our second aim was to determine the temperature dependence of the  $^{195}\text{Pt}$  chemical shift of simple  $\text{X}_2[\text{PtCl}_6]$ , ( $\text{X}$  = various cations) salts, with a view of understanding its origin, and to probe the link of the temperature dependence of the  $\delta(^{195}\text{Pt})$  NMR shielding (measured as the chemical shift) on the anticipated Pt-Cl bond displacement increase as a function of temperature. After numerous attempts not a single crystal structure was obtained experimentally from our crystal engineering approach with water molecules, which was associated with the  $[\text{PtCl}_6]^{2-}$  anion. This made it difficult to assess the influence that changing intramolecular interaction between the water and the  $[\text{PtCl}_6]^{2-}$  anion has on the Pt-Cl bond displacement, since the sensitivity of  $^{195}\text{Pt}$  chemical shift in  $[\text{PtCl}_6]^{2-}$  anion has been shown to be extremely sensitive to subtle changes in Pt-Cl bond displacement.

We had hoped to study the Pt-Cl bond displacement in the solid state using a crystal structure which displayed the water associated with the  $[\text{PtCl}_6]^{2-}$  anion to see if Pt-Cl bond displacement could be correlated to  $^{195}\text{Pt}$  chemical shift in the solid state. We explored the option of recrystallizing one of the 17 crystal structures to perform variable temperature single crystal X-ray diffraction measurements but the symmetry of these the  $[\text{PtCl}_6]^{2-}$  anion in all 17 crystal structures obtained from the CSD analysis no longer retained its  $\text{O}_h$  symmetry which caused the Pt-Cl bond lengths in anions to be non-equivalent. This was problematic since all the previous experimental and computational studies by Jameson *et al.*<sup>2</sup> and Koch *et al.*<sup>3</sup> were performed on  $[\text{PtCl}_6]^{2-}$  anion with  $\text{O}_h$  symmetry. We therefore opted not to pursue this option.

We then opted to use three highly symmetrical *dication hexachloridoplatinate(IV)* salts are crystallized *i.e.* *dirubidium hexachloridoplatinate(IV)*  $\text{Rb}_2\text{PtCl}_6$ , *diammonium hexachloridoplatinate(IV)*  $(\text{NH}_4)_2\text{PtCl}_6$  and *bis(tetramethylammonium) hexachloridoplatinate(IV)*  $[\text{N}(\text{CH}_3)_4]_2\text{PtCl}_6$  salts, which is well known to have its  $[\text{PtCl}_6]^{2-}$  anion with  $\text{O}_h$  symmetry. The *rubidium* salt which has a purely electrostatic interaction ( $\text{Rb}^+\cdots\text{Cl-Pt}$ ) to the  $[\text{PtCl}_6]^{2-}$  anion are different from the *ammonium* salt that induces a partially electrostatic and strongly directed hydrogen bonding interaction ( $\text{N-H}\cdots\text{Cl-Pt}$ ). The *tetramethylammonium* ion is larger than the *rubidium* and *ammonium* cations which would have multiple hydrogen bonding interaction with  $[\text{PtCl}_6]^{2-}$  anion, due to its methyl groups. These three crystals although already well-studied in the literature are used to perform a series of temperature dependent SCXRD measurements. The results from these measurements are used to give insight into the degree of atomic displacement which would occur as a result of lattice expansion as a function of increasing temperature. The Pt-Cl bond lengths obtained from the SCXRD measurements performed as a function of temperature of the  $\text{Rb}_2\text{PtCl}_6$  and  $(\text{NH}_4)_2\text{PtCl}_6$  salts are used to calculate the expected  $^{195}\text{Pt}$  chemical shift over the temperature range at which the experiments were conducted.

The results from variable temperature SCXRD analysis show how the intra- and intermolecular interactions are affected upon lattice expansion as a function of temperature.

The data from these experiments also gave us some indication with respect to the degree of Pt-Cl bond displacement within the  $[\text{PtCl}_6]^{2-}$  anion as a function of temperature.

The same salts were used to perform the MAS SSNMR experiments to investigate the sensitivity of the  $^{195}\text{Pt}$  chemical shift as a function of temperature. The  $^{195}\text{Pt}$  chemical shifts of these salts show a remarkable sensitivity with respect to the type of cation used *i.e.* *rubidium*, *ammonium* and *tetramethylammonium*. The results from the variable temperature SCXRD measurements were used to account for the  $^{195}\text{Pt}$  chemical shift sensitivity and shed some light on the changing inter- and intramolecular atomic displacements. The predicted sensitivity of the  $^{195}\text{Pt}$  chemical shift is in very good agreement with that of experimental  $^{195}\text{Pt}$  chemical shifts sensitivity. This is in excellent agreement to previous studies<sup>3,4,5</sup> which suggest the Pt-Cl bond displacement to be central to  $^{195}\text{Pt}$  chemical shift.

The  $\text{Rb}_2\text{PtCl}_6$  and  $(\text{NH}_4)_2\text{PtCl}_6$  salt crystal structures were then used to compute SSNMR shielding parameters and electrostatic potential to give additional insights, which aided with the interpretation of experimental temperature dependence  $^{195}\text{Pt}$  chemical shift. The computed  $^{195}\text{Pt}$  isotropic shielding trends of the  $\text{Rb}_2\text{PtCl}_6$  salt agrees well with our observed experimentally observed  $^{195}\text{Pt}$  chemical shift trend displaying a linear change in its chemical shift as a function of temperature. The computed  $^{195}\text{Pt}$  isotropic shielding trends of the  $(\text{NH}_4)_2\text{PtCl}_6$  salt did not agree well with that of the experimental  $^{195}\text{Pt}$  chemical shift trends and more specifically the computed  $^{195}\text{Pt}$  isotropic shielding parameter at 400 K. The  $^{35}\text{Cl}$  quadrupolar coupling parameter is the dominant shielding contribution to the overall observed experimental  $^{195}\text{Pt}$  chemical shielding in *dication hexachloridoplatinate(IV)* salts.<sup>6</sup> Therefore, computing these parameters is of utmost importance since it influences all the shielding parameters of the neighboring NMR active nuclei in the  $(\text{NH}_4)_2\text{PtCl}_6$  salt. Computational and experimental  $^{35}\text{Cl}$  SSNMR studies<sup>7</sup> has shown that computational models have some difficulty computing the  $^{35}\text{Cl}$  quadrupolar coupling parameter of Cl atom/ion involved with hydrogen bonding interactions. They concluded that the computational basis set, geometry of the hydrogen bonding interaction, and distance between H atom/ion and Cl atom/ion play a key roles with respect to accurately calculating the  $^{35}\text{Cl}$  quadrupolar coupling parameter. If the hydrogen bonding distance falls outside 2.7 Å it has a high probability of being inaccurately

computed. The hydrogen bonding interaction between the ammonium and *hexachloridoplatinate(IV)* anion of the crystal structure at 400 K is greater than 2.7 Å and it could be due to the distance of the hydrogen bonding interaction in this structure that our computed  $^{195}\text{Pt}$  shielding parameter at 400 K is the outlier.

The semi-empirical quantum mechanically derived electrostatic potentials in both  $\text{Rb}_2\text{PtCl}_6$  and  $(\text{NH}_4)_2\text{PtCl}_6$  salts gave some interesting insights into the electrostatic behavior of these crystal structures as a function of temperature. The  $\text{Pt}^{\text{IV}}$  ion in both these salts show a steady increase of its electrostatic potential as a function of increasing temperature which is an indication of a loss electronic charge density on this ion. This coincides well with our experimentally observed downfield shift of the  $^{195}\text{Pt}$  chemical shift in both the  $\text{Rb}_2\text{PtCl}_6$  and  $(\text{NH}_4)_2\text{PtCl}_6$  salts as a function of temperature. The  $\text{Cl}^-$  ion in both  $\text{Rb}_2\text{PtCl}_6$  and  $(\text{NH}_4)_2\text{PtCl}_6$  salts shows a decrease in its electrostatic potential which indicated an increase in its electronic charge distribution. This implies that the electronic charge distribution from the  $\text{Pt}^{\text{IV}}$  ion is transferred to the  $\text{Cl}^-$  ion.

This work has reasoned that the three usually independently used analytical techniques *i.e.* SCXRD, SSNMR and DFT if used together are fundamental in understanding the overall observed experimental temperature dependent  $^{195}\text{Pt}$  chemical shift trends. One of the more significant findings to materialize from this study is how the interpretation of experimental temperature dependent  $^{195}\text{Pt}$  chemical shift trends in *dication hexachloridoplatinate(IV)* salts are dependent on a multitude of factors. The  $\text{Cl}^-$  ions have an extremely large quadrupolar coupling interaction ( $C_Q$ ) which is well known to be the largest contribution to the overall observed SSNMR chemical shielding in *dication hexachloridoplatinate(IV)* salts. The evidence from this study suggests that the chemical environment of the  $\text{Cl}^-$  ion in *dication hexachloridoplatinate(IV)* salts is crucial for interpreting the experimentally observed  $^{195}\text{Pt}$  chemical shift trends.

The results of this study show that the type of interaction to the  $\text{Cl}^-$  ion in *dication hexachloridoplatinate(IV)* salts influences the behavior of the  $^{195}\text{Pt}$  chemical shift trends. Our experimental and computational results support our theory of a “polarization of electron



density" from the  $\text{Pt}^{\text{IV}}$  ion towards the  $\text{Cl}^-$  ion in the  $[\text{PtCl}_6]^{2-}$  anion due to a weakening of intra-molecular interaction between anion and cation. This work contributes to the existing knowledge of highly symmetrical *dication hexahalometallate(IV)* salts and its behaviour upon lattice expansion. The methods used in this study have assisted in our understanding of experimental temperature dependent  $^{195}\text{Pt}$  chemical shift trends in the solid state. These findings enhanced our understanding of the quantum mechanical behavior in *dication hexachloridoplatinate(IV)* salts upon lattice expansion.

This work shows that using all three analytical techniques *i.e.* variable temperature SCXRD, SSNMR and DFT are vital to understanding and interpreting the dynamics of nuclei within a crystal lattice upon lattice expansion.

## Recommendation for future work

The experimental  $^{195}\text{Pt}$  chemical shift of *dication hexachloridoplatinate(IV)* salts have numerous overlapping chemical shielding parameters *i.e.* J-coupling, indirect coupling and isotope shifts of the  $^{195}\text{Pt}$  to the  $^{35/37}\text{Cl}$  nuclei. This makes it quite difficult to deconvolute all the chemical shielding contribution of these parameters on the experimentally observed  $^{195}\text{Pt}$  chemical shift. A computational approach can be taken to resolve this problem, by simulating the  $^{195}\text{Pt}$ - $^{35}\text{Cl}$  spectrum as well as the  $^{195}\text{Pt}$ - $^{37}\text{Cl}$  spectrum. One could overlay these spectra to see if they coincide with that of the experimental  $^{195}\text{Pt}$  chemical shift spectrum. The effect of the Pt-Cl dipole-dipole coupling, modified by the large  $\text{Cl}^-$  ion quadrupolar interactions, can be simulated. With the axial symmetry, this calculation is simplified since the quadrupolar and dipolar interactions are axially symmetric and have the same axis.

A DFT method has been developed to calculate J-coupling in the solid state,<sup>8</sup> where  $^{31}\text{P}$ - $^{29}\text{Si}$  coupling were calculated and showed excellent agreement to that of experimental SSNMR measurements. This method could be used to investigate the J-coupling, indirect and direct dipole-dipole interaction of the  $^{195}\text{Pt}$ - $^{35/37}\text{Cl}$  coupling parameters. The experiments we conducted on these salts were done on a 500 MHz instrument and if done at a higher

magnetic field more detailers could be extracted which would make the nature of these individual shielding parameters more prominent. If possible one could also use a triple resonance probe to decouple one of the two Cl isotopes to investigate the effect that a single Cl isotope has on the J coupling, indirect coupling and isotope shifts on the  $^{195}\text{Pt}$  nucleus.

An additional hindrance for calculating SSNMR parameters from *dication hexachloridoplatinate(IV)* salts is higher order effects (second order and higher). These effects occur when nuclei are coupled to quadrupolar nuclei *i.e.*  $^{195}\text{Pt}$  to  $^{35/37}\text{Cl}$  nuclei. An analytical expression has been developed for many higher order frequencies in which authors designed and computed SSNMR simulation<sup>9</sup> by incorporating all possible chemical shielding parameters one by one to see how they influence experimental SSNMR chemical shielding. A similar approach could be used to investigate the  $^{195}\text{Pt}$  isotropic shielding in order to determine the magnitude of the various chemical shielding parameters and quadrupolar coupling interaction within *dication hexachloridoplatinate(IV)* salts.

It is not possible with our current SSNMR experimental capabilities to study the  $\text{Cl}^-$  ions  $^{35/37}\text{Cl}$  isotopes of the  $[\text{PtCl}_6]^{2-}$  anion. The quadrupolar coupling of the  $\text{Cl}^-$  ion in *dication hexahalometallate(IV)* salts is extremely large and difficult to measure using conventional SSNMR. The computed temperature dependence  $^{35}\text{Cl}$  SSNMR parameters serve as a probe for investigating the electronic structure of this ion until such methods become available to study quadrupolar nuclei with such high quadrupolar coupling parameters. This thesis has only examined the experimental  $^{195}\text{Pt}$ ,  $^{85}\text{Rb}$  nuclei in  $\text{Rb}_2\text{PtCl}_6$  salt and the  $^{195}\text{Pt}$  nucleus in the  $(\text{NH}_4)_2\text{PtCl}_6$  salt since the  $^{35/37}\text{Cl}$  nuclei in both salts are extremely difficult to measure experimentally. The  $^1\text{H}$  nucleus was not studied using SSNMR since the instrument had some technical problems. These measurements could aid and complement the calculated SSNMR parameters and aid in the interpretation of the experimentally observed  $^{195}\text{Pt}$  chemical shift trends.

The computed SSNMR parameters of the  $(\text{NH}_4)_2\text{PtCl}_6$  salt showed that a dispersion correction functional, which accounts for long range London forces had some influence on the  $^{195}\text{Pt}$  isotropic shielding parameter. A more up-to-date dispersion correction functional<sup>10</sup>

which is parameterized for heavy metal elements such as the Pt nucleus, could improve the computational results and could even correct the outlying  $^{195}\text{Pt}$  shielding parameter and quadrupolar coupling interactions computed at 400 K. A more comprehensive computational investigation regarding the hydrogen bonding interaction between the anion and cation ( $\text{Pt}\cdots\text{Cl}\cdots\text{H}-\text{N}$ ) in the  $(\text{NH}_4)_2\text{PtCl}_6$  salt could establish a relationship regarding the strange behavior of the  $^{35}\text{Cl}$  ( $C_Q$ ) and  $^{195}\text{Pt}$  isotropic shielding parameters.

With the aid of variable temperature Raman spectroscopy it may be possible to probe the Pt-Cl stretching frequency in *dication hexachloridoplatinate(IV)* salts. The stretching frequency may be more sensitive to changes in Pt-Cl bond displacement to temperature increasing.<sup>11</sup> This could give additional information on the Pt-Cl bond displacement as a function of temperature, which could aid in the understanding of the experimental  $^{195}\text{Pt}$  chemical shift observed from the salts studied in this body of work.

## References

1. K. J. Naidoo, G. Klatt, K. R. Koch, D. J. Robinson, *Inorg. Chem.*, **2002**, 41, 1845.
2. C. J. Jameson, A. K. Jameson, *J. Phys. Chem.* **1986**, 85, 5484.
3. M. R. Burger, J. Kramer, H. Chermette, K. R. Koch, *Magn. Reson. Chem.*, **2010**, 48, S38.
4. Klaus R. Koch, M. R. Burger, J. Kramer, A. N. Westra, *Dalton Trans.*, **2006**, 3277.
5. C. J. Jameson, A. K. Jameson, *J. Chem. Phys.*, **1986**, 85, 5448.
6. S. Hayashi, K. Hayamizu, *Magn. Reson. Chem.*, **1992**, 30, 658
7. G. H. Penner, R. Webber, L. A. O'Dell, *Can. J. Chem.*, **2011**, 89, 1036, M. Hildebrand, H. Hamaed, A. M. Namespetra, J. M. Donohue, R. Fu, b I. Hung, Z. Ganb, Robert W. Schurko, *CrystEngComm*, **2014**, 16, 7334.
8. S. A. Joyce, J. R. Yates, C. J. Pickard, F. Mauri, *J. Chem. Phys.*, **2007**, 127, 204107.
9. P. J. Grandinetti, J. T. Ash, N. M. Trease, *Prog. NMR spectr.*, **2011**, 59, 121.
10. S. Grimme, *Comput. Mole. Sci.*, **2011**, 1, 211, S: Grimme, J. Antony, S. Ehrlich, H. Krieg, *J. Chem. Phys.*, **2010**, 132, 154104, I: D: Mackie, G: A: DiLabio, *J. Phys. Chem. A.*, **2008**, 112, 10968, S: Grimme, *J. Comput. Chem.*, **2006**, 27, 1787.
11. W. Preetz, G. Peters, D. Bubnitz, *Chem. Rev.*, **1996**, 96, 977.

# Appendix A

## Solid state Hydration of the $[\text{PtCl}_6]^{2-}$ anion

	Dibenzo-24-crown-8-ether disodium hexachloroplatinate(IV)	Dibenzo-24-crown-8-ether dipotassium hexachloroplatinate(IV)
chemical formula	$\text{C}_{48}\text{H}_{64}\text{Cl}_6\text{Na}_2\text{O}_{16}\text{Pt}$	$\text{C}_{24}\text{H}_{32}\text{Cl}_6\text{KO}_8\text{Pt}$
formula weight	1350.76	895.39
crystal system	monoclinic	triclinic
space group	$Cc$	$P1$
a (Å)	24.429(3)	8.4215(10)
b (Å)	17.0303(18)	10.506(2)
c (Å)	16.734(3)	10.5931(13)
$\alpha$ (°)	90.00	102.918(2)
$\beta$ (°)	129.5020(10)	111.1280(10)
$\gamma$ (°)	90.00	105.380(2)
Z	4	1
temperature (K)	100(2)	100(2)
calculated density ( $\text{g cm}^{-3}$ )	1.670	1.887
$\mu$ ( $\text{mm}^{-1}$ )	2.994	5.136
Reflections collected	12899	7159
$R_{\text{int}}$	0.010	0.0254
$R1$ [ $I > 2\sigma(I)$ ]	$R1 = 0.0271$ , $wR2 = 0.0538$	$R1 = 0.0349$ , $wR2 = 0.0689$

# Appendix B

## Single Crystal X-ray Diffraction

Table 1 Temperature dependence Single Crystal Diffraction measurement of diammonium hexachloroplatinate(IV) crystal data

	100	150	200	250	300	350	400
<b>chemical formula</b>	H <sub>8</sub> Cl <sub>6</sub> N <sub>2</sub> Pt	H <sub>8</sub> Cl <sub>6</sub> N <sub>2</sub> Pt	H <sub>8</sub> Cl <sub>6</sub> N <sub>2</sub> Pt	H <sub>8</sub> Cl <sub>6</sub> N <sub>2</sub> Pt	H <sub>8</sub> Cl <sub>6</sub> N <sub>2</sub> Pt	H <sub>8</sub> Cl <sub>6</sub> N <sub>2</sub> Pt	H <sub>8</sub> Cl <sub>6</sub> N <sub>2</sub> Pt
<b>formula weight</b>	443.87	443.87	443.87	443.87	443.87	443.87	443.87
<b>crystal system</b>	cubic	cubic	cubic	cubic	cubic	cubic	cubic
<b>space group</b>	<i>Fm</i> $\bar{3}$ <i>m</i>	<i>Fm</i> $\bar{3}$ <i>m</i>	<i>Fm</i> $\bar{3}$ <i>m</i>	<i>Fm</i> $\bar{3}$ <i>m</i>	<i>Fm</i> $\bar{3}$ <i>m</i>	<i>Fm</i> $\bar{3}$ <i>m</i>	<i>Fm</i> $\bar{3}$ <i>m</i>
<b>a (Å)</b>	9.772(2)	9.7957(15)	9.8180(7)	9.8416(7)	9.866(5)	9.892(3)	9.910(4)
<b>b (Å)</b>	9.772(2)	9.7957(15)	9.8180(7)	9.8416(7)	9.866(5)	9.892(3)	9.910(4)
<b>c (Å)</b>	9.772(2)	9.7957(15)	9.8180(7)	9.8416(7)	9.866(5)	9.892(3)	9.910(4)
<b><math>\alpha</math> (°)</b>	90.00	90.00	90.00	90.00	90.00	90.00	90.00
<b><math>\beta</math> (°)</b>	90.00	90.00	90.00	90.00	90.00	90.00	90.00
<b><math>\gamma</math> (°)</b>	90.00	90.00	90.00	90.00	90.00	90.00	90.00
<b>Z</b>	4	4	4	4	4	4	4
<b>temperature (K)</b>	100	150	200	250	300	350	400
<b>calculated density (g cm<sup>-3</sup>)</b>	3.159	3.137	3.115	3.093	3.014	3.045	3.030
<b><math>\mu</math> (mm<sup>-1</sup>)</b>	16.678	16.559	16.447	16.329	16.204	16.078	15.995
<b>Reflections collected</b>	1403	1424	1426	1448	1435	1510	1433
<b>R<sub>int</sub></b>	0.0215	0.0164	0.0192	0.0181	0.0149	0.0215	0.0182
<b>R1 [I&gt;2<math>\sigma</math>(I)]</b>	R1 = 0.0089, wR2 = 0.0219	R1 = 0.0085, wR2 = 0.0211	R1 = 0.0087, wR2 = 0.0202	R1 = 0.0083, wR2 = 0.0193	R1 = 0.0215, wR2 = 0.0440	R1 = 0.0073, wR2 = 0.0168	R1 = 0.0083, wR2 = 0.0194

Table 2 Temperature dependence Single Crystal Diffraction measurement of dirubidium hexachloroplatinate(IV) crystal data

	100	150	200	250	300	350	400
<b>chemical formula</b>	Cl <sub>6</sub> PtRb <sub>2</sub>	Cl <sub>6</sub> PtRb <sub>2</sub>	Cl <sub>6</sub> PtRb <sub>2</sub>	Cl <sub>6</sub> PtRb <sub>2</sub>	Cl <sub>6</sub> PtRb <sub>2</sub>	Cl <sub>6</sub> PtRb <sub>2</sub>	Cl <sub>6</sub> PtRb <sub>2</sub>
<b>formula weight</b>	578.73	578.73	578.73	578.73	578.73	578.73	578.73
<b>crystal system</b>	cubic	cubic	cubic	cubic	cubic	cubic	cubic
<b>space group</b>	<i>Fm<math>\bar{3}</math>m</i>	<i>Fm<math>\bar{3}</math>m</i>	<i>Fm<math>\bar{3}</math>m</i>	<i>Fm<math>\bar{3}</math>m</i>	<i>Fm<math>\bar{3}</math>m</i>	<i>Fm<math>\bar{3}</math>m</i>	<i>Fm<math>\bar{3}</math>m</i>
<b>a (Å)</b>	9.825(2)	9.844(2)	9.8616(12)	9.880(2)	9.9100(17)	9.932(3)	9.973(7)
<b>b (Å)</b>	9.825(2)	9.844(2)	9.8616(12)	9.880(2)	9.9100(17)	9.932(3)	9.973(7)
<b>c (Å)</b>	9.825(2)	9.844(2)	9.8616(12)	9.880(2)	9.9100(17)	9.932(3)	9.973(7)
<b><math>\alpha</math> (°)</b>	90.00	90.00	90.00	90.00	90.00	90.00	90.00
<b><math>\beta</math> (°)</b>	90.00	90.00	90.00	90.00	90.00	90.00	90.00
<b><math>\gamma</math> (°)</b>	90.00	90.00	90.00	90.00	90.00	90.00	90.00
<b>Z</b>	4	4	4	4	4	4	4
<b>temperature (K)</b>	100	150	200	250	300	350	400
<b>calculated density (g cm<sup>-3</sup>)</b>	4.053	4.030	4.008	3.986	3.950	3.923	3.876
<b><math>\mu</math> (mm<sup>-1</sup>)</b>	26.599	26.445	26.304	26.158	25.921	25.748	25.434
<b>Reflections collected</b>	1538	1540	1554	1558	1568	1592	1570
<b>R<sub>int</sub></b>	0.0295	0.0282	0.0292	0.0301	0.0297	0.0298	0.0315
<b>R1 [I&gt;2<math>\sigma</math>(I)]</b>	R1 = 0.0086, wR2 = 0.0218	R1 = 0.0080, wR2 = 0.0207	R1 = 0.0064, wR2 = 0.0171	R1 = 0.0082, wR2 = 0.0157	R1 = 0.0082, wR2 = 0.0176	R1 = 0.0069, wR2 = 0.0140	R1 = 0.0075, wR2 = 0.0255

Table 3 Temperature dependence Single Crystal Diffraction measurement of bis(tetramethyl)ammonium hexachloroplatinate(IV) crystal data

	100	150	200	250	300	350	400	450	500
chemical formula	C <sub>4</sub> H <sub>12</sub> Cl <sub>6</sub> NPt	C <sub>4</sub> H <sub>12</sub> Cl <sub>6</sub> NPt	C <sub>4</sub> H <sub>12</sub> Cl <sub>6</sub> NPt	C <sub>4</sub> H <sub>12</sub> Cl <sub>6</sub> NPt	C <sub>4</sub> H <sub>12</sub> Cl <sub>6</sub> NPt	C <sub>4</sub> H <sub>12</sub> Cl <sub>6</sub> NPt	C <sub>4</sub> H <sub>12</sub> Cl <sub>6</sub> NPt	C <sub>4</sub> H <sub>12</sub> Cl <sub>6</sub> NPt	C <sub>4</sub> H <sub>12</sub> Cl <sub>6</sub> NPt
formula weight	481.94	481.94	481.94	481.94	481.94	481.94	481.94	481.94	481.94
crystal system	tetragonal	tetragonal	Cubic superlattice	cubic	cubic	cubic	cubic	cubic	cubic
space group	<i>I4/m</i>	<i>I4/m</i>	<i>Fd3c</i>	<i>Fm3m</i>	<i>Fm3m</i>	<i>Fm3m</i>	<i>Fm3m</i>	<i>Fm3m</i>	<i>Fm3m</i>
a (Å)	8.8666(6)	8.9031(4)	25.3219(16)	12.6990(15)	12.731(7)	12.787(3)	12.865(18)	12.878(9)	12.929(11)
b (Å)	8.8666(6)	8.9031(4)	25.3219(16)	12.6990(15)	12.731(7)	12.787(3)	12.865(18)	12.878(9)	12.929(11)
c (Å)	12.6892(9)	12.6797(8)	25.3219(16)	12.6990(15)	12.731(7)	12.787(3)	12.865(18)	12.878(9)	12.929(11)
$\alpha$ (°)	90.00	90.00	90.00	90.00	90.00	90.00	90.00	90.00	90.00
$\beta$ (°)	90.00	90.00	90.00	90.00	90.00	90.00	90.00	90.00	90.00
$\gamma$ (°)	90.00	90.00	90.00	90.00	90.00	90.00	90.00	90.00	90.00
Z	4	4	48	12	8	8	8		
temperature (K)	100	150	200	250	300	350	400	450	500
calculated density (g cm <sup>-3</sup> )	3.209	3.185	4.053	2.965	3.103	1.767	3.007	2.998	2.963
$\mu$ (mm <sup>-1</sup> )	15.614	15.498	26.599	20.832	15.097	7.465	14.630	14.587	14.416
Reflections collected	2980	3046	1538	2232	3154	3189	3119	3406	3398
R <sub>int</sub>	0.0210	0.0219	0.0295	0.0844	0.0277	0.0284	0.0285	0.0318	0.0405
R1 [I>2 $\sigma$ (I)]	R1 = 0.0129,	R1 = 0.0138,	R1 = 0.0086,	R1 = 0.0432,	R1 = 0.0234,	R1 = 0.0211,	R1 = 0.0188,	R1 = 0.0175,	R1 = 0.0178,
	wR2 = 0.0317	wR2 = 0.0347	wR2 = 0.0218	wR2 = 0.1235	wR2 = 0.0610	wR2 = 0.0492	wR2 = 0.0421	wR2 = 0.0371	wR2 = 0.0458

# Appendix C

## Solid state Nuclear Magnetic Resonance spectroscopy

---

Table 1 Temperature dependent  $^{87}\text{Rb}$  MAS SSNMR for both  $\text{RbCl}$  and  $\text{Rb}_2\text{PtCl}_6$  and  $^{195}\text{Pt}$  MAS SSNMR of  $\text{Rb}_2\text{PtCl}_6$

Kelvin	Temp	$^{87}\text{Rb}$ SSNMR $\text{Rb-Cl}$	$^{87}\text{Rb}$ SSNMR $\text{Rb}_2\text{PtCl}_6$	$^{195}\text{Pt}$ MAS SSNMR
123	-150	139,3	39,1	146,4
133	-140	139,0	39,4	150,2
153	-120	138,3	40,1	155,0
173	-100	137,7	40,6	160,6
213	-60	136,6	41,9	174,3
233	-40	135,9	42,1	180,9
253	-20	135,4	42,7	187,8
273	0	134,7	43,3	194,9
293	20	134,2	43,8	201,6
299	26	134,0	44,1	203,8
313	40	133,4	44,4	209,1
333	60	132,7	44,9	215,9
353	80	132,2	45,6	223,8
373	100	131,3	46,1	231,5
393	120	130,6	46,6	239,3
413	140	129,8	47,0	253,5
423	150	129,6	47,3	



Table 2 Temperature dependence  $^{195}\text{Pt}$  MAS SSNMR of  $(\text{NH}_4)_2\text{PtCl}_6$ 

Kelvin(K)	Temp in °C	$^{195}\text{Pt}$ CPMAS SSNMR in ppm
153	-120	190.7
173	-100	191.3
213	-60	192.7
233	-40	194.9
253	-20	198.4
273	0	203.3
293	20	207.1
299	26	211.1
313	40	217.1
333	60	215.9
353	80	222.5
373	100	228.2
393	120	234.7
413	140	241.4
423	150	248.5
433	160	256.2

Table 3 Temperature dependence  $^{195}\text{Pt}$  MAS SSNMR of  $[(\text{CH}_3)_4\text{N}]_2\text{PtCl}_6$ 

Kelvin(K)	Temp in °C	$^{195}\text{Pt}$ CP/MAS SSNMR in ppm
148	-125	327.9
153	-120	325.5
158	-115	308.8
163	-110	323.9
173	-100	324.5
183	-90	323.0
193	-80	323.2
203	-70	324.3
213	-60	324.6
223	-50	325.5
233	-40	333.4
243	-30	329.2
253	-20	330.8
263	-10	334.8
273	0	336.6
283	10	348.0
288	15	343.7
293	20	345.4
303	30	350.8
313	40	355.3
323	50	359.2
333	60	366
343	70	373.4
353	80	380.0
373	100	387.4
383	110	392.3
393	120	398.2
403	130	403.4
413	140	409.2
423	150	415.2
433	160	420.9

# Appendix D

## Density Functional Theory and semi-empirical calculations

---

### Geometry optimization of the $(\text{NH}_4)_2\text{PtCl}_6$ salts crystal structures

The N, Cl and Pt atom in 7 seven crystal structures were fixed. The H atom in all the crystal structures were optimized using GGA, PBE functionals using a  $E_{\text{cut}} = 400$  eV and K-point mesh at  $4 \times 4 \times 4$  using the CASTEP-Geometry optimization command.

The lattice parameters of all crystal structures used for the NMR-CASTEP calculations were adjusted using the slopes obtained from the temperature dependence SCXRD measurements. The  $\text{Rb}_2\text{PtCl}_6$  and  $(\text{NH}_4)_2\text{PtCl}_6$  crystal structures all have a cubic  $Fm\bar{3}m$  space group. This makes the lattice parameters  $a = b = c$  and  $\alpha = \beta = \gamma$ . Therefore by plotting the lattice parameters  $a$  as a function of temperature gives a linear slope (Fig.1 and 2). The slopes obtained from these plots are used to adjust lattice parameters in computational calculation since these computational calculations are performed at static molecular motion at 0 K. The parameters are adjusted to simulate the motion at which the SCXRD experiments were conducted.

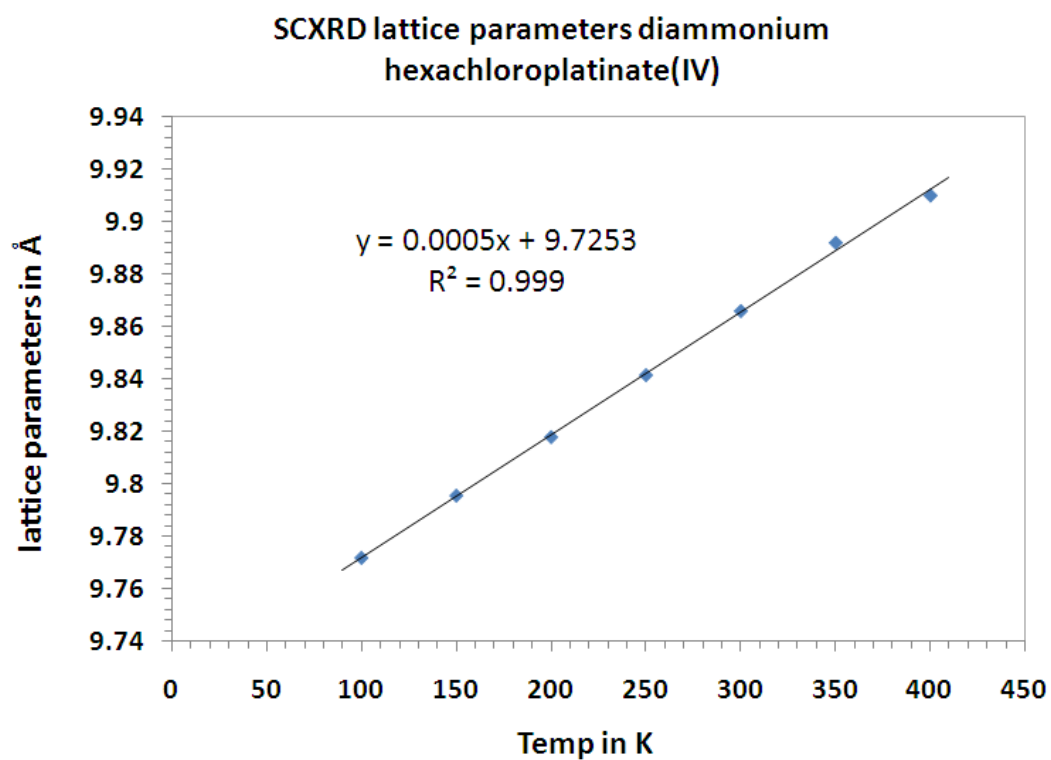


Figure 1 Temperature dependence lattice parameters of diammonium hexachloroplatinate(IV) salts

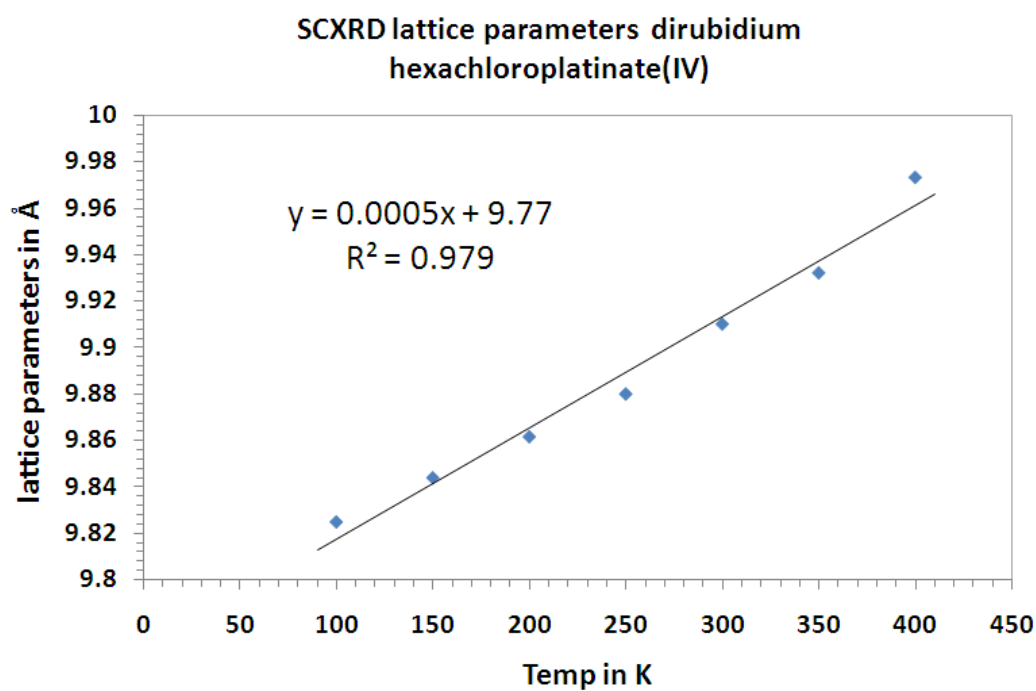


Figure 2 Temperature dependence lattice parameters of dirubidium hexachloroplatinate(IV) salts

This is done by using the slope obtained from Fig. 1 and 2. The equation  $[(y_E - y_C) = 0.0005(x_E - x_C) + 9.7253]$  where  $y_E$  is the experimental lattice parameter,  $y_C$  is the parameter to be calculated for the computational calculation. The value  $x_E$  is the experimental temperature and  $x_C$  is the computational temperature which equals 0.

## Results

### diammonium hexachloroplatinate(IV)

Temperature in K	SCXRD lattice parameters	adjusted lattice parameters
100	9.772	9.7753
150	9.7957	9.8003
200	9.818	9.8253
250	9.8416	9.8503
300	9.866	9.8753
350	9.892	9.9003
400	9.91	9.9253

### dirubidium hexachloroplatinate(IV)

Temperature in K	SCXRD lattice parameters	adjusted lattice parameters
100	9.825	9.82
150	9.844	9.845
200	9.8616	9.87
250	9.88	9.895
300	9.91	9.92
350	9.932	9.945
400	9.973	9.97